Contributions to Disturbance-Observer-Based Control : Application to Synchronous Motor-Based Variable Speed Drive Systems

Yongchao Liu

THESE DE DOCTORAT DE L'ETABLISSEMENT UNIVERSITE BOURGOGNE FRANCHE-COMTE

PREPAREE A L'INSTITUT FEMTO-ST, UMR 6174, CNRS

Ecole doctorale n°37

Sciences pour l'Ingénieur et microtechniques (SPIM)

Doctorat d'Automatique

Par

LIU Yongchao

Contributions to Disturbance-Observer-Based Control: Application to Synchronous Motor-Based Variable Speed Drive Systems

Thèse présentée et soutenue à Belfort, le 16 Décembre 2020.

Composition du Jury:

Pr. WIRA Patrice	Université de Haute Alsace	Président
Pr. BENBOUZID Mohamed	Université de Bretagne Occidentale	Rapporteur
Dr. PUCCI Marcello	National Research Council of Italy/INM	Rapporteur
Dr. DEPERNET Daniel	Université Bourgogne Franche-Comté	Examinateur
Dr. LIDOZZI Alessandro	Roma Tre University	Examinateur
Dr. LAGHROUCHE Salah	Université Bourgogne Franche-Comté	Directeur de thèse
Pr. CIRRINCIONE Maurizio	The University of the South Pacific	Codirecteur de thèse
Dr. N'DIAYE Abdoul	Université Bourgogne Franche-Comté	Codirecteur de thèse

ACKNOWLEDGMENTS

First of all, I would like to express my deepest gratitude to my supervisor, Dr. Salah Laghrouche, for his continuous support and guidance in my research and the preparation of the thesis. I would also like to express my deepest appreciation to my co-supervisors, Prof. Maurizio Cirrincione, for his insightful comments on the motor drive system and, Dr. Abdoul N'Diaye, for his help in the hardware-in-the-loop and experimental studies.

I am very grateful to Dr. Daniel Depernet for his help in the experimental studies. During my doctoral studies, I have had the pleasure of working with many capable doctoral students and research engineers. I am particularly grateful to Mr. Kui Chen, Mr. Yu Wu, Mr. Jinjian Li, Mr. Lei Zhang, Mr. Chen Liu, Mr. Zhihao Peng, Mr. Djelalli Larioumlil, Mr. Patrice Luberda, Mr. Pierre Diebolt and Mr. Minh-Dinh Tran.

I would like to thank Prof. Mohamed Benbouzid and Dr. Marcello Pucci for reviewing the thesis. I would also like to thank Prof. Patrice Wira, Dr. Daniel Depernet and Dr. Alessandro Lidozzi for accepting as jury members.

I sincerely appreciate the support of China Scholarship Council and USP-SRT Research Project ACOSREV during my doctoral studies.

Finally, I am deeply grateful to my parents for their selfless love and encouragement, which support me to finish the thesis.

ACRONYMS

2L-VSI	Two-level voltage-source inverter
AC	Alternating current
ANN-DO	Artificial neural network-based disturbance observer
BP	Back-propagation
CSM	Complementary sliding-mode
DC	Direct current
DO	Disturbance observer
DOC	Disturbance observer-based control
DSP	Digital signal processor
DTC	Direct torque control
ENN	Elman neural network
ENN-DO	Elman neural network-based disturbance observer
ENN-ICSM	Elman neural network-based intelligent complementary sliding-mode
ESO	Extended state observer
FNN	Feedforward neural network
FNN-DO	Feedforward neural network-based disturbance observer
FOC	Field-oriented control
FOSM	First-order sliding-mode
FOSMO	Frist-order sliding-mode observer
HIL	Hardware-in-the-loop
HNN	Hermite neural network
HNN-DO	Hermite neural network-based disturbance observer
ICSM	Intelligent complementary sliding-mode
IGBT	Insulated-gate bipolar transistor
IPMSM	Interior permanent-magnet synchronous motor
MRA	Model reference adaptive
NdFeB	Neodymium-iron-boron
PMSM	Permanent-magnet synchronous motor

PMSM-VSD	Permanent-magnet synchronous motor-based variable speed drive
PWM	Pulse-width modulation
RBFNN	Radial basis function neural network
RBFNN-DO	Radial basis function neural network-based disturbance observer
RBFNN-MRA	Radial basis function neural network-based model reference adaptive
RBFNN-ICSM	Radial basis function neural network-based intelligent complementary sliding-mode
RNN	Recurrent neural network
RNN-DO	Recurrent neural network-based disturbance observer
SOSM	Second-order sliding-mode
SPMSM	Surface-mounted permanent-magnet synchronous motor
SPMSM-VSD	Surface-mounted permanent-magnet synchronous motor-based variable speed drive
SPWM	Sinusoidal pulse-width modulation
STA	Super-twisting algorithm
STSM	Super-twisting sliding-mode
STSMO	Super-twisting sliding-mode observer
SynRM	Synchronous reluctance motor
SynRM-VSD	Synchronous reluctance motor-based variable speed drive
TLP	Three-layer perceptron
VSD	Variable speed drive
VSI	Voltage-source inverter

LIST OF FIGURES

LIST OF TABLES

CONTENTS

1

GENERAL INTRODUCTION

1.1 Overview of Variable Speed Drive System

The electrical drive technology is one of the most critical technologies for the quality of life of human beings. It has found wide applications in domestic and industrial sectors, including, but certainly not limited to, *transportation electrification* such as pure electrical vehicles, hybrid electrical vehicles, locomotives, metros, electrical multiple units and electrical boats, *renewable energy conversion* such as wind power generation systems, hydroelectric power plants, fuel cell power generation systems and marine power generation systems, *industrial manufacturing* such as machine tools, robots and conveyors, *home appliances* such as washing machines, electrical fans and air conditioning systems [1]-[6]. In recent decades, with the acceleration of urbanization and modernization of many countries in the world, there are increasing concerns about global warming and air quality issues, leading to the increasing demand for the environmentally-friendly alternatives to fossil-fuel-based electrical power generation systems and transportation systems, most of which require the advanced electrical drive technology [3].

The variable speed drive (VSD) system, which is the electrical drive system used for the regulation of both speed and torque of the electrical motor, plays a key role in the existing environmentally-friendly transportation systems [2]. Such a system is an electromechanical device that converts the electrical energy from the direct current (DC) or the alternating current (AC) electrical power supply into mechanical energy for the mechanical load. The VSD system can work in a hostile environment, offer a wide range of torques over a wide speed range, provide excellent starting and acceleration performance, and achieve zero-emission, low-noise and four-quadrant operation [1]. As illustrated in Figure 1.1, the VSD system is mainly composed of six parts: the

electrical power supply, the power electronic converter, the electrical motor, the mechanical load, the control unit and the measurement unit [1].

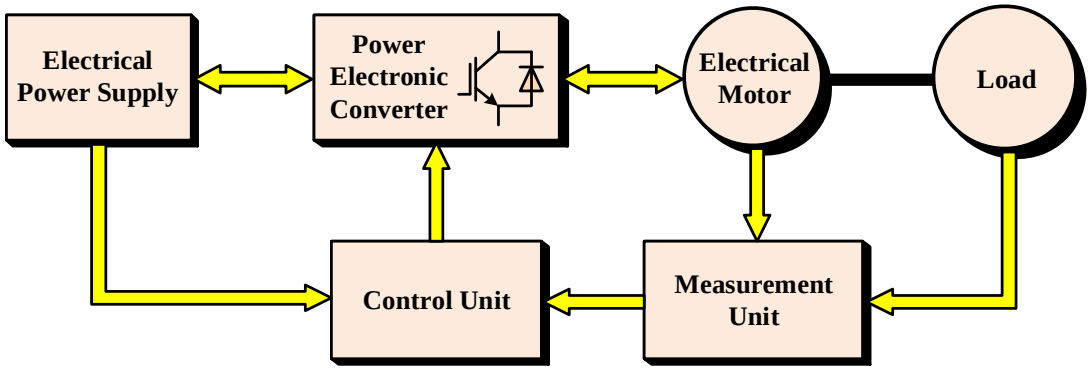

Figure 1.1 Block diagram of the variable speed drive system.

The electrical power supply in the VSD system is used to meet different electrical power requirements of power electronic converters and electrical motors in different applications. In general, it receives the electrical energy from one or more power sources, such as electrical power grids, renewable energy storage devices, and generators in thermal, wind or hydro power stations [1], [4], [6]. Furthermore, it can also receive the electrical power generated by the electrical motor operating in the regenerating mode, and feed it back to the power source.

The power electronic converter in the VSD system is constructed using uncontrollable and/or controllable power semiconductor devices, including diodes, silicon controlled rectifiers, metal-oxide-semiconductor field-effect transistors and insulated-gate bipolar transistors (IGBTs) [1]-[3]. By means of the high-frequency switching of adopted controllable power semiconductor devices, power electronic converters can convert the electrical energy received from the electrical power supply into appropriate forms in terms of the voltage or the current based on the requirements of electrical motors. Although there exist many topologies of power electronic converters for different purposes, the most widely used topologies in VSD systems are uncontrolled and controlled AC-DC converters, commonly known as rectifiers, AC-DC converters, commonly known as inverters, and DC-DC converters. The existing inverters used in VSD systems can be divided into various types based on different criteria [1]-[3]. According to the types of energy storage devices in the DC-link, they can be divided into current-source and voltage-source inverters (VSIs). Based on the utilization ratio of the DC-link voltage, they can be divided into half-bridge and full-bridge inverters. Depending on the number of output voltage or current levels, they can be divided into two-level and multilevel inverters. According to the number of electrical motor's phases, they can be divided into

one-phase, two-phase, three-phase and multiphase inverters. Among these different types of inverters, the three-phase two-level half-bridge VSI, or two-level VSI (2L-VSI) for short, is the most widely used inverter for commercial VSD systems [1]-[3].

The electrical motor in the VSD system achieves the electromechanical energy conversion and can be regarded as the heart of the VSD system. In fact, the purpose of the use of the control unit and the power electronic converter in the VSD system is to make it possible for the electrical motor to achieve the high-performance operation. The existing electrical motors can be divided into DC and AC motors according to the types of supplying electrical power. Moreover, they can be divided into single-phase, two-phase, three-phase and multiphase motors based on the number of phases [1]. Compared with DC motors, AC motors provide wider speed range, achieve better speed and torque control performance, and require less maintenance [3]. Owing to such attractive features, AC motors are dominant in high-performance VSD systems. Until now, various types of AC motors have been designed for VSD systems [1]-[10]. Among them, induction motors, permanent-magnet synchronous motors (PMSMs) and switched reluctance motors have gained much attention in recent decades [1]-[10]. The PMSMs used in VSD systems can be divided into surface-mounted PMSMs (SPMSMs) and interior PMSMs (IPMSMs) depending on the location of permanent-magnet materials in the rotor [1]-[3].

The mechanical load in the VSD system has different characteristics in different applications. Meeting the requirement of the mechanical load in terms of the torque and the power is the purpose of designing the VSD system. Therefore, before starting to design the VSD system, the characteristics of the mechanical load should be obtained, such that some unexpected phenomena including overloading, overheating and instability can be avoided [1].

The measurement unit in the VSD system is mainly dependent on various measuring devices, including the absolute or the incremental encoder for acquiring the rotor position information of the electrical motor, the Hall-effect current sensors for measuring two-phase or three-phase stator currents of the electrical motor, and the DC-link voltage sensor for measuring the DC-link voltage. The main task of the measurement unit is to achieve the real-time measurement of all necessary information required by the control unit.

The control unit in the VSD system is mainly based on hardware controllers, such as microprocessors, field programmable gate arrays and digital signal processors (DSPs), and relevant software. The control unit can be regarded as the head of the VSD system. Through the measurement unit, the control unit samples all necessary information required by the implementation of the control strategy. Afterward, based on the implemented control strategy, the control unit generates the high-

frequency switching command for the controllable power semiconductor devices in the power electronic converter such that the desired response of the electrical motor and the required characteristics of the mechanical load can be accomplished.

In order to achieve certain traction characteristics of the VSD system, high-performance control strategy should be implemented in the control unit. With the rapid development of hardware controllers, the closed-loop vector-based control strategies have been widely used in high-performance VSD systems, where the field-oriented control (FOC) strategy and the direct torque control (DTC) strategy are two most widely used control strategies [1]-[3], [7]. Both these two control strategies adopt the cascaded control structure composed of the inner loop and the outer loop. With respect to the inner loop, the FOC strategy uses it to achieve the tracking control of the certain current components and the DTC strategy use it to achieve the tracking control of the stator flux linkage and the torque. With respect to the outer loop, both these two control strategies use it to achieve the tracking control of the rotor speed.

1.2 Motivation

In this thesis, the focus is on the field-oriented controlled three-phase SynRM-based VSD (SynRM-VSD) system and the field-oriented controlled three-phase SPMSM-based VSD (SPMSM-VSD) system. Note that all AC motors mentioned in the rest of this thesis are three-phase AC motors. In the FOC strategy for each considered VSD system, the rotor speed controller used in the outer loop, or as often called the speed control loop, is designed based on the speed dynamics, while two stator current controllers used in the inner loop, or as often called the current control loop, are designed using two current dynamics in the rotor reference frame. From a practical point of view, the speed and the current dynamics of each considered motor are nonlinear systems subjected to *unmodeled dynamics*, such as the current measurement errors, the cogging torque and the rotor flux linkage harmonics of the SPMSM, and the inverter nonlinearities, *parametric uncertainties*, including the variations of mechanical and electrical parameters, and *external disturbances*, such as the load torque and the friction torque [11]. In the speed or the current tracking error dynamics of each considered motor, the aforementioned unmodeled dynamics, parametric uncertainties and external disturbances can be lumped together, and the lumped disturbance in each tracking error dynamics is time-varying in practice.

In the FOC strategy, the linear proportional-integral (PI) controller is the most popular choice for the speed or the current control [1]-[3]. On the basis of the integral action, the linear PI controller

can asymptotically stabilize the tracking error dynamics in the presence of the constant lumped disturbance [12]. However, as has been stated above, the lumped disturbance in the speed or the current tracking error dynamics of each considered motor is time-varying rather than constant. Therefore, the linear PI controller cannot provide satisfactory control performance over a wide operating range of each considered VSD system. In order to address the robust tracking control problem of each considered VSD system, the nonlinear controller has been regarded as a better solution compared with the linear PI controller [13]-[30].

In the last three decades, with the rapid development of the hardware controller, various nonlinear controllers have been designed and integrated into the FOC strategies for two considered VSD systems, such as adaptive controllers [13]-[16], sliding-mode controllers [17]-[20], backstepping controllers [21]-[24], predictive controllers [25]-[28] and robust controllers [29], [30]. In theory, with the controller parameters satisfying some stability criteria, these nonlinear controllers can achieve the asymptotic or the finite-time stabilization of the tracking error dynamics in the presence of the time-varying lumped disturbance. The tracking control system based on any one of the aforementioned controllers can be regarded as a one-degree-of-freedom system in which the feedback regulation mechanism is used to deal with several control performance indices, such as system stability, tracking performance, disturbance attenuation and robustness [31]. However, with the feedback regulation mechanism, there often exist contradictions among some above-mentioned control performance indices for the tracking control system, and one of the most remarkable contradictions is the tracking performance versus disturbance attenuation [31]. Taking the sliding-mode speed controller as an example, such a controller is dependent on the bounded-function-based feedback regulation mechanism [17]-[20]. When the gains of such a controller increase, the disturbance attenuation ability of the speed tracking control system improves, leading to the better dynamic response and the lower steady-state tracking error. On the other hand, if the controller gains are too large, severe high-frequency oscillations, or as often called the *chattering*, arise in the controller output, resulting in significantly degraded speed tracking performance and large noise [18], [32]. Therefore, the conservative gains are usually selected for the adopted nonlinear controller to trade off some above-mentioned control performance indices, which makes it difficult for this nonlinear controller to meet the performance requirements in some applications.

In order to improve the disturbance attenuation ability without sacrificing the tracking performance of the tracking control system, the idea of the *disturbance-observer-based control* (DOC) can be introduced to the controller design [12], [31], [33]. As illustrated in Figure 1.2, the principle behind the DOC is that the disturbance observer (DO) is introduced to the tracking control system such that the disturbance attenuation is accomplished by the DO-based feedforward

compensation mechanism, adding an extra degree of freedom to the tacking control system. Note that the internal disturbances shown in Figure 1.2 denote the disturbances caused by the parametric uncertainties of the plant. With the help of the DO, the design of the nonlinear controller is able to focus on the tracking performance specifications without considering the disturbance attenuation problem. In other words, the design of the DO-based nonlinear controller, or as often called the *composite controller*, follows the separation principle, i.e., the required tracking performance and the disturbance attenuation are accomplished by the nonlinear-controller-based feedback regulation mechanism and the DO-based feedforward compensation mechanism, respectively [12], [31], [33]. With the same conservative controller gains, the composite controller can achieve better tracking performance than the adopted nonlinear controller.

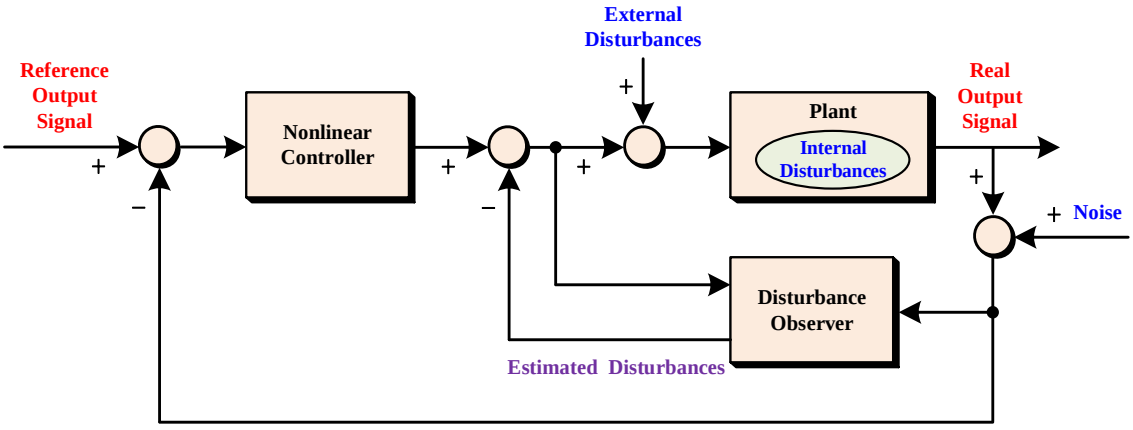

Figure 1.2 Block diagram of the disturbance-observer-based nonlinear control.

Until now, assorted types of DOs have been used to construct composite controllers for the field-oriented controlled AC motor drive systems, including the frequency-domain DO [34], the unknown input observer [35], the generalized PI observer [36], the extended state observer (ESO) [37], the first-order sliding-mode observer (FOSMO) [38], the extended FOSMO [39], the super-twisting sliding-mode observer (STSMO) [40] and the artificial neural network-based disturbance observers (ANN-DOs) [41]-[50]. However, the composite controllers for some existing nonlinear controllers such as the modified super-twisting sliding-mode (STSM) controller proposed in [51] still need to be developed. Moreover, with respect to some existing composite controllers such as the one proposed in [52], there are some issues that need to be tackled.

1.3 Main Contributions

This thesis is dedicated to the development of novel composite controllers for a single-input uncertain nonlinear system with relative degree one and their application to the construction of robust FOC strategies for 2L-VSI-fed SynRM-VSD and 2L-VSI-fed SPMSM-VSD systems. The main contributions of this thesis are summarized as follows:

1) A composite controller consisting of a standard STSM controller, a Hermite neural network-based disturbance observer (HNN-DO) and an error compensator is proposed for a single-input uncertain nonlinear system with relative degree one and applied to the speed control loop of the FOC strategy for the 2L-VSI-fed SynRM-VSD system. In such a composite controller, the standard STSM controller is used to achieve the finite-time stabilization of the sliding variable dynamics, the HNN-DO is used to compensate the lumped disturbance in the sliding variable dynamics and the error compensator is used to compensate the approximation error of the adopted HNN-DO. The rigorous stability analysis of the sliding variable dynamics with the proposed composite controller is presented. Based on that, the learning laws for the connective weights between the output neuron and the hidden neurons in the HNN-DO and the error compensator are rigorously derived. Even though the HNN-DO is replaced by another type of ANN-DO in this composite controller, such learning laws can still be used to update the connective weights between the output neuron and the hidden neurons in the adopted ANN-DO and its corresponding error compensator online. Besides the composite speed controller, two composite current controllers, each of which consists of two standard STSM controllers and takes the magnetic saturation effect into account, are also proposed for the current control loop of the FOC strategy for the 2L-VSI-fed SynRM-VSD system. Rigorous stability analysis of each current tracking error dynamics using the corresponding composite current controller is presented. Comparative hardware-in-the-loop (HIL) tests between the proposed FOC strategy, which uses the proposed composite speed controller and two composite current controllers, and the classic STA-based FOC strategy, which uses a standard STSM speed controller and two linear PI current controllers, for the 2L-VSI-fed SynRM drive system are performed to verify the feasibility and the superiority of the former.

2) A composite controller consisting of a modified STSM controller and a second-order ESO is proposed for a single-input uncertain nonlinear system with relative degree one and applied to the speed control loop of the FOC strategy for the 2L-VSI-fed SPMSM-VSD system. In such a composite controller, the modified STSM controller is used to achieve the finite-time stabilization of the sliding variable dynamics and the second-order ESO is used to compensate the lumped disturbance in the sliding variable dynamics. The rigorous stability analysis of the

sliding variable dynamics with the proposed composite controller is presented. Comparative experimental tests among the standard STSM speed controller, the ESO-based standard STSM speed controller, the modified STSM speed controller and the proposed composite speed controller are performed on a suitably developed experimental test bench in the frame of the FOC strategy for the 2L-VSI-fed SPMSM-VSD system. Experimental results validate the feasibility and the superiority of this proposed composite speed controller.

3) A composite controller consisting of a sign function-based complementary sliding-mode (CSM) controller and a STSMO is proposed for a single-input uncertain nonlinear system with relative degree one and applied to the speed control loop of the FOC strategy for the 2L-VSI-fed SPMSM-VSD system. In such a composite controller, the sign function-based CSM controller is used to achieve the asymptotic stabilization of the output tracking error dynamics and the STSMO is used to compensate the lumped disturbance in the output tracking error dynamics. The rigorous stability analysis of the output tracking error dynamics with the proposed composite controller is presented. Comparative experimental tests among the classic CSM speed controller, three selected Elman neural network (ENN)-based intelligent CSM (ENN-ICSM) speed controllers, each of which is dependent on a ENN-based DO (ENN-DO) and an error compensator, and the proposed composite speed controller are performed on a suitably developed experimental test bench in the frame of the FOC strategy for the 2L-VSI-fed SPMSM-VSD system. Experimental results validate the feasibility and the superiority of this proposed composite speed controller.

4) A composite controller based on a classic model reference adaptive (MRA) controller and a STSMO is proposed for a single-input uncertain nonlinear system with relative degree one and applied to the speed control loop of the FOC strategy for the 2L-VSI-fed SPMSM-VSD system. A stable first-order linear model is selected as the reference model to describe the desired output trajectory. The proposed composite controller comprises three terms. The first term is the stabilization term, which is dependent on known parameters of the system and the selected reference model, for stabilizing the output tracking error dynamics asymptotically. The second term is the disturbance compensation term, which is based on the STSMO, for compensating the lumped disturbance in the output tracking error dynamics. The third term is the error compensation term, which is updated online by an adaptive law, for confronting the estimation error of the STSMO in practice. The rigorous stability analysis of the output tracking error dynamics with the proposed composite controller is presented. Based on that, the adaptive law for the error compensation term in the proposed composite controller is rigorously derived.

Comparative experimental tests among three selected classic MRA speed controllers, three radial basis function neural network-based MRA (RBFNN-MRA) speed controllers, each of which is dependent on a RBFNN-based DO (RBFNN-DO), and the proposed composite speed controller are performed on a suitably developed experimental test bench in the frame of the FOC strategy for the 2L-VSI-fed SPMSM-VSD system. Experimental results validate the feasibility and the superiority of this proposed composite speed controller.

Remark 1.1. In this thesis, to distinguish above-mentioned proposed composite controllers from each other, the proposed composite controller consisting of a standard STSM controller, a HNN-DO and an error compensator is named as the *type-1 composite controller*, the proposed composite controller consisting of a modified STSM controller and a second-order ESO is named as the *type-2 composite controller*, the proposed composite controller consisting of a sign function-based CSM controller and a STSMO is named as the *type-3 composite controller*, and the proposed composite controller consisting of a classic MRA controller and a STSMO is named as the *type-4 composite controller*.

1.4 Scientific Publications

Journal Paper

[1] Y. -C. Liu, S. Laghrouche, A. N'Diaye, and M. Cirrincione, "Hermite neural network-based second-order sliding-mode control of synchronous reluctance motor drive systems," *Journal of the Franklin Institute*, Accepted.

[2] Y. -C. Liu, S. Laghrouche, D. Depernet, A. Djerdir, and M. Cirrincione, "Disturbance-observer-based complementary sliding-mode speed control for PMSM drives: A super-twisting sliding-mode observer-based approach." *IEEE Journal of Emerging and Selected Topics in Power Electronics*, Accepted.

Journal Papers Submitted for Peer-Reviewing

[1] Y. -C. Liu, S. Laghrouche, D. Depernet, A. N'Diaye, A. Djerdir, and M. Cirrincione, "Disturbance-observer-based speed control for SPMSM drives using modified super-twisting algorithm and extended state observer."

[2] Y. -C. Liu, S. Laghrouche, D. Depernet, A. Djerdir, and M. Cirrincione, "Super-twisting sliding-mode observer-based model reference adaptive speed control for PMSM drives."

Conference Papers

[1] Y. -C. Liu, S. Laghrouche, A. N'Diaye, and M. Cirrincione, "Active-flux-based super-twisting sliding mode observer for sensorless vector control of synchronous reluctance motor drives," in *Proceedings of 7th International Conference on Renewable Energy Research and Applications*, pp. 402-406, Oct. 2018.

[2] Y. -C. Liu, S. Laghrouche, A. N'Diaye, S. Narayan, G. Cirrincione, and M. Cirrincione, "Sensorless control of synchronous reluctance motor drives based on the TLS EXIN neuron," in *Proceedings of 2019 IEEE International Electric Machines & Drives Conference*, pp. 1737-1741, May 2019.

[3] Y. -C. Liu, S. Laghrouche, A. N'Diaye, and M. Cirrincione, "Model predictive current and capacitor voltage control of post-fault three-level NPC inverter-fed synchronous reluctance motor drives," in *Proceedings of 2019 International Aegean Conference on Electrical Machines and Power Electronics & 2019 International Conference on Optimization of Electrical and Electronic Equipment*, pp. 221-226, Aug. 2019.

[4] Y. -C. Liu, A. N'Diaye, S. Laghrouche, A. Djerdir, and M. Cirrincione, "Identification of neural network magnetic models of synchronous reluctance motors based on Levenberg-Marquardt back-propagation algorithm and genetic algorithm optimization," in *Proceedings of 2019 International Conference on Innovation Energy*, pp. 1-10, Oct. 2019.

1.5 Outline of the Thesis

This thesis is divided into eight chapters. The remaining chapters are organized as follows:

Chapter 2: At first, the practical dynamic models of the SPMSM and the SynRM in terms of the rotor mechanical speed and two stator current components in the rotor reference frame are presented, respectively. In the practical dynamic model of the SPMSM, the unmodeled dynamics, including the inverter nonlinearities, the cogging torque, the rotor flux linkage harmonics and the current measurement errors, the external disturbances consisting of the load torque and the friction torque, and the parametric uncertainties comprising the variations of mechanical and electrical parameters are taken into account. In the practical dynamic model of the SynRM, the unmodeled dynamics, including the inverter nonlinearities and the current measurement errors, the external disturbances composed of the load torque and the friction torque, and the parametric uncertainties consisting of the variations of mechanical and electrical parameters are taken into account. Afterward, the principles of the FOC strategies for these two considered VSD systems are briefly introduced.

Finally, the descriptions of the HIL test bench and the experimental test bench are presented.

Chapter 3: Two model-based extended DOs and four model-free DOs for a single-input uncertain nonlinear system with relative degree one are briefly reviewed. More specifically, the two model-based extended DOs are the second-order ESO and the STSMO. Four model-free DOs include three widely used feedforward neural network-based DOs (FNN-DOs), i.e., the three-layer perceptron-based DO (TLP-DO), the RBFNN-DO and the HNN-DO, and a widely used recurrent neural network-based DO (RNN-DO), i.e., the ENN-DO. Furthermore, regarding the derivation of the learning laws for some parameters in above-mentioned model-free DOs, two widely used approaches are introduced.

Chapter 4: The design and the rigorous stability analysis of the type-1 composite controller for a single-input uncertain nonlinear system with relative degree one are presented. Afterward, based on the practical speed dynamics of the SynRM, the type-1 composite controller is designed as a rotor speed controller for the construction of a novel robust FOC strategy for the 2L-VSI-fed SynRM-VSD system. Moreover, based on the practical current dynamics of the SynRM, two composite current controllers, each of which consists of two standard STSM controllers, are designed for such a robust FOC strategy, and related rigorous stability analyses are presented. The results of comparative HIL tests between the proposed FOC strategy and the classic STA-based FOC strategy, which is based on a standard STSM speed controller and two linear PI current controllers, for the 2L-VSI-fed SynRM drive system are presented and analyzed.

Chapter 5: The design and the rigorous stability analysis of the type-2 composite controller for a single-input uncertain nonlinear system with relative degree one are presented. Afterward, based on the practical speed dynamics of the SPMSM, the type-2 composite controller is designed as a rotor speed controller for the construction of a novel robust FOC strategy for the 2L-VSI-fed SPMSM-VSD system. The results of comparative experimental tests among the standard STSM speed controller, the ESO-based standard STSM speed controller, the modified STSM speed controller and the type-2 composite speed controller in the frame of the FOC strategy for the 2L-VSI-fed SPMSM-VSD system are presented and analyzed.

Chapter 6: The design and the rigorous stability analysis of the type-3 composite controller for a single-input uncertain nonlinear system with relative degree one are presented. Afterward, based on the practical speed dynamics of the SPMSM, the type-3 composite controller is designed as a rotor speed controller for the construction of a novel robust FOC strategy for the 2L-VSI-fed SPMSM-VSD system. The results of comparative experimental tests among the classic CSM speed controller,

three selected ENN-ICSM speed controllers and the type-3 composite speed controller in the frame of the FOC strategy of the 2L-VSI-fed SPMSM-VSD system are presented and analyzed.

Chapter 7: The design and the rigorous stability analysis of the type-4 composite controller for a single-input uncertain nonlinear system with relative degree one is presented. Afterward, based on the practical speed dynamics of the SPMSM, the type-4 composite controller is designed as a rotor speed controller for the construction of a novel robust FOC strategy for the 2L-VSI-fed SPMSM-VSD system. The results of comparative experimental tests among the three selected classic MRA speed controllers, three selected RBFNN-MRA speed controllers and the type-4 composite speed controller in the frame of the FOC strategy for the 2L-VSI-fed SPMSM-VSD system are presented and analyzed.

Chapter 8: Conclusions and perspectives for future work are presented.

References

[1] S. N. Manias, *Power Electronics and Motor Drive Systems*, Cambridge. USA: Academic Press, 2016.

[2] G. Abad, *Power Electronics and Electric Drives for Traction Applications*. Chichester, UK: Wiley, 2016.

[3] J. Pyrhönen, V. Hrabovcová, R. S. Semken, *Electrical Machine Drives Control: An Introduction*. Chichester, UK: Wiley, 2016.

[4] M. Mueller, H. Polinder, *Electrical Drives for Direct Drive Renewable Energy Systems*. Cambridge, UK: Woodhead Publishing, 2013.

[5] B. Blunier, M. Pucci, G. Cirrincione, M. Cirrincione, and A. Miraoui, "A scroll compressor with a high-performance sensorless induction motor drive for the air management of a PEMFC system for automotive applications," *IEEE Transactions on Vehicular Technology*, vol. 57, no. 6, pp. 3413-3427, Nov. 2008.

[6] B. Guo, "Modelling and advanced controls of variable speed hydro-electric plants," Ph.D. thesis, Université Grenoble Alpes, Grenoble, France, 2019.

[7] K. T. Chau, *Electrical Vehicle Machines and Drives: Design, Analysis and Application*. Singapore, Singapore: Wiley-IEEE Press, 2015.

[8] G. Pellegrino, T.M. Jahns, N. Bianchi, W.L. Soong, F. Cupertino, *The Rediscovery of Synchronous Reluctance and Ferrite Permanent Magnet Motors*. Basel, Switzerland: Springer International Publishing, 2016.

[9] M. Chen, W. Hua, J. Zhang, and W. Zhao, "Overview of stator-permanent magnet brushless machines," *IEEE Transactions on Industrial Electronics*, vol. 58, no. 11, pp. 5087-5101, Nov. 2011.

[10] S. Li, S. Zhang, T. G. Habetler, and R. G. Harley, "Modeling, design optimization, and applications of switched reluctance machines—A review," *IEEE Transactions on Industry Applications*, vol. 55, no. 3, pp. 2660-2681, May/Jun. 2019.

[11] J. Yang, W. -H. Chen, S. Li, L. Guo, and Y. Yan, "Disturbance/uncertainty estimation and attenuation techniques in PMSM drives—A survey," *IEEE Transactions on Industrial Electronics*, vol. 64, no. 4, pp. 3273-3285, Apr. 2017.

[12] S. Li, J. Yang, W. -H. Chen, and X. Chen, *Disturbance Observer-Based Control Methods and Applications*. Boca Raton, USA: CRC Press, 2017.

[13] H. H. Choi, N. T. -T. Vu, and J. -W. Jung, "Digital implementation of an adaptive speed

regulator for a PMSM," *IEEE Transactions on Power Electronics*, vol. 26, no. 1, pp. 3-8, Jan. 2011.

[14] M. -Y. Mei and T. -H. Liu, "Design and implementation of an online tuning adaptive controller for synchronous reluctance motor drives," *IEEE Transactions on Industrial Electronics*, vol. 60, no. 9, pp. 3644-3657, Sep. 2013.

[15] S. -K. Kim, K. -G. Lee, and K. -B. Lee, "Singularity-free adaptive speed tracking control for uncertain permanent magnet synchronous motor," *IEEE Transactions on Power Electronics*, vol. 31, no. 2, pp. 1692-1701, Feb. 2016.

[16] A. -T. Nguyen, M. -S. Rafaq, H. H. Choi and J. -W. Jung, "A model reference adaptive control based speed controller for a surface-mounted permanent magnet synchronous motor drive," *IEEE Transactions on Industrial Electronics*, vol. 65, no. 12, pp. 9399-9409, Dec. 2018.

[17] T. Sharaf-Eldin, M. W. Dunnigan, J. E. Fletcher, and B. W. Williams, "Nonlinear robust control of a vector-controlled synchronous reluctance machine," *IEEE Transactions on Power Electronics*, vol. 14, no. 6, pp. 1111-1121, Nov. 1999.

[18] V. Utkin, J. Guldner, and J. Shi, *Sliding Mode Control in Electro-Mechanical Systems*. Boca Raton, USA: CRC Press, 2009.

[19] S. Di Gennaro, J. Rivera, and B. Castillo-Toledo, "Super-twisting sensorless control of permanent magnet synchronous motors," in *Proceedings of the 49th IEEE Conference on Decision and Control*, pp. 4018-4023, Dec. 2010.

[20] H. -K. Chiang and W. -B. Li, "Sub-optimal algorithm second-order sliding mode control for a synchronous reluctance motor speed drive," *Transactions of the Canadian Society for Mechanical Engineering*, vol. 40, no. 5, pp. 897-908, Dec. 2016.

[21] J. Zhou and Y. Wang, "Adaptive backstepping speed controller design for a permanent magnet synchronous motor," *IEE Proceedings-Electric Power Applications*, vol. 149, no. 2, pp. 165-172, Mar. 2002.

[22] P. -C. Pan, T. -H. Liu, and U. K. Madawala, "Adaptive controller with an improved high-frequency injection technique for sensorless synchronous reluctance drive systems," *IET Electric Power Applications*, vol. 10, no. 4, pp. 240-250, Apr. 2016.

[23] S. -K. Kim, J. -S. Lee, and K. -B. Lee, "Offset-free robust adaptive back-stepping speed control for uncertain permanent magnet synchronous motor," *IEEE Transactions on Power Electronics*, vol. 31, no. 10, pp. 7065-7076, Oct. 2016.

[24] F. -J. Lin, M. -S. Huang, S. -G. Chen, C. -W. Hsu, and C. -H. Liang, "Adaptive backstepping control for synchronous reluctance motor based on intelligent current angle control," *IEEE Transactions on Power Electronics*, vol. 35, no. 7, pp. 7465-7479, Jul. 2020.

[25] R. Errouissi, M. Ouhrouche, W. -H. Chen, and A. M. Trzynadlowski, "Robust cascaded nonlinear predictive control of a permanent magnet synchronous motor with antiwindup compensator," *IEEE Transactions on Industrial Electronics*, vol. 59, no. 8, pp. 3078-3088, Aug. 2012.

[26] A. D. Alexandrou, N. K. Adamopoulos, and A. G. Kladas, "Development of a constant switching frequency deadbeat predictive control technique for field-oriented synchronous permanent-magnet motor drive," *IEEE Transactions on Industrial Electronics*, vol. 63, no. 8, pp. 5167-5175, Aug. 2016.

[27] T. -H. Liu, H. S. Haslim, and S. -K. Tseng, "Predictive controller design for a high-frequency injection sensorless synchronous reluctance drive system," *IET Electric Power Applications*, vol. 11, no. 5, pp. 902-910, May 2017.

[28] P. G. Carlet, F. Tinazzi, S. Bolognani, and M. Zigliotto, "An effective model-free predictive current control for synchronous reluctance motor drives," *IEEE Transactions on Industry Applications*, vol. 55, no. 4, pp. 3781-3790, Jul./Aug. 2019.

[29] A. Guagnano, G. Rizzello, F. Cupertino, and D. Naso, "Robust control of high-speed synchronous reluctance machines," *IEEE Transactions on Industry Applications*, vol. 52, no. 5, pp. 3990-4000, Sep./Oct. 2016.

[30] W. Wang, H. Shen, L. Hou, and H. Gu, "H_∞ robust control of permanent magnet synchronous motor based on PCHD," *IEEE Access*, vol. 7, pp. 49150-49156, Mar. 2019.

[31] W. -H. Chen, J. Yang, L. Guo, and S. Li, "Disturbance-observer-based control and related methods—An overview," *IEEE Transactions on Industrial Electronics*, vol. 63, no. 2, pp. 1083-1095, Feb. 2016.

[32] V. Utkin and H. Lee, "Chattering problem in sliding mode control systems," in *Proceedings of the International Workshop on Variable Structure Systems*, pp. 346-350, Jun. 2006.

[33] Z. Gao, "On the centrality of disturbance rejection in automatic control," *ISA Transactions*, vol. 53, no. 4, pp. 850-857, Jul. 2014.

[34] S. Li, M. Zhou, and X. Yu, "Design and implementation of terminal sliding mode control method for PMSM speed regulation system," *IEEE Transactions on Industrial Informatics*, vol. 9, no. 4, pp. 1879-1891, Nov. 2013.

[35] S. Wang, J. Na, X. Ren, H. Yu, and J. Yu, "Unknown input observer-based robust adaptive funnel motion control for nonlinear servomechanisms," *International Journal of Robust and Nonlinear Control*, vol. 28, no. 18, pp. 6163-6179, Dec. 2018.

[36] J. Wang, F. Wang, G. Wang, S. Li, and L. Yu, "Generalized Proportional integral observer based robust finite control set predictive current control for induction motor systems with time-

varying disturbances," *IEEE Transactions on Industrial Informatics*, vol. 14, no. 9, pp. 4159-4168, Sep. 2018.

[37] H. Liu and S. Li, "Speed control for PMSM servo system using predictive functional control and extended state observer," *IEEE Transactions on Industrial Electronics*, vol. 59, no. 2, pp. 1171-1183, Feb. 2016.

[38] H. Yang, Y. Zhang, J. Liang, B. Xia, P. D. Walker, and N. Zhang, "Deadbeat control based on a multipurpose disturbance observer for permanent magnet synchronous motors," *IET Electric Power Applications*, vol. 12, no. 5, pp. 708-716, May 2018.

[39] X. Zhang, L. Sun, K. Zhao, and L. Sun, "Nonlinear speed control for PMSM system using sliding-mode cotnrol and disturbance compensation techniques," *IEEE Transactions on Power Electronics*, vol. 28, no. 3, pp. 1358-1365, Mar. 2013.

[40] B. Wang, Z. Dong, Y. Yu, G. Wang, and D. Xu, "Static-errorless deadbeat predictive current control using second-order sliding-mode disturbance observer observer for induction machine drives," *IEEE Transactions on Power Electronics*, vol. 33, no. 3, pp. 2395-2403, Mar. 2018.

[41] F. J. Lin, C. -H. Lin, X. Gu, and P. -H. Shen, "Self-constructing fuzzy neural network speed controller for permanent-magnet synchronous motor drive," *IEEE transactions on Fuzzy Systems*, vol. 9, no. 5, pp. 751-759, Oct. 2001.

[42] F. -J. Lin, L. -T. Teng, and H. Chu, "Robust control using neural network uncertainty observer for linear induction motor servo drive," *IEEE Transactions on Power Electronics*, vol. 17, no. 2, pp. 241-254, Mar. 2002.

[43] F. -J. Lin, L. -T. Teng, and H. Chu, "A robust recurrent wavelet neural network controller with improved particle swarm optimization for linear synchronous motor drive," *IEEE Transactions on Power Electronics*, vol. 23, no. 6, pp. 3067-3078, Nov. 2008.

[44] F. F. M. El-Sousy, "Adaptive dynamic sliding-mode control system using recurrent RBFN for high-performance induction motor servo drive," *IEEE Transactions on Industrial Informatics*, vol. 9, no. 4, pp. 1922-1936, Nov. 2013.

[45] C. -H. Lin and C. -P. Lin, "Hybrid modified Elman NN controller design on permanent magnet synchronous motor driven electric scooter," *Transactions of the Canadian Society for Mechanical Engineering*, vol. 37, no. 4, pp. 1127-1145, Dec. 2013.

[46] F. -J. Lin, Y. -C. Hung, and M. -T. Tsai, "Fault-tolerant control for six-phase PMSM drive system via intelligent complementary sliding-mode control using TSKFNN-AMF," *IEEE Transactions on Industrial Electronics*, vol. 60, no. 12, pp. 5747-5762, Dec. 2013.

[47] C. -H. Lin, "Dynamic control of V-belt continuously variable transmission-driven electric scooter using hybrid modified recurrent Legendre neural network control system," *Nonlinear*

Dynamics, vol. 79, no. 2, pp. 787-808, Dec. 2013.

[48] C. -H. Lin and Y. -C. Shih, "Novel hybrid recurrent Hermite neural network control for switched reluctance motor drive," in *Proceedings of the 13th IEEE Conference on Industrial Electronics and Applications*, pp. 1022-1027, May. 2018.

[49] J. Zhang, H. Wang, Z. Cao, J. Zheng, M. Yu, A. Yazdani, and F. Shahnia, "Fast nonsingular terminal sliding mode control for permanent-magnet linear motor via ELM," *Neural Computing and Applications*, Sep. 2019. [Online].

[50] C. -H. Lin and K. -T. Chang, "Admixed recurrent Gegenbauer polynomials neural network with mended particle swarm optimization control system for synchronous reluctance motor driving continuously variable transmission system," *Proceedings of the Institution of Mechanical Engineers, Part I: Journal of Systems and Control Engineering*, vol. 234, no. 2, pp. 1-16, Feb. 2020.

[51] J. A. Moreno and M. Osorio, "A Lyapunov approach to second-order sliding mode controllers and observers," in *Proceedings of the 47th IEEE Conference on Decision and Control*, pp. 2856-2861, Dec. 2008.

[52] Z. Feng and J. Fei, "Super-twisting sliding mode control for micro gyroscope based on RBF neural network," *IEEE Access*, vol. 6, pp. 64993-65001, Oct. 2018.

2

MODELING AND CONTROL OF SPMSM-VSD AND SYNRM-VSD SYSTEMS

2.1 Introduction

The AC synchronous motor, as its name implies, is the AC motor that rotates synchronously with the frequency of the stator current in the steady-state operation. Nowadays, among existing AC synchronous motors, PMSMs are the most attractive AC synchronous motors for high-performance VSD systems [1]-[4]. Since there is no field winding in the rotor and the permanent-magnet materials are used to generate the rotor flux linkage, the PMSM has smaller mass and volume, higher efficiency, torque and power densities compared with the induction motor and the switched reluctance motor at the same power level. Such attractive features make the PMSM-based VSD (PMSM-VSD) system popular and even dominant in many applications. However, there are some shortcomings for the PMSM, and the most concerned one is the costs of the permanent-magnet materials [5]. Generally speaking, the higher the strength of the adopted permanent-magnet materials is, the larger the benefits enjoyed by the PMSM are. The neodymium-iron-boron (NdFeB) magnet materials are the most widely used high-strength rare-earth permanent-magnet materials for PMSMs [5]. It can be said that the commercial availability of such permanent-magnet materials makes it possible to achieve the mass commercialization of PMSMs in domestic and industrial sectors. For example, nearly all PMSMs used in existing commercial electrical vehicles adopt the NdFeB magnet materials [6]. The price of the neodymium metal experienced a huge increase between the beginning of 2010 and the middle of 2011, resulting in the significant rise of the costs of the NdFeB magnet materials [6]. Although the price of the neodymium metal decreased quickly after reaching the peak, the drastic variation of such a price have motivated many researchers from industry and academia

to start to find powerful alternatives to the PMSM using the NdFeB magnet materials [6]. The SynRM, which can date back to the 1920s [7], has been considered as a potential choice in recent decades [5], [6], [8], [9]. This type of AC synchronous motor is equipped with a simple, windingless, magnetless and salient-pole rotor structure. Such a rotor structure makes the SynRM enjoy the advantages in terms of robustness and costs. However, the price we have to pay for obtaining these attractive features is that the torque and the power densities of the SynRM are poorer than those of the PMSM [5]. Therefore, before the advent of a breakthrough in the SynRM design, the PMSM cannot be replaced by the SynRM in high-performance VSD systems [6]. On the other hand, compared with the induction motor, the SynRM have some advantages, such as higher efficiency, higher overload capacity and lower rotor losses. Hence, the well-designed SynRM has been deemed as a powerful alternative to the induction motor in recent years, and have been successfully applied in the water pumping system, the fan system and the compression refrigeration system [9]-[12].

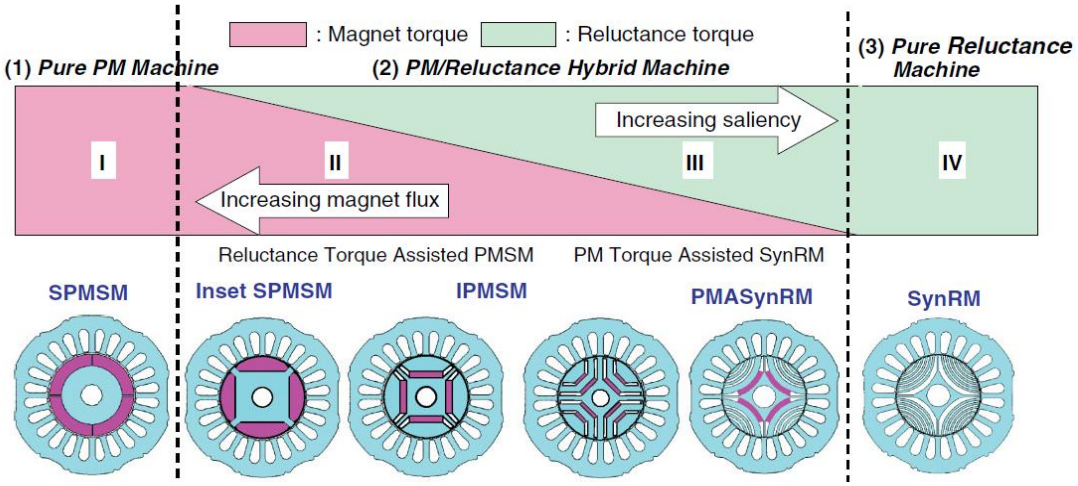

Figure 2.1 Categorization of AC synchronous motors based on the torque generation mechanism [13].

Up to now, various types of PMSMs have been proposed. They have the same stator structure as the SynRM. To distinguish them from each other, the motor's torque generation mechanism can be selected as an index. In general, the torque generated by PMSMs consists of two terms: the magnet torque and the reluctance torque [5], [13]. The former is proportional to the rotor flux linkage and the latter is proportional to the difference between the direct-axis and the quadrature-axis inductances, namely the rotor saliency. Different combinations of the magnet torque and the reluctance torque in the motor's torque correspond to different PMSMs, as shown in Figure 2.1, where the PMASynRM denotes the permanent-magnet-assisted SynRM which is a type of IPMSM

that the value of the reluctance torque is larger than that of the magnet torque [13]. From Figure 2.1, it can be seen that the SPMSM only generates the magnet torque while the SynRM only generates the reluctance torque.

This chapter focuses on modeling and control of 2L-VSI-fed SPMSM-VSD and 2L-VSI-fed SynRM-VSD systems. Firstly, the mathematical models of the 2L-VSI considering the effects of inverter nonlinearities are given. Afterward, the dynamic models of the SPMSM and the SynRM in terms of the rotor mechanical speed and two stator current components in the rotor reference frame are presented, respectively. As has been stated in Section 1.2, two considered VSD systems are subject to various types of unmodeled dynamics, parametric uncertainties and external disturbances. Their effects on the dynamic models of two considered motors have been taken into account. Next, the principles of the FOC strategies for two considered VSD systems are briefly introduced. Finally, the descriptions of the HIL test bench for the 2L-VSI-fed SynRM drive system and the experimental test bench based on the 2L-VSI-fed SPMSM drive system are presented.

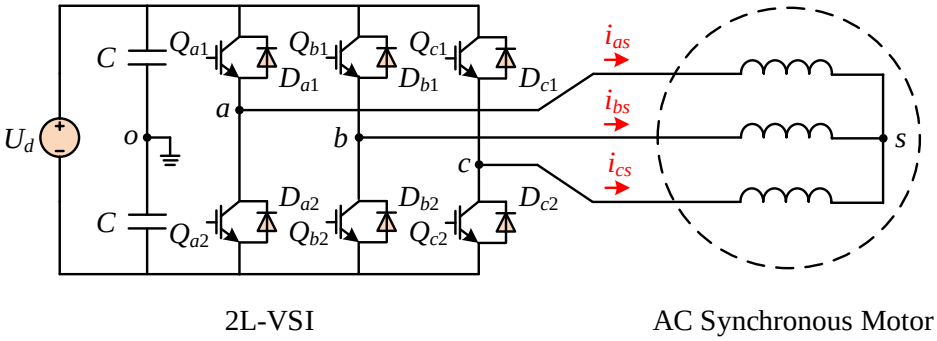

Figure 2.2 2L-VSI-fed AC synchronous motor-based VSD system.

2.2 Modeling of the 2L-VSI

The 2L-VSI-fed AC synchronous motor-based VSD system is illustrated in Figure 2.2, where U_d is the voltage of the DC electrical power supply, C denotes the DC-link capacitor, Q_{xy} and D_{xy} for all $x \in \{a, b, c\}$ and $y \in \{1, 2, 3\}$ denote each IGBT and freewheeling diode in the 2L-VSI, respectively, i_{as}, i_{bs} and i_{cs} are three-phase stator currents. It can be seen that each leg of the 2L-VSI is equipped with two IGBTs and two freewheeling diodes. There are two switching states in each leg of the 2L-VSI:

1) Q_{x1} is on and Q_{x2} is off.
2) Q_{x2} is on and Q_{x1} is off.

Since the on-off condition of Q_{x1} is always opposite to that of Q_{x2}, the switching function for each leg of the 2L-VSI can be defined as

$$S_x = \begin{cases} 1, & \text{if } Q_{x1} \text{ on}, Q_{x2} \text{ off} \\ 0, & \text{if } Q_{x1} \text{ off}, Q_{x2} \text{ on} \end{cases}, \quad x = a,b,c \tag{2.1}$$

where S_x denotes the switching function for the leg *x*.

According to (2.1), (S_a, S_b, S_c) has eight possible combinations corresponding to eight switching states of the 2L-VSI. In practice, the 2L-VSI is continuously switched from one switching state to another to generate the required three-phase output voltages, such that the operation of the VSD system follows the implemented control strategy. However, there exist several nonlinearities in the 2L-VSI, including the *dead time*, the *turn-on/off time* and the *saturation voltage* of the controllable power semiconductor device, the *diode forward voltage*, the *zero current clamping* and the *parasitic capacitance* [1]. The existence of such inverter nonlinearities introduces the distorted voltage and current components to the output voltages provided by the 2L-VSI and the stator currents of the AC synchronous motor fed by the 2L-VSI, respectively. In this thesis, the first four aforementioned inverter nonlinearities are considered into the modeling of the 2L-VSI. Taking the leg *x* of the 2L-VSI as an example, the effects of the considered inverter nonlinearities on the switching sequence and the pole voltage can be described as Figure 2.3 [14], where u_{xo} denotes the pole voltage of the phase *x*, T_s represents the sampling period, T_x^* and T_x denote the applied and the actual conducting time of Q_{x1}, respectively.

2.2.1 High-Frequency Model

In this subsection, the three-phase *high-frequency model* of the 2L-VSI, which is based on the switching function, is derived. Owing to the discrete nature of the switching function, such a model is also named as the discrete model of the 2L-VSI. At first, according to Figure 2.3, the relationship between T_x and T_x^* can be described as

$$T_x = T_x^* + \left(T_{off} - T_{on} - T_{dead}\right)\text{sgn}\left(i_{xs}\right) \tag{2.2}$$

where T_{dead}, T_{on} and T_{off} denote the dead time, the turn-on time and the turn-off time for Q_{x1}, respectively, and sgn(•) represents the sign function expressed as

$$\text{sgn}(z) = \begin{cases} +1, & \text{if } z > 0 \\ 0, & \text{if } z = 0 \\ -1, & \text{if } z < 0 \end{cases} \tag{2.3}$$

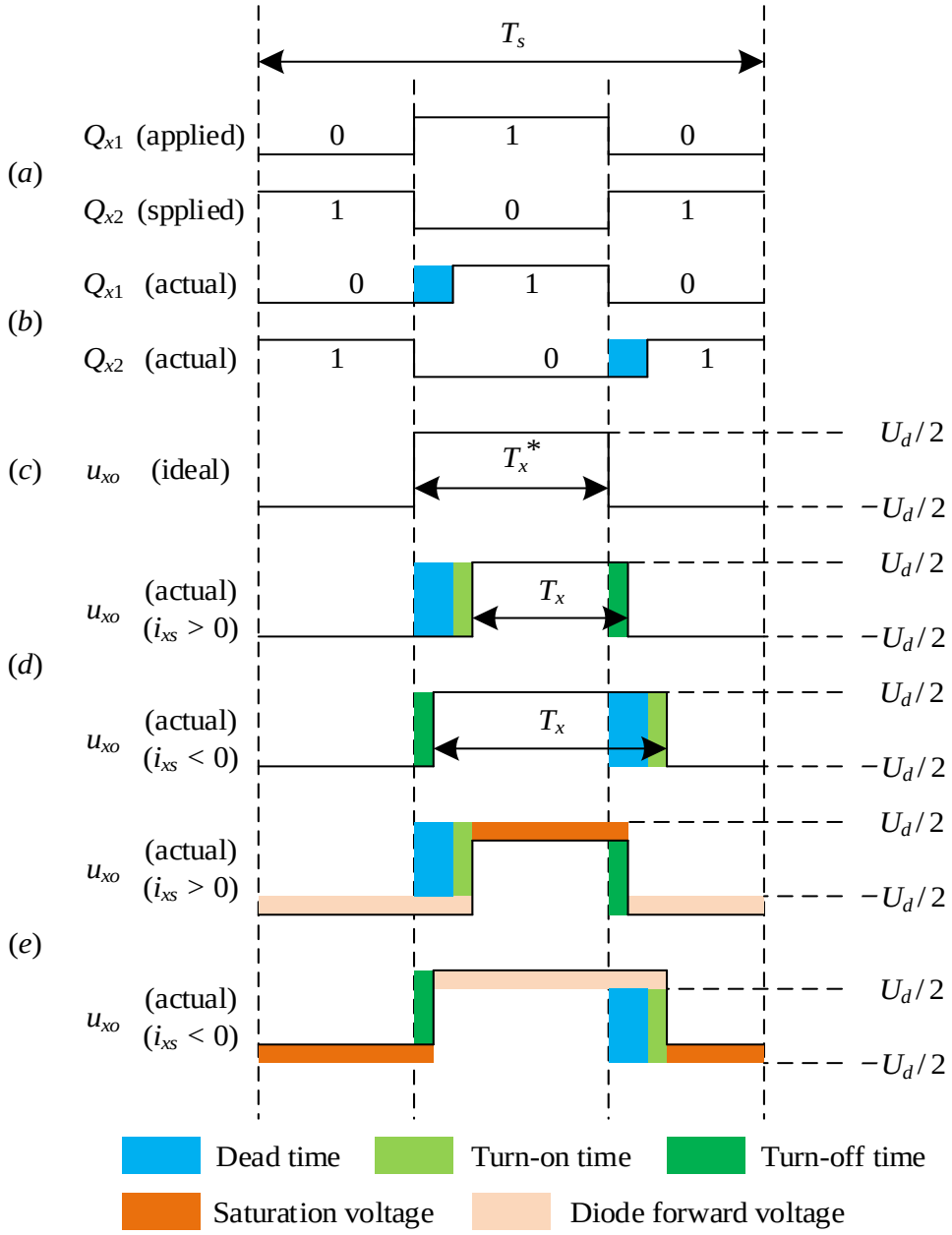

Figure 2.3 Single-phase switching sequence and pole voltage of the 2L-VSI considering inverter nonlinearities. (a) Applied switching sequence for leg x. (b) Actual switching sequence for leg x with dead time. (c) Ideal phase x pole voltage. (d) Actual phase x pole voltage with dead time and turn-on/off time. (e) Actual phase x pole voltage with all considered inverter nonlinearities.

According to Figure 2.3, considering the effects of the saturation voltage of the IGBT and the diode forward voltage, when i_{xs} is positive, i.e., i_{xs} flows to the load, u_{xo} can be calculated as

$$u_{xo}=\begin{cases}\dfrac{U_d}{2}-U_{sat}, & \text{if } S_x=1\\ -\dfrac{U_d}{2}-U_{diode}, & \text{if } S_x=0\end{cases} \tag{2.4}$$

where U_{sat} and U_{diode} denote the saturation voltage of the IGBT and the diode forward voltage, respectively.

Moreover, when i_{xs} is negative, i.e., i_{xs} flows from the load, u_{xo} can be calculated as

$$. \ u_{xo}=\begin{cases}\dfrac{U_d}{2}+U_{diode}, & \text{if } S_x=1\\ -\dfrac{U_d}{2}+U_{sat}, & \text{if } S_x=0\end{cases} . \tag{2.5}$$

Based on (2.4) and (2.5), u_{xo} can be expressed as the following expression.

$$u_{xo}=\left(U_{dc}-U_{sat}+U_{diode}\right)\left(S_x-\frac{1}{2}\right)-\frac{U_{sat}+U_{diode}}{2}\operatorname{sgn}\left(i_{xs}\right) \tag{2.6}$$

Remark 2.1. In some literature, the slope resistances of the IGBT and the freewheeling diode are considered into the modeling of the pole voltage of the 2L-VSI. In practice, however, through some popular parameter identification schemes, the obtained stator resistance of the AC synchronous motor has included such slope resistances. In this thesis, therefore, the derivation of the 2L-VSI's model neglects the slope resistances of the IGBT and the freewheeling diode.

For the balanced three-phase loads, the three-phase output voltages of the 2L-VSI, which are also the three-phase stator voltages of the AC synchronous motor, can be calculated as

$$\begin{bmatrix}u_{as}\\ u_{bs}\\ u_{cs}\end{bmatrix}=\frac{1}{3}\begin{bmatrix}2 & -1 & -1\\ -1 & 2 & -1\\ -1 & -1 & 2\end{bmatrix}\begin{bmatrix}u_{ao}\\ u_{bo}\\ u_{co}\end{bmatrix} \tag{2.7}$$

where u_{an}, u_{bn} and u_{cn} are three-phase stator voltages of the AC synchronous motor.

Substituting (2.6) into (2.7), u_{as}, u_{bs} and u_{cs} can be expressed as

$$\cdot\begin{cases}u_{as}=\dfrac{2S_a-S_b-S_c}{3}U_d+\dfrac{2S_a-S_b-S_c}{3}\left(U_{diode}-U_{sat}\right)-\dfrac{U_{sat}+U_{diode}}{6}\left[2\operatorname{sgn}\left(i_{as}\right)-\operatorname{sgn}\left(i_{bs}\right)-\operatorname{sgn}\left(i_{cs}\right)\right]\\ u_{bs}=\dfrac{2S_b-S_a-S_c}{3}U_d+\dfrac{2S_b-S_a-S_c}{3}\left(U_{diode}-U_{sat}\right)-\dfrac{U_{sat}+U_{diode}}{6}\left[2\operatorname{sgn}\left(i_{bs}\right)-\operatorname{sgn}\left(i_{as}\right)-\operatorname{sgn}\left(i_{cs}\right)\right]\\ u_{cs}=\dfrac{2S_c-S_a-S_b}{3}U_d+\dfrac{2S_c-S_a-S_b}{3}\left(U_{diode}-U_{sat}\right)-\dfrac{U_{sat}+U_{diode}}{6}\left[2\operatorname{sgn}\left(i_{cs}\right)-\operatorname{sgn}\left(i_{as}\right)-\operatorname{sgn}\left(i_{bs}\right)\right]\end{cases}\cdot \tag{2.8}$$

The three-phase *high-frequency model* of the 2L-VSI is presented as (2.8). From this model, it can be seen that the existence of U_{sat} and U_{diode} introduces two types of distorted voltage

components to each phase stator voltage. However, such an inverter model does not reveal the effect of the existence of T_{dead}, T_{on} and T_{off} on the three-phase stator voltages.

2.2.2 Low-Frequency Model

In this subsection, the three-phase *low-frequency model* of the 2L-VSI, which is based on the duty cycle, is derived. Since the duty cycle, which is an average value of the switching function in a sampling period, is a continuous function, such a model is also named as the continuous model of the 2L-VSI. At first, according to Figure 2.3, the applied and the actual duty cycles of Q_{x1} can be expressed as

$$d_x^* = \frac{T_x^*}{T_s}, \quad d_x = d_x^* + \frac{T_{off} - T_{on} - T_{dead}}{T_s}\mathrm{sgn}(i_{xs}) \tag{2.9}$$

where d_x^* and d_x represent the applied and actual duty cycles of Q_{x1}, respectively.

By replacing S_x in (2.6) with d_x, the low-frequency model of the pole voltage considering inverter nonlinearities can be derived as

$$u_{xo} = (U_{dc} - U_{sat} + U_{diode})\left(d_x^* - \frac{1}{2}\right) + U_{dead}\mathrm{sgn}(i_{xs}) \tag{2.10}$$

where U_{dead} is expressed as

$$U_{dead} = (U_{dc} - U_{sat} + U_{diode})\frac{T_{off} - T_{on} - T_{dead}}{T_s} - \frac{U_{sat} + U_{diode}}{2} \tag{2.11}$$

Substituting (2.11) into (2.7), the three-phase *low-frequency model* of the 2L-VSI is derived as (2.12), where u_{as}^l, u_{bs}^l and u_{cs}^l are the fundamental components of u_{as}, u_{bs} and u_{cs}, respectively.

$$\begin{cases} u_{as}^l = \dfrac{2d_a^* - d_b^* - d_c^*}{3}U_d + \dfrac{2d_a^* - d_b^* - d_c^*}{3}(U_{diode} - U_{sat}) + \dfrac{U_{dead}}{3}\left[2\mathrm{sgn}(i_{as}) - \mathrm{sgn}(i_{bs}) - \mathrm{sgn}(i_{cs})\right] \\ u_{bs}^l = \dfrac{2d_b^* - d_a^* - d_c^*}{3}U_d + \dfrac{2d_b^* - d_a^* - d_c^*}{3}(U_{diode} - U_{sat}) + \dfrac{U_{dead}}{3}\left[2\mathrm{sgn}(i_{bs}) - \mathrm{sgn}(i_{as}) - \mathrm{sgn}(i_{cs})\right] \\ u_{cs}^l = \dfrac{2d_c^* - d_a^* - d_b^*}{3}U_d + \dfrac{2d_c^* - d_a^* - d_b^*}{3}(U_{diode} - U_{sat}) + \dfrac{U_{dead}}{3}\left[2\mathrm{sgn}(i_{cs}) - \mathrm{sgn}(i_{as}) - \mathrm{sgn}(i_{bs})\right] \end{cases} \tag{2.12}$$

In the derived *low-frequency model* of the 2L-VSI, the effects of all considered inverter nonlinearities are taken into account. It can be seen that the existence of inverter nonlinearities introduces two types of distorted voltage components to each phase stator voltage. For analyzing the effects of these distorted voltage components on u_{as}^l, u_{bs}^l and u_{cs}^l, the three-phase *low-frequency model* of the 2L-VSI can be expressed as the following form.

$$\begin{cases} u_{as}^{l} = u_{as}^{l*} + u_{as}^{d} = u_{as}^{l*} + u_{as}^{d1} + u_{as}^{d2} \\ u_{bs}^{l} = u_{bs}^{l*} + u_{bs}^{d} = u_{bs}^{l*} + u_{bs}^{d1} + u_{bs}^{d2} \\ u_{cs}^{l} = u_{cs}^{l*} + u_{cs}^{d} = u_{cs}^{l*} + u_{cs}^{d1} + u_{cs}^{d2} \end{cases} \tag{2.13}$$

where u_{as}^{d}, u_{bs}^{d} and u_{cs}^{d} denote the total three-phase distorted stator voltage components, u_{as}^{l*}, u_{bs}^{l*} and u_{cs}^{l*} represent the ideal fundamental components of three-phase stator voltages expressed as (2.14), u_{as}^{d1}, u_{bs}^{d1} and u_{cs}^{d1} denote the first type of three-phase distorted stator voltage components expressed as (2.15), u_{as}^{d2}, u_{bs}^{d2} and u_{cs}^{d2} denote the second type of three-phase distorted stator voltage components expressed as (2.16).

$$u_{as}^{l*} = \frac{2d_a^* - d_b^* - d_c^*}{3}U_d, \quad u_{bs}^{l*} = \frac{2d_b^* - d_a^* - d_c^*}{3}U_d, \quad u_{cs}^{l*} = \frac{2d_c^* - d_a^* - d_b^*}{3}U_d \tag{2.14}$$

$$\begin{cases} u_{as}^{d1} = \dfrac{2d_a^* - d_b^* - d_c^*}{3}\left(U_{diode} - U_{sat}\right) \\ u_{bs}^{d1} = \dfrac{2d_b^* - d_a^* - d_c^*}{3}\left(U_{diode} - U_{sat}\right) \\ u_{cs}^{d1} = \dfrac{2d_c^* - d_a^* - d_b^*}{3}\left(U_{diode} - U_{sat}\right) \end{cases} \tag{2.15}$$

$$\begin{cases} u_{as}^{d2} = \dfrac{U_{dead}}{3}\left[2\mathrm{sgn}\left(i_{as}\right) - \mathrm{sgn}\left(i_{bs}\right) - \mathrm{sgn}\left(i_{cs}\right)\right] \\ u_{bs}^{d2} = \dfrac{U_{dead}}{3}\left[2\mathrm{sgn}\left(i_{bs}\right) - \mathrm{sgn}\left(i_{as}\right) - \mathrm{sgn}\left(i_{cs}\right)\right] \\ u_{cs}^{d2} = \dfrac{U_{dead}}{3}\left[2\mathrm{sgn}\left(i_{cs}\right) - \mathrm{sgn}\left(i_{as}\right) - \mathrm{sgn}\left(i_{bs}\right)\right] \end{cases} \tag{2.16}$$

Since u_{xs}^{d1} has the same duty-cycle-based coefficient as u_{xs}^{l*}, u_{as}^{d1}, u_{bs}^{d1} and u_{cs}^{d1} can be regarded as the "amplitude losses" of three-phase stator voltages. As for u_{xs}^{d2}, it is dependent on the poles of three-phase stator currents. For the balanced three-phase stator currents, u_{as}^{d2}, u_{bs}^{d2} and u_{cs}^{d2} can be expanded as Fourier series, i.e.,

$$\begin{cases} u_{as}^{d2} = \dfrac{4U_{dead}}{\pi}\displaystyle\sum_k \frac{1}{k}\sin k\omega_i t \\ u_{bs}^{d2} = \dfrac{4U_{dead}}{\pi}\displaystyle\sum_k \frac{1}{k}\sin k\left(\omega_i t - \frac{2\pi}{3}\right), \quad k = 1,5,7,11,13... \\ u_{cs}^{d2} = \dfrac{4U_{dead}}{\pi}\displaystyle\sum_k \frac{1}{k}\sin k\left(\omega_i t + \frac{2\pi}{3}\right) \end{cases} \tag{2.17}$$

where ω_i denotes the frequency of the fundamental component of i_{an}.

According to (2.17), it can be concluded that the existence of u_{as}^{d2}, u_{bs}^{d2} and u_{cs}^{d2} introduces the

first, the $(6n-1)$th and the $(6n+1)$th harmonic components in terms of ω_i ($n = 1, 2, 3,\ldots$) to u_{as}^l, u_{bs}^l and u_{cs}^l. Moreover, the amplitude of each voltage harmonic component is inversely proportional to its harmonic order.

Combining (2.13) with (2.17), the three-phase *low-frequency model* of the 2L-VSI can be rewritten as

$$\begin{cases} u_{as}^l = \dfrac{2d_a^* - d_b^* - d_c^*}{3}\left(U_d + U_{diode} - U_{sat}\right) + \dfrac{4U_{dead}}{\pi}\sum_k \dfrac{1}{k}\sin k\omega_i t \\ u_{bs}^l = \dfrac{2d_b^* - d_a^* - d_c^*}{3}\left(U_d + U_{diode} - U_{sat}\right) + \dfrac{4U_{dead}}{\pi}\sum_k \dfrac{1}{k}\sin k\left(\omega_i t - \dfrac{2\pi}{3}\right), \quad k = 1,5,7,11,13... \\ u_{cs}^l = \dfrac{2d_c^* - d_a^* - d_b^*}{3}\left(U_d + U_{diode} - U_{sat}\right) + \dfrac{4U_{dead}}{\pi}\sum_k \dfrac{1}{k}\sin k\left(\omega_i t + \dfrac{2\pi}{3}\right) \end{cases} \quad (2.18)$$

2.3 Modeling of PMSM-VSD and SynRM-VSD Systems

The advent of the space-vector theory makes it possible to model the transient behavior of AC synchronous motors and develop high-performance closed-loop control strategies for AC synchronous motor-based VSD systems [4]. Such a theory uses the space vectors to describe the spatial distribution of some physical quantities of AC synchronous motors, including the stator voltage, the stator current and the stator flux linkage. These space vectors can be projected to different reference frames to derive corresponding dynamic models of AC synchronous motors for different purposes, such as the controller design and the observer design.

2.3.1 Reference Frame Transformation

The three-axis stator reference frame, the two-axis stator reference frame and the two-axis rotor reference frame, which are commonly known as the *abc* frame, the $\alpha\beta$ frame and the *dq* frame, respectively, are three widely used reference frames to describe dynamic models of AC synchronous motors [1]. For a certain space vector rotating in the plane, it has different axes components in these three reference frames. The *abc* frame is a static frame in which every two axes have 120° phase difference. The $\alpha\beta$ frame is also a static frame in which the α-axis is aligned with the *a*-axis of the *abc* frame and perpendicular to the β-axis. Since the *abc* frame and the $\alpha\beta$ frame are both static, the components of the space vector in the axes of these two reference frame are AC components. As for the *dq* frame, it rotates in the plane with the same angular speed as the considered space vector and the *d*-axis is perpendicular to the *q*-axis. Therefore, the *d*- and *q*-axes components of the considered

space vector are DC components.

In general, based on physical laws, the dynamic models of AC synchronous motors in the *abc* frame can be derived. On the other hand, the dynamic models of AC synchronous motors in the $\alpha\beta$ frame or the *dq* frame are used to design controllers and observers. Therefore, transformation matrices are required to achieve the reference frame transformation to obtain the required dynamics models for the controller design and the observer design.

With respect to the transformation from the *abc* frame to the $\alpha\beta$ frame, two different transformations are available. One is known as the amplitude-invariant transformation, or as often called the *Clarke's transformation*, the other is known as the power-invariant transformation, or as often called the *Concordia's transformation*. Since the former is more frequently used in the design of the controller or the observer for VSD systems, only such a transformation is introduced in this subsection.

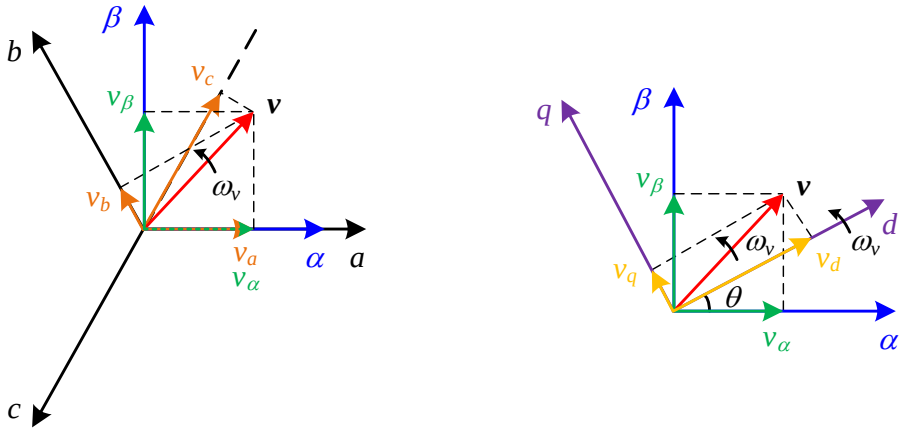

(a) (b)

Figure 2.4 Distribution of the space vector components in three different reference frames. (a) The *abc* frame and the $\alpha\beta$ frame. (b) The $\alpha\beta$ frame and the *dq* frame.

Considering a generic space vector $\boldsymbol{v}$ whose angular speed is ω_v, the distribution of its axes components in three different reference frames are presented in Figure 2.4, where v_a, v_b and v_c are *a*-, *b*- and *c*-axes components of $\boldsymbol{v}$ in the *abc* frame, respectively, v_α and v_β are α- and β-axes components of $\boldsymbol{v}$ in the $\alpha\beta$ frame, respectively, v_d and v_q are *d*- and *q*-axes components of $\boldsymbol{v}$ in the *dq* frame, respectively, and θ denotes the phase difference between the *d*-axis and the α-axis. The *Clarke's transformation* in which v_α and v_β are calculated from v_a, v_b and v_c is described as

$$v_\alpha = \frac{2}{3}\left(v_a - \frac{1}{2}v_b - \frac{1}{2}v_c\right), \quad v_\beta = \frac{1}{\sqrt{3}}\left(v_b - v_c\right) \tag{2.19}$$

The *inverse Clarke's transformation* in which v_a, v_b and v_c are calculated from v_α and v_β is described as

$$v_a = v_\alpha, \quad v_b = \frac{1}{2}\left(-v_\alpha + \sqrt{3}v_\beta\right), \quad v_c = \frac{1}{2}\left(-v_\alpha - \sqrt{3}v_\beta\right) \tag{2.20}$$

The transformation from the *abc* frame to the *dq* frame is called the *Park's transformation*. It can be described as

$$\begin{cases} v_d = \frac{2}{3}\left[v_a \cos\theta + v_b \cos\left(\theta - \frac{2}{3}\pi\right) + v_c \cos\left(\theta + \frac{2}{3}\pi\right)\right] \\ v_q = \frac{2}{3}\left[-v_a \sin\theta - v_b \sin\left(\theta - \frac{2}{3}\pi\right) - v_c \sin\left(\theta + \frac{2}{3}\pi\right)\right] \end{cases} \tag{2.21}$$

The *inverse Park's transformation* in which v_a, v_b and v_c are calculated from v_d and v_q is described as

$$\begin{cases} v_a = v_d \cos\theta - v_q \sin\theta \\ v_b = v_d \cos\left(\theta - \frac{2}{3}\pi\right) - v_q \sin\left(\theta - \frac{2}{3}\pi\right) \\ v_c = v_d \cos\left(\theta + \frac{2}{3}\pi\right) - v_q \sin\left(\theta + \frac{2}{3}\pi\right) \end{cases} \tag{2.22}$$

2.3.2 Classic Dynamic Models

With respect to the FOC strategies of AC synchronous motors, the controller design depends on the dynamic models of AC synchronous motors in the *dq* frame. In this subsection, the classic dynamic models of the SPMSM and the SynRM in terms of rotor mechanical speed and stator current components in the *dq* frame are presented. Deriving such dynamic models is based on the following assumptions.

1) Three-phase stator windings are symmetrical and the stator slotting effect is neglected.
2) The Magnetomotive force distributes sinusoidally and the rotor flux linkage harmonics are neglected.
3) The saturation of the magnetic circuit, the core loss and the damping effect are neglected.
4) The temperature variation effect is neglected.

Taking the four-pole SPMSM and SynRM as examples, the locations of *d*- and *q*-axes of the *dq* frame for these two motors are presented in Figure 2.5. Since the SPMSM is a non-salient pole AC synchronous motor and the permeability of permanent magnet materials is close to that of the

air, the *d*-axis is aligned with the rotor flux linkage vector in the SPMSM. As for the SynRM, since it is a salient pole AC synchronous motor, the *d*-axis is aligned with the direction of the maximum permeability and the *q*-axis is aligned with the direction of the minimum permeability. Note that, in the four-pole AC synchronous motor, the mechanical phase difference between the *d*- and *q*-axes is 45° such that the electrical phase difference between these two axes is 90°.

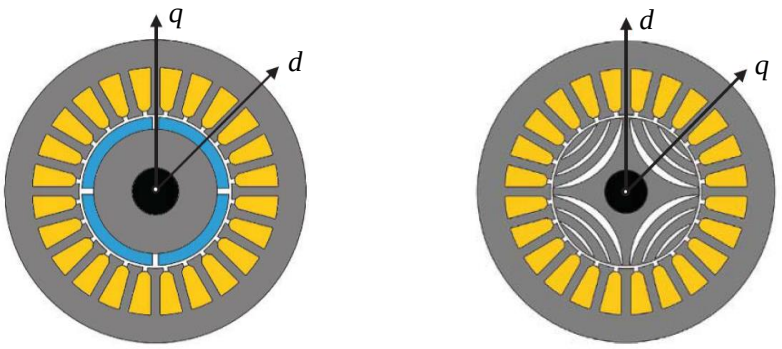

(a) (b)

Figure 2.5 Locations of two axes in the *dq* frame for considered AC synchronous motors [3]. (a) SPMSM. (b) SynRM.

In the *dq* frame, the classic generic stator voltage equation for the SPMSM and the SynRM are expressed as the following expressions [4].

$$u_{ds} = R_s i_{ds} + \frac{d\lambda_{ds}}{dt} - n_p \omega_m \lambda_{qs}, \quad u_{qs} = R_s i_{qs} + \frac{d\lambda_{qs}}{dt} + n_p \omega_m \lambda_{ds} \tag{2.23}$$

where u_{ds} and u_{qs} denote the *d*- and *q*-axes stator voltage components of each considered motor, respectively, λ_{ds} and λ_{qs} represent the *d*- and *q*-axes stator flux linkage components of each considered motor, respectively, R_s, n_p and ω_m represent the stator resistance, the pole pairs and the rotor mechanical speed of each considered motor, respectively.

In the *dq* frame, the classic stator flux linkage equations for the SPMSM and the SynRM are expressed as the following expressions [4].

$$\lambda_{ds} = \begin{cases} L_d i_{ds} + \lambda_m, & \text{SPMSM} \\ L_d i_{ds}, & \text{SynRM} \end{cases}, \quad \lambda_{qs} = L_q i_{qs} \tag{2.24}$$

where i_{ds} and i_{qs} denote the *d*- and *q*-axes stator current components of each considered motor, respectively, L_d and L_q represent the synchronous inductances of each considered motor and λ_m denotes the rotor flux linkage of the SPMSM.

The classic generic motion equation for the SPMSM and the SynRM is expressed as the

following expression [4].

$$J\frac{d\omega_m}{dt}=T_e-T_L-T_f \tag{2.25}$$

where T_e, T_L and T_f denote the motor torque, the load torque and the friction torque of each considered motor, respectively, and J represents the rotor inertia of each considered motor.

With respect to the SPMSM, the synchronous inductances are usually considered to be equal to each other. Therefore, assuming that $L_d = L_q = L_s$ for the SPMSM, the classic torque equation for the SPMSM and the SynRM can be expressed as

$$T_e=\frac{3}{2}n_p\left(\lambda_{ds}i_{qs}-\lambda_{qs}i_{ds}\right)=\begin{cases}\dfrac{3}{2}n_p\lambda_m i_{qs}, & \text{SPMSM}\\ \dfrac{3}{2}n_p\left(L_d-L_q\right)i_{ds}i_{qs}, & \text{SynRM}\end{cases} \tag{2.26}$$

With respect to T_f of the SPMSM and the SynRM, its classic generic equation only considers the viscous friction torque, i.e.,

$$T_f=B_m\omega_m \tag{2.27}$$

where B_m denotes the viscous friction coefficient of each considered motor.

Based on (2.23)-(2.27), the classic dynamic models of the SPMSM and the SynRM in terms of i_{ds}, i_{qs} and ω_m can be derived as (2.28) and (2.29), respectively.

$$\begin{cases}\dot{i}_{ds}=-\dfrac{R_s}{L_s}i_{ds}+n_p\omega_m i_{qs}+\dfrac{1}{L_s}u_{ds}\\ \dot{i}_{qs}=-\dfrac{R_s}{L_s}i_{qs}-n_p\omega_m i_{ds}-\dfrac{n_p\lambda_m}{L_s}\omega_m+\dfrac{1}{L_s}u_{qs}\\ \dot{\omega}_m=\dfrac{3n_p\lambda_m}{2J}i_{qs}-\dfrac{1}{J}T_L-\dfrac{B_m}{J}\omega_m\end{cases} \tag{2.28}$$

$$\begin{cases}\dot{i}_{ds}=-\dfrac{R_s}{L_d}i_{ds}+\dfrac{n_p\omega_m L_q}{L_d}i_{qs}+\dfrac{1}{L_d}u_{ds}\\ \dot{i}_{qs}=-\dfrac{R_s}{L_q}i_{qs}-\dfrac{n_p\omega_m L_d}{L_q}i_{ds}+\dfrac{1}{L_q}u_{qs}\\ \dot{\omega}_m=\dfrac{3n_p\left(L_d-L_q\right)}{2J}i_{ds}i_{qs}-\dfrac{1}{J}T_L-\dfrac{B_m}{J}\omega_m\end{cases} \tag{2.29}$$

It can be observed that unmodeled dynamics, parametric uncertainties and external disturbances in the VSD system, which are mentioned in Section 1.2, are neglected in the classic dynamic models of the SPMSM and the SynRM, resulting in the mismatch between the derived and

the actual lumped disturbances in the speed and current tacking error dynamics. On the other hand, regarding many types of nonlinear speed/current controllers used in the FOC strategies of SPMSM-VSD and SynRM-VSD systems, in theory, the selection of controller gains is dependent on the boundary of the derived lumped disturbance in the speed or the current tacking error dynamics. Therefore, if unmodeled dynamics, parametric uncertainties and external disturbances are not considered into the derived lumped disturbances in the speed and the current tacking error dynamics of the SPMSM and the SynRM, many types of nonlinear speed/current controllers used in the FOC strategies of SPMSM-VSD and SynRM-VSD systems cannot accomplish desired tracking performance in theory. It motivates the derivation of the practical dynamic models of the SPMSM and the SynRM considering various types of unmodeled dynamics, parametric uncertainties and external disturbances.

2.3.3 Unmodeled Dynamics

In this thesis, the considered unmodeled dynamics contain the inverter nonlinearities, the current measurement errors, the cogging torque and the rotor flux linkage harmonics. The effects of such unmodeled dynamics on modeling of the SPMSM and the SynRM are presented in this subsection.

By applying the Park's transformation to the low-frequency model of the 2L-VSI in the *abc* frame presented in (2.18), the low-frequency model of the 2L-VSI in the *dq* frame is derived as

$$u_{ds}^{l}=u_{ds}^{l*}+u_{ds}^{d}=u_{ds}^{l*}+u_{ds}^{d1}+u_{ds}^{d2},\quad u_{qs}^{l}=u_{qs}^{l*}+u_{qs}^{d}=u_{qs}^{l*}+u_{qs}^{d1}+u_{qs}^{d2} \tag{2.30}$$

where u_{ds}^{l} and u_{qs}^{l} are the fundamental components of u_{ds} and u_{qs}, respectively, u_{ds}^{l*} and u_{qs}^{l*} represent the ideal fundamental components of u_{ds} and u_{qs}, respectively, u_{ds}^{d} and u_{qs}^{d} denote the total *d*- and *q*-axes distorted stator voltage components, respectively, u_{ds}^{d1} and u_{qs}^{d1} are two DC components that represent the first type of *d*- and *q*-axes distorted stator voltage components, respectively, u_{ds}^{d2} and u_{qs}^{d2} denote the second type of *d*- and *q*-axes distorted stator voltage components, respectively, which are expressed as

$$\begin{cases} u_{ds}^{d2}=\dfrac{4U_{dead}}{\pi}\left\{\sin\delta+\displaystyle\sum_{k=6n}^{\infty}\left[\frac{\sin\left[k\left(\omega_e t+\delta\right)-\delta\right]}{k-1}+\frac{\sin\left[k\left(\omega_e t+\delta\right)+\delta\right]}{k+1}\right]\right\} \\ u_{qs}^{d2}=\dfrac{4U_{dead}}{\pi}\left\{-\cos\delta+\displaystyle\sum_{k=6n}^{\infty}\left[\frac{\cos\left[k\left(\omega_e t+\delta\right)-\delta\right]}{k-1}-\frac{\cos\left[k\left(\omega_e t+\delta\right)+\delta\right]}{k+1}\right]\right\} \end{cases},\quad n=1,2,3... \tag{2.31}$$

where $\omega_e=n_p\omega_m$ denotes the rotor electrical speed and δ is the phase difference between the *q*-axis of the *dq* frame and the stator current vector.

According to (2.30) and (2.31), the considered inverter nonlinearities introduce the DC component and the 6*n*th harmonic component in terms of ω_e ($n = 1, 2, 3,\ldots$) to u_{ds}^{l} and u_{qs}^{l}. Furthermore, the amplitude of each voltage harmonic component is inversely proportional to its harmonic order.

Based on the above analysis, the effects of the inverter nonlinearities on u_{ds} and u_{qs} of the SPMSM and the SynRM can be described as

$$u_{ds} = u_{ds}^{*} + \Delta u_{ds} + \sum_{k=1}^{\infty} U_{dn} \sin\left(6k\omega_e t\right), \quad u_{qs} = u_{qs}^{*} + \Delta u_{qs} + \sum_{k=1}^{\infty} U_{qn} \cos\left(6k\omega_e t\right) \tag{2.32}$$

where u_{ds}^{*} and u_{qs}^{*} denote the ideal *d*- and *q*-axes stator voltage components of each considered motor, respectively, Δu_{ds} and Δu_{qs} represent the *d*- and *q*-axes DC distorted stator voltage components of each considered motor, respectively, U_{dn} and U_{qn} denote the amplitudes of the *d*- and *q*-axes 6*n*th distorted stator voltage harmonics of each considered motor, respectively.

In general, with respect to i_{as}, i_{bs} and i_{cs}, only two of them are measured by current sensors and the rest is calculated based on the fact that the sum of i_{as}, i_{bs} and i_{cs} is equal to zero. Each measured stator current is converted into the voltage signal by a current sensor at first. Then, the obtained voltage signal is transformed into the digital form in the hardware controller through the low-pass filter and the analog-to-digital converter [15]. The current errors caused by this measurement process can be classified as the current offset error and the current scaling error [15]. The former is caused by the imbalanced supply voltage of the current sensor and the inherent DC offset in the analog device adopted in the measurement process, the latter is resulted from the measured signal scaling due to the use of the analog-to-digital converter [15]. Considering these two types of current errors, i_{ds} and i_{qs} of the SPMSM and the SynRM can be expressed as

$$i_{ds} = i_{ds}^{*} + \Delta i_{ds}^{o} + \Delta i_{ds}^{s}, \quad i_{qs} = i_{qs}^{*} + \Delta i_{qs}^{o} + \Delta i_{qs}^{s} \tag{2.33}$$

where i_{ds}^{*} and i_{qs}^{*} denote the actual *d*- and *q*-axes stator current components of each considered motor, respectively, Δi_{ds}^{o} and Δi_{qs}^{o} represent the *d*- and *q*-axes current offset error components of each considered motor, respectively, which are expressed as (2.34), Δi_{ds}^{s} and Δi_{qs}^{s} denote the *d*- and *q*-axes current scaling error components of each considered motor, respectively, which are expressed as (2.35) [1], [15].

$$\Delta i_{ds}^{o} = I_o \sin\left(\omega_e t + \delta_o\right), \quad \Delta i_{qs}^{o} = I_o \cos\left(\omega_e t + \delta_o\right) \tag{2.34}$$

where I_o and δ_o denote the amplitude and the initial phase angle of the *d*- and *q*-axes current offset error components of each considered motor, respectively.

$$\Delta i_{ds}^{s} = I_d^{d} + I_s \sin\left(2\omega_e t + \delta_s\right), \quad \Delta i_{qs}^{s} = I_q^{d} + I_s \cos\left(2\omega_e t + \delta_s\right) \tag{2.35}$$

where I_d^d and I_q^d denotes the DC current error components caused by the current scaling error of each considered motor, I_s and δ_s represent the amplitude and the initial phase angle of the sinusoidal current error components caused by the current scaling error of each considered motor, respectively.

According to (2.33)-(2.35), the current measurement errors introduce the DC component, the first and the second harmonic component in terms of ω_e to i_{ds} and i_{qs} of the SPMSM and the SynRM.

The cogging torque is generated by the interaction between the rotor flux linkage created by the permanent-magnet materials and the stator anisotropy caused by the stator slotting [16]. Therefore, such a type of pulsating torque does not exists in the SynRM. In general, the cogging torque of the SPMSM can be expressed as the following expression [17].

$$T_c = \sum_{k=1}^{\infty} A_k \sin\left(kQ\omega_m t + \varphi_{ck}\right) \tag{2.36}$$

where T_c denotes the cogging torque, A_k and φ_{ck} are the amplitude and the initial phase angle of the kth harmonic component of the cogging torque, respectively, Q is the number of stator slots

The long-time operation of the SPMSM-VSD system makes the SPMSM operate at relatively high temperature, which affects the strength of the NdFeB magnet materials [5]. Moreover, in practice, there exist 6nth harmonic components in terms of ω_e ($n = 1, 2, 3 \ldots$) in the rotor flux linkage in the dq frame [18]. Therefore, λ_m can be expressed as the following expression in the dq frame [18].

$$\lambda_m = \sum_{k=0}^{\infty} \lambda_{mk} \cos 6k\omega_m t \tag{2.37}$$

where λ_{mk} is the amplitude of the kth harmonic component of the rotor flux linkage.

2.3.4 Parametric Uncertainties

In practice, the mechanical and electrical parameters in the dynamic models of the SPMSM and the SynRM are time-varying rather than constant. The variations of these parameters have significant effects on modeling of the SPMSM and the SynRM.

The values of J and B_m are usually calculated based on the results of relevant measuring experiments. Nevertheless, regarding each of these two mechanical parameters, there always exists the error between calculated and actual values. Therefore, these two mechanical parameters can be described as

$$J = J_0 + \Delta J \tag{2.38}$$

$$B_m = B_{m0} + \Delta B_m \tag{2.39}$$

where J_0 and ΔJ denote the rated value and the measurement error of the rotor inertia, respectively, B_{m0} and ΔB_m denote the rated value and the measurement error of the viscous friction coefficient, respectively.

It is well known that the stator resistance of the AC motor is sensitive to the temperature [19]. In a certain temperature range, its value is proportional to the temperature [19]. Therefore, considering the temperature effect, R_s can be described as

$$R_s = R_{s0} + \Delta R_s \tag{2.40}$$

where R_{s0} and ΔR_s denote the rated value and the variation of the stator resistance, respectively,

As shown in (2.24), since the magnetic saturation effect is neglected, the stator flux linkage versus current characteristics of the SPMSM and the SynRM are linear. However, in many applications, these two AC synchronous motors operate with high level of magnetic saturation, making the stator flux linkage versus current characteristics become nonlinear. The magnetic saturation effect on the AC synchronous motor can be classified as the self-saturation effect and the cross-saturation effect [20]. Since the latter has a slight effect on the SPMSM, it is neglected by the dynamic model of the SPMSM in this thesis. As for the SynRM, these two types of magnetic saturation effects have to be taken into account [21].

Considering the self-saturation effect, L_d and L_q of the SPMSM are nonlinear functions in terms of the stator current component in the same axis, i.e.,

$$L_d = L_d(i_{ds}) = L_s + \Delta L_d(i_{ds}), \quad L_q = L_q(i_{qs}) = L_s + \Delta L_q(i_{qs}) \tag{2.41}$$

where $\Delta L_d(i_{ds})$ and $\Delta L_q(i_{qs})$ represent the variations of the d- and q-axes synchronous inductances of the SPMSM, respectively.

With respect to the SynRM, considering the self- and cross-saturation effects, λ_{sd} and λ_{sq} are nonlinear functions in terms of i_{sd} and i_{sq}, i.e.,

$$\lambda_{sd} = \lambda_{sd}(i_{ds}, i_{qs}) = L_d(i_{ds}, i_{qs}) i_{ds}, \quad \lambda_{sq} = \lambda_{sq}(i_{ds}, i_{qs}) = L_q(i_{ds}, i_{qs}) i_{qs} \tag{2.42}$$

where $L_d(i_{ds}, i_{qs})$ and $L_q(i_{ds}, i_{qs})$ are usually named as the apparent inductances of the SynRM.

Moreover, λ_{sd} and λ_{sq} can be linearized at the operating point, i.e., [22]

$$\lambda_{sd} = L_{dd}(i_{ds}, i_{qs}) i_{ds} + L_{dq}(i_{ds}, i_{qs}) i_{qs}, \quad \lambda_{sq} = L_{qd}(i_{ds}, i_{qs}) i_{ds} + L_{qq}(i_{ds}, i_{qs}) i_{qs} \tag{2.43}$$

where $L_{dd}(i_{ds}, i_{qs})$, $L_{dq}(i_{ds}, i_{qs})$, $L_{qd}(i_{ds}, i_{qs})$ and $L_{qq}(i_{ds}, i_{qs})$ denote the incremental inductances of the SynRM, which can be calculated as

$$L_{dd}=\frac{\partial\lambda_{sd}}{\partial i_{sd}}\approx\left.\frac{\Delta\lambda_{sd}}{\Delta i_{sd}}\right|_{i_{sq}=\text{constant}},\quad L_{dq}=\frac{\partial\lambda_{sd}}{\partial i_{sq}}\approx\left.\frac{\Delta\lambda_{sd}}{\Delta i_{sq}}\right|_{i_{sd}=\text{constant}}$$
$$L_{qd}=\frac{\partial\lambda_{sq}}{\partial i_{sd}}\approx\left.\frac{\Delta\lambda_{sq}}{\Delta i_{sd}}\right|_{i_{sq}=\text{constant}},\quad L_{qq}=\frac{\partial\lambda_{sq}}{\partial i_{sq}}\approx\left.\frac{\Delta\lambda_{sq}}{\Delta i_{sq}}\right|_{i_{sd}=\text{constant}} \tag{2.44}$$

Defining L_{d0}, L_{q0}, L_{dd0}, L_{dq0}, L_{qd0} and L_{qq0} as rated apparent and incremental inductances of the SynRM for a certain combination of i_{ds} and i_{qs}, the apparent and incremental inductances of the SynRM can be expressed as

$$\begin{aligned}
&L_d(i_{ds},i_{qs})=L_{d0}+\Delta L_d(i_{ds},i_{qs}),\quad L_q(i_{ds},i_{qs})=L_{q0}+\Delta L_q(i_{ds},i_{qs})\\
&L_{dd}(i_{ds},i_{qs})=L_{dd0}+\Delta L_{dd}(i_{ds},i_{qs}),\quad L_{dq}(i_{ds},i_{qs})=L_{dq0}+\Delta L_{dq}(i_{ds},i_{qs})\\
&L_{qd}(i_{ds},i_{qs})=L_{qd0}+\Delta L_{qd}(i_{ds},i_{qs}),\quad L_{qq}(i_{ds},i_{qs})=L_{qq0}+\Delta L_{qq}(i_{ds},i_{qs})
\end{aligned} \tag{2.45}$$

where $\Delta L_d(i_{ds},i_{qs})$, $\Delta L_q(i_{ds},i_{qs})$, $\Delta L_{dd}(i_{ds},i_{qs})$, $\Delta L_{dq}(i_{ds},i_{qs})$, $\Delta L_{qd}(i_{ds},i_{qs})$ and $\Delta L_{qq}(i_{ds},i_{qs})$ denote the variations of apparent and incremental inductances of the SynRM.

2.3.5 External Disturbances

The load torque and the friction torque are two types of external disturbances considered in this thesis. The former depends on the characteristics of the mechanical load and has a significant impact on the dynamic performance of the VSD system. As for the latter, it has highly nonlinear characteristics in practice and can result in the steady-state errors and the limit cycles in the VSD system [23]. Until now, some static models, including the Karnopp model and the Armstrong's model, and dynamic models, such as the Dahl model, the Bristle model, the Bliman-Sorine model and the LuGre model, have been proposed to formulate the friction torque [23]. Among them, the LuGre model proposed in [24] is the most widely used one in the design of high-performance speed controllers for the VSD system [25]-[27]. Therefore, such a model is adopted in this thesis.

According to the LuGre model, T_f can be formulated as

$$T_f=B_0\vartheta+B_1\dot{\vartheta}+B_m\omega_m \tag{2.46}$$

where B_0 and B_1 are the averaged stiffness and the damping coefficient of bristles, respectively, and ϑ is an intermediate variable describing the average deflection of the bristles between two contact surfaces, whose dynamics can be expressed as the following expression [24].

$$\dot{\vartheta}=\omega_m-\frac{|\omega_m|}{g(\omega_m)}\vartheta \tag{2.47}$$

where $g(\omega_m)$ is a nonlinear function describing the Stribeck effect, which is expressed as

$$g(\omega_m) = T_c + (T_s - T_c)e^{-(\omega_m/\omega_s)^2} \tag{2.48}$$

where T_c is the Coulomb friction torque, T_s is the static friction torque, and ω_s is the Stribeck speed.

2.3.6 Practical Dynamic Models

With respect to the SPMSM-VSD system, considering the above-mentioned unmodeled dynamics, parametric uncertainties and external disturbances, the practical stator voltage and motion equations can be derived as (2.49) and (2.50), respectively.

$$u_{ds}^{*} = R_{s0}i_{ds} + L_s\frac{di_{ds}}{dt} - n_p\omega_m L_s i_{qs} + u_d^{dP}, \quad u_{qs}^{*} = R_{s0}i_{qs} + L_s\frac{di_{qs}}{dt} + n_p\omega_m L_s i_{ds} + n_p\omega_m\lambda_{m0} + u_q^{dP} \tag{2.49}$$

$$J_0\frac{d\omega_m}{dt} = \frac{3}{2}n_p\lambda_{m0}i_{qs} - T_L - B_{m0}\omega_m + T_\omega^{dP} \tag{2.50}$$

where u_d^{dP}, u_q^{dP} and T_ω^{dP} represent the d- and q-axes disturbance voltages and disturbance torque, respectively, which are expressed as

$$u_d^{dP} = \Delta R_s i_{ds} + \Delta L_d(i_{ds})\frac{di_{ds}}{dt} - n_p\omega_m\Delta L_q(i_{qs})i_{qs} + \varepsilon_d^P \tag{2.51}$$

$$u_q^{dP} = \Delta R_s i_{qs} + \Delta L_q(i_{qs})\frac{di_{qs}}{dt} + n_p\omega_m\left(\Delta L_d(i_{ds})i_{ds} + \sum_{k=1}^{\infty}\lambda_{mk}\cos 6k\omega_m t\right) + \varepsilon_q^P \tag{2.52}$$

$$T_\omega^{dP} = i_{qs}\sum_{k=1}^{\infty}\lambda_{mk}\cos 6k\omega_m t - \left(B_0\vartheta + B_1\dot{\vartheta} + \Delta B_m\omega_m\right) - \Delta J\frac{d\omega_m}{dt} + \varepsilon_\omega^P \tag{2.53}$$

where ε_d^P and ε_q^P denote the unmodeled dynamics in the d- and q-axes stator voltage equations of the SPMSM, respectively, and ε_ω^P represents the unmodeled dynamics in the motion equation of the SPMSM.

Based on (2.49) and (2.50), the practical dynamic model of the SPMSM in terms of i_{ds}, i_{qs} and ω_m can be derived as

$$\begin{cases} \dot{i}_{ds} = -\dfrac{R_{s0}}{L_s}i_{ds} + n_p\omega_m i_{qs} + \dfrac{1}{L_s}u_{ds}^{*} + \rho_d^P \\ \dot{i}_{qs} = -\dfrac{R_{s0}}{L_s}i_{qs} - n_p\omega_m i_{ds} - \dfrac{n_p\lambda_{m0}}{L_s}\omega_m + \dfrac{1}{L_s}u_{qs}^{*} + \rho_q^P \\ \dot{\omega}_m = \dfrac{3n_p\lambda_{m0}}{2J_0}i_{qs} - \dfrac{1}{J_0}T_L - \dfrac{B_{m0}}{J_0}\omega_m + \rho_\omega^P \end{cases} \tag{2.54}$$

where $\rho_d^P = -u_d^{dP}/L_s$, $\rho_q^P = -u_q^{dP}/L_s$ and $\rho_\omega^P = T_\omega^{dP}/J_0$ denote the lumped disturbances in the i_{ds}-, i_{qs}- and ω_m-dynamics of the SPMSM, respectively.

With respect to the SynRM-VSD system, considering unmodeled dynamics, parametric uncertainties and external disturbances which are mentioned in Section 2.3.3-Section 2.3.5, the practical stator voltage and motion equations can be derived as (2.55) and (2.56), respectively.

$$\begin{cases} u_{ds}^{*} = R_{s0} i_{ds} + L_{dd0} \dfrac{di_{ds}}{dt} + L_{dq0} \dfrac{di_{qs}}{dt} - n_p \omega_m L_{q0} i_{qs} + u_d^{dS} \\ u_{qs}^{*} = R_{s0} i_{qs} + L_{qd0} \dfrac{di_{ds}}{dt} + L_{qq0} \dfrac{di_{qs}}{dt} + n_p \omega_m L_{d0} i_{ds} + u_q^{dS} \end{cases} \tag{2.55}$$

$$J_0 \frac{d\omega_m}{dt} = \frac{3}{2} n_p \left(L_{d0} - L_{q0} \right) i_{ds} i_{qs} - T_L - B_{m0} \omega_m + T_\omega^{dS} \tag{2.56}$$

where u_d^{dS}, u_q^{dS} and T_ω^{dS}represent the d- and q-axes disturbance voltages and disturbance torque of the SynRM, respectively, which are expressed as

$$u_d^{dS} = \Delta R_s i_{ds} + \Delta L_{dd}(i_{ds}, i_{qs}) \frac{di_{ds}}{dt} + \Delta L_{dq}(i_{ds}, i_{qs}) \frac{di_{qs}}{dt} - n_p \omega_m \Delta L_q (i_{ds}, i_{qs}) i_{qs} + \varepsilon_d^S \tag{2.57}$$

$$u_q^{dS} = \Delta R_s i_{qs} + \Delta L_{qd}(i_{ds}, i_{qs}) \frac{di_{ds}}{dt} + \Delta L_{qq}(i_{ds}, i_{qs}) \frac{di_{qs}}{dt} + n_p \omega_m \Delta L_d (i_{ds}, i_{qs}) i_{ds} + + \varepsilon_q^S \tag{2.58}$$

$$T_\omega^{dS} = \frac{3}{2} n_p \left(\Delta L_d (i_{ds}, i_{qs}) - \Delta L_q (i_{ds}, i_{qs}) \right) i_{ds} i_{qs} - \left(B_0 \vartheta + B_1 \dot{\vartheta} + \Delta B_m \omega_m \right) - \Delta J \frac{d\omega_m}{dt} + \varepsilon_\omega^S \tag{2.59}$$

where ε_d^S and ε_q^S denote the unmodeled dynamics in the d- and q-axes stator voltage equations of the SynRM, respectively, and ε_ω^S represents the unmodeled dynamics in the motion equation of the SynRM.

Based on (2.55) and (2.56), the practical dynamic model of the SynRM in terms of i_{ds}, i_{qs} and ω_m can be derived as

$$\begin{cases} \dot{i}_{ds} = \dfrac{L_{qq0}}{M_0} \left(u_{ds}^{*} - R_{s0} i_{ds} + n_p \omega_m L_{q0} i_{qs} \right) - \dfrac{L_{dq0}}{M_0} \left(u_{qs}^{*} - R_{s0} i_{qs} - n_p \omega_m L_{d0} i_{ds} \right) + \rho_d^S \\ \dot{i}_{qs} = -\dfrac{L_{qd0}}{M_0} \left(u_{ds}^{*} - R_{s0} i_{ds} + n_p \omega_m L_{q0} i_{qs} \right) + \dfrac{L_{dd0}}{M_0} \left(u_{qs}^{*} - R_{s0} i_{qs} - n_p \omega_m L_{d0} i_{ds} \right) + \rho_q^S \\ \dot{\omega}_m = \dfrac{3 n_p \left(L_{d0} - L_{q0} \right)}{2 J_0} i_{ds} i_{qs} - \dfrac{1}{J_0} T_L - \dfrac{B_{m0}}{J_0} \omega_m + \rho_\omega^S \end{cases} \tag{2.60}$$

where $M_0 = L_{dd0} L_{qq0} - L_{dq0} L_{qd0}$, $\rho_\omega^S = T_\omega^{dS} / J_0$ denotes the lumped disturbance in the ω_m-dynamics of the SynRM, ρ_d^S and ρ_q^S represent the lumped disturbances in the i_{ds}- and i_{qs}-dynamics of the SynRM, respectively, which are expressed as

$$\rho_d^S = -\frac{L_{qq0}}{M_0} u_d^{dS} + \frac{L_{dq0}}{M_0} u_q^{dS}, \quad \rho_q^S = \frac{L_{qd0}}{M_0} u_d^{dS} - \frac{L_{dd0}}{M_0} u_q^{dS} \tag{2.61}$$

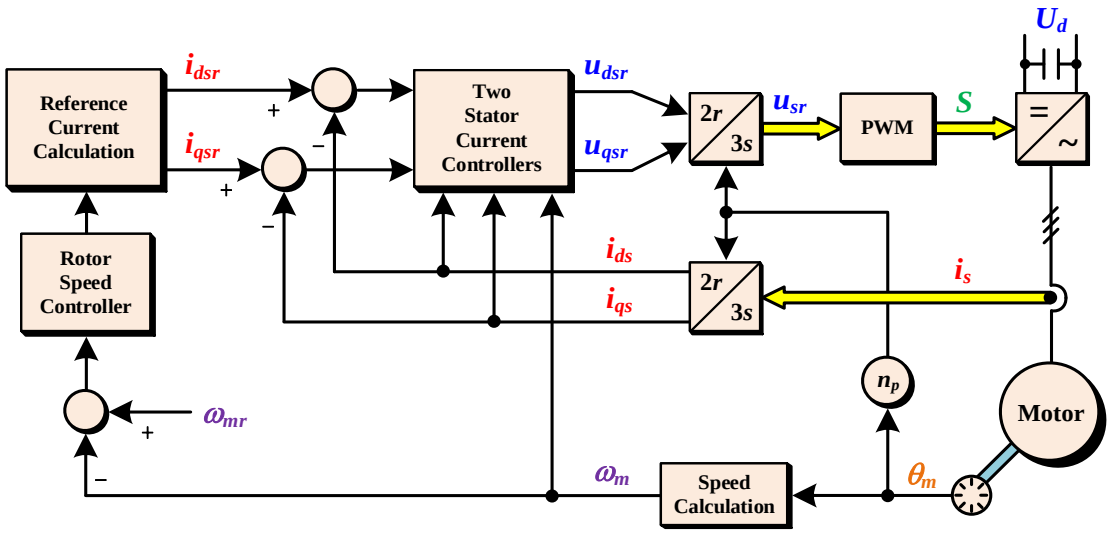

Figure 2.6 Block diagram of the field-oriented control strategy.

2.4 Field-Oriented Control Strategy

The FOC strategy for the AC synchronous motor-based VSD system follows a principle akin to the control of a separately excited DC motor. It is designed using the dynamic model of the AC synchronous motor in the *dq* frame and requires Park's transformation and its inverse form to achieve the reference frame transformation, which is based on the rotor mechanical position θ_m usually measured by the built in incremental encoder. As for ω_m, it is usually calculated from θ_m by the digital differentiator and the low-pass filter implemented in the adopted hardware controller. Moreover, as has been stated in Section 1.1, the FOC strategy adopts the cascaded control structure composed of the speed control loop and the current control loop. Since the dynamics of the current control loop is much faster than that of the speed control loop, the rotor speed controller and two stator current controllers are designed separately.

With respect to the FOC strategies for SPMSM-VSD and SynRM-VSD systems, in the speed control loop, the rotor speed controller is designed to make ω_m track its reference ω_{mr}. Moreover, it can be used to generate the reference torque such that the reference *d*- and *q*-axes stator current components i_{dsr} and i_{qsr} can be indirectly calculated from it for a certain purpose or generate i_{qsr} such that i_{dsr} can be directly set by the designer. In the current control loop, two stator current controllers are designed to make i_{ds} and i_{qs} track i_{dsr} and i_{qsr}, respectively, and provide the reference stator voltage *d*- and *q*-axes components u_{dsr} and u_{qsr}. Based on them, a pulse-width modulation (PWM) algorithm is implemented for the voltage-source inverter adopted in the VSD

system. The block diagram of the FOC strategy is illustrated in Figure 2.6, where $\boldsymbol{S} = [S_a, S_b, S_c]$, $\boldsymbol{i}_s = [i_{as}, i_{bs}, i_{cs}]$ and $\boldsymbol{u}_{sr} = [u_{asr}, u_{bsr}, u_{csr}]$.

In this thesis, the FOC strategy is selected as the main control strategy to integrate with the composite controllers presented in the following chapters.

2.5 HIL and Experimental Test Benches

In this thesis, the proposed composite controller-based FOC strategy for the SynRM-VSD system is tested in the HIL test bench, which is a cost-effective real-time verification platform as described in Figure 2.7. In this test bench, there are two dSPACE DS1104 Research and Development Boards: one is used as the hardware controller to implement the tested FOC strategy, the other is employed as the emulator to emulate the 2L-VSI-fed SynRM-VSD system. Moreover, the sampling period of each Research and Development Boards is different from each other.

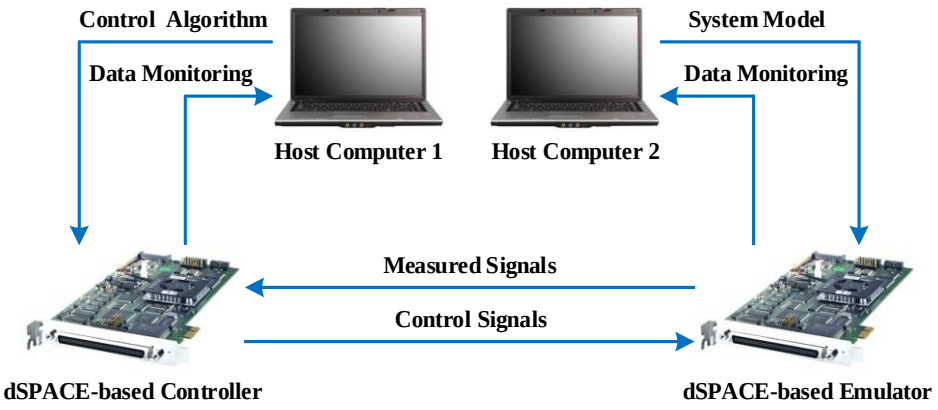

Figure 2.7 Description of the HIL test bench.

The proposed composite controller-based FOC strategies for the SPMSM-VSD system are tested in the experimental test bench illustrated in Figure 2.8. In this test bench, two identical three-phase SPMSMs are mechanically coupled. One operates at the speed mode as the tested motor, the other operates at the torque mode as the load motor. Each motor is connected to a Texas Instruments High Voltage Motor Control and PFC Developer's Kit in which a Texas Instruments floating-point DSP TMS320F28335 and a 1 kW 2L-VSI are used in the experimental tests. Two adopted 2L-VSIs are supplied by the same DC power source. The rotor mechanical position of each SPMSM is measured by a 2500 pulses per revolution built in incremental encoder. Furthermore, the parameters

of each SPMSM are listed in Table 2.1. Regarding the DSP, T_s is set to 100 μs, and the PWM switching frequency is set to 10 kHz with the dead time of 2 μs. The DSP software Code Composer Studio is used to accomplish the real-time data acquisition of the measurable variables and their visualization.

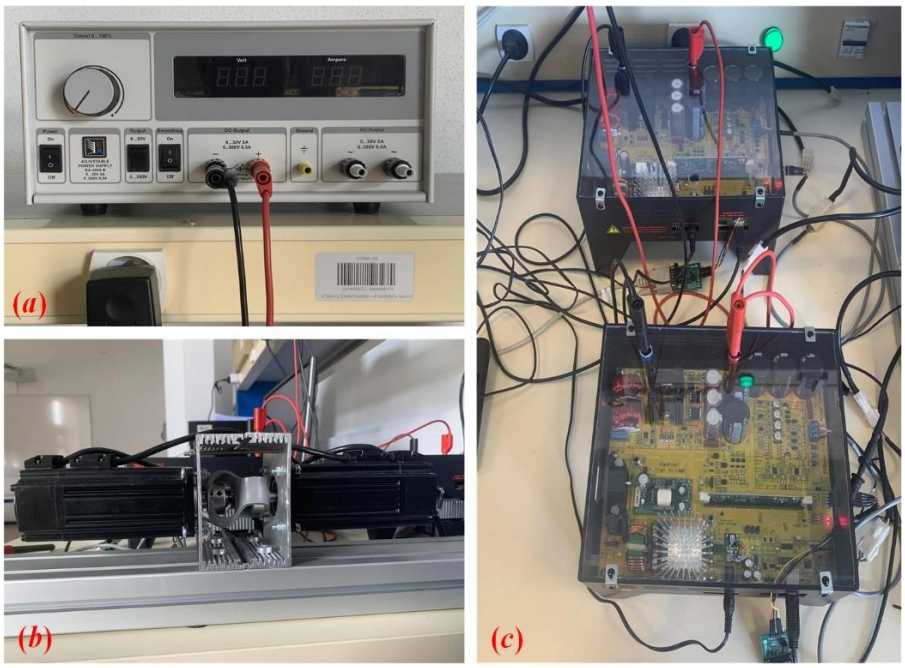

Figure 2.8 Description of the experimental test bench. (a) DC voltage source. (b) Two coupled SPMSMs. (c) Two TMDSHVMTRPFCKITs.

Table 2.1 Parameters of the SPMSM

Parameter	Value
Rated power (W)	400
Rated current (A)	2.8
Stator resistance (Ω)	2.35
Stator inductance (mH)	6.5
Rotor flux linkage (Wb)	0.065
Rated speed (rpm)	3000
Rotor inertia (kg·m^2)	0.00007
Viscous friction coefficient (N·m·s/rad)	0.0015
Rated torque (N·m)	1.27
Pole pairs	4

2.6 Summary

In this chapter, the effects of the considered unmodeled dynamics, parametric uncertainties and external disturbances on modeling of the SPMSM and the SynRM are presented. Based on them, the practical dynamic models of these two considered motors in terms of rotor mechanical speed and stator current components in the *dq* frame are derived. Then, the principles of the FOC strategies for SPMSM-VSD and SynRM-VSD systems are briefly introduced. Finally, the HIL test bench used to test the control strategy for the 2L-VSI-fed SynRM-VSD system and the experimental test bench adopted to test the control strategy for the 2L-VSI-fed SPMSM-VSD system are described.

References

[1] S. -K. Sul, *Control of Electric Machine Drive Systems*. Hoboken, USA: Wiley-IEEE Press, 2010.

[2] S. N. Manias, *Power Electronics and Motor Drive Systems*, Cambridge. USA: Academic Press, 2016.

[3] G. Abad, *Power Electronics and Electric Drives for Traction Applications*. Chichester, UK: Wiley, 2016.

[4] J. Pyrhönen, V. Hrabovcová, R. S. Semken, *Electrical Machine Drives Control: An Introduction*. Chichester, UK: Wiley, 2016.

[5] G. Pellegrino, T.M. Jahns, N. Bianchi, W.L. Soong, F. Cupertino, *The Rediscovery of Synchronous Reluctance and Ferrite Permanent Magnet Motors*. Basel, Switzerland: Springer International Publishing, 2016.

[6] T. Jahns, "Getting rare-earth magnets out of EV traction machines: A review of the many approaches being pursued to minimize or eliminate rare-earth magnets from future EV drivetrains," *IEEE Electrification Magazine*, vol. 5, no. 1, pp. 6-18, Mar. 2017.

[7] R. E. Doherty and C. A. Nickle, "Synchronous machines: I—An extension of Blondel's two-reaction theory," *Journal of the A.I.E.E.*, vol. 45, no. 10, pp. 974-987, Oct. 1926.

[8] A. Vagati, "The synchronous reluctance solution: a new alternative in AC drives," in *Proceedings of the 20th Annual Conference of the IEEE Industrial Electronics Society*, pp. 1-13, Sep. 1994.

[9] R. R. Moghaddam, F. Magnussen, and C. Sadarangani, "Theoretical and experimental reevaluation of synchronous reluctance machine," *IEEE Transactions on Industrial Electronics*, vol. 57, no. 1, pp. 6-13, Jan. 2010.

[10] Pioneering energy efficiency for reliable drinking water supply in the Netherlands. ABB Group, Switzerland, [Online]. Available: https://new.abb.com/drives/segments/water-and-wastewater/case-evides-waterbedrijf-article

[11] ABB helped meat company to reduce energy on smoking good sausages. ABB Group, Switzerland. [Online]. Available: https://new.abb.com/drives/media/smoking-good-sausages

[12] Campbell's Australia cuts costs with SynRM. ABB Group, Switzerland. [Online]. Available: https://new.abb.com/news/detail/65757/campbells-australia-cuts-costs-with-synrm

[13] S. Morimoto, "Trend of permanent magnet synchronous machines," *IEEJ Transactions on Electrical and Electronic Engineering*, vol. 2, no. 2, pp. 101-108, Mar. 2007.

[14] T. Qiu, X. Wen, and F. Zhao, "Adaptive-linear-neuron-based dead-time effects compensation scheme for PMSM drives," *IEEE Transactions on Power Electronics*, vol. 31, no. 3, pp. 2530-2538, Mar. 2016.

[15] D. -W. Chung and S. -K. Sul, "Analysis and compensation of current measurement error in vector-controlled AC motor drives," *IEEE Transactions on Industrial Applications*, vol. 34, no. 2, pp. 340-345, Mar./Apr. 1998.

[16] T. M. Jahns and W. L. Soong, "Pulsating torque minization techniques for permanent magent AC motor drives—A review," *IEEE Transactions on Industrial Electronics*, vol. 43, no. 2, pp. 321-330, Apr. 1996.

[17] N. Bianchi and S. Bolognani, "Design techniques for reducing the cogging torque in surface-mounted PM motors," *IEEE Transactions on Industrial Applications*, vol. 38, no. 5, pp. 1259-1265, Sep./Oct. 2002.

[18] W. Qian, S. K. Panda, and J. -X. Xu, "Troque ripple minization in PM synchronous motors using iterative learning control," *IEEE Transactions on Power Electronics*, vol. 19, no. 2, pp. 272-279, Mar. 2004.

[19] T. Sebastian, "Temperature effects on torque production and efficiency of PM motors using NdFeB magnets," *IEEE Transactions on Industrial Applications*, vol. 31, no. 2, pp. 353-357, Mar./Apr. 1995.

[20] K. M. Rahman and S. Hiti, "Identification of machine parameters of a synchronous motor," *IEEE Transactions on Industrial Applications*, vol. 41, no. 2, pp. 557-565, Mar./Apr. 2005.

[21] A. Vagati, M. Pastorelli, F. Scapino, and G. Franceschini, "Impact of cross saturation in synchronous reluctance motors of the transverse-laminated type," *IEEE Transactions on Industrial Applications*, vol. 36, no. 4, pp. 1039-1046, Jul./Aug. 2000.

[22] H. Eldeeb, C. M. Hackl, L. Horlbeck, and J. Kullick, "A unified theory for optimal feedforward torque control of anisotropic synchronous machines," *International Journal of Control*, vol. 91, no. 10, pp. 2273-2302, Oct. 2018.

[23] H. Olsson, K. J. Åström, C. Canudas de Wit, M. Gäfvert, and P. Lischinsky "Friction models and friction compensation", *European Journal of Control*, vol. 4, no. 3, pp. 176-195, Dec. 1998.

[24] C. Canudes de Wit, H. Olsson, K. J. Åström, and P. Lischinsky, "A new model for control of systems with friction," *IEEE Transactions on Automatic Control*, vol. 40, no. 3, pp. 419-425, Mar. 1995.

[25] Y. Tan, J. Chang and H. Tan, "Adaptive backstepping control and friction compensation for AC servo with inertia and load uncertainties," *IEEE Transactions on Industrial Electronics*, vol. 50, no. 5, pp. 944-952, Oct. 2003.

[26] C. -I. Huang and L. -C. Fu, “Adaptive approach to motion controller of linear induction motor with friction compensation,” *IEEE/ASME Transactions on Mechatronics*, vol. 12, no. 4, pp. 480-490,Aug. 2007.

[27] F. S. Ahmed, S. Laghrouche, and M. Harmouche, “Adaptive backstepping output feedback control of DC motor actuator with friction and load uncertainty compensation,” *International Journal of Robust and Nonlinear Control*, vol. 25, no. 13, pp. 1967-1992, Sep. 2015.

3

SELECTED MODEL-BASED AND MODEL-FREE DISTURBANCE OBSERVERS

3.1 Introduction

As mentioned in Section 1.2, there are various types of DOs for constructing composite controllers. Based on whether or not the system model is used in the DO design, the existing DOs can be classified into two categories: the model-based DOs and the model-free DOs. With respect to the former, as their name implies, the designs of these DOs are based on the system model. Among the existing model-based DOs, the extended DOs have gained much attention [1]-[8]. For the constructions of such DOs, unmodeled dynamics, parametric uncertainties and external disturbances in the system are lumped together, and the lumped disturbance is regarded as an augmented state to be estimated [1], [2]. Therefore, the extended DOs require minimum information of the system. Owing to this attractive feature, the extended DOs have been widely used in the DOC of AC motor drive systems [2]-[8]. The existing extended DOs can be divided into linear and nonlinear extended DOs. For the DOC of AC motor drive systems, the ESO and the extended sliding-mode DO are the most popular linear and nonlinear extended DOs, respectively. There are two widely used extended sliding-mode DOs for the DOC of AC motor drive systems. One is the extended FOSMO, and the other is the STSMO [6]-[8]. The extended FOSMO is based on the first-order sliding-mode (FOSM) algorithm, which can guarantee the finite-time convergence of the state estimation error to the origin in theory. In this sliding-mode algorithm, the discontinuous sign function with a large gain is used to achieve the disturbance estimation. In practice, however, the implementation of the discontinuous sign function with a large gain in the hardware controller yields severe chattering. There are two popular methods to overcome this drawback. One is to add a low-pass filter to the observer, and the

other is to use a continuous function, such as the saturation function, the sigmoid function and the hyperbolic tangent function, to replace the sign function in the observer. However, the price we pay for the chattering alleviation is the reduction of the disturbance estimation accuracy. The STSMO is designed using the standard super-twisting algorithm (STA), which is a continuous sliding-mode algorithm [9]-[11]. Compared with the FOSM algorithm, the standard STA is able to significantly alleviate the chattering in practice without sacrificing the disturbance estimation accuracy. Therefore, compared with the extended FOSMO, the STSMO is more suitable for the DOC of AC motor drive systems.

With respect to the model-free DOs, since ANNs are able to provide excellent input-output mapping ability without requiring the system model, ANN-DOs are the most popular choices to construct the model-free DO-based composite controllers for AC motor drive systems. Until now, various types of ANN-DOs with different activation functions and different structures have been proposed for the DOC of AC motor drive systems [12]-[27]. Among them, the ANN-DOs with single hidden layer are dominant. Based on whether or not the feedback loop is adopted in ANN-DOs, the existing ANN-DOs with single hidden layer can be divided into FNN-DOs with single hidden layer, each of which does not use any feedback loop, and RNN-DOs with single hidden layer, each of which adopts at least one feedback loop. The former can be regarded as static functions and the latter can be deemed as dynamic systems due to the use of feedback loops. Therefore, the RNN-DOs can store and process the temporal information and provide more powerful input-output mapping ability.

The speed/current tracking error dynamics of the SPMSM or the SynRM can be regarded as a single-input uncertain nonlinear system with relative degree one. In this chapter, the designs and the rigorous stability analyses of two extended DOs, i.e., the second-order ESO and the STSMO for a single-input uncertain nonlinear system with relative degree one are presented. Next, the structures of three widely used FNN-DOs with single hidden layer, i.e., the TLP-DO, the RBFNN-DO and the HNN-DO, and a widely used RNN-DO with single hidden layer, i.e., the ENN-DO for a single-input uncertain nonlinear system with relative degree one are presented. Moreover, two widely used approaches for deriving the learning laws, which are adopted to update some parameters in these ANN-DOs online, are introduced.

3.2 Problem Statement

A single-input uncertain nonlinear system with relative degree one expressed as (3.1) is considered

in this chapter.

$$\begin{cases} \dot{x} = a(x,t) + b(x,t)\mu \\ y = x \end{cases} \tag{3.1}$$

where $x \in R$ represents the state variable, $\mu \in R$ denotes the control law, $y \in R$ represents the controlled output, $a(x,t)$ and $b(x,t) \neq 0$ are smooth uncertain functions expressed as

$$a(x,t) = a_n + \Delta a(x,t), \quad b(x,t) = b_n + \Delta b(x,t) \tag{3.2}$$

where $a_n > 0$ and $b_n > 0$ are the known parts of $a(x,t)$ and $b(x,t)$, respectively, $\Delta a(x,t)$ and $\Delta b(x,t)$ are bounded uncertainties of $a(x,t)$ and $b(x,t)$, respectively, for $\forall x \in R$ and $t \in [0, \infty)$.

Combing (3.1) with (3.2), the x-dynamics can be rewritten as

$$\begin{aligned} \dot{x} &= \left(a_n + \Delta a(x,t)\right) + \left(b_n + \Delta b(x,t)\right)\mu = b_n\mu + \underbrace{a_n + \Delta a(x,t) + \Delta b(x,t)\mu}_{\rho_x(x,t)} \\ &= b_n\mu + \rho_x(x,t) \end{aligned} \tag{3.3}$$

where $\rho_x(x,t)$ denotes the lumped disturbance in the x-dynamics.

Assumption 3.1. ρ_x and its time derivative $\dot{\rho}_x$ are bounded as $|\rho_x| \leq L_1^x$ and $|\dot{\rho}_x| \leq L_2^x$, respectively, for positive constants L_1^x and L_2^x.

The task of the DO designed for the system (3.3) is to estimate ρ_x.

3.3 Two Extended DOs

The designs and the rigorous stability analyses of the second-order ESO and the STSMO for the estimation of ρ_x will presented in this section.

The designs of the extended DOs for the estimation of ρ_x are based on the extended x-dynamics. Based on (3.3), selecting ρ_x as an augmented state variable, the extended x-dynamics can be derived as

$$\begin{cases} \dot{z}_1^x = b_n\mu + z_2^x \\ \dot{z}_2^x = \dot{\rho}_x \end{cases} \tag{3.4}$$

where $z_1^x = x$ and $z_2^x = \rho_x$ are state variables of the extended x-dynamics.

3.3.1 ESO

From (3.4), the second-order ESO for the estimation of ρ_x is designed as

$$\begin{cases} \dot{\hat{z}}_{e1}^x = b_n\mu + \hat{z}_{e2}^x + \beta_1(z_1^x - \hat{z}_{e1}^x) \\ \dot{\hat{z}}_{e2}^x = \beta_2(z_1^x - \hat{z}_{e1}^x) \end{cases} \tag{3.5}$$

where $\hat{z}_{e1}^x = \hat{x}$ and $\hat{z}_{e2}^x = \hat{\rho}_x$ denote the estimated state variable and lumped disturbance, respectively, β_1 and β_2 are the positive constant gains of the second-order ESO.

Based on (3.4) and (3.5), the state estimation error system for the second-order ESO can be obtained as

$$\begin{cases} \dot{e}_{e1}^x = e_{e2}^x - \beta_1 e_{e1}^x \\ \dot{e}_{e2}^x = \dot{z}_{e2}^x - \beta_2 e_{e1}^x \end{cases} \tag{3.6}$$

where $e_{e1}^x = z_1^x - \hat{z}_{e1}^x$ and $e_{e2}^x = z_2^x - \hat{z}_{e2}^x$ represent state estimation errors.

According to (3.6), the transfer function between $\hat{\rho}_x$ and ρ_x can be expressed as

$$\frac{\hat{\rho}_x}{\rho_x} = \frac{\beta_2}{s^2 + \beta_1 s + \beta_2} \tag{3.7}$$

where s denotes the Laplace operator.

From (3.7), it can be seen that the characteristics of the second-order ESO-based lumped disturbance estimation is the same as that of a second-order low-pass filter. Thus, the state estimation performance of the second-order ESO depends on the values of β_1 and β_2. In order to tune these two parameters, a simple yet effective method presented in [28] is adopted in this thesis. In this method, the values of β_1 and β_2 are selected such that the second-order ESO has two identical negative real poles. Toward this end, β_1 and β_2 are selected as

$$\beta_1 = 2\omega_b, \quad \beta_2 = \omega_b^2 \tag{3.8}$$

such that characteristic polynomial of (3.7) is expressed as

$$s^2 + \beta_1 s + \beta_2 = (s + \omega_b)^2 \tag{3.9}$$

where ω_b is the bandwidth of the second-order ESO.

Regarding the second-order ESO, in general, with the growth of the bandwidth, namely the value of ω_b, not only the rate of convergence improves, but also the noise sensitivity increases. Thus, the value of ω_b should be selected to trade off the state estimation performance and the noise rejection ability.

Lemma 3.1 [29]. Considering the state estimation error system (3.6), suppose ρ_x and $\dot{\rho}_x$ are bounded. Then, for any positive ω_b, there are two positive constants L_3^x and L_4^x such that e_{e1}^x and

e_{e2}^x satisfy the following conditions in a finite time.

$$\left|e_{e1}^x\right| \le L_3^x, \quad \left|e_{e2}^x\right| \le L_4^x \tag{3.10}$$

Considering the state estimation error system (3.6), from Assumption 3.1 and Lemma 3.1, it can be concluded that $\dot{e}_{e2}^x$ is bounded. Thus, the following assumption can be stated.

Assumption 3.2. $\dot{e}_{e2}^x$ is bounded as $|\dot{e}_{e2}^x| \le L_5^x$ for a positive constant L_5^x.

3.3.2 STSMO

From (3.4), the STSMO for the estimation of ρ_x is designed as

$$\begin{cases} \dot{\hat{z}}_{s1}^x = b_n\mu + \hat{z}_{s2}^x + k_1\sqrt{|z_1^x - \hat{z}_{s1}^x|}\,\mathrm{sgn}(z_1^x - \hat{z}_{s1}^x) \\ \dot{\hat{z}}_{s2}^x = k_2\,\mathrm{sgn}(z_1^x - \hat{z}_{s1}^x) \end{cases} \tag{3.11}$$

where $\hat{z}_{s1}^x = \hat{x}$ and $\hat{z}_{s2}^x = \hat{\rho}_x$ denote the estimated state variable and lumped disturbance, respectively, k_1 and k_2 are the positive constant gains of the STSMO.

Based on (3.4) and (3.11), the state estimation error system for the STSMO can be described as the following form.

$$\begin{cases} \dot{e}_{s1}^x = -k_1\sqrt{|e_{s1}^x|}\,\mathrm{sgn}(e_{s1}^x) + e_{s2}^x \\ \dot{e}_{s2}^x = -k_2\,\mathrm{sgn}(e_{s1}^x) + \dot{z}_2^x \end{cases} \tag{3.12}$$

where $e_{s1}^x = z_1^x - \hat{z}_{s1}^x$ and $e_{s2}^x = z_2^x - \hat{z}_{s2}^x$ represent state estimation errors.

Theoretically, the finite-time convergence of e_{s1}^x and e_{s2}^x to the origin can be guaranteed by the following Theorem.

Theorem 3.1. Considering the state estimation error system (3.12) and $|\dot{z}_2^x| = |\dot{\rho}_x| \le L_2^x$, if k_1 and k_2 are selected as (3.13), e_{s1}^x and e_{s2}^x will converge to the origin in a finite time.

$$k_1 > 2, \quad k_2 > \frac{k_1^2 + 4(L_2^x)^2}{4(k_1 - 2)} \tag{3.13}$$

Proof. At first, a new state vector is introduced as follow:

$$\boldsymbol{\xi} = [\xi_1, \quad \xi_2]^T = \left[\sqrt{|e_{s1}^x|}\,\mathrm{sgn}(e_{s1}^x), \quad e_{s2}^x\right]^T \tag{3.14}$$

The time derivative of $\boldsymbol{\xi}$ along the trajectories of the system (3.12) is calculated as

$$\dot{\boldsymbol{\xi}} = \frac{1}{|\xi_1|}\left(\underbrace{\begin{bmatrix} -\frac{1}{2}k_1 & \frac{1}{2} \\ -k_2 & 0 \end{bmatrix}}_{\boldsymbol{A}} \boldsymbol{\xi} + \underbrace{\begin{bmatrix} 0 \\ 1 \end{bmatrix}}_{\boldsymbol{B}} \underbrace{|\xi_1| \dot{z}_2^x}_{\psi} \right) = \frac{1}{|\xi_1|}\left(\boldsymbol{A}\boldsymbol{\xi} + \boldsymbol{B}\psi \right) \tag{3.15}$$

For the system (3.12), the Lyapunov candidate function V_{STA} is selected as follows [30].

$$V_{STA} = \boldsymbol{\xi}^T \boldsymbol{P} \boldsymbol{\xi} \tag{3.16}$$

where $\boldsymbol{P}$ is a positive definite symmetric matrix expressed as

$$\boldsymbol{P} = \frac{1}{2}\begin{bmatrix} k_1^2 + 4k_2 & -k_1 \\ -k_1 & 2 \end{bmatrix} \tag{3.17}$$

Since $\boldsymbol{P}$ is a positive definite symmetric matrix, the following inequality holds.

$$\lambda_{min}\{\boldsymbol{P}\}\|\boldsymbol{\xi}\|_2^2 \le V_{STA} \le \lambda_{max}\{\boldsymbol{P}\}\|\boldsymbol{\xi}\|_2^2 \tag{3.18}$$

where $\lambda_{min}\{\boldsymbol{P}\}$ and $\lambda_{max}\{\boldsymbol{P}\}$ represent the minimum and maximum eigenvalues of $\boldsymbol{P}$, respectively, and $\|\bullet\|_2$ denotes the Euclidean norm of a vector.

The time derivative of V_{STA} along the trajectory of the $\boldsymbol{\xi}$-dynamics is calculated as

$$\dot{V}_{STA} = \frac{1}{|\xi_1|}\begin{bmatrix} \boldsymbol{\xi} \\ \psi \end{bmatrix}^T \begin{bmatrix} \boldsymbol{A}^T\boldsymbol{P} + \boldsymbol{P}\boldsymbol{A} & \boldsymbol{P}\boldsymbol{B} \\ \boldsymbol{B}^T\boldsymbol{P} & 0 \end{bmatrix} \begin{bmatrix} \boldsymbol{\xi} \\ \psi \end{bmatrix} \tag{3.19}$$

The time derivative of V_{STA} along the trajectory of the $\boldsymbol{\xi}$-dynamics is calculated as

$$\dot{V}_{STA} = \frac{1}{|\xi_1|}\begin{bmatrix} \boldsymbol{\xi} \\ \psi \end{bmatrix}^T \begin{bmatrix} \boldsymbol{A}^T\boldsymbol{P} + \boldsymbol{P}\boldsymbol{A} & \boldsymbol{P}\boldsymbol{B} \\ \boldsymbol{B}^T\boldsymbol{P} & 0 \end{bmatrix} \begin{bmatrix} \boldsymbol{\xi} \\ \psi \end{bmatrix} \tag{3.20}$$

Since $|\dot{z}_2^x| \le L_2^x$, the following inequality holds.

$$\varphi^2 = \xi_1^2(\dot{z}_2^x)^2 \le \xi_1^2(L_2^x)^2 \tag{3.21}$$

Based on (3.20) and (3.21), the following matrix inequality holds

$$\begin{aligned} \dot{V}_{STA} &\le \frac{1}{|\xi_1|}\left\{ \begin{bmatrix} \boldsymbol{\xi} \\ \psi \end{bmatrix}^T \begin{bmatrix} \boldsymbol{A}^T\boldsymbol{P} + \boldsymbol{P}\boldsymbol{A} & \boldsymbol{P}\boldsymbol{B} \\ \boldsymbol{B}^T\boldsymbol{P} & 0 \end{bmatrix} \begin{bmatrix} \boldsymbol{\xi} \\ \psi \end{bmatrix} + \xi_1^2(L_2^x)^2 - \psi^2 \right\} \\ &= \frac{1}{|\xi_1|}\begin{bmatrix} \boldsymbol{\xi} \\ \psi \end{bmatrix}^T \begin{bmatrix} \boldsymbol{A}^T\boldsymbol{P} + \boldsymbol{P}\boldsymbol{A} + (L_2^x)^2\boldsymbol{C} & \boldsymbol{P}\boldsymbol{B} \\ \boldsymbol{B}^T\boldsymbol{P} & -1 \end{bmatrix} \begin{bmatrix} \boldsymbol{\xi} \\ \psi \end{bmatrix} \\ &\le -\frac{1}{|\xi_1|}\boldsymbol{\xi}^T\boldsymbol{Q}\boldsymbol{\xi} \end{aligned} \tag{3.22}$$

Where $\boldsymbol{C} = \begin{bmatrix} 1 & 0 \\ 0 & 0 \end{bmatrix}$ and $\boldsymbol{Q}$ can be expressed as the following expression [31].

$$\begin{aligned}\boldsymbol{Q} &= -\left(\boldsymbol{A}^T\boldsymbol{P} + \boldsymbol{P}\boldsymbol{A} + (L_2^x)^2\boldsymbol{C} + \boldsymbol{P}\boldsymbol{B}\boldsymbol{B}^T\boldsymbol{P}\right) \\ &= \frac{1}{2}\begin{bmatrix} k_1^3 - \frac{1}{2}k_1^2 + 2k_1k_2 - 2(L_2^x)^2 & -k_1^2 + k_1 \\ -k_1^2 + k_1 & k_1 - 2 \end{bmatrix}\end{aligned} \tag{3.23}$$

Since k_1 and k_2 are selected as (3.13), based on the principle of the Schur complement of a matrix, $\boldsymbol{Q}$ is a positive definite symmetric matrix. As a result, the following inequality holds.

$$\dot{V}_{STA} \le -\frac{1}{|\xi_1|}\boldsymbol{\xi}^T\boldsymbol{Q}\boldsymbol{\xi} \le -\frac{1}{|\xi_1|}\lambda_{min}\{\boldsymbol{Q}\}\|\boldsymbol{\xi}\|_2^2 \le -\zeta\sqrt{V_{STA}} \tag{3.24}$$

where $\lambda_{min}\{\boldsymbol{Q}\}$ represents the minimum eigenvalue of $\boldsymbol{Q}$ and ζ is a positive constant expressed as

$$\zeta = \frac{\lambda_{min}\{\boldsymbol{Q}\}\sqrt{\lambda_{min}\{\boldsymbol{P}\}}}{\lambda_{max}\{\boldsymbol{P}\}} \tag{3.25}$$

On the basis of (3.24) and the comparison principle [32], e_{s1}^x and e_{s2}^x will converge to the origin in a finite time. The proof is completed. ■

Since e_{s2}^x will converge to the origin in a finite time, the following assumption can be stated.

Assumption 3.3. e_{s2}^x is bounded as $|e_{s2}^x| \le L_6^x$ for a positive constant L_6^x.

3.4 Selected ANN-DOs

In this section, the structures of three widely used FNN-DOs with single hidden layer, i.e., the TLP-DO, the RBFNN-DO and the HNN-DO, and the ENN-DO, which is a widely used RNN-DOs with single hidden layer, for the estimation of ρ_x are introduced. Moreover, with respect to the derivation of the learning laws for some parameters in these ANN-DOs, two widely used approaches are introduced.

3.4.1 Three FNN-DOs

The structure of a FNN-DO with single hidden layer for the estimation of ρ_x can be described as Figure 3.1. It consists of the input layer, the hidden layer and the output layer. In the input layer, there are *N* neurons corresponding to *N* input signals. In the hidden layer, there are *M* neurons, and each of them uses an activation function to achieve signal processing. In the output layer, one neuron is adopted and its output signal is the estimated ρ_x, which is a weighted sum of output signals of hidden neurons. The TLP-DO, the RBFNN-DO and the HNN-DO have the same structure as

presented in Figure 3.1. The main difference among them is the activation function in each hidden neuron.

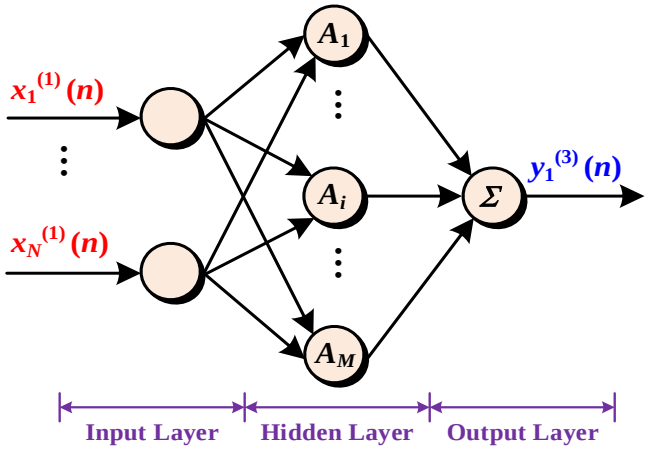

Figure 3.1 Block diagram of a FNN-DO with single hidden layer.

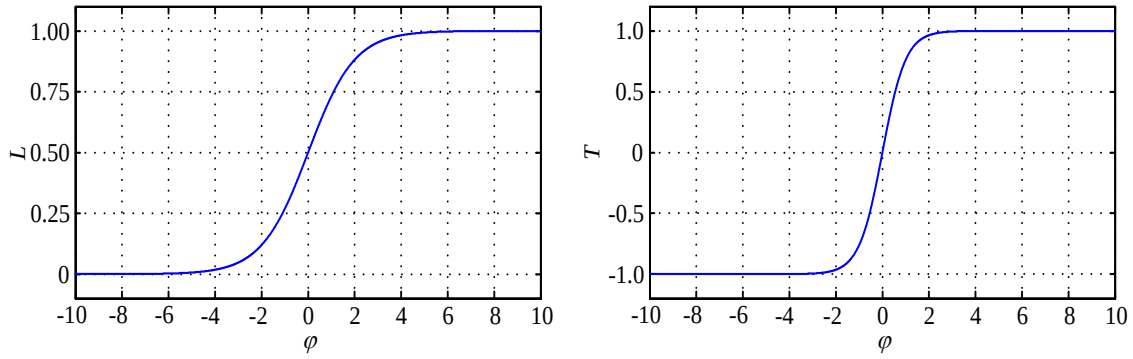

(a) (b)

Figure 3.2 Activation function in each hidden neuron of the TLP-DO. (a) The logistic function. (b) The hyperbolic tangent function

3.4.1.1 TLP-DO

The TLP-DO uses the logistic function expressed as (3.26) or the hyperbolic tangent function expressed as (3.27) as the activation function in each hidden neuron.

$$L(\varphi) = \frac{1}{1+e^{-a_1\varphi}} \tag{3.26}$$

$$T(\varphi) = a_2 \frac{e^{a_3\varphi} - e^{-a_3\varphi}}{e^{a_3\varphi} + e^{-a_3\varphi}} \tag{3.27}$$

where a_1, a_2 and a_3 are three positive constants.

When $a_1 = a_2 = a_3 = 1$, the logistic function and the hyperbolic tangent function in the interval $[-10, 10]$ are illustrated in Figure 3.2.

As presented in Figure 3.1, the signal propagation and the activation function of each layer of the TLP-DO are described as follows.

Input Layer: In this layer, regarding the *j*th input neuron ($j = 1, 2, \ldots, N$), the signal propagation can be described as

$$y_j^{(1)}(n) = x_j^{(1)}(n), \quad j = 1, 2, ..., N \tag{3.28}$$

where $y_j^{(1)}(n)$ is the output signal of the *j*th input neuron at the *n*th instant, $x_j^{(1)}(n)$ is the input signal of the *j*th input neuron at the *n*th instant.

Hidden Layer: In this layer, regarding the *i*th hidden neuron ($i = 1, 2, \ldots, M$), the signal propagation can be described as

$$x_i^{(2)}(n) = \sum_{j=1}^{N} W_{ij}^{(1)}(n) y_j^{(1)}(n), \quad i = 1, 2, ..., M \tag{3.29}$$

$$y_i^{(2)}(n) = L(x_i^{(2)}(n)) \quad \text{or} \quad y_i^{(2)}(n) = T(x_i^{(2)}(n)) \tag{3.30}$$

where $x_i^{(2)}(n)$ and $y_i^{(2)}(n)$ represent the input and output signals of the *i*th hidden neuron at the *n*th instant, respectively, $W_{ij}^{(1)}(n)$ denotes the connective weight between the *i*th hidden neuron and the *j*th input neuron at the *n*th instant.

Output Layer: In this layer, the output signal is $\hat{\rho}_x$, which can be calculated as

$$\hat{\rho}_x = y_1^{(3)}(n) = \sum_{i=1}^{M} W_i^{(2)}(n) y_i^{(2)}(n) \tag{3.31}$$

where $y_1^{(3)}(n)$ represents the output signal of the output neuron at the *n*th instant, $W_i^{(2)}(n)$ denotes the connective weight between the output neuron and the *i*th hidden neuron at the *n*th instant.

Remark 3.1. In the TLP-DO, *N*, *M*, $W_{ij}^{(1)}(n)$ and $W_i^{(2)}(n)$ ($i = 1, 2, \ldots, M$, $j = 1, 2, \ldots, N$) need to be determined. In general, *N* and *M* are set in advance, while $W_{ij}^{(1)}(n)$ and $W_i^{(2)}(n)$ are updated online by the learning laws [12].

3.4.1.2 RBFNN-DO

The RBFNN-DO usually uses the Gaussian function as the activation function in each hidden neuron. The Gaussian function with single input signal is written as

$$G(\varphi)=e^{-g},\quad g=\frac{(\varphi-c)^2}{2\delta^2} \tag{3.32}$$

where δ and c are the width and the center of the Gaussian function, respectively.

When $c=0$ and $\delta=2$, the Gaussian function with single input signal in the interval $[-10, 10]$ is illustrated in Figure 3.3.

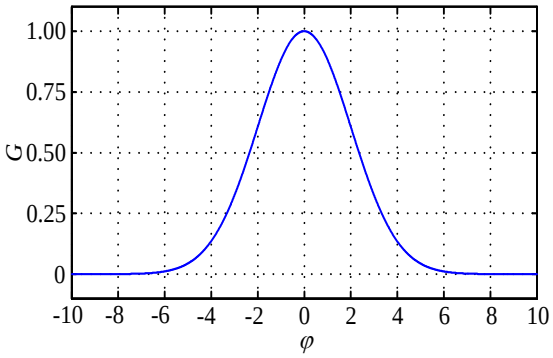

Figure 3.3 Gaussian function with single input signal.

As presented in Figure 3.1, the signal propagation and the activation function of each layer of the RBFNN-DO are described as follows.

Input Layer: In this layer, like the TLP-DO, the signal propagation of the *j*th input neuron ($j = 1, 2, \ldots, N$) can be described as

$$y_j^{(1)}(n)=x_j^{(1)}(n),\quad j=1,2,...,N \tag{3.33}$$

Hidden Layer: In this layer, regarding the *i*th hidden neuron ($i = 1, 2,\ldots, M$), the signal propagation can be described as

$$x_i^{(2)}(n)=\sum_{j=1}^{N}\frac{\left[y_j^{(1)}(n)-c_{ji}\right]^2}{2\delta_{ji}^2},\quad i=1,2,...,M \tag{3.34}$$

$$y_i^{(2)}(n)=e^{-x_i^{(2)}(n)} \tag{3.35}$$

where δ_{ji} and c_{ji} represent the width and the center of the Gaussian function in the *i*th hidden neuron for the *j*th input neuron, respectively.

Output Layer: In this layer, like the TLP-DO, the output signal is $\hat{\rho}_x$, which can be calculated as

$$\hat{\rho}_x=y_1^{(3)}(n)=\sum_{i=1}^{M}W_i^{(2)}(n)y_i^{(2)}(n) \tag{3.36}$$

Remark 3.2. In the RBFNN-DO, N, M, δ_{ji}, c_{ji} and $W_i^{(2)}(n)$ ($i = 1, 2, \ldots, M$, $j = 1, 2, \ldots, N$) need to be determined. In general, N, M, δ_{ji} and c_{ji} are set in advance [13]-[15]. As for $W_i^{(2)}(n)$, it is updated online by the learning laws.

3.4.1.3 HNN-DO

The HNN-DO uses the Hermite function, which is derived from the Hermite polynomials, as the activation function in each hidden neuron.

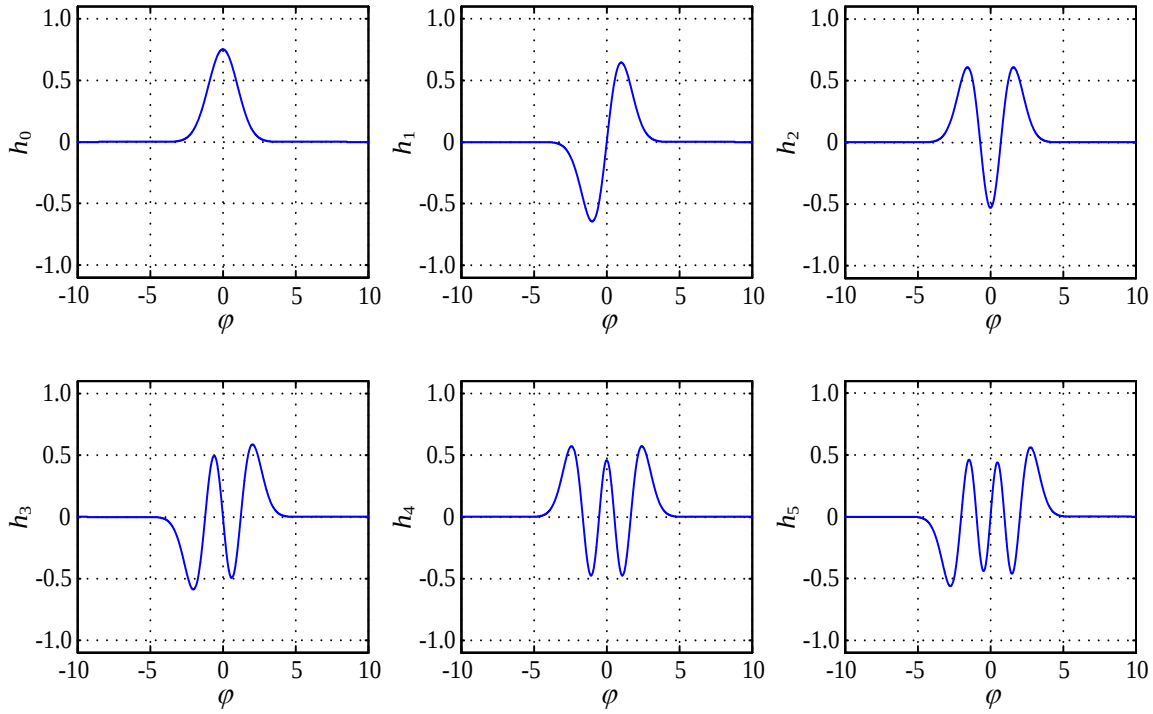

Figure 3.4 First six Hermite functions.

The Hermite polynomials $\{H_n(\varphi)\}_{n=0}^{\infty}$, which is defined in the interval $(-\infty, \infty)$, can be expressed by the following so-called Rodrigues' formula.

$$H_n(\varphi) = (-1)^n e^{\varphi^2} \frac{d^n}{d\varphi^n}(e^{-\varphi^2}), \quad n = 0,1,2,... \tag{3.37}$$

Based on (3.37), a useful recurrence relation for the calculation of each $H_n(\varphi)$ can be derived as

$$H_0(\varphi) = 1, \quad H_1(\varphi) = 2\varphi, \quad H_n(\varphi) = 2\varphi H_{n-1}(\varphi) - 2(n-1)H_{n-2}(\varphi), \quad n > 2 \tag{3.38}$$

Although $\{H_n(\varphi)\}_{n=0}^{\infty}$ are orthogonal with regard to the weight function $\kappa(\varphi) = e^{-\varphi^2}$, they

are not orthonormal. Regarding the polynomial-based activation functions in the hidden layer of FNNs, the orthonormal polynomials are preferred [33]. Toward this end, based on $\{H_n(\varphi)\}_{n=0}^{\infty}$, the Hermite functions $\{h_n(\varphi)\}_{n=0}^{\infty}$, which are orthonormal functions, are derived as follows [33]-[35].

$$h_n(\varphi)=\frac{1}{\sqrt{\sqrt{\pi}2^n n!}}H_n(\varphi)e^{-\frac{\varphi^2}{2}} \tag{3.39}$$

The first six Hermite functions in the interval $[-10, 10]$ is illustrated in Figure 3.4.

As presented in Figure 3.1, the signal propagation and the activation function of each layer of the HNN-DO are described as follows.

Input Layer: In this layer, like the aforementioned two FNN-DOs, the signal propagation of the *j*th input neuron ($j = 1, 2, \ldots, N$) can be described as

$$y_j^{(1)}(n)=x_j^{(1)}(n),\quad j=1,2,...,N \tag{3.40}$$

Hidden Layer: In this layer, regarding the *i*th hidden neuron ($i = 1, 2,\ldots, M$), the signal propagation can be described as

$$x_i^{(2)}(n)=\sum_{j=1}^{N}y_j^{(1)}(n),\quad i=1,2,...,M \tag{3.41}$$

$$y_i^{(2)}(n)=h_i(x_i^{(2)}(n)) \tag{3.42}$$

Output Layer: In this layer, like the aforementioned two FNN-DOs, the output signal is $\hat{\rho}_x$, which can be calculated as

$$\hat{\rho}_x=y_1^{(3)}(n)=\sum_{i=1}^{M}W_i^{(2)}(n)y_i^{(2)}(n) \tag{3.43}$$

Remark 3.3. In the HNN-DO, *N*, *M* and $W_i^{(2)}(n)$ ($i = 1, 2,\ldots, M, j = 1, 2, \ldots, N$) need to be determined. In general, *N* and *M* are set in advance, while $W_i^{(2)}(n)$ are updated online by the learning laws. Among three FNN-DOs presented in this subsection, the parameters that need to be determined in the HNN-DO is minimum.

3.4.2 ENN-DO

The ENN-DO is one of the most widely used RNN-DO for the DOC of AC motor drive systems. The structure of such a model-free DO for the estimation of ρ_x is illustrated as Figure 3.5 [16]-[19]. It consists of the input layer, the hidden layer, the context layer and the output layer. In the input layer, there are *N* neurons corresponding to *N* input signals. In the hidden layer, there are *M* neurons, each of which selects a logistic function as an activation function. Moreover, different from the

FNN-DOs presented in Section 3.4.1, each hidden neuron of the ENN-DO receives not only output signals of all input neurons but also output signals of all context neurons. In the context layer, there are also M neurons, each of which receives the output signal of a certain hidden neuron and then feed it back to all hidden neurons with one-step delay. In the output layer, like the FNN-DOs presented in Section 3.4.1, one neuron is adopted and its output signal is the estimated ρ_x, which is a weighted sum of output signals of hidden neurons.

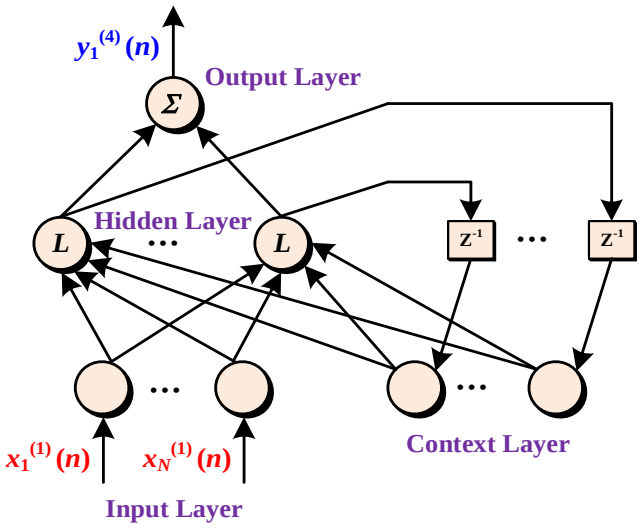

Figure 3.5 Block diagram of the ENN-DO.

As presented in Figure 3.5, the signal propagation and the activation function of each layer of the ENN-DO are described as follows.

Input Layer: In this layer, like the FNN-DOs presented in Section 3.4.1, the signal propagation of the jth input neuron ($j = 1, 2, \ldots, N$) can be described as

$$y_j^{(1)}(n) = x_j^{(1)}(n), \quad j = 1, 2, ..., N \tag{3.44}$$

Hidden Layer: In this layer, regarding the ith hidden neuron ($i = 1, 2, \ldots, M$), the signal propagation can be described as

$$x_i^{(2)}(n) = \sum_{j=1}^{N} \Phi_{ij}^{(1)}(n) y_j^{(1)}(n) + \sum_{i=1}^{M} y_i^{(3)}(n), \quad i = 1, 2, ..., M \tag{3.45}$$

$$y_i^{(2)}(n) = L(x_i^{(2)}(n)) \tag{3.46}$$

where $y_i^{(3)}(n)$ represents the output signal of the ith context neuron at the nth instant, $\Phi_{ij}^{(1)}(n)$ denotes the connective weight between the ith hidden neuron and the jth input neuron at the nth

instant.

Context Layer: In this layer, regarding the *i*th context neuron ($i = 1, 2,\ldots, M$), the signal propagation can be described as

$$y_i^{(3)}(n) = x_i^{(3)}(n) = y_i^{(2)}(n-1), \quad i = 1,2,...,M \tag{3.47}$$

where $x_i^{(3)}(n)$ is the input signal of the *i*th context neuron at the *n*th instant, and $y_i^{(2)}(n-1)$ is the output signal of the *i*th hidden neuron at the $(n-1)$th instant.

Output Layer: In this layer, the output signal is $\hat{\rho}_x$, which can be calculated as

$$\hat{\rho}_x = y_1^{(4)}(n) = \sum_{i=1}^{M} \Phi_i^{(2)}(n) y_i^{(2)}(n) \tag{3.48}$$

where $y_1^{(4)}(n)$ represents the output signal of the output neuron at the *n*th instant, $\Phi_i^{(2)}(n)$ denotes the connective weight between the output neuron and the *i*th hidden neuron at the *n*th instant.

Remark 3.4. In the ENN-DO, *N*, *M*, $\Phi_{ij}^{(1)}(n)$ and $\Phi_i^{(2)}(n)$ ($i = 1, 2,\ldots, M, j = 1, 2, \ldots, N$) need to be determined. In general, *N* and *M* are set in advance, while $\Phi_{ij}^{(1)}(n)$ and $\Phi_i^{(2)}(n)$ are updated online by the learning laws.

3.4.3 Learning Law Derivation

In each aforementioned ANN-DO, there are some parameters that need to be updated online by the learning laws. The derivation of these learning laws has to take into account the stability issue of the composite controller-based tracking control system. Toward this end, there are two widely used approaches for deriving these learning laws. One is the Lyapunov synthesis approach, and the other is the hybrid approach. The former uses the Lyapunov stability analysis of the tracking control system to derive the learning laws for all parameters that need to be updated online. As for the latter, only the learning law for the connective weights between the output neuron and the hidden neurons are derived by the Lyapunov stability analysis of the tracking control system, and the learning laws for other parameters that need to be updated online are derived from other algorithms such as the well-known back-propagation (BP) algorithm.

In above-mentioned two approaches, the Lyapunov stability analysis of the tracking control system is used to derive the learning laws for the connective weights between the output neuron and the hidden neurons. Therefore, the derived learning law is related to the controller used by the tracking control system. Since the aforementioned ANN-DOs have the same output layer structure, the learning laws for the connective weights between the output neuron and the hidden neurons in each aforementioned ANN-DO are the same for a certain controller.

3.5 Summary

In this chapter, two model-based extended DOs, i.e., the second-order ESO and the STSMO, and four model-free DOs, i.e., the TLP-DO, the RBFNN-DO, the HNN-DO and the ENN-DO for a single-input uncertain nonlinear system with relative degree one are presented. At first, the designs and the rigorous stability analyses of the second-order ESO and the STSMO are given. Afterward, the structures of the TLP-DO, the RBFNN-DO, the HNN-DO and the ENN-DO are presented. Finally, two widely used approaches for deriving the learning laws, which are adopted to update some parameters in these model-free DOs online, are introduced.

References

[1] W. -H. Chen, J. Yang, L. Guo, and S. Li, "Disturbance-observer-based control and related methods—An overview," *IEEE Transactions on Industrial Electronics*, vol. 63, no. 2, pp. 1083-1095, Feb. 2016.

[2] J. Yang, W. -H. Chen, S. Li, L. Guo, and Y. Yan, "Disturbance/uncertainty estimation and attenuation techniques in PMSM drives—A survey," *IEEE Transactions on Industrial Electronics*, vol. 64, no. 4, pp. 3273-3285, Apr. 2017.

[3] S. Li, J. Yang, W. -H. Chen, and X. Chen, *Disturbance Observer-Based Control Methods and Applications*. Boca Raton, USA: CRC Press, 2017.

[4] S. Li and Z. Liu, "Adaptive speed control for permanent-magnet synchronous motor system with variations of load inertia," *IEEE Transactions on Industrial Electronics*, vol. 56, no. 8, pp. 3050-3059, Aug. 2009.

[5] B. Du, S. Wu, S. Han, and S. Cui, "Application of linear active disturbance rejection controller for snesorless control of internal permanent-magnet synchronous motor," *IEEE Transactions on Industrial Electronics*, vol. 63, no. 5, pp. 3019-3027, May 2016.

[6] X. Zhang, L. Sun, K. Zhao, and L. Sun, "Nonlinear speed control for PMSM system using sliding-mode control and disturbance compensation techniques," *IEEE Transactions on Power Electronics*, vol. 28, no. 3, pp. 1358-1365, Mar. 2013.

[7] J. Davila, L. Fridman, and A. Levant, "Second-order sliding-mode observer for mechanical systems," *IEEE Transactions on Automatic Control*, vol. 50, no. 11, pp. 1785-1789, Nov. 2005.

[8] B. Wang, Z. Dong, Y. Yu, G. Wang, and D. Xu, "Static-errorless deadbeat predictive current control using second-order sliding-mode disturbance observer for induction machine drives," *IEEE Transactions on Power Electronics*, vol. 33, no. 3, pp. 2395-2403, Mar. 2018.

[9] A. Levant, "Sliding order and sliding accuracy in sliding mode control," *Internation Journal of Control*, vol. 58, no. 6, pp. 1247-1263, Jun. 1993.

[10] A. Levant, "Principles of 2-sliding mode design," *Automatica*, vol. 43, no. 4, pp. 576-586, Apr. 2007.

[11] Y. Shtessel, C. Edwards, L. Fridman, and A. Levant, *Sliding Mode Control and Observation*. Basel, Switzerland: Birkhäuser, 2014.

[12] F. -J. Lin and R. -J. Wai, "Robust control using neural network uncertainty observer for linear induction motor servo drive," *IEEE Transactions on Power Electronics*, vol. 17, no. 2, pp. 241-254, Mar. 2002.

[13] F. -J. Lin, L. -T. Teng, and M. -H. Yu, "Radial basis function network control with improved particle swarm optimization for induction generaor system," *IEEE Transactions on Power Electronics*, vol. 23, no. 4, pp. 2157-2169, Jul. 2008

[14] F. -J. Lin, J. -C. Hwang, P. -H. Chou, and Y. -C. Hung, "FPGA-based intelligent-complementary sliding-mode control for PMLSM servo-drive system," *IEEE Transactions on Power Electronics*, vol. 25, no. 10, pp. 2573-2587, Oct. 2010.

[15] L. Qi and H. Shi, "Adaptive position tracking control of permanent magnet synchronous motor based on RBF fast terminal sliding mode control," *Neurocomputing*, vol. 115, pp. 23-30, Sep. 2013.

[16] F. -J. Lin and R. -J. Wai, "FPGA-based Elman neural network control system for linear ultrasonic motor," *IEEE Transactions on Ultrasonic, Ferroelectrics, and Frequency Control*, vol. 56, no. 1, pp. 101-113, Jan. 2009.

[17] F. -J. Lin and R. -J. Wai, "FPGA-based computed force control system using Elman neural network for linear ultrasonic motor," *IEEE Transactions on Industrial Electronics*, vol. 56, no. 4, pp. 1238-1253, Apr. 2009.

[18] F. -J. Lin, K. -H. Tan and C. -H. Tsai, "Improved differential evolution-based Elman neural network controller for squirrel-cage induction generator system," *IET Renewable Power Generation*, vol. 10, no. 7, pp. 988-1001, Aug. 2016.

[19] H. Jin and X. Zhao, "Complementary sliding-mode control via Elman neural network for permanent magnet linear servo system," *IEEE Access*, vol. 7, pp. 82183-82193, Jun. 2019.

[20] F. -J. Lin, L. -T. Teng, and H. Chu, "Modified Elman neural network controller with improved particle swarm optimization for linear synchronous motor drive," *IET Electric Power Applications*, vol. 2, no. 3, pp. 201-214, Aug. 2016.

[21] F. J. Lin, C. -H. Lin, X. Gu, and P. -H. Shen, "Self-constructing fuzzy neural network speed controller for permanent-magnet synchronous motor drive," *IEEE transactions on Fuzzy Systems*, vol. 9, no. 5, pp. 751-759, Oct. 2001.

[22] F. -J. Lin, L. -T. Teng, and H. Chu, "A robust recurrent wavelet neural network controller with improved particle swarm optimization for linear synchronous motor drive," *IEEE Transactions on Power Electronics*, vol. 23, no. 6, pp. 3067-3078, Nov. 2008.

[23] F. -J. Lin, Y. -C. Hung, and M. -T. Tsai, "Fault-tolerant control for six-phase PMSM drive system via intelligent complementary sliding-mode control using TSKFNN-AMF," *IEEE Transactions on Industrial Electronics*, vol. 60, no. 12, pp. 5747-5762, Dec. 2013.

[24] C. -H. Lin, "Dynamic control of V-belt continuously variable transmission-driven electric scooter using hybrid modified recurrent Legendre neural network control system," *Nonlinear*

Dynamics, vol. 79, no. 2, pp. 787-808, Dec. 2013.

[25] C. -H. Lin and Y. -C. Shih, "Novel hybrid recurrent Hermite neural network control for switched reluctance motor drive," in *Proceedings of the 13th IEEE Conference on Industrial Electronics and Applications*, pp. 1022-1027, May. 2018.

[26] J. Zhang, H. Wang, Z. Cao, J. Zheng, M. Yu, A. Yazdani, and F. Shahnia, "Fast nonsingular terminal sliding mode control for permanent-magnet linear motor via ELM," *Neural Computing and Applications*, Sep. 2019. [Online].

[27] C. -H. Lin and K. -T. Chang, "Admixed recurrent Gegenbauer polynomials neural network with mended particle swarm optimization control system for synchronous reluctance motor driving continuously variable transmission system," *Proceedings of the Institution of Mechanical Engineers, Part I: Journal of Systems and Control Engineering*, vol. 234, no. 2, pp. 1-16, Feb. 2020.

[28] Z. Gao, "Scaling and bandwidth-parameterization based controller tuning," in *Proceedings of the 2003 American Control Conference*, pp. 4989-4996, Jun. 2003.

[29] C. Ren, X. Li, X. Yang, and S. Ma, "Extended state observer-based sliding mode control of an omnidirectional mobile robot with friction compensation," *IEEE Transactions on Industrial Electronics*, vol. 66, no. 12, pp. 9480-9489, Dec. 2019.

[30] J. A. Moreno and M. Osorio, "A Lyapunov approach to second-order sliding mode controllers and observers," in *Proceedings of the 47th IEEE Conference on Decision and Control*, pp. 2856-2861, Dec. 2008.

[31] A. Dávila, J. A. Moreno, and L. Fridman, "Optimal Lyapunov function selection for reaching time estimation of super twisting algorithm," in *Proceedings of the 48th IEEE Conference on Decision and Control*, pp. 8405-8410, Dec. 2009.

[32] H. K. Khalil, *Nonlinear Systems*, 3rd ed. Englewood Cliffs, NJ, USA: Prentice-Hall, 2001.

[33] A. Zou, Y. Zhang, *Basis Function Neural Networks and Their Applications*. Guangzhou, China: Sun Yat-sen University Press, 2009.

[34] L. Ma and K. Khorasani, "Constructive feedforward neural network using Hermite polynomial activation functions," *IEEE Transactions on Neural Networks*, vol. 16, no. 4, pp. 821-833, Jul. 2005.

[35] S. M. Siniscalchi, J. Li, and C. -H. Lee, "Hermite polynomial for speaker adaptation of connectionist speech recognition systems," *IEEE Transactions on Audio, Speech, and Language Processing*, vol. 21, no. 10, pp. 2152-2161, Oct. 2013.

4

TYPE-1 COMPOSITE CONTROLLER: DESIGN AND APPLICATION

4.1 Introduction

With respect to the single-input uncertain nonlinear system with relative degree one, the sliding-mode controller is one of the most promising robust nonlinear controllers. In theory, it can completely reject the bounded lumped disturbance, which consists of unmodeled dynamics, parametric uncertainties and external disturbances in the system [1]. In general, the first step of designing a sliding-mode controller is to select the sliding variable based on the control objective. Afterward, a sliding-mode control law is designed to make the selected sliding variable converge to the origin, commonly known as the sliding surface, in a finite time, and keep it at the origin thereafter, such that the control objective is accomplished in a finite time in the presence of unmodeled dynamics, parametric uncertainties and external disturbances. For the classic sliding-mode controller, it is based on the FOSM algorithm. As mentioned in Section 3.1, the implementation of such a sliding-mode algorithm in the hardware controller results in severe chattering in practice.

To alleviate the chattering, several modified sliding-mode algorithms have been proposed [1], [2]. Among them, the second-order sliding-mode (SOSM) algorithms, which can guarantee the finite-time convergence of the sliding variable and its time derivative to the origin in a finite time, is an approach to chattering alleviation that has gained much attention in the sliding-mode control community in recent decades [1]-[4]. Amongst the existing SOSM algorithms, the standard STA is a unique absolutely continuous SOSM algorithm that can be applied to the relative degree one system and only require the information of the sliding variable. Because of such attractive features,

the standard STSM controller, which is based on the standard STA, has found wide applications [5]-[18]. The nonlinear correction terms of the standard STA are dependent on the bounded sign function. In other words, the standard STSM controller is based on the bounded function-based feedback regulation mechanism. As has been stated in Section 1.2, the use of such a feedback regulation mechanism results in a trade-off problem between the tracking performance and the disturbance attenuation during the selection of controller gains, and the development of a composite controller is an effective method to tackle such an issue.

In recent years, some composite controllers combining a standard STSM controller with a model-based or model-free DO have been proposed. For example, the composite controller combining a standard STSM controller with a ESO [14]-[16], the composite controller combining a standard STSM controller with a STSMO [17], and the composite controller combining a standard STSM controller with a RBFNN-DO [18]. For the last-mentioned composite controller, although its performance has been verified by simulation results, the presented Lyapunov stability analysis for the tracking control system is *not rigorous* in theory. It means that the derivation of the learning laws for the connective weights between the output neuron and the hidden neurons in the adopted RBFNN-DO is also *not rigorous* in theory. Therefore, from a theoretical viewpoint, the rigorous stability analysis for the composite controller combining a standard STSM controller with an ANN-DO and the rigorous derivation of the learning laws for the connective weights between the output neuron and the hidden neurons in the adopted ANN-DO still need to be explored.

In this chapter, the type-1 composite controller, which consists of a standard STSM controller, a HNN-DO and an error compensator, is proposed for a single-input uncertain nonlinear system with relative degree one. In such a composite controller, the finite-time stabilization of the sliding variable dynamics is guaranteed by the standard STSM controller, the lumped disturbance in the sliding variable dynamics is compensated by the HNN-DO, and the approximation error of such an ANN-DO is compensated by the error compensator. The *rigorous* stability analysis of the sliding variable dynamics with the type-1 composite controller is presented. On the basis of that, the learning laws for the connective weights between the output neuron and the hidden neurons in the HNN-DO and the error compensator are *rigorously* derived. In fact, such learning laws are suitable for any type of ANN-DO, including the MLP-DO, the RBFNN-DO and the ENN-DO, and its corresponding error compensator used in the standard STSM controller-based composite controller.

After the rigorous theoretical analysis of the proposed type-1 composite controller, such a controller applies to the construction of a novel robust FOC strategy for the 2L-VSI-fed SynRM-VSD system. In such a FOC strategy, the proposed type-1 composite controller serves as the rotor

speed controller for the robust rotor speed tracking control. Moreover, based on the current dynamics of the SynRM in the dq frame, each of which is a nonlinear system in terms of i_{ds} and i_{qs} considering the magnetic saturation effect, two composite current controllers, each of which is composed of two standard STSM controllers, are designed to achieve the robust stator current tracking control. Rigorous stability analysis of each current tracking error dynamics using the corresponding composite current controller is presented. Finally, the results of the comparative HIL tests between the proposed FOC strategy and the classic STA-based FOC strategy proposed in [19], which is based on a standard STSM speed controller and two linear PI current controllers, for the 2L-VSI-fed SynRM-VSD system are presented and analyzed.

4.2 Type-1 Composite Controller Design

4.2.1 Problem Statement

Considering the single-input uncertain nonlinear system with relative degree one presented in (3.1), the sliding variable can be designed as

$$s_1 = y_r - y \tag{4.1}$$

where y_r is the reference output for the considered system.

Assumption 4.1. $\dot{s}_1$ is bounded and $\dot{y}_r$ is known.

Based on (3.1) and (4.1), the s_1-dynamics can be derived as

$$\dot{s}_1 = \dot{y}_r - \dot{y} = \dot{y}_r - a(x,t) - b(x,t)\mu \tag{4.2}$$

Combing (4.2) with (3.2), the s_1-dynamics can be rewritten as

$$\begin{aligned} \dot{s}_1 &= \dot{y}_r - \big(a_n + \Delta a(x,t)\big) - \big(b_n + \Delta b(x,t)\big)\mu \\ &= -b_n\mu + \underbrace{\dot{y}_r - a_n - \Delta a(x,t) - \Delta b(x,t)\mu}_{\rho_s(x,t)} \\ &= -b_n\mu + \rho_s(x,t) \end{aligned} \tag{4.3}$$

where $\rho_s(x,t)$ denotes the lumped disturbance in the s_1-dynamics.

Assumption 4.2. ρ_s and its time derivative $\dot{\rho}_s$ are bounded as $|\rho_s| \leq L_1^s$ and $|\dot{\rho}_s| \leq L_2^s$, respectively, for positive constants L_1^s and L_2^s.

The control objective is to let s_1 converge to the origin in a finite time.

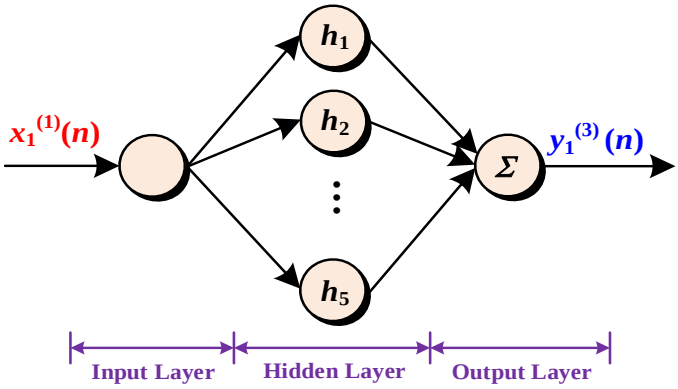

Figure 4.1 Block diagram of a HNN-DO in the type-1 composite controller.

4.2.2 HNN-DO Design

The HNN-DO used in the type-1 composite controller is illustrated in Figure 4.1. It can be seen that there are one input neuron, five hidden neurons and one output neuron in such an ANN-DO. The signal propagation and the activation function of each layer are described as follows.

Input Layer: In this layer, s_1 is selected as the input signal. Thus, the output signal of the input neuron can be expressed as

$$y_1^{(1)}(n) = x_1^{(1)}(n) = s_1(n) \tag{4.4}$$

where $s_1(n)$ is the sliding variable at the *n*th instant.

Hidden Layer: In this layer, regarding the *i*th hidden neuron (i = 1, 2,…, 5), the signal propagation can be described as

$$x_i^{(2)}(n) = y_1^{(1)}(n), \quad i = 1,2,...,5 \tag{4.5}$$

$$y_i^{(2)}(n) = h_i(x_i^{(2)}(n)) \tag{4.6}$$

Output Layer: In this layer, the output signal is the estimated lumped disturbance in the s_1-dynamics, which can be calculated as

$$\hat{\rho}_{HNN} = y_1^{(3)}(n) = \sum_{i=1}^{5} W_{hi}^{(2)}(n) y_i^{(2)}(n), \quad i = 1,2,...,5 \tag{4.7}$$

where $\hat{\rho}_{HNN}$ is the estimated lumped disturbance from the HNN-DO, $W_{hi}^{(2)}(n)$ denotes the connective weight between the output neuron and the *i*th hidden neuron at the *n*th instant.

Based on the universal approximation property of the ANN, there is an optimal estimated lumped disturbance $\hat{\rho}_{HNN}^{*}$ for the HNN-DO such that

$$\rho_s = \hat{\rho}_{HNN}^{*} + \varepsilon_{HNN} = \boldsymbol{W}_h^{(2)*T}(n)\boldsymbol{y}^{(2)}(n) + \varepsilon_{HNN} \tag{4.8}$$

where $\boldsymbol{W}_h^{(2)*}(n) = [W_{h1}^{(2)*}(n),\ W_{h2}^{(2)*}(n),\ W_{h3}^{(2)*}(n),\ W_{h4}^{(2)*}(n),\ W_{h5}^{(2)*}(n)]^T$ and $\boldsymbol{y}^{(2)}(n) = [y_1^{(2)}(n),\ y_2^{(2)}(n),\ y_3^{(2)}(n),\ y_4^{(2)}(n),\ y_5^{(2)}(n)]^T$ are the optimal output weight vector and the output signal vector of the hidden layer of the HNN-DO, respectively, ε_{HNN} is the minimum approximation error of the HNN-DO.

Assumption 4.3. $W_{hi}^{(2)*}(n)$ and ε_{HNN} are constant in each sampling period.

Remark 4.1. In the HNN-DO, all elements in the output weight vector $\boldsymbol{W}_h^{(2)}(n) = [W_{h1}^{(2)}(n),\ W_{h2}^{(2)}(n),\ W_{h3}^{(2)}(n),\ W_{h4}^{(2)}(n),\ W_{h5}^{(2)}(n)]^T$ need to be updated online. To maintain the stability of the tracking control system, the learning laws for these connective weights are derived from the Lyapunov synthesis approach.

4.2.3 Controller Design

To achieve the control objective, the type-1 composite control law μ_{c1} is designed as

$$\mu_{c1} = \frac{1}{b_n}\left(\mu_{STA} + y_h + y_{c1}\right) \tag{4.9}$$

where μ_{STA}, y_h and y_{c1} are the standard STA for the finite-time stabilization of the s_1-dynamics, the output signal of the adopted HNN-DO for the compensation of the lumped disturbance in the s_1-dynamics and the output signal of the error compensator for the compensation of the approximation error of the adopted HNN-DO, respectively, which are expressed as

$$\mu_{STA} = k_1^{c1}\sqrt{|s_1|}\,\mathrm{sgn}(s_1) + k_2^{c1}\int \mathrm{sgn}(s_1)dt \tag{4.10}$$

$$y_h = \boldsymbol{W}_h^{(2)T}(n)\boldsymbol{y}^{(2)}(n) \tag{4.11}$$

$$y_{c1} = \varepsilon_{c1} \tag{4.12}$$

where k_1^{c1} and k_2^{c1} are the positive constant gains, ε_{c1} is the estimated approximation error of the adopted HNN-DO.

Remark 4.2. If $y_h = y_{c1} = 0$, the type-1 composite control law is converted to the standard STSM control law.

Remark 4.3. In the type-1 composite control law, ε_{c1} is updated online. To maintain the stability of the tracking control system, the learning law for ε_{c1} is derived by the Lyapunov synthesis approach.

Substituting (4.8) and (4.9) into (4.3), the closed-loop s_1-dynamics with the type-1 composite control law is expressed as

$$\begin{aligned}\dot{s}_1 &= -k_1^{c1}\sqrt{|s_1|}\,\mathrm{sgn}(s_1) - k_2^{c1}\int \mathrm{sgn}(s_1)dt - \boldsymbol{W}_h^{(2)T}(n)\boldsymbol{y}^{(2)}(n) - \varepsilon_{c1} + \rho_s \\ &= -k_1^{c1}\sqrt{|s_1|}\,\mathrm{sgn}(s_1) - k_2^{c1}\int \mathrm{sgn}(s_1)dt - \boldsymbol{W}_h^{(2)T}(n)\boldsymbol{y}^{(2)}(n) - \varepsilon_{c1} + \boldsymbol{W}_h^{(2)*T}(n)\boldsymbol{y}^{(2)}(n) + \varepsilon_{HNN} \\ &= -k_1^{c1}\sqrt{|s_1|}\,\mathrm{sgn}(s_1) - k_2^{c1}\int \mathrm{sgn}(s_1)dt + \tilde{\boldsymbol{W}}_h^{(2)T}(n)\boldsymbol{y}^{(2)}(n) + \tilde{\varepsilon}_{HNN}\end{aligned} \tag{4.13}$$

where $\tilde{\boldsymbol{W}}_h^{(2)}(n) = \boldsymbol{W}_h^{(2)*}(n) - \boldsymbol{W}_h^{(2)}(n) = [\tilde{W}_{h1}^{(2)}(n),\ \tilde{W}_{h2}^{(2)}(n),\ \tilde{W}_{h3}^{(2)}(n),\ \tilde{W}_{h4}^{(2)}(n),\ \tilde{W}_{h5}^{(2)}(n)]^T$ and $\tilde{\varepsilon}_{HNN} = \varepsilon_{HNN} - \varepsilon_{c1}$.

The following Theorem can be used to derive the learning laws for $\boldsymbol{W}_h^{(2)}$ and ε_{c1}.

Theorem 4.1. Considering the system (4.13), if the learning laws for $\boldsymbol{W}_h^{(2)}$ and ε_{c1} are designed as (4.14) and (4.15), respectively, the origin is a globally asymptotically stable equilibrium point.

$$\dot{\boldsymbol{W}}_h^{(2)} = \eta_{c1}k_2^{c1}\mathrm{sgn}(s_1)\boldsymbol{y}^{(2)} \tag{4.14}$$

$$\dot{\varepsilon}_{c1} = \eta_{c2}k_2^{c1}\mathrm{sgn}(s_1) \tag{4.15}$$

where η_{c1} and η_{c2} are positive learning rates.

Proof. At first, the system (4.13) is converted to the following equivalent system.

$$\begin{cases}\dot{s}_1 = -k_1^{c1}\sqrt{|s_1|}\,\mathrm{sgn}(s_1) + \phi_1 + \tilde{\boldsymbol{W}}_h^{(2)T}\boldsymbol{y}^{(2)} + \tilde{\varepsilon}_{HNN} \\ \dot{\phi}_1 = -k_2^{c1}\,\mathrm{sgn}(s_1)\end{cases} \tag{4.16}$$

For the system (4.16), the Lyapunov candidate function V_{c1} is selected as follows

$$V_{c1} = k_2^{c1}|s_1| + \frac{1}{2}\phi_1^2 + \frac{1}{2\eta_{c1}}\tilde{\boldsymbol{W}}_h^{(2)T}\tilde{\boldsymbol{W}}_h^{(2)} + \frac{1}{2\eta_{c2}}\tilde{\varepsilon}_{HNN}^2 \tag{4.17}$$

Considering Assumption 4.3, $\dot{V}_{c1}$ along the trajectories of the system (4.16) can be obtained as

$$\begin{aligned}\dot{V}_{c1} &= k_2^{c1}\mathrm{sgn}(s_1)\dot{s}_1 + \phi_1\dot{\phi}_1 - \frac{1}{\eta_{c1}}\tilde{\boldsymbol{W}}_h^{(2)T}\dot{\boldsymbol{W}}_h^{(2)} - \frac{1}{\eta_{c2}}\tilde{\varepsilon}_{HNN}\dot{\varepsilon}_{c1} \\ &= k_2^{c1}\mathrm{sgn}(s_1)\left(-k_1^{c1}\sqrt{|s_1|}\,\mathrm{sgn}(s_1) + \phi_1 + \tilde{\boldsymbol{W}}_h^{(2)T}\boldsymbol{y}^{(2)} + \tilde{\varepsilon}_{HNN}\right) \\ &\quad -\phi_1 k_2^{c1}\mathrm{sgn}(s_1) - \frac{1}{\eta_{c1}}\tilde{\boldsymbol{W}}_h^{(2)T}\dot{\boldsymbol{W}}_h^{(2)} - \frac{1}{\eta_{c2}}\tilde{\varepsilon}_{HNN}\dot{\varepsilon}_{c1} \\ &= -k_1^{c1}k_2^{c1}\sqrt{|s_1|} + k_2^{c1}\mathrm{sgn}(s_1)\tilde{\boldsymbol{W}}_h^{(2)T}\boldsymbol{y}^{(2)} + k_2^{c1}\mathrm{sgn}(s_1)\tilde{\varepsilon}_{HNN} - \frac{1}{\eta_{c1}}\tilde{\boldsymbol{W}}_h^{(2)T}\dot{\boldsymbol{W}}_h^{(2)} - \frac{1}{\eta_{c2}}\tilde{\varepsilon}_{HNN}\dot{\varepsilon}_{c1} \\ &= -k_1^{c1}k_2^{c1}\sqrt{|s_1|} + \tilde{\boldsymbol{W}}_h^{(2)T}\left[k_2^{c1}\mathrm{sgn}(s_1)\boldsymbol{y}^{(2)} - \frac{1}{\eta_{c1}}\dot{\boldsymbol{W}}_h^{(2)}\right] + \tilde{\varepsilon}_{HNN}\left[k_2^{c1}\mathrm{sgn}(s_1) - \frac{1}{\eta_{c2}}\dot{\varepsilon}_{c1}\right]\end{aligned} \tag{4.18}$$

Substituting (4.14) and (4.15) into (4.18), $\dot{V}_{c1}$ can be expressed as

$$\dot{V}_{c1} = -k_1^{c1} k_2^{c1} \sqrt{|s_1|} \le 0 \tag{4.19}$$

Since $\dot{V}_{c1}$ is negative semidefinite, the following inequality can be derived.

$$V_{c1}\left(s_1(t), \phi_1(t), \tilde{\boldsymbol{W}}_h^{(2)}(t), \tilde{\varepsilon}_{HNN}(t)\right) \le V_{c1}\left(s_1(0), \phi_1(0), \tilde{\boldsymbol{W}}_h^{(2)}(0), \tilde{\varepsilon}_{HNN}(0)\right) \tag{4.20}$$

According to (4.20), $s_1(t)$, $\phi_1(t)$, $\tilde{\boldsymbol{W}}_h^{(2)}(t)$ and $\tilde{\varepsilon}_{HNN}(t)$ are bounded. Based on (4.19) and (4.20), the following function is defined.

$$\Omega_{HNN}(t) = -k_1^{c1} k_2^{c1} \sqrt{|s_1|} \le -\dot{V}_{c1}\left(s_1(t), \phi_1(t), \tilde{\boldsymbol{W}}_h^{(2)}(t), \tilde{\varepsilon}_{HNN}(t)\right) \tag{4.21}$$

Since $V_{c1}(s_1(0), \phi_1(0), \tilde{\boldsymbol{W}}_h^{(2)}(0), \tilde{\varepsilon}_{HNN}(0))$ is bounded and $V_{c1}(s_1(t), \phi_1(t), \tilde{\boldsymbol{W}}_h^{(2)}(t), \tilde{\varepsilon}_{HNN}(t))$ is a non-increasing bounded function, the following inequality can be derived.

$$\lim_{t\to\infty} \int_0^t \Omega_{HNN}(\tau) d\tau < \infty \tag{4.22}$$

Since $\lim_{t\to\infty} \int_0^t \Omega_{HNN}(\tau) d\tau$ exists and $\Omega_{HNN}(t)$ is a uniformly continuous function, according to Barbălat's Lemma [20], $\lim_{t\to\infty} \Omega_{HNN}(t) = 0$ holds. It means that $\lim_{t\to\infty} s_1(t) = 0$ holds. Therefore, the origin is a globally asymptotically stable equilibrium point of the system (4.13). The proof is completed. ■

The system (4.13) can be converted to another equivalent system described as

$$\begin{cases} \dot{s}_1 = -k_1^{c1} \sqrt{|s_1|}\, \mathrm{sgn}(s_1) + \phi_2 \\ \dot{\phi}_2 = -k_2^{c1}\, \mathrm{sgn}(s_1) dt + \rho_{s1} \end{cases} \tag{4.23}$$

where ρ_{s1} is expressed as

$$\begin{aligned} \rho_{s1} &= \frac{d}{dt}\left(\tilde{\boldsymbol{W}}_h^{(2)T} \boldsymbol{y}^{(2)} + \tilde{\varepsilon}_{HNN}\right) = -\boldsymbol{y}^{(2)T} \dot{\boldsymbol{W}}_h^{(2)} + \tilde{\boldsymbol{W}}_h^{(2)T} \dot{\boldsymbol{y}}^{(2)} - \dot{\varepsilon}_{c1} \\ &= -\eta_{c1} k_2^{c1} \mathrm{sgn}(s_1) \boldsymbol{y}^{(2)T} \boldsymbol{y}^{(2)} + \tilde{\boldsymbol{W}}_h^{(2)T} \dot{\boldsymbol{y}}^{(2)} - \eta_{c2} k_2^{c1} \mathrm{sgn}(s_1) \end{aligned} \tag{4.24}$$

Assumption 4.4. $\dot{s}_1$ is bounded.

Since $\tilde{\boldsymbol{W}}_h^{(2)}$, s_1 and $\dot{s}_1$ are bounded, based on (3.38), (3.39) and (4.6), it can be concluded that $\boldsymbol{y}^{(2)}$ and $\dot{\boldsymbol{y}}^{(2)}$ are bounded. Thus, ρ_{s1} is bounded.

Assumption 4.5. ρ_{s1} is bounded as $|\rho_{s1}| \le L_3^s$ for a positive constant L_3^s.

The following Theorem can be used to select k_1^{c1} and k_2^{c1} for accomplishing the control objective.

Theorem 4.2. Considering the system (4.23) and $|\rho_{s1}| \le L_3^s$, if k_1^{c1} and k_2^{c1} are selected as (4.25),

s_1 will converge to the origin in a finite time.

$$k_1^{c1} > 2, \quad k_2^{c1} > \frac{(k_1^{c1})^2 + 4(L_3^s)^2}{4\left(k_1^{c1} - 2\right)} \tag{4.25}$$

Proof. It can be observed that the system (4.23) has the same structure as the system (3.12). Since ρ_{s1} is bounded as $|\rho_{s1}| \leq L_3^s$, the inequalities (4.25) can be obtained from (3.13) by replacing k_1, k_2 and L_2^x with k_1^{c1}, k_2^{c1} and L_3^s, respectively. Therefore, according to Theorem 3.1, it can be concluded that, with k_1^{c1} and k_2^{c1} selected as (4.25), s_1 will converge to the origin in a finite time. The proof is completed. ■

4.3 Application

In this section, a novel robust FOC strategy based on the type-1 composite speed controller and two composite current controllers for the 2L-VSI-fed SynRM-VSD system is presented. The designs of the type-1 composite speed controller and two composite current controllers are based on the practical dynamic model of the SynRM presented in (2.60). In this FOC strategy, i_{dsr} is a constant set in advance and i_{qsr} is generated by the type-1 composite speed controller. Finally, the results of comparative HIL tests between the proposed FOC strategy and the classic STA-based FOC strategy for the 2L-VSI-fed SynRM-VSD system are presented to demonstrate the superiority of the former.

4.3.1 Type-1 Composite Speed Controller Design

The speed tracking error $e_{\omega 1}$ for the field-oriented controlled SynRM-VSD system is defined as

$$e_{\omega 1} = \omega_{mr} - \omega_m \tag{4.26}$$

Since the dynamics of the current control loop is much faster than that of the speed control loop, it can be considered that $i_{ds} = i_{dsr}$ and $i_{qs} = i_{qsr}$ in the rotor speed controller design. Therefore, based on (2.60) and (4.26), the $e_{\omega 1}$-dynamics can be expressed as

$$\dot{e}_{\omega 1} = \underbrace{\dot{\omega}_{mr} + \frac{1}{J_0} T_L + \frac{B_{m0}}{J_0} \omega_m - \rho_\omega^S}_{\rho_{\omega 1}^{(1)}} - \underbrace{\frac{3n_p \left(L_{d0} - L_{q0}\right)}{2J_0} i_{dsr}}_{b_{\omega n1}} i_{qsr} = \rho_{\omega 1}^{(1)} - b_{\omega n1} i_{qsr} \tag{4.27}$$

where $b_{\omega n1}$ is a constant and $\rho_{\omega 1}^{(1)}$ denotes the lumped disturbance in the $e_{\omega 1}$-dynamics.

Selecting $e_{\omega 1}$ as the sliding variable, the type-1 composite speed control law i_{qsr}^{c1} is designed as

$$i_{qsr}^{c1} = \frac{1}{b_{\omega n1}}\left(\mu_{s\omega 1} + y_{h\omega} + y_{c\omega 1}\right) \tag{4.28}$$

where $\mu_{s\omega 1}$, $y_{h\omega 1}$ and $y_{c\omega 1}$ are the standard STA for the finite-time rotor speed tracking control, the output signal of the adopted HNN-DO for the compensation of the lumped disturbance in the e_ω-dynamics and the output signal of the error compensator for the compensation of the approximation error of the adopted HNN-DO, respectively, which are expressed as

$$\mu_{s\omega 1} = k_{\omega 1}^{c1}\sqrt{|e_{\omega 1}|}\,\mathrm{sgn}(e_{\omega 1}) + k_{\omega 2}^{c1}\int \mathrm{sgn}(e_{\omega 1})dt \tag{4.29}$$

$$y_{h\omega} = \boldsymbol{W}_{h\omega}^{(2)T}\boldsymbol{y}_{h\omega}^{(2)} \tag{4.30}$$

$$y_{c\omega 1} = \varepsilon_{c\omega 1} \tag{4.31}$$

where $k_{\omega 1}^{c1}$ and $k_{\omega 2}^{c1}$ are the positive constant gains, $\boldsymbol{W}_{h\omega}^{(2)} = [W_{h\omega 1}^{(2)},\ W_{h\omega 2}^{(2)},\ W_{h\omega 3}^{(2)},\ W_{h\omega 4}^{(2)},\ W_{h\omega 5}^{(2)}]^T$ and $\boldsymbol{y}_{h\omega}^{(2)} = [y_{h\omega 1}^{(2)},\ y_{h\omega 2}^{(2)},\ y_{h\omega 3}^{(2)},\ y_{h\omega 4}^{(2)},\ y_{h\omega 5}^{(2)}]^T$ are the output weight vector and the output signal vector of the hidden layer of the adopted HNN-DO, respectively, $\varepsilon_{c\omega 1}$ is the estimated approximation error of the adopted HNN-DO.

Remark 4.4. If $y_{h\omega} = y_{c\omega 1} = 0$, the type-1 composite speed control law is converted to the standard STSM speed control law.

The structure of the HNN-DO used in the type-1 composite speed controller is illustrated in Figure 4.1. $e_{\omega 1}$ is selected as the input signal of the HNN-DO and the learning laws for $\boldsymbol{W}_{h\omega}^{(2)}$ and $\varepsilon_{c\omega 1}$ are designed as

$$\dot{\boldsymbol{W}}_{h\omega}^{(2)} = \eta_{c\omega 1}^{c1}k_{\omega 2}^{c1}\mathrm{sgn}\left(e_{\omega 1}\right)\boldsymbol{y}_{h\omega}^{(2)} \tag{4.32}$$

$$\dot{\varepsilon}_{c\omega 1} = \eta_{c\omega 2}^{c1}k_{\omega 2}^{c1}\mathrm{sgn}\left(e_{\omega 1}\right) \tag{4.33}$$

where $\eta_{c\omega 1}^{c1}$ and $\eta_{c\omega 2}^{c1}$ are positive learning rates.

Substituting (4.28) into (4.27), the closed-loop $e_{\omega 1}$-dynamics with the type-1 composite speed control law is expressed as

$$\begin{aligned}\dot{e}_{\omega 1} &= -\mu_{s\omega 1} - y_{h\omega} - y_{c\omega 1} + \rho_{\omega 1}^{(1)} = -k_{\omega 1}^{c1}\sqrt{|e_{\omega 1}|}\,\mathrm{sgn}(e_{\omega 1}) - k_{\omega 2}^{c1}\int \mathrm{sgn}(e_{\omega 1})dt \underbrace{-\boldsymbol{W}_{h\omega}^{(2)T}\boldsymbol{y}_{h\omega}^{(2)} - \varepsilon_{c\omega 1} + \rho_{\omega 1}^{(1)}}_{\rho_{\omega 1}^{(2)}} \\ &= -k_{\omega 1}^{c1}\sqrt{|e_{\omega 1}|}\,\mathrm{sgn}(e_{\omega 1}) - k_{\omega 2}^{c1}\int \mathrm{sgn}(e_{\omega 1})dt + \rho_{\omega 1}^{(2)}\end{aligned} \tag{4.34}$$

Assumption 4.6. $\rho_{\omega 1}^{(2)}$ and its time derivative $\dot{\rho}_{\omega 1}^{(2)}$ are bounded as $|\rho_{\omega 1}^{(2)}| \le L_{\omega 1}^{c1}$ and $|\dot{\rho}_{\omega 1}^{(2)}| \le L_{\omega 2}^{c1}$, respectively, for positive constants $L_{\omega 1}^{c1}$ and $L_{\omega 2}^{c1}$.

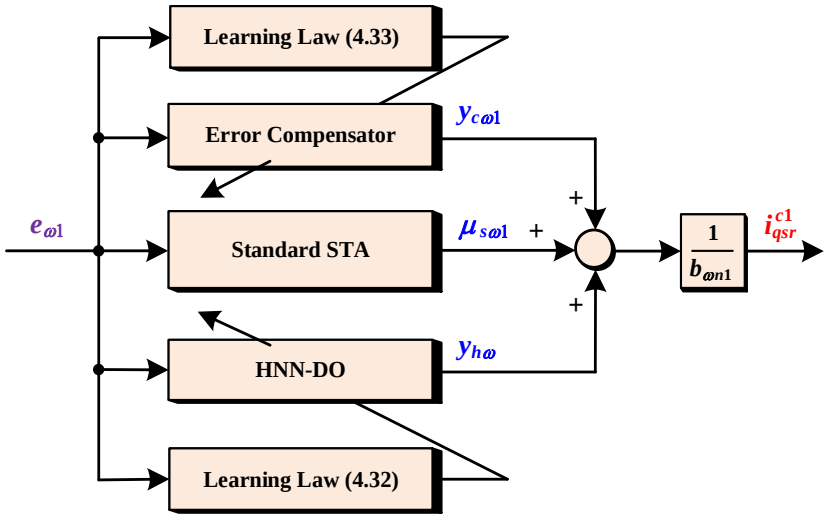

Figure 4.2 Block diagram of the type-1 composite speed controller.

Considering Assumption 4.5, based on Theorem 4.1 and Theorem 4.2, it can be concluded that, with the type-1 composite speed control law (4.28) as well as learning laws (4.32) and (4.33), $e_{\omega 1}$ will converge to the origin in a finite time if $k_{\omega 1}^{c1}$ and $k_{\omega 2}^{c1}$ are selected as

$$k_{\omega 1}^{c1} > 2, \quad k_{\omega 2}^{c1} > \frac{(k_{\omega 1}^{c1})^2 + 4(L_{\omega 2}^{c1})^2}{4\left(k_{\omega 1}^{c1} - 2\right)} \tag{4.35}$$

The block diagram of the type-1 composite speed controller is shown in Figure 4.2.

4.3.2 Composite Current Controller Design

Two current tracking errors e_d and e_q for the field-oriented controlled SynRM-VSD system are defined as

$$e_d = i_{dsr} - i_{ds}, \quad e_q = i_{qsr} - i_{qs} \tag{4.36}$$

It can be considered that $u_{ds}^* = u_{dsr}^*$ and $u_{qs}^* = u_{qsr}^*$ in the stator current controller design. Therefore, according to (2.60) and (4.36), the e_d- and e_q-dynamics can be expressed as

$$\begin{aligned} \dot{e}_d &= -\frac{L_{qq0}}{M_0}[u_{dsr}^* - \underbrace{(R_{s0}i_{ds} - n_p\omega_m L_{q0}i_{qs})}_{b_{dn}}] + \frac{L_{dq0}}{M_0}[u_{qsr}^* - \underbrace{(R_{s0}i_{qs} + n_p\omega_m L_{d0}i_{ds})}_{b_{qn}}] + \underbrace{\dot{i}_{dsr} - \rho_d^S}_{\rho_d^{(1)}} \\ &= -\frac{L_{qq0}}{M_0}(u_{dsr}^* - b_{dn}) + \frac{L_{dq0}}{M_0}(u_{qsr}^* - b_{qn}) + \rho_d^{(1)} \end{aligned} \tag{4.37}$$

$$\begin{aligned}\dot{e}_q &= \frac{L_{qd0}}{M_0}[u_{dsr}^* - \underbrace{(R_{s0}i_{ds} - n_p\omega_m L_{q0}i_{qs})}_{b_{dn}}] - \frac{L_{dd0}}{M_0}[u_{qsr}^* - \underbrace{(R_{s0}i_{qs} + n_p\omega_m L_{d0}i_{ds})}_{b_{qn}}] + \underbrace{\dot{i}_{qsr} - \rho_q^S}_{\rho_q^{(1)}} \\ &= \frac{L_{qd0}}{M_0}(u_{dsr}^* - b_{dn}) - \frac{L_{dd0}}{M_0}(u_{qsr}^* - b_{qn}) + \rho_q^{(1)}\end{aligned} \tag{4.38}$$

where $\rho_d^{(1)}$ and $\rho_q^{(1)}$ denote the lumped disturbance in the e_d- and e_q-dynamics, respectively.

Assumption 4.7. There are four positive constants L_{d1}^{c1}, L_{d2}^{c1}, L_{q1}^{c1} and L_{q2}^{c1} such that $\rho_d^{(1)}$ and $\rho_q^{(1)}$ and their time derivatives $\dot{\rho}_d^{(1)}$ and $\dot{\rho}_q^{(1)}$ are bounded as $\left|\rho_d^{(1)}\right| \le L_{d1}^{c1}$, $\left|\rho_q^{(1)}\right| \le L_{q1}^{c1}$, $\left|\dot{\rho}_d^{(1)}\right| \le L_{d2}^{c1}$ and $\left|\dot{\rho}_q^{(1)}\right| \le L_{q2}^{c1}$, respectively.

Selecting e_d and e_q as the sliding variables, two composite current control laws u_{dsr}^* and u_{qsr}^* are designed as

$$u_{dsr}^* = b_{dn} + L_{dd0}\mu_d + L_{dq0}\mu_q, \quad u_{qsr}^* = b_{qn} + L_{qd0}\mu_d + L_{qq0}\mu_q \tag{4.39}$$

where μ_d and μ_q are two standard STSM control laws expressed as

$$\mu_d = k_{d1}^{c1}\sqrt{|e_d|}\,\mathrm{sgn}(e_d) + k_{d2}^{c1}\int \mathrm{sgn}(e_d)dt \tag{4.40}$$

$$\mu_q = k_{q1}^{c1}\sqrt{|e_q|}\,\mathrm{sgn}(e_q) + k_{q2}^{c1}\int \mathrm{sgn}(e_q)dt \tag{4.41}$$

where k_{d1}^{c1}, k_{d2}^{c1}, k_{q1}^{c1} and k_{q2}^{c1} are the positive constant gains.

Substituting (4.39) into (4.37) and (4.38), the closed-loop e_d- and e_q-dynamics with the proposed composite current control laws are expressed as

$$\begin{cases}\dot{e}_d = -k_{d1}^{c1}\sqrt{|e_d|}\,\mathrm{sgn}(e_d) - k_{d2}^{c1}\int \mathrm{sgn}(e_d)dt + \rho_d^{(1)} \\ \dot{e}_q = -k_{q1}^{c1}\sqrt{|e_q|}\,\mathrm{sgn}(e_q) - k_{q2}^{c1}\int \mathrm{sgn}(e_q)dt + \rho_q^{(1)}\end{cases} \tag{4.42}$$

Considering Assumption 4.7, based on Theorem 3.1, it can be concluded that, with the proposed composite current control laws expressed as (4.39), e_d and e_q will converge to the origin in a finite time if k_{d1}^{c1}, k_{d2}^{c1}, k_{q1}^{c1} and k_{q2}^{c1} are selected as

$$k_{d1}^{c1} > 2, \quad k_{d2}^{c1} > \frac{(k_{d1}^{c1})^2 + 4(L_{d2}^{c1})^2}{4\left(k_{d1}^{c1} - 2\right)}, \quad k_{q1}^{c1} > 2, \quad k_{q2}^{c1} > \frac{(k_{q1}^{c1})^2 + 4(L_{q2}^{c1})^2}{4\left(k_{q1}^{c1} - 2\right)} \tag{4.43}$$

The block diagram of the composite current controllers are shown in Figure 4.3.

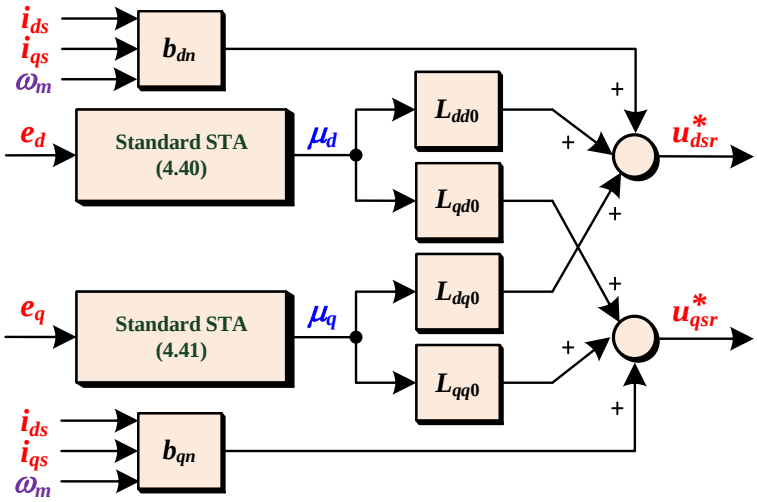

Figure 4.3 Block diagram of the proposed composite current controllers.

4.3.3 HIL Test Results

The HIL test bench described in Section 3.5 is used to perform comparative tests between the proposed FOC strategy and the classic STA-based FOC strategy for the 2L-VSI-fed SynRM-VSD system. In the HIL tests, the sampling frequencies of the hardware controller and the emulator are set to 5 kHz and 10 kHz, respectively. In the emulator, the three-phase low-frequency model presented in (2.12) is used to describe the 2L-VSI, and the following dynamic model modified from (2.60) is adopted to describe the SynRM.

$$\begin{cases} \dot{i}_{ds} = \dfrac{L_{qq}}{M}\left(u^l_{ds} - R_s i_{ds} + n_p \omega_m L_q i_{qs}\right) - \dfrac{L_{dq}}{M}\left(u^l_{qs} - R_s i_{qs} - n_p \omega_m L_d i_{ds}\right) \\ \dot{i}_{qs} = -\dfrac{L_{qd}}{M}\left(u^l_{ds} - R_s i_{ds} + n_p \omega_m L_q i_{qs}\right) + \dfrac{L_{dd}}{M}\left(u^l_{qs} - R_s i_{qs} - n_p \omega_m L_d i_{ds}\right) \\ \dot{\omega}_m = \dfrac{3n_p\left(L_d - L_q\right)}{2J} i_{ds} i_{qs} - \dfrac{1}{J} T_L - \dfrac{1}{J} T_f \end{cases} \tag{4.44}$$

where $M = L_{dd}L_{qq} - L_{dq}L_{qd}$.

To describe the magnetic saturation effect of the SynRM in the emulator, the apparent inductance model proposed in [21], which can approximate the values of L_d and L_q for different combinations of i_{ds} and i_{qs} in a wide range, is adopted. According to such a model, L_d and L_q can be formulated as

$$L_d(i_{ds}, i_{qs}) = L_{d0}(i_{ds}) - L_{d1}(i_{ds}) L_{q2}(i_{qs}), \quad L_q(i_{ds}, i_{qs}) = L_{q0}(i_{qs}) - L_{d2}(i_{ds}) L_{q1}(i_{qs}) \tag{4.45}$$

where

$$L_{d0}(i_{ds}) = c_{d0} + c_{d1}/(i_{ds}^4 + c_{d2}i_{ds}^2 + c_{d3}), \quad L_{q0}(i_{qs}) = c_{q0} + c_{q1}/(i_{qs}^4 + c_{q2}i_{qs}^2 + c_{q3})$$
$$L_{d1}(i_{ds}) = c_{d4}/(i_{ds}^4 + c_{d5}i_{ds}^2 + c_{d6}), \quad L_{q1}(i_{qs}) = c_{q4}/(i_{qs}^4 + c_{q5}i_{qs}^2 + c_{q6}) \tag{4.46}$$
$$L_{d2}(i_{ds}) = 1 - 1/(c_{dq}i_{ds}^2 + 1), \quad L_{q2}(i_{qs}) = 1 - 1/(c_{qd}i_{qs}^2 + 1)$$

Based on (2.42), (2.43), (2.44) and (4.45), the incremental inductances can also be formulated.

For the hardware controller, it not only generates d_a^*, d_b^* and d_c^* based on the principle of the space vector modulation for the 2L-VSI in the emulator but also samples i_{as}, i_{bs}, i_{cs} and θ_m from the emulator. The implementation of the field-oriented controlled 2L-VSI-fed SynRM-VSD system is illustrated in Figure 4.4. The parameters of the SynRM are presented in Table 4.1 [23]. The specifications of the 2L-VSI are shown in Table 4.2. [23]. The adopted apparent inductance model of the SynRM is illustrated in Figure 4.5, where the parameters are presented as follow: c_{d1} = 0.0391, c_{d2} = 45.4, c_{d3} = −12.9, c_{d4} = 1329, c_{d5} = 19.9, c_{d6} = −13, c_{d7} = 795, c_{dq} = 0.0133, c_{q1} = 0.01, c_{q2} = 0.571, c_{q3} = 0, c_{q4} = 58, c_{q5} = 0.825, c_{q6} = 0, c_{q7} = 63.8, c_{qd} = 0.0833 [21]. With respect to the proposed FOC strategy, the parameters of the composite speed controller are selected as $L_{d0} = L_d(0,0)$, $L_{q0} = L_q(0,0)$, $k_{\omega 1}^{c1}$ = 100, $k_{\omega 2}^{c1}$ = 200, $\eta_{c\omega 1}^{c1}$ = 100, $\eta_{c\omega 2}^{c1}$ = 0.1, and the parameters of two composite current controllers are selected as $L_{d0} = L_d(0,0)$, $L_{q0} = L_q(0,0)$, $L_{dd0} = L_{dd}(1,1)$, $L_{dq0} = L_{dq}(1,1)$, $L_{qd0} = L_{qd}(1,1)$, $L_{qq0} = L_{qq}(1,1)$, $k_{d1}^{c1} = k_{q1}^{c1}$ = 5000, $k_{d2}^{c1} = k_{q2}^{c1}$ = 20000. With respect to the classic STA-based FOC strategy, the parameters of the standard STSM speed controller are selected as $L_{d0} = L_d(0,0)$, $L_{q0} = L_q(0,0)$, $k_{\omega 1}^{c1}$ = 100, $k_{\omega 2}^{c1}$ = 200, and the parameters of two linear PI current controllers are the same as each other, i.e., the proportional gain is selected as 30 and the integral gain is selected as 4000.

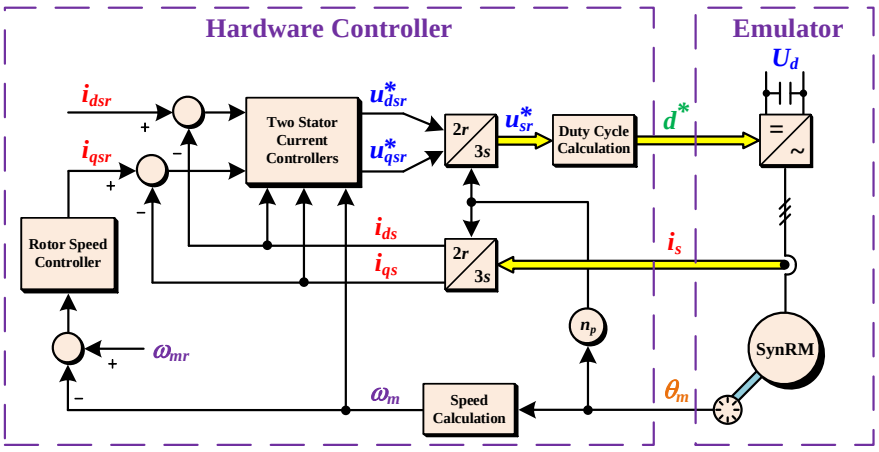

Figure 4.4 Implementation of the field-oriented controlled 2L-VSI-fed SynRM-VSD system in HIL tests.

Table 4.1 Parameters of the SynRM

Parameter	Value
Rated power (W)	1100
Rated current (A)	6.3
Stator resistance (Ω)	1.05
Rated speed (rpm)	1500
Rotor inertia (kg·m^2)	0.0208
Viscous friction coefficient (N·m·s/rad)	0.00268
Rated torque (N·m)	4.8
Pole pairs	2

Table 4.2 Specifications of the 2L-VSI

Parameter	Value
DC-bus voltage (V)	200
Switching period (μs)	100
Turn-on time (μs)	1.3
Turn-off time (μs)	1.3
Dead time (μs)	2.0
Saturation voltage (V)	1.6
Diode forward voltage (V)	1.5

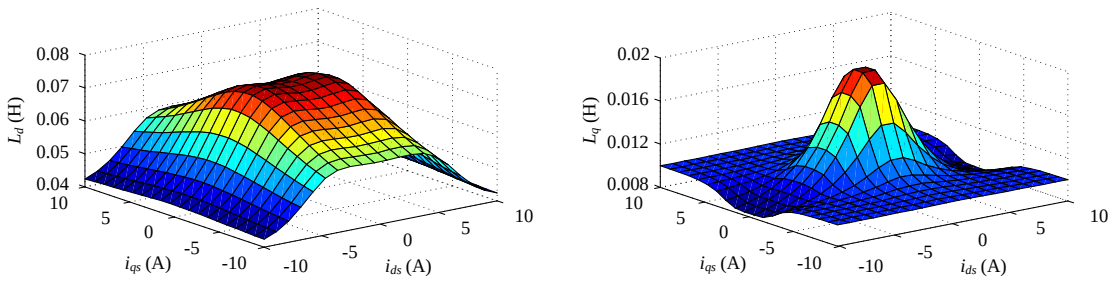

(a) (b)

Figure 4.5 Apparent inductance model of the SynRM. (a) $L_d(i_{ds}, i_{qs})$. (b) $L_q(i_{ds}, i_{qs})$.

Regarding the implementation of standard STA in the hardware controller, the sign function is usually replaced by a continuous function, including the saturation function and the hyperbolic tangent function, to further alleviate the chattering in practice [13], [16]. Therefore, in this chapter,

the sign function in each standard STA-based controller is replaced by the following saturation function in HIL tests.

$$\mathrm{sat}(z)=\begin{cases}\dfrac{z}{\Pi}, & \text{if } |z|\le\Pi\\ \mathrm{sgn}(z), & \text{if } |z|>\Pi\end{cases} \tag{4.47}$$

where Π denotes the boundary layer that is set to 1.0 in HIL tests.

In the first test, the values of ω_{mr}, i_{dsr}, ΔJ and ΔR_s are set to 1000 rpm, 5 A, 0 and 0, respectively. The value of T_L declines from 4.8 N·m to 0 N·m at first, and then the value of T_f steps tenfold by raising the value of B_m to ten times. Figure 4.6 presents the rotor mechanical speed responses of the proposed FOC strategy and the classic STA-based FOC strategy, while the stator current responses of these two tested FOC strategies are illustrated in Figure 4.7. It can be seen that, in comparison with the classic STA-based FOC strategy, the proposed FOC strategy can achieve smaller maximum tracking error and shorter settling time for the speed and current tracking control under the sudden change of external disturbances.

In the second test, the values of T_L, i_{dsr}, ΔJ and ΔR_s are set to 2.4 N·m, 5 A, $4J_0$ and 0, respectively. The value of ω_{mr} steps from 1000 rpm to 1500 rpm at first, and then it is back to 1000 rpm. The rotor mechanical speed responses and the stator current responses of two tested FOC strategies are presented in Figure 4.8 and Figure 4.9, respectively. It can be observed that, in the presence of the rotor inertia uncertainty, the proposed FOC strategy can accomplish smaller overshoot and shorter settling time for the speed and current tracking control under the sudden change of the reference rotor mechanical speed, compared with the classic STA-based FOC strategy.

In the third test, the values of ω_{mr}, T_L, i_{dsr} and ΔJ are set to 1000 rpm, 2.4 N·m, 5 A and 0, respectively, while the value of ΔR_s steps from 0 to $2R_s$. The stator current responses of two tested FOC strategies are shown in Figure 4.10. It can be seen that the proposed FOC strategy is able to achieve smaller variations of *d*- and *q*-axes stator current components compared with the classic STA-based FOC strategy.

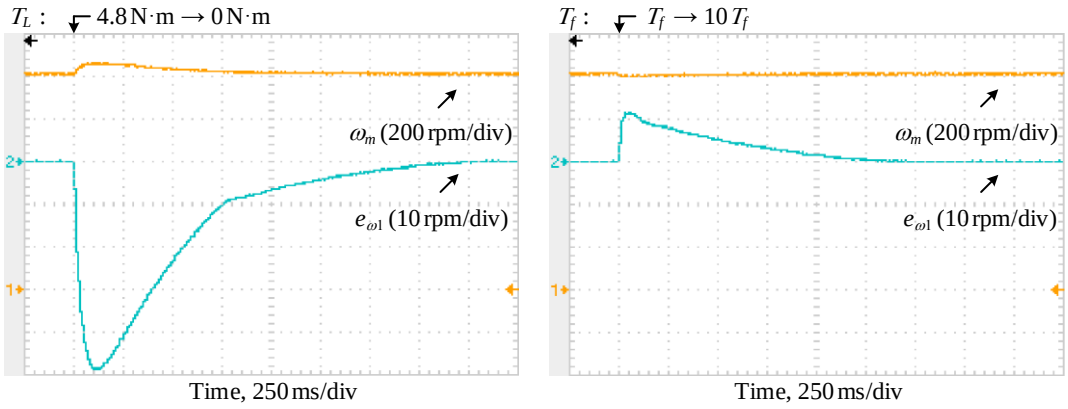

(a)

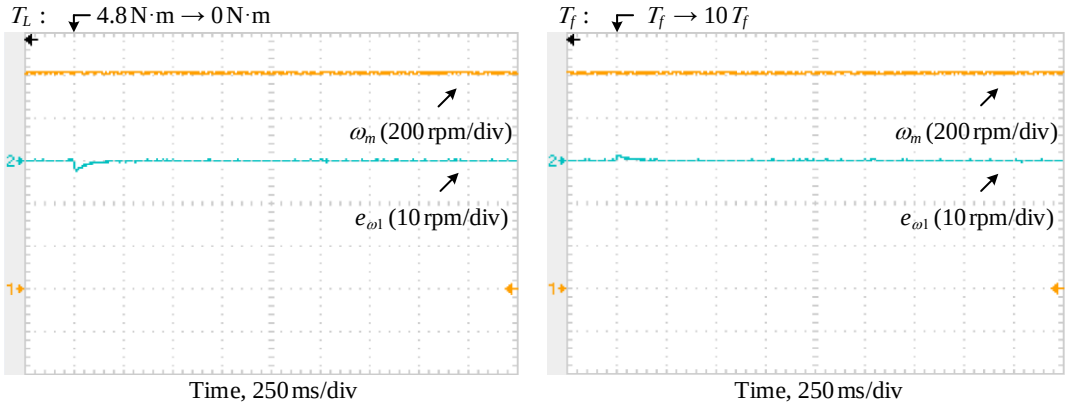

(b)

Figure 4.6 Rotor mechanical speed responses for the first test. (a) Classic STA-based FOC strategy. (b) Proposed FOC strategy.

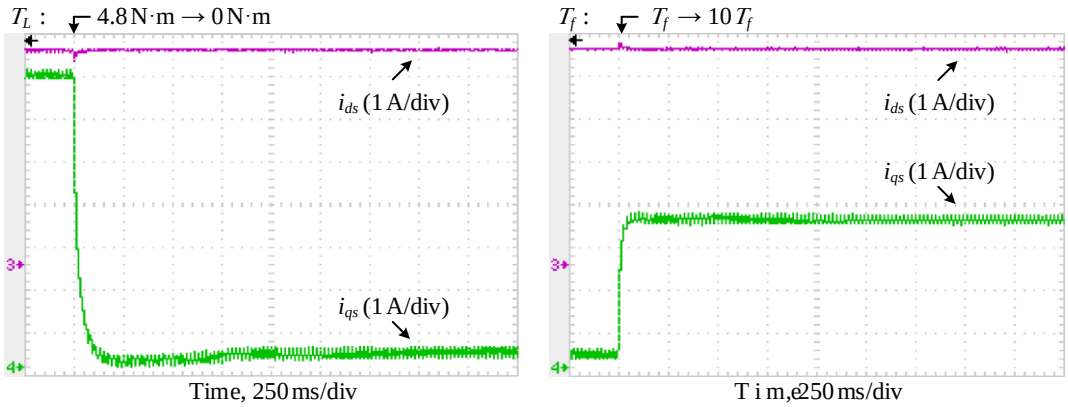

(a)

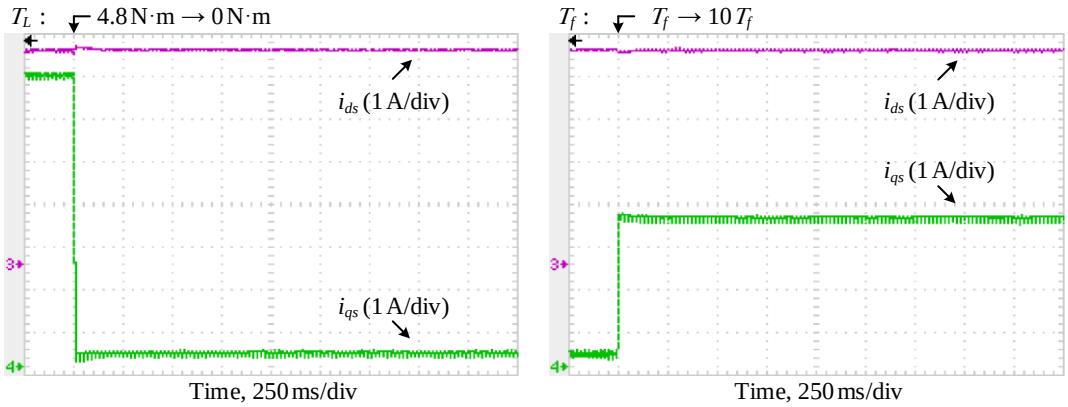

(b)

Figure 4.7 Stator current responses for the first test. (a) Classic STA-based FOC strategy. (b) Proposed FOC strategy.

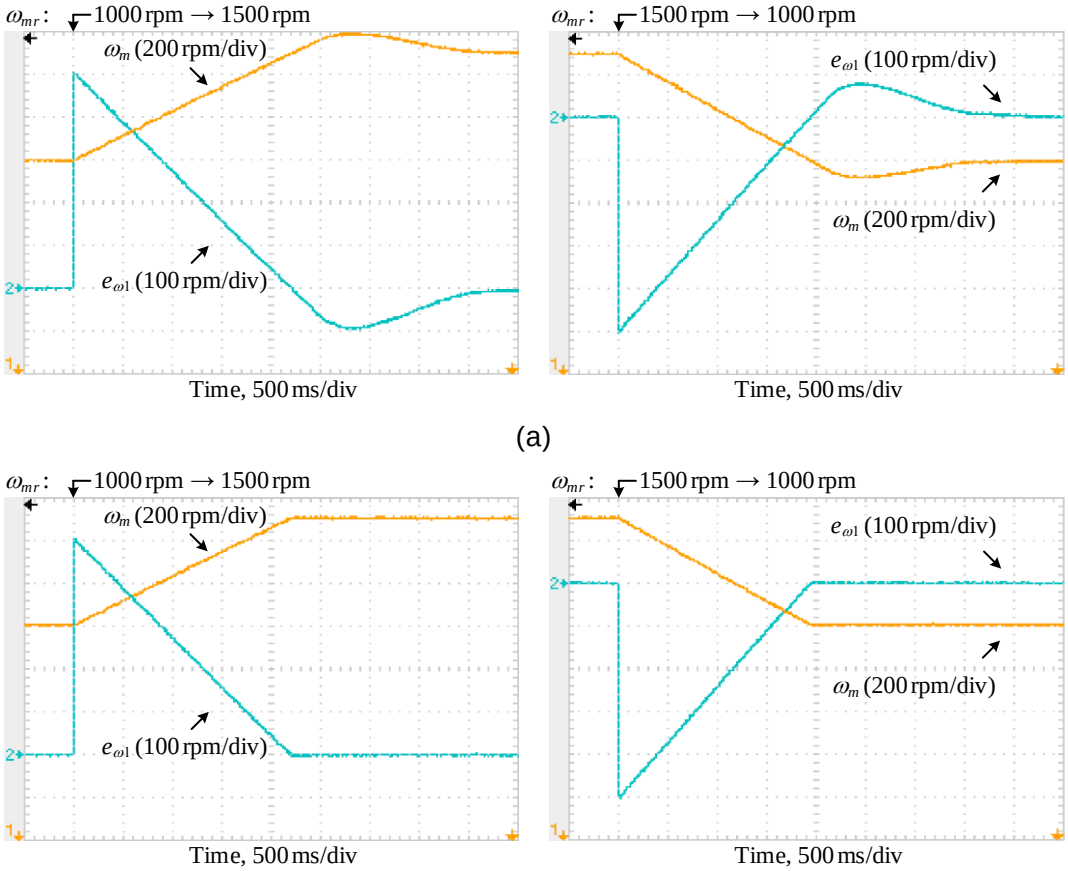

Figure 4.8 Rotor mechanical speed responses for the second test. (a) Classic STA-based FOC strategy. (b) Proposed FOC strategy.

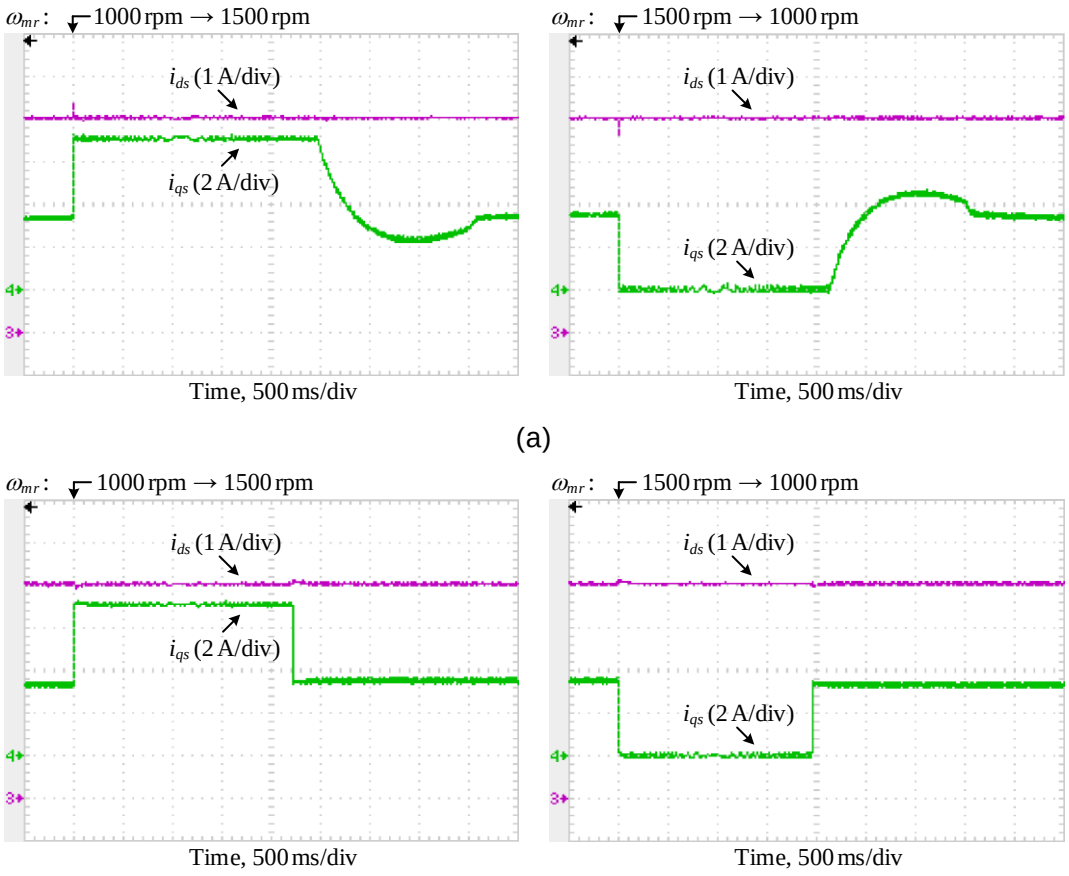

Figure 4.9 Stator current responses for the second test. (a) Classic STA-based FOC strategy. (b) Proposed FOC strategy.

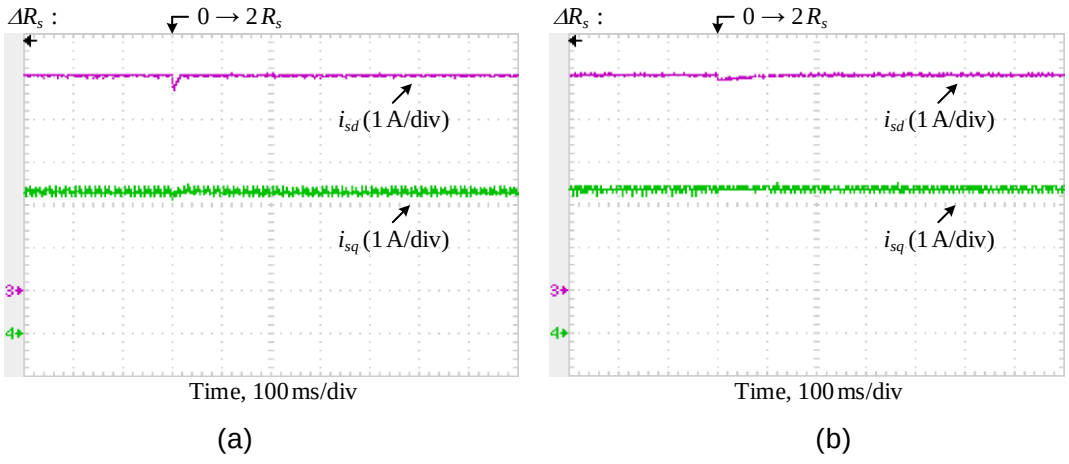

(a) (b)

Figure 4.10 Stator current responses for the third test. (a) Classic STA-based FOC strategy. (b) Proposed FOC strategy.

4.4 Summary

In this chapter, a novel composite controller named as the type-1 composite controller is proposed for a single-input uncertain nonlinear system with relative degree one. The proposed composite controller consists of a standard STSM controller, a HNN-DO and an error compensator. The standard STSM controller is used to achieve the finite-time convergence of the sliding variable to the origin. The HNN-DO is used to estimate and compensate the lumped disturbance in the sliding variable dynamics for the disturbance attenuation ability improvement. The error compensator is used compensate the approximation error of the adopted HNN-DO. The rigorous stability analysis of the sliding variable dynamics with the type-1 composite controller is presented. Based on that, the learning laws for the connective weights between the output neuron and the hidden neurons in the adopted HNN-DO and the error compensator are rigorously derived. Moreover, with respect to any composite controller combining a standard STSM controller with a ANN-DO for a single-input uncertain nonlinear system with relative degree one, these derived learning laws can be used to update online the connective weights between the output neuron and the hidden neurons in the adopted ANN-DO and its corresponding error compensator.

With respect to the 2L-VSI-fed SynRM-VSD system, a novel robust FOC strategy is proposed. In the speed control loop, the type-1 composite controller is designed as a rotor speed controller for the robust rotor speed tracking control. In the current control loop, since each current dynamics of the SynRM in the dq frame is a nonlinear system in terms of i_{ds} and i_{qs} considering the magnetic saturation effect, two composite current controllers, each of which is composed of two standard STSM controllers, are proposed to achieve the robust stator current tracking control. The rigorous stability analysis for each current tracking error dynamics using the corresponding composite current controller is presented. The results of the comparative HIL tests show that the SynRM-VSD system using the proposed FOC strategy is able to accomplish better tracking performance and higher robustness against disturbances/uncertainties in comparison with the SynRM-VSD system using the classic STA-based FOC strategy, which is based on a standard STSM controller and two linear PI current controllers.

References

[1] Y. Shtessel, C. Edwards, L. Fridman, and A. Levant, *Sliding Mode Control and Observation*. Basel, Switzerland: Birkhäuser, 2014.

[2] V. Utkin, A. Poznyak, Y. Orlov, and A. Polyakov, "Conventional and high order sliding mode control," *Journal of the Franklin Institute*, Jun. 2020. [Online].

[3] A. Levant, "Sliding order and sliding accuracy in sliding mode control," *Internation Journal of Control*, vol. 58, no. 6, pp. 1247-1263, Jun. 1993.

[4] A. Levant, "Principles of 2-sliding mode design," *Automatica*, vol. 43, no. 4, pp. 576-586, Apr. 2007.

[5] F. Valenciaga and P. F. Puleston, "High-order sliding control for a wind energy conversion system based on a permanent magnet synchronous generator," *IEEE Transactions on Energy Conversion*, vol. 23, no. 3, pp. 860-867, Sep. 2008.

[6] S. Benelghali, M. E. H. Benbouzid, J. F. Charpentier, T. Ahmed-Ali, and I. Munteanu, "Experimental validation of a marine current turbine simulator: application to a permanent magnet synchronous generator-based system second-order sliding-mode control," *IEEE Transactions on Industrial Electronics*, vol. 58, no. 1, pp. 118-126, Jan. 2011.

[7] L. Derafa, A. Benallegue, and L. Fridman, "Super twisting control algorithm for the attitude tracking of a four rotors UAV," *Journal of the Franklin Institute*, vol. 349, no. 2, pp. 685-699, Mar. 2012.

[8] C. Vázquez, J. Collado, and L. Fridman, "Super twisting control of a parametrically excited overhead crane," *Journal of the Franklin Institute*, vol. 351, no. 4, pp. 2283-2298, Apr. 2014.

[9] Z. Zhao, J. Yang, S. Li, Z. Zhang, and L. Guo, "Finite-time super-twisting sliding mode control for Mars entry trajectory tracking," *Journal of the Franklin Institute*, vol. 352, no. 11, pp. 5226-5248, Nov. 2015.

[10] A. Chalanga, S. Kamal, L. M. Fridman, B. Bandyopadhyay, and J. A. Moreno, "Implementation of super-twisting control: super-twisting and higher order sliding-mode observer-based approaches," *IEEE Transactions on Industrial Electronics*, vol. 63, no. 6, pp. 3677-3685, Jun. 2016.

[11] Y. Huangfu, S. Zhuo, F. Chen, S. Pang, D. Zhao, and F. Gao, "Robust voltage control of floating interleaved boost converter for fuel cell systems," *IEEE Transactions on Industry Applications*, vol. 54, no. 1, pp. 665-674, Jan./Feb. 2018.

[12] R. Sadeghi, S. M. Madani, M. Ataei, M. R. A. Kashkooli, and S. Ademi, "Super-twisting sliding

mode direct power control of a brushless doubly fed induction generator," *IEEE Transactions on Industrial Electronics*, vol. 65, no. 11, pp. 9147-9156, Jun. 2018.

[13] Y. Huangfu, L. Guo, R. Ma, and F. Gao, "An advanced robust noise suppression control of bidirectional DC-DC converter for fuel cell electric vehicle," *IEEE Transactions on Transportation Electrification*, vol. 5, no. 4, pp. 1268-1278, Dec. 2019.

[14] J. Liu, S. Vazquez, L. Wu, A. Marquez, H. Gao, and L. G. Franquelo, "Extended state observer-based sliding-mode control for three-phase power converters," *IEEE Transactions on Industrial Electronics*, vol. 64, no. 1, pp. 22-31, Jan. 2017.

[15] C. Ren, X. Li, X. Yang, and S. Ma, "Extended state observer-based sliding mode control of an omnidirectional mobile robot with friction compensation," *IEEE Transactions on Industrial Electronics*, vol. 66, no. 12, pp. 9480-9489, Dec. 2019.

[16] X. Shen, J. Liu, W. Luo, J. I. Leon, S. Vazquez, A. Marquez, and L. G. Franquelo, "High-performance second-order sliding mode control for NPC converters," *IEEE Transactions on Industrial Informatics*, vol. 16, no. 8, pp. 5345-5356, Aug. 2020.

[17] W. Luo, S. Vazquez, J. Liu, F. Gordillo, L. G. Franquelo, and L. Wu, "Control system design of a three-phase active front end using a sliding-mode observer," *IEEE Transactions on Systems, Man, and Cybernetics: Systems*, Jul. 2020. [Online].

[18] Z. Feng and J. Fei, "Super-twisting sliding mode control for micro gyroscope based on RBF neural network," *IEEE Access*, vol. 6, pp. 64993-65001, Aug. 2018.

[19] W. -B. Li and H. -K. Chiang, "Super-twisting algorithm second-order sliding mode control for a synchronous reluctance motor speed drive," *Mathematical Problems in Engineering*, vol. 2013, Aug. 2013, Article ID 632061.

[20] P. A. Ioannou and J. Sun, *Robust Adaptive Control*. Moneola, USA: Dover Publications, 2012.

[21] S. Yamamoto, K. Tomishige, and T. Ara, "Maximum efficiency operation of vector-controlled synchronous reluctance motors considering cross-magnetic saturation," *IEEJ Transactions on Industry Applications*, vol. 126, no. 7, pp. 1021-1027, Oct. 2006.

[22] S. Yamamoto, T. Ara and K. Matsuse, "A method to calculate transient characteristics of synchronous reluctance motors considering iron loss and cross-magnetic saturation," *IEEE Transactions on Industry Applications*, vol. 43, no. 1, pp. 47-56, Jan./Feb. 2007.

[23] Z. Tang and B. Akin, "A new LMS algorithm based dead-time compensation method for PMSM FOC drives," *IEEE Transactions on Industry Applications*, vol. 54, no. 6, pp. 6472-6484, Nov./Dec. 2018.

5

TYPE-2 COMPOSITE CONTROLLER: DESIGN AND APPLICATION

5.1 Introduction

As mentioned in Section 4.1, since the standard STSM controller, which is designed using the standard STA, is based on the bounded function-based feedback regulation mechanism, a trade-off problem between the tracking performance and the disturbance attenuation arises during the selection of controller gains. To alleviate such a problem, the modified STA, which is developed from the standard STA by adding the linear correction terms, is proposed [1], [2]. Until now, the modified STSM controller, which is designed using the modified STA, has been used in some applications, including the five-phase induction motor-based VSD system [3] and the unmanned aircraft system [4].

Although the modified STSM controller can provide more powerful feedback regulation mechanism than the standard STSM controller due to the use of the linear correction terms, selecting the gains of the modified STSM controller still has to face the above-mentioned trade-off problem, which may make it difficult for such a controller to provide satisfactory performance in some applications. To deal with such an issue, the development of a composite controller combining a modified STSM controller with a DO is an effective method. As mentioned in Section 3.1, the ESO is the most popular linear extended DO for the DOC of AC motor drive systems. Up to now, the ESO has been combined with assorted feedback control algorithms, including the proportional control algorithm [5], [6], the robust control algorithm [7], [8], the predictive control algorithm [9], [10], the feedback linearization algorithm [11], [12], the dynamic surface control algorithm [13],

[14], the backstepping control algorithm [15], [16], the repetitive control algorithm [17], [18], the first-order sliding-mode algorithm [19], [20], and the standard STA [21], [22], for constructing composite controllers. However, to the best of the author's knowledge, no published literature investigates the composite controller combining a modified STA with an ESO; let alone the application of this controller to the PMSM-VSD system.

In this chapter, the type-2 composite controller, which consists of a modified STSM controller and a second-order ESO, is proposed for a single-input uncertain nonlinear system with relative degree one. In such a composite controller, the modified STSM controller is used to stabilize the sliding variable dynamics in a finite time and the lumped disturbance in the sliding variable dynamics is compensated by the second-order ESO. The rigorous stability analysis of the sliding variable dynamics with the type-2 composite controller is presented.

After the rigorous theoretical analysis of the proposed type-2 composite controller, such a controller applies to the construction of a novel robust FOC strategy for the 2L-VSI-fed SPMSM-VSD system. In such a FOC strategy, the proposed type-2 composite controller serves as the rotor speed controller in the speed control loop and two linear PI current controllers are used in the current control loop. To validate the effectiveness and the superiority of the type-2 composite speed controller, based on the experimental test bench described in Section 2.5, comparative experimental tests among the standard STSM speed controller, the ESO-based standard STSM speed controller, the modified STSM speed controller and the type-2 composite speed controller in the frame of the FOC strategy are performed. Finally, the experimental results are presented and analyzed.

5.2 Type-2 Composite Controller Design

Considering the single-input uncertain nonlinear system with relative degree one presented in (3.1), the sliding variable s_1 is designed as (4.1) and its dynamics is presented in (4.3). The control objective is to let s_1 converge to the origin in a finite time.

5.2.1 ESO Design

As mentioned in Section 3.3.1, the ESO design is based on the extended dynamics in which the lumped disturbance is selected as an augmented state variable to be estimated. According to (3.3) and (4.3), the relationship between the lumped disturbance in the x-dynamics and the lumped disturbance in the s_1-dynamics is expressed as

$$\rho_s = \dot{y}_r - \rho_x \tag{5.1}$$

According to (5.1) and Assumption 4.1, the estimation of ρ_s is equivalent to the estimation of ρ_x. It means that the second-order ESO designed as (3.5) can be directly used in the type-2 composite controller.

5.2.2 Controller Design

To achieve the control objective, the type-2 composite control law μ_{c2} is designed as

$$\mu_{c2} = \frac{1}{b_n}\left(\mu_{MSTA} + \dot{y}_r - \hat{\rho}_{ESO}\right) \tag{5.2}$$

where μ_{MSTA} is the modified STA for the finite-time stabilization of the s_1-dynamics, which is expressed as (5.3), and $\hat{\rho}_{ESO}$ is the estimated lumped disturbance from the adopted ESO for the compensation of ρ_x.

$$\mu_{MSTA} = k_1^{c2}\mu_1^{c2} + k_2^{c2}\int_0^t \mu_2^{c2} d\tau \tag{5.3}$$

$$\mu_1^{c2} = p_1^{c2}\sqrt{|s_1|}\,\mathrm{sgn}(s_1) + p_2^{c2}s_1, \quad \mu_2^{c2} = p_1^{c2}\,\mathrm{sgn}(s_1) + p_2^{c2}s_1 \tag{5.4}$$

where k_1^{c2}, k_2^{c2}, p_1^{c2} and p_2^{c2} are the positive constant gains.

Remark 5.1. If $\hat{\rho}_{ESO}$ in (5.2) is set to zero, the modified STSM control law is obtained.

Remark 5.2. If p_2^{c2} in (5.4) is set to zero, the ESO-based standard STSM control law is obtained.

Remark 5.3. If both $\hat{\rho}_{ESO}$ in (5.2) and p_2^{c2} in (5.4) are set to zero, the standard STSM control law is obtained.

Substituting (5.2) into (4.3), the closed-loop s_1-dynamics with the type-2 composite control law is expressed as

$$\begin{aligned}\dot{s}_1 &= -k_1^{c2}\mu_1^{c2} - k_2^{c2}\int_0^t \mu_2^{c2} d\tau - \underbrace{(\rho_x - \hat{\rho}_{ESO})}_{e_{ESO}} \\ &= -k_1^{c2}\mu_1^{c2} - k_2^{c2}\int_0^t \mu_2^{c2} d\tau - e_{ESO}\end{aligned} \tag{5.5}$$

where e_{ESO} is the lumped disturbance estimation error of the ESO.

Considering Assumption 3.2, $\dot{e}_{ESO}$ is bounded as $|\dot{e}_{ESO}| \leq L_5^x$ for a positive constant L_5^x.

Lemma 5.1 [23]. Let $y \geq 0$, $z \geq 0$, $1 > a_1 > 0$, and $b > 0$. If a constant a_2 satisfies $\frac{1}{a_1} + \frac{1}{a_2} = 1$, the following inequality holds.

$$yz \le \frac{b^{a_1}}{a_1} y^{a_1} + \frac{b^{-a_2}}{a_2} z^{a_2} \tag{5.6}$$

Lemma 5.2 [23]. Let $y > 0, z > 0$. If $a_1 > a_2 > 0$, the following inequality holds.

$$\left(y^{a_2} + z^{a_2}\right)^{\frac{1}{a_2}} \le \left(y^{a_1} + z^{a_1}\right)^{\frac{1}{a_1}} \tag{5.7}$$

The following Theorem can be used to select k_1^{c2}, k_2^{c2}, p_1^{c2} and p_2^{c2} for accomplishing the control objective.

Theorem 5.1. Considering the system (5.5) and $|\dot{e}_{ESO}| \le L_5^x$, for two positive constants γ_1 and γ_2 satisfying (5.8), if k_1^{c2}, k_2^{c2}, p_1^{c2} and p_2^{c2} are selected as (5.9), s_1 will converge to the origin in a finite time.

$$\gamma_1 > \gamma_2 > 0 \tag{5.8}$$

$$p_1^{c2} > 0, \quad p_2^{c2} > 0, \quad k_1^{c2} > \frac{L_5^x}{p_1^{c2}\sqrt{2\left(k_2^{c2} p_1^{c2} - L_5^x\right)}}\left(1 + \frac{\gamma_1}{\gamma_2}\right), \quad k_2^{c2} > \frac{L_5^x}{p_1^{c2}} \tag{5.9}$$

Proof. The system (5.5) can be rearranged as

$$\begin{cases} \dot{s}_1 = -k_1^{c2}\mu_1^{c2} + \phi_3 = -k_1^{c2} p_1^{c2}\sqrt{|s_1|}\,\mathrm{sgn}(s_1) - k_1^{c2} p_2^{c2} s_1 + \phi_3 \\ \dot{\phi}_3 = -k_2^{c2}\mu_2^{c2} - \dot{e}_{ESO} = -k_2^{c2} p_1^{c2}\,\mathrm{sgn}(s_1) - k_2^{c2} p_2^{c2} s_1 - \dot{e}_{ESO} \end{cases} \tag{5.10}$$

At first, the following state variable vector is defined.

$$\boldsymbol{\eta} = \begin{bmatrix} \eta_1^{c2} \\ \eta_2^{c2} \end{bmatrix} = \begin{bmatrix} \mu_1^{c2} \\ k_1^{c2}\mu_1^{c2} - \phi_3 \end{bmatrix} = \begin{bmatrix} p_1^{c2}\sqrt{|s_1|}\,\mathrm{sgn}(s_1) + p_2^{c2} s_1 \\ k_1^{c2} p_1^{c2}\sqrt{|s_1|}\,\mathrm{sgn}(s_1) + k_1^{c2} p_2^{c2} s_1 - \phi_3 \end{bmatrix} \tag{5.11}$$

For the system (5.10), the Lyapunov candidate function V_{c2} is selected as follows [2].

$$V_{c2} = (\boldsymbol{\eta}^{c2})^T \boldsymbol{R}\boldsymbol{\eta}^{c2} + (\gamma_1 + \gamma_2)k_2^{c2}\left(p_1^{c2}|s_1| + \frac{1}{2}p_2^{c2}|s_1|^2\right) \tag{5.12}$$

where $\boldsymbol{R}$ is a symmetric and positive definite matrix expressed as

$$\boldsymbol{R} = \frac{1}{2}\begin{bmatrix} \gamma_1 (k_1^{c2})^2 & -\gamma_1 k_1^{c2} \\ -\gamma_1 k_1^{c2} & \gamma_1 + \gamma_2 \end{bmatrix} \tag{5.13}$$

Based on (5.12), $\dot{V}_{c2}$ is expressed as

$$\dot{V}_{c2} = (\dot{\boldsymbol{\eta}}^{c2})^T \boldsymbol{R}\boldsymbol{\eta}^{c2} + (\boldsymbol{\eta}^{c2})^T \boldsymbol{R}\dot{\boldsymbol{\eta}}^{c2} + \left(\gamma_1 + \gamma_2\right)k_2^{c2}\left(p_1^{c2} + p_2^{c2}|s_1|\right)\dot{s}_1\,\mathrm{sgn}(s_1) \tag{5.14}$$

Combining (5.14) with (5.10), $\dot{V}_{c2}$ can be calculated as

$$
\begin{aligned}
\dot{V}_{c2} &= -k_2^{c2}\eta_2^{c2}(\gamma_1+\gamma_2)\left(p_1^{c2}+p_2^{c2}|s_1|\right)\mathrm{sgn}(s_1)-\gamma_1(k_1^{c2})^2\mu_1^{c2}\eta_2^{c2}\left(\frac{p_1^{c2}}{2\sqrt{|s_1|}}+p_2^{c2}\right)\\
&\quad+\eta_2^{c2}(\gamma_1+\gamma_2)\left[-k_1^{c2}\eta_2^{c2}\left(\frac{p_1^{c2}}{2\sqrt{|s_1|}}+p_2^{c2}\right)+k_2^{c2}\mu_2^{c2}+\dot{e}_{ESO}\right]\\
&\quad-\gamma_1 k_1^{c2}\left[-(\eta_2^{c2})^2\left(\frac{p_1^{c2}}{2\sqrt{|s_1|}}+p_2^{c2}\right)-k_1^{c2}\mu_1^{c2}\eta_2^{c2}\left(\frac{p_1^{c2}}{2\sqrt{|s_1|}}+p_2^{c2}\right)+k_2^{c2}\mu_1^{c2}\mu_2^{c2}+\mu_1^{c2}\dot{e}_{ESO}\right]\\
&=\left(\frac{p_1^{c2}}{2\sqrt{|s_1|}}+p_2^{c2}\right)\left[-\gamma_1(k_1^{c2})^2\mu_1^{c2}\eta_2^{c2}+\gamma_1 k_1^{c2}(\eta_2^{c2})^2+\gamma_1(k_1^{c2})^2\mu_1^{c2}\eta_2^{c2}-(\gamma_1+\gamma_2)k_1^{c2}(\eta_2^{c2})^2\right]\\
&\quad-\gamma_1 k_1^{c2}\left(k_2^{c2}\mu_1^{c2}\mu_2^{c2}+\mu_1^{c2}\dot{e}_{ESO}\right)+\eta_2^{c2}(\gamma_1+\gamma_2)\left(k_2^{c2}\mu_2^{c2}+\dot{e}_{ESO}\right)\\
&\quad-(\gamma_1+\gamma_2)k_2^{c2}\left(p_1^{c2}+p_2^{c2}|s_1|\right)\eta_2^{c2}\,\mathrm{sgn}(s_1)\\
&=-\gamma_2 k_1^{c2}(\eta_2^{c2})^2\left(\frac{p_1^{c2}}{2\sqrt{|s_1|}}+p_2^{c2}\right)-\gamma_1 k_1^{c2}\mu_1^{c2}\dot{e}_{ESO}+(\gamma_1+\gamma_2)(\eta_2^{c2})^2\dot{e}_{ESO}-\gamma_1 k_1^{c2}k_2^{c2}\mu_1^{c2}\mu_2^{c2}\\
&\quad+(\gamma_1+\gamma_2)\eta_2^{c2}k_2^{c2}\mu_2-(\gamma_1+\gamma_2)k_2^{c2}\left(p_1^{c2}+p_2^{c2}|s_1|\right)\eta_2^{c2}\,\mathrm{sgn}(s_1)\\
&=-\gamma_2 k_1^{c2}(\eta_2^{c2})^2\left(\frac{p_1^{c2}}{2\sqrt{|s_1|}}+p_2^{c2}\right)-\gamma_1 k_1^{c2}\mu_1^{c2}\dot{e}_2+(\gamma_1+\gamma_2)\eta_2^{c2}\dot{e}_{ESO}\\
&\quad-\gamma_1 k_1^{c2}k_2^{c2}\left(p_1^{c2}\sqrt{|s_1|}\,\mathrm{sgn}(s_1)+p_2^{c2}s_1\right)\left(p_1^{c2}\,\mathrm{sgn}(s_1)+p_2^{c2}s_1\right)\\
&\quad+(\gamma_1+\gamma_2)\eta_2^{c2}k_2^{c2}\left(p_1^{c2}\,\mathrm{sgn}(s_1)+p_2^{c2}s_1\right)-(\gamma_1+\gamma_2)k_2^{c2}\left(p_1^{c2}+p_2^{c2}|s_1|\right)\eta_2^{c2}\,\mathrm{sgn}(s_1)\\
&=-\gamma_2 k_1^{c2}(\eta_2^{c2})^2\left(\frac{p_1^{c2}}{2\sqrt{|s_1|}}+p_2^{c2}\right)-\gamma_1 k_1^{c2}\mu_1^{c2}\dot{e}_2+(\gamma_1+\gamma_2)\eta_2^{c2}\dot{e}_{ESO}\\
&\quad-\gamma_1 k_1^{c2}k_2^{c2}\left(p_1^{c2}+p_2^{c2}|s_1|\right)\left(p_1^{c2}+p_2^{c2}|s_1|\right)\\
&=-\gamma_2 k_1^{c2}(\eta_2^{c2})^2\left(\frac{p_1^{c2}}{2\sqrt{|s_1|}}+p_2^{c2}\right)-\gamma_1 k_1^{c2}\mu_1^{c2}\dot{e}_{ESO}+(\gamma_1+\gamma_2)\eta_2\dot{e}_2\\
&\quad-\gamma_1 k_1^{c2}k_2^{c2}\left(p_1^{c2}+p_2^{c2}|s_1|\right)\left|p_1^{c2}\sqrt{|s_1|}+p_2^{c2}|s_1|\right|\left|\mathrm{sgn}(s_1)\right|\\
&=-\frac{\gamma_2 k_1^{c2}p_1^{c2}(\eta_2^{c2})^2}{2\sqrt{|s_1|}}-\gamma_2 k_1^{c2}p_2^{c2}(\eta_2^{c2})^2-\gamma_1 k_1^{c2}\mu_1^{c2}\dot{e}_2+(\gamma_1+\gamma_2)\eta_2^{c2}\dot{e}_{ESO}\\
&\quad-\gamma_1 k_1^{c2}k_2^{c2}\left(p_1^{c2}+p_2^{c2}|s_1|\right)\left|\mu_1^{c2}\right|
\end{aligned}
\tag{5.15}
$$

Considering Lemma 5.1 and (5.9), let $y=(\eta_2^{c2})^2$, $z=\frac{1}{\sqrt{|s_1|}}$, $a_1=0.5$, $a_2=-1$ and $b=2(k_2^{c2}p_1^{c2}-L_5^x)$, such that

$$
\frac{(\eta_2^{c2})^2}{\sqrt{|s_1|}}\geq 2\sqrt{2\left(k_2^{c2}p_1^{c2}-L_5^x\right)\left|\eta_2^{c2}\right|}-2\left(k_2^{c2}p_1^{c2}-L_5^x\right)\sqrt{|s_1|}
\tag{5.16}
$$

Combining (5.15) with (5.16) and considering the fact that $|\dot{e}_{ESO}| \le L_5^x$, the following inequality can be obtained.

$$\begin{aligned}\dot{V}_{c2} &\le \gamma_2 k_1^{c2} p_1^{c2}\left[\left(k_2^{c2} p_1^{c2} - L_5^x\right)\sqrt{|s_1|} - \sqrt{2\left(k_2^{c2} p_1^{c2} - L_5^x\right)}\left|\eta_2^{c2}\right|\right] - \gamma_2 k_1^{c2} p_2^{c2} (\eta_2^{c2})^2 \\ &\quad + \gamma_1 k_1^{c2}\left|\mu_1^{c2}\right|\left|\dot{e}_{ESO}\right| + \left(\gamma_1+\gamma_2\right)\left|\eta_2^{c2}\right|\left|\dot{e}_{ESO}\right| - \gamma_1 k_1^{c2} k_2^{c2}\left(p_1^{c2} + p_2^{c2}|s_1|\right)\left|\mu_1^{c2}\right| \\ &\le \gamma_2 k_1^{c2} p_1^{c2}\left[\left(k_2^{c2} p_1^{c2} - L_5^x\right)\sqrt{|s_1|} - \sqrt{2\left(k_2^{c2} p_1^{c2} - L_5^x\right)}\left|\eta_2^{c2}\right|\right] - \gamma_2 k_1^{c2} p_2^{c2} (\eta_2^{c2})^2 \\ &\quad + L_5^x \gamma_1 k_1^{c2}\left|\mu_1^{c2}\right| + L_5^x\left(\gamma_1+\gamma_2\right)\left|\eta_2^{c2}\right| - \gamma_1 k_1^{c2} k_2^{c2}\left(p_1^{c2} + p_2^{c2}|s_1|\right)\left|\mu_1^{c2}\right|\end{aligned} \tag{5.17}$$

With respect to μ_1^{c2}, the following inequality holds.

$$\left|\mu_1^{c2}\right| = \left|p_1^{c2}\sqrt{|s_1|}\,\mathrm{sgn}(s_1) + p_2^{c2} s_1\right| = \left|p_1^{c2}\sqrt{|s_1|} + p_2^{c2}|s_1|\right| \ge p_1^{c2}\sqrt{|s_1|} \tag{5.18}$$

Substituting (5.18) into (5.17), the following inequality can be derived.

$$\begin{aligned}\dot{V}_{c2} &\le \gamma_2 k_1^{c2} p_1^{c2}\left[\left(k_2^{c2} p_1^{c2} - L_5^x\right)\frac{\left|\mu_1^{c2}\right|}{p_1^{c2}} - \sqrt{2\left(k_2^{c2} p_1^{c2} - L_5^x\right)}\left|\eta_2^{c2}\right|\right] - \gamma_2 k_1^{c2} p_2^{c2} (\eta_2^{c2})^2 + L_5^x \gamma_1 k_1^{c2}\left|\mu_1^{c2}\right| \\ &\quad + L_5^x\left(\gamma_1+\gamma_2\right)\left|\eta_2^{c2}\right| - \gamma_1 k_1^{c2} k_2^{c2}\left(p_1^{c2} + p_2^{c2}|s_1|\right)\left|\mu_1^{c2}\right| \\ &= \gamma_2 k_1^{c2}\left[\left(k_2^{c2} p_1^{c2} - L_5^x\right)\left|\mu_1^{c2}\right| - p_1^{c2}\sqrt{2\left(k_2^{c2} p_1^{c2} - L_5^x\right)}\left|\eta_2^{c2}\right|\right] - \gamma_2 k_1^{c2} p_2^{c2} (\eta_2^{c2})^2 + L_5^x \gamma_1 k_1^{c2}\left|\mu_1^{c2}\right| \\ &\quad + L_5^x\left(\gamma_1+\gamma_2\right)\left|\eta_2^{c2}\right| - \gamma_1 k_1^{c2} k_2^{c2}\left(p_1^{c2} + p_2^{c2}|s_1|\right)\left|\mu_1^{c2}\right| \\ &= -k_1^{c2}\left[\gamma_1 k_2^{c2}\left(p_1^{c2} + p_2^{c2}|s_1|\right) - \gamma_2\left(k_2^{c2} p_1^{c2} - L_5^x\right) - L_5^x\gamma_1\right]\left|\mu_1^{c2}\right| - \gamma_2 k_1^{c2} p_2^{c2} (\eta_2^{c2})^2 + L_5^x\left(\gamma_1+\gamma_2\right)\left|\eta_2^{c2}\right| \\ &\quad - \gamma_2 k_1^{c2} p_1^{c2}\sqrt{2\left(k_2^{c2} p_1^{c2} - L_5^x\right)}\left|\eta_2^{c2}\right| \\ &\le -k_1^{c2}\left[\gamma_1 k_2^{c2} p_1^{c2} - \gamma_2\left(k_2^{c2} p_1^{c2} - L_5^x\right) - L_5^x\gamma_1\right]\left|\mu_1^{c2}\right| - \gamma_2 k_1^{c2} p_2^{c2} (\eta_2^{c2})^2 + L_5^x\left(\gamma_1+\gamma_2\right)\left|\eta_2^{c2}\right| \\ &\quad - \gamma_2 k_1^{c2} p_1^{c2}\sqrt{2\left(k_2^{c2} p_1^{c2} - L_5^x\right)}\left|\eta_2^{c2}\right| \\ &\le -k_1^{c2}\left(k_2^{c2} p_1^{c2} - L_5^x\right)\left(\gamma_1-\gamma_2\right)\left|\mu_1^{c2}\right| - \left[\gamma_2 k_1^{c2} p_1^{c2}\sqrt{2\left(k_2^{c2} p_1^{c2} - L_5^x\right)} - L_5^x\left(\gamma_1+\gamma_2\right)\right]\left|\eta_2^{c2}\right| \\ &\le \underbrace{-k_1^{c2} p_1^{c2}\left(k_2^{c2} p_1^{c2} - L_5^x\right)\left(\gamma_1-\gamma_2\right)}_{\lambda_1^{c2}}\sqrt{|s_1|} - \underbrace{\left[\gamma_2 c_1 p_1\sqrt{2\left(c_2 p_1 - L_5\right)} - L_5\left(\gamma_1+\gamma_2\right)\right]}_{\lambda_2^{c2}}\left|\eta_2^{c2}\right| \\ &= -\lambda_1^{c2}\sqrt{|s_1|} - \lambda_2^{c2}\left|\eta_2^{c2}\right|\end{aligned} \tag{5.19}$$

According to (5.8) and (5.9), λ_1^{c2} and λ_2^{c2}in (5.19) are two positive constants. Since $\boldsymbol{R}$ is positive definite, based on (5.12), the following inequality can be derived.

$$\begin{aligned}V_{c2} &\le \lambda_{\max}\{\boldsymbol{R}\}\left(\left|\eta_1^{c2}\right|^2 + \left|\eta_2^{c2}\right|^2\right) + \left(\gamma_1+\gamma_2\right)k_2^{c2}\left[p_1^{c2}|s_1| + \frac{1}{2}p_2^{c2}|s_1|^2\right] \\ &= \lambda_{\max}\{\boldsymbol{R}\}\left|\eta_2^{c2}\right|^2 + \chi|s_1|\end{aligned} \tag{5.20}$$

where $\lambda_{\max}\{\boldsymbol{R}\}$ represents the maximum eigenvalue of $\boldsymbol{R}$, χ is written as

$$\chi = \lambda_{\max}\{\boldsymbol{R}\}\left((p_1^{c2})^2 + 2p_1^{c2}p_2^{c2}\sqrt{|s_1|} + (p_2^{c2})^2|s_1|\right) + k_2^{c2}(\gamma_1+\gamma_2)\left(p_1^{c2} + \frac{1}{2}p_2^{c2}|s_1|\right) \tag{5.21}$$

Based on Lemma 5.2, (5.8) and (5.9), the following inequality holds.

$$\begin{aligned}\left(-\dot{V}_{c2}\right)^2 &\geq \left((\lambda_1^{c2})^2|s_1| + \sqrt{(\lambda_2^{c2})^2\left|\eta_2^{c2}\right|^2}\right)^2 \\ &\geq (\lambda_1^{c2})^2|s_1| + (\lambda_2^{c2})^2\left|\eta_2^{c2}\right|^2 \geq k_{c2}\chi|s_1| + k_{c2}\lambda_{\max}\{\boldsymbol{R}\}\left|\eta_2^{c2}\right|^2 \geq k_{c2}V_{c2}\end{aligned} \tag{5.22}$$

where k_{c2} is a positive constant such that

$$k_{c2} \leq \min\left\{\frac{(\lambda_1^{c2})^2}{\chi}, \quad \frac{(\lambda_2^{c2})^2}{\lambda_{\max}\{\boldsymbol{R}\}}\right\} \tag{5.23}$$

According to (5.22), the following inequality holds.

$$\dot{V}_{c2} \leq -\sqrt{k_{c2}}\sqrt{V_{c2}} \tag{5.24}$$

On the basis of (5.24) and the comparison principle [24], all trajectories of the system (5.10) will converge to the origin in a finite time. It means that s_1 will converge to the origin in a finite time. The proof is completed. ■

5.3 Application

In this section, the type-2 composite speed controller, which is designed using the practical speed dynamics of the SPMSM presented in (2.54), is applied to the construction of a novel robust FOC strategy for the 2L-VSI-fed SPMSM-VSD system. In this FOC strategy, two linear PI current controllers are used as stator current controllers. Moreover, i_{dsr} is set to 0 and i_{qsr} is generated by the type-2 composite speed controller. The results of the comparative experimental tests among the standard STSM speed controller, the ESO-based standard STSM speed controller, the modified STSM speed controller and the type-2 composite speed controller in the frame of the FOC strategy for the 2L-VSI-fed SPMSM-VSD system are presented to demonstrate the superiority of the type-2 composite speed controller.

5.3.1 Type-2 Composite Speed Controller Design

Since the dynamics of the current control loop is much faster than that of the speed control loop, it can be considered that $i_{qs} = i_{qsr}$ in the rotor speed controller design. Therefore, based on (2.54), the ω_m-dynamics of the SPMSM can be rewritten as

$$\dot{\omega}_m = \underbrace{-\frac{B_{m0}}{J_0}}_{a_{\omega n2}}\omega_m + \underbrace{\frac{3n_p\lambda_{m0}}{2J_0}}_{b_{\omega n2}} i_{qsr} \underbrace{-\frac{1}{J_0}T_L + \rho_\omega^P}_{\rho_{\omega 2}} = -a_{\omega n2}\omega_m + b_{\omega n2} i_{qsr} + \rho_{\omega 2} \tag{5.25}$$

where $a_{\omega n2}$ and $b_{\omega n2}$ are two constants and $\rho_{\omega 2}$ denotes the lumped disturbance in the ω_m-dynamics.

Assumption 5.1. $\rho_{\omega 2}$ and its time derivative $\dot{\rho}_{\omega 2}$ are bounded as $|\rho_{\omega 2}| \leq L_{\omega 1}^{c2}$ and $|\dot{\rho}_{\omega 2}| \leq L_{\omega 2}^{c2}$, respectively, for positive constants $L_{\omega 1}^{c2}$ and $L_{\omega 2}^{c2}$.

According to the ESO design presented in Section 3.3.1, the ESO can be designed as (5.26) for the estimation of $\rho_{\omega 2}$, where two positive constant gains $\beta_{\omega 1}$ and $\beta_{\omega 2}$ are selected as (5.27) and the time derivative of the lumped disturbance estimation error $\dot{e}_{E\omega}$ is bounded as $|\dot{e}_{E\omega}| \leq L_{\omega 3}^{c2}$ for a positive constant $L_{\omega 3}^{c2}$.

$$\begin{cases} \dot{\hat{z}}_{e\omega 1} = -a_{\omega n2}\omega_m + b_{\omega n2} i_{qsr}^{c2} + \hat{z}_{e\omega 2} + \beta_{\omega 1}(\omega_m - \hat{z}_{e\omega 1}) \\ \dot{\hat{z}}_{e\omega 2} = \beta_{\omega 2}(\omega_m - \hat{z}_{e\omega 1}) \end{cases} \tag{5.26}$$

$$\beta_{\omega 1} = 2\omega_{b\omega}, \quad \beta_{\omega 2} = \omega_{b\omega}^2 \tag{5.27}$$

where $\hat{z}_{e\omega 1} = \hat{\omega}_m$ and $\hat{z}_{e\omega 2} = \hat{\rho}_{e\omega}$ denote the estimated rotor mechanical speed and lumped disturbance, respectively, $\omega_{b\omega}$ is the bandwidth of the ESO, and i_{qsr}^{c2} is the type-2 composite speed control law.

The speed tracking error $e_{\omega 2}$ for the field-oriented controlled SPMSM-VSD system is defined as

$$e_{\omega 2} = \omega_{mr} - \omega_m \tag{5.28}$$

Based on (5.25) and (5.28), the $e_{\omega 2}$-dynamics can be expressed as

$$\dot{e}_{\omega 2} = \dot{\omega}_{mr} + a_{\omega n2}\omega_m - b_{\omega n2} i_{qsr} - \rho_{\omega 2} \tag{5.29}$$

Selecting $e_{\omega 2}$ as the sliding variable, the type-2 composite speed control law i_{qsr}^{c2} is designed as

$$i_{qsr}^{c2} = \frac{1}{b_{\omega n2}}\left(\mu_{s\omega 2} + a_{\omega n2}\omega_m + \dot{\omega}_{mr} - \hat{\rho}_{e\omega}\right) \tag{5.30}$$

where $\mu_{s\omega 2}$ is the modified STA for the finite-time rotor speed tracking control, which is expressed as (5.31), and $\hat{\rho}_{e\omega}$ is the estimated lumped disturbance from the adopted ESO for the compensation of $\rho_{\omega 2}$.

$$\mu_{s\omega 2} = k_{\omega 1}^{c2}\mu_{\omega 1}^{c2} + k_{\omega 2}^{c2}\int_0^t \mu_{\omega 2}^{c2} d\tau \tag{5.31}$$

$$\mu_{\omega 1}^{c2} = p_{\omega 1}^{c2}\sqrt{|e_{\omega 2}|}\,\mathrm{sgn}(e_{\omega 2}) + p_{\omega 2}^{c2}e_{\omega 2}, \quad \mu_{\omega 2}^{c2} = p_{\omega 1}^{c2}\,\mathrm{sgn}(e_{\omega 2}) + p_{\omega 2}^{c2}e_{\omega 2} \tag{5.32}$$

where $k_{\omega 1}^{c2}$, $k_{\omega 2}^{c2}$, $p_{\omega 1}^{c2}$ and $p_{\omega 2}^{c2}$ are the positive constant gains.

Remark 5.4. If $\hat{\rho}_{e\omega}$ in (5.30) is set to zero, the modified STSM speed control law is obtained.

Remark 5.5. If $p_{\omega 2}^{c2}$ in (5.32) is set to zero, the ESO-based standard STSM speed control law is obtained.

Remark 5.6. If both $\hat{\rho}_{e\omega}$ in (5.30) and $p_{\omega 2}^{c2}$ in (5.32) are set to zero, the standard STSM speed control law is obtained.

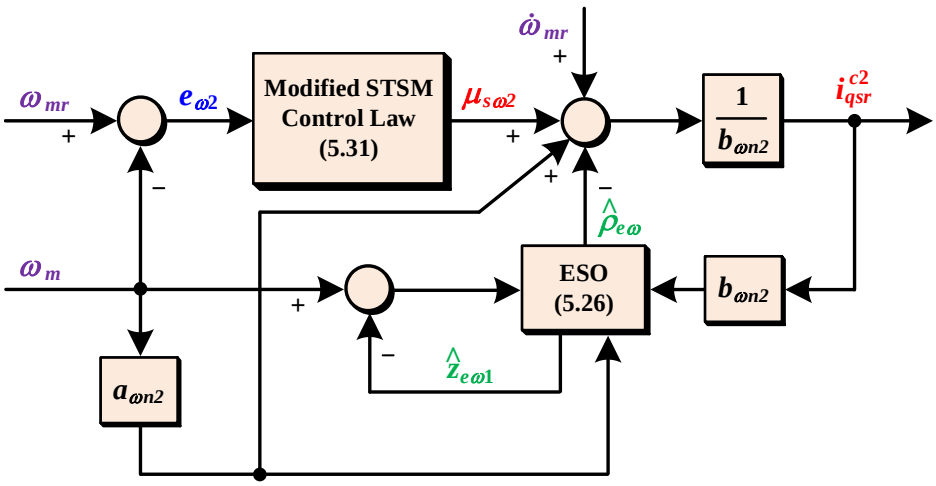

Figure 5.1 Block diagram of the type-2 composite speed controller.

Substituting (5.30) into (5.29), the closed-loop $e_{\omega 2}$-dynamics with the type-2 composite speed control law is expressed as

$$\begin{aligned}\dot{e}_{\omega 2} &= -k_{\omega 1}^{c2}\mu_{\omega 1}^{c2} - k_{\omega 2}^{c2}\int_0^t \mu_{\omega 2}^{c2}d\tau - \underbrace{(\rho_{\omega 2} - \hat{\rho}_{e\omega})}_{e_{E\omega}} \\ &= -k_{\omega 1}^{c2}\mu_{\omega 1}^{c2} - k_{\omega 2}^{c2}\int_0^t \mu_{\omega 2}^{c2}d\tau - e_{E\omega}\end{aligned} \tag{5.33}$$

Based on Theorem 5.1, it can be concluded that, with the type-2 composite speed control law (5.30), $e_{\omega 2}$ will converge to the origin in a finite time if $k_{\omega 1}^{c2}$, $k_{\omega 2}^{c2}$, $p_{\omega 1}^{c2}$ and $p_{\omega 2}^{c2}$ are selected as

$$p_{\omega 1}^{c2} > 0, \quad p_{\omega 2}^{c2} > 0, \quad k_{\omega 1}^{c2} > \frac{L_{\omega 3}^{c2}}{p_{\omega 1}^{c2}\sqrt{2\left(k_{\omega 2}^{c2}p_{\omega 1}^{c2} - L_{\omega 3}^{c2}\right)}}\left(1 + \frac{\gamma_{\omega 1}}{\gamma_{\omega 2}}\right), \quad k_{\omega 2}^{c2} > \frac{L_{\omega 3}^{c2}}{p_{\omega 1}^{c2}} \tag{5.34}$$

where $\gamma_{\omega 1}$ and $\gamma_{\omega 2}$ are two positive constants such that $\gamma_{\omega 1} > \gamma_{\omega 2}$.

The block diagram of the type-2 composite speed controller is shown in Figure 5.1.

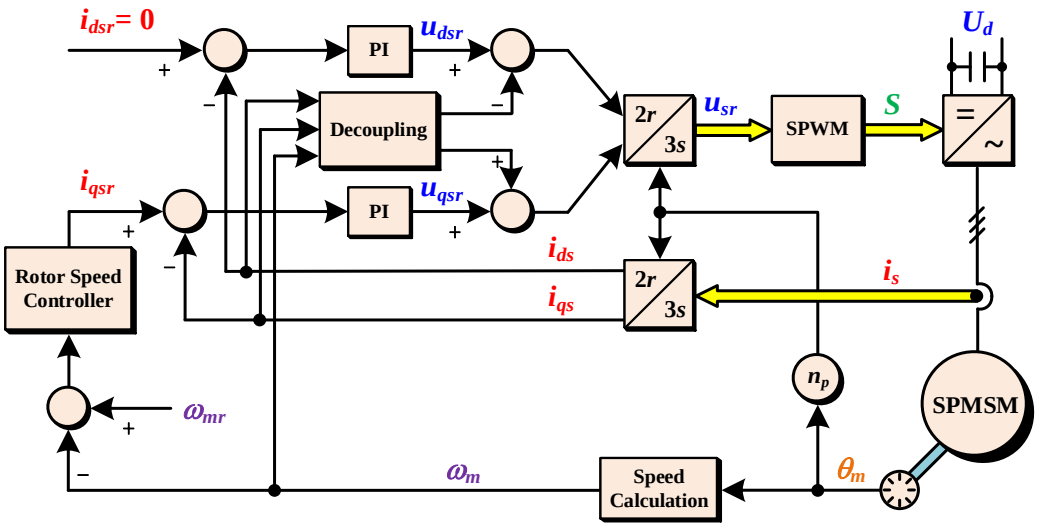

Figure 5.2 Block diagram of the $i_{ds} = 0$ control strategy for the SPMSM-VSD system.

Table 5.1 Parameters of tested rotor speed controllers

Rotor speed controller	Controller parameters	Observer parameters
Standard STSM speed controller	$k_{\omega 1}^{c2} = 500,\ k_{\omega 2}^{c2} = 20000,$ $p_{\omega 1}^{c2} = 4,\ p_{\omega 2}^{c2} = 0, \Pi = 5$	–
ESO-based standard STSM speed controller	$k_{\omega 1}^{c2} = 500,\ k_{\omega 2}^{c2} = 20000,$ $p_{\omega 1}^{c2} = 4,\ p_{\omega 2}^{c2} = 0, \Pi = 5$	$\beta_{\omega 1} = 400,$ $\beta_{\omega 2} = 40000$
Modified STSM speed controller	$k_{\omega 1}^{c2} = 500,\ k_{\omega 2}^{c2} = 20000,$ $p_{\omega 1}^{c2} = 4,\ p_{\omega 2}^{c2} = 0.4, \Pi = 5$	–
Type-2 composite speed controller	$k_{\omega 1}^{c2} = 500,\ k_{\omega 2}^{c2} = 20000,$ $p_{\omega 1}^{c2} = 4,\ p_{\omega 2}^{c2} = 0.4, \Pi = 5$	$\beta_{\omega 1} = 400,$ $\beta_{\omega 2} = 40000$

5.3.2 Experimental Results

The experimental test bench described in Section 2.5 is used to perform comparative experimental tests among the standard STSM speed controller, the ESO-based standard STSM speed controller, the modified STSM speed controller and the type-2 composite speed controller in the frame of the FOC strategy in which i_{dsr} is set to 0. Such a FOC strategy is commonly known as the $i_{ds} = 0$ control strategy whose block diagram is illustrated in Figure 5.2, where the sinusoidal PWM (SPWM) algorithm is adopted for the 2L-VSI. To further alleviate the chattering and the noise in practice, for the implementation of each tested rotor speed controller in the DSP, the sign function is replaced by the saturation function expressed as (4.47).

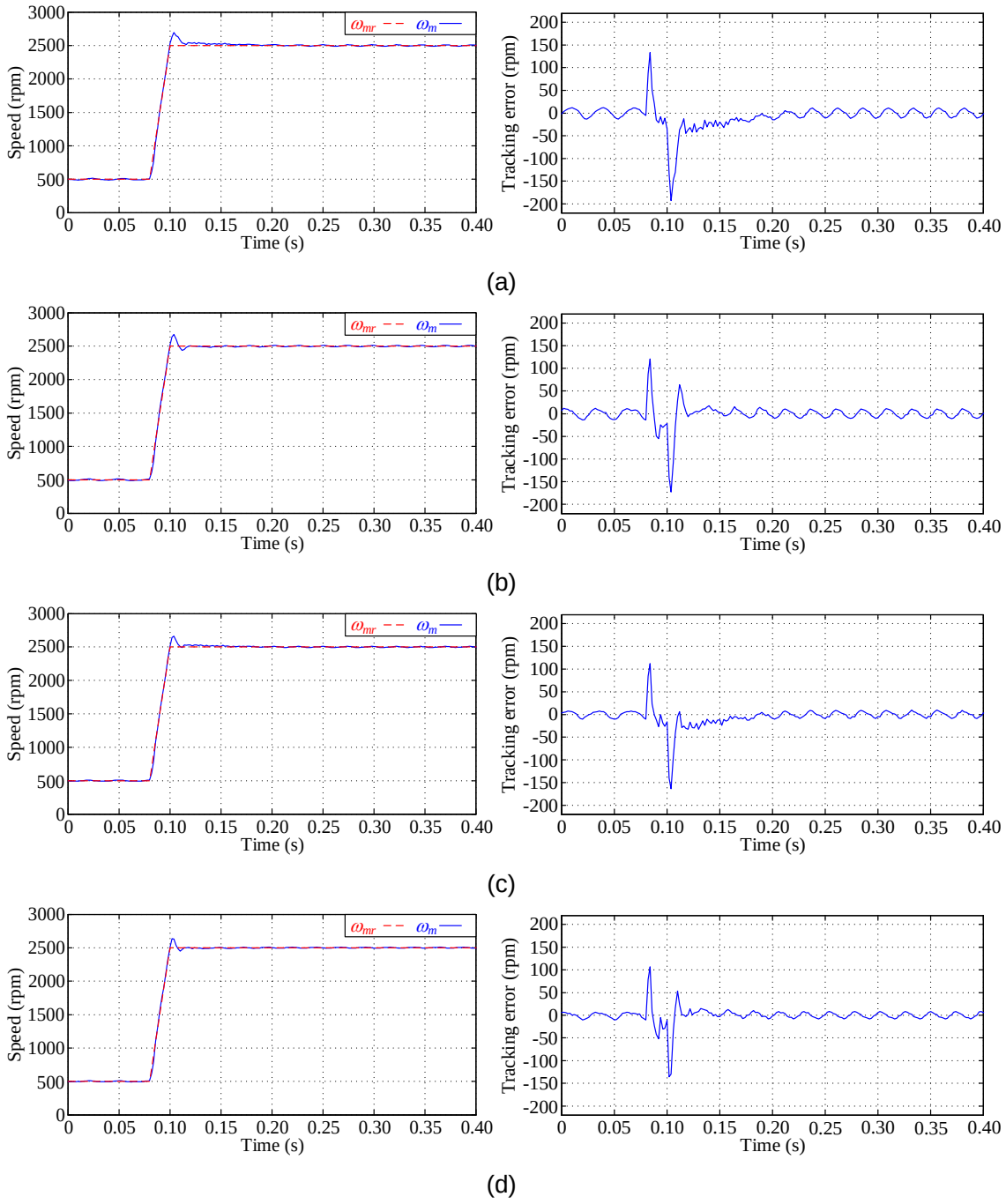

Figure 5.3 Rotor mechanical speed responses and corresponding tracking errors for the first test. (a) Standard STSM speed controller. (b) ESO-based standard STSM speed controller. (c) Modified STSM speed controller. (d) Type-2 composite speed controller.

Parameters of four tested rotor speed controllers are presented in Table 5.1. With respect to two identical linear PI current controllers, their parameters are selected based on the rated values of the stator resistance and the stator inductance of the adopted SPMSM presented in Table 2.1. The

proportional and integral gains of each PI stator current controller are set to 20.42 and 7379, respectively.

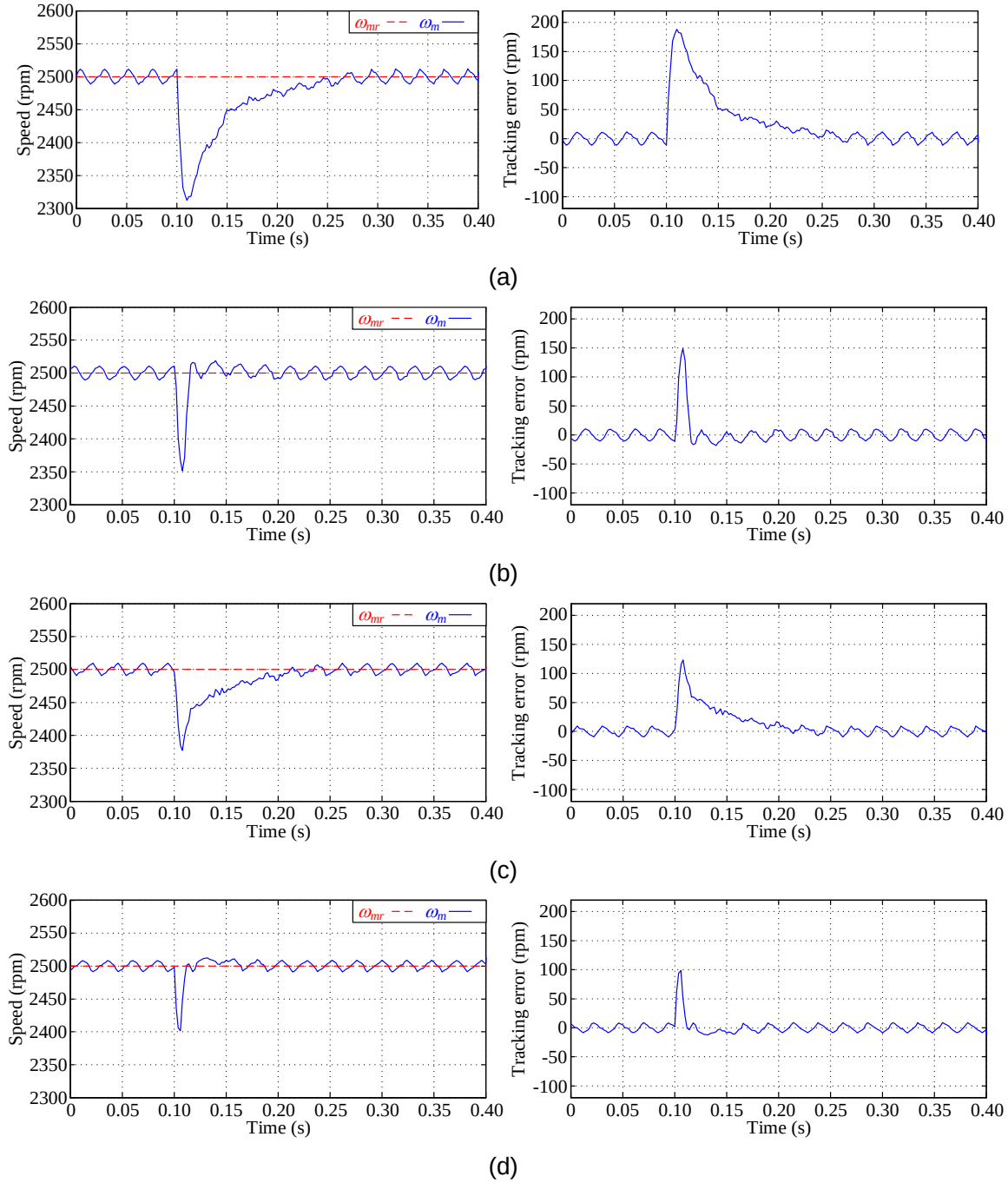

Figure 5.4 Rotor mechanical speed responses and corresponding tracking errors for the second test. (a) Standard STSM speed controller. (b) ESO-based standard STSM speed controller. (c) Modified STSM speed controller. (d) Type-2 composite speed controller.

Table 5.2 Dynamic performance of tested rotor speed controllers in the first test

Rotor speed controller	Overshoot (%)	Settling time (ms)
Standard STSM speed controller	7.732	80
ESO-based standard STSM speed controller	6.894	36
Modified STSM speed controller	6.541	52
Type-2 composite speed controller	5.446	32

Table 5.3 Dynamic performance of tested rotor speed controllers in the second test

Rotor speed controller	Maximum tracking error (rpm)	Settling time (ms)
Standard STSM speed controller	187.87	110
ESO-based standard STSM speed controller	148.47	14
Modified STSM speed controller	122.94	58
Type-2 composite speed controller	98.58	10

In the first test, the reference rotor mechanical speed increases from 500 rpm to 2500 rpm with the acceleration of 100 rpm/ms and the load torque provided by the load motor is set to 0 N·m. The rotor mechanical speed responses and corresponding tracking errors for four tested rotor speed controllers are illustrated in Figure 5.3. The dynamic performance of four tested rotor speed controllers are summarized in Table 5.2. Note that the tolerance band is chosen as $\pm$ 25 rpm, namely $\pm$ 1 % of 2500 rpm, for the settling time calculation. It can be seen that, in the frame of the FOC strategy, the standard STSM speed controller provides the highest overshoot and the longest settling time among four tested rotor speed controllers. With the integration of the ESO, the ESO-based standard STSM speed controller can achieve lower overshoot and the significant reduction of the settling time compared with the standard STSM speed controller. In comparison with the aforementioned two standard STA-based rotor speed controllers, the overshoot for the modified STSM speed controller is able to reduce by 15.403 % (29.79 rpm) and 5.120 % (8.82 rpm), respectively. Although the settling time of the modified STSM speed controller is shorter than that of the standard STSM speed controller, it is much longer than that of the ESO-based standard STSM speed controller. Regarding the type-2 composite speed controller, it can be observed that such a rotor speed controller accomplish the smallest overshoot and the shortest settling time.

In the second test, the reference rotor mechanical speed is kept at 2500 rpm and the load torque provided by the load motor steps from 0 to 0.6 N·m at 0.1 s. The rotor mechanical speed responses and corresponding tracking errors for four tested rotor speed controllers are illustrated in Figure 5.4.

The dynamic performance of four tested rotor speed controllers are summarized in Table 5.3 in which the criterion for the settling time calculation is the same as the first test. It can be observed that, among four tested rotor speed controllers, the use of the standard STSM speed controller results in the highest maximum tracking error and the longest settling time. In comparison with such a rotor speed controller, the ESO-based standard STSM speed controller can reduce both the maximum tracking error and the settling time. Compared with these two standard STA-based rotor speed controllers, the modified STSM speed controller can further reduce the maximum tracking error whose value is about 82.804 % of that resulted by the ESO-based standard STSM speed controller. Nevertheless, the settling time of the ESO-based standard STSM speed controller is still much shorter than that of the modified STSM speed controller. With respect to the type-2 composite speed controller, it can be seen that the maximum tracking error is 98.58 rpm, which is the lowest one among four tested rotor speed controllers. Furthermore, the settling time of the type-2 composite speed controller is also the shortest one among four tested rotor speed controllers.

5.4 Summary

In this chapter, a novel composite controller named as the type-2 composite controller is proposed for a single-input uncertain nonlinear system with relative degree one. The proposed composite controller comprises a modified STSM controller and a second-order ESO. The finite-time convergence of the sliding variable to the origin is guaranteed by the modified STSM controller and the second-order ESO is adopted to compensate the lumped disturbance in the sliding variable dynamics for the disturbance attenuation ability improvement. The rigorous stability analysis of the sliding variable dynamics with the type-2 composite controller is presented.

With respect to the 2L-VSI-fed SPMSM-VSD system, a novel robust FOC strategy is proposed, where a type-2 composite speed controller and two linear PI current controllers are used. Comparative experimental tests among the standard STSM speed controller, the ESO-based standard STSM speed controller, the modified STSM speed controller and the type-2 composite speed controller in the frame of the FOC strategy are performed on the experimental test bench described in Section 2.5. Corresponding experimental results demonstrate that the type-2 composite speed controller can achieve the minimum rotor speed transient variation and the fastest dynamic response.

References

[1] J. A. Moreno and M. Osorio, "A Lyapunov approach to second-order sliding mode controllers and observers," in *Proceedings of the 47th IEEE Conference on Decision and Control*, pp. 2856-2861, Dec. 2008.

[2] J. A. Moreno, "On strict Lyapunov functions for some non-homogeneous super-twisting algorithms," *Journal of the Franklin Institute*, vol. 351, no. 4, pp. 1902-1919, Apr. 2014.

[3] Y. Kali, J. Rodas, M. Saad, R. Gregor, K. Benjelloun, J. Doval-Gandoy, and G. Goodwin, "Speed control of a five-phase induction motor drive using modified super-twisting algorithm," in *Proceedings of the International Symposium on Power Electronics, Electrical Drives, Automation and Motion*, pp. 938-943, Jun. 2018 .

[4] F. Muñoz, M. Bonilla, I. González-Hernández, S. Salazar, and R. Lozano, "Super-twisting vs modified super-twisting algorithm for altitude control of an unmanned aircraft system," in *Proceedings of the 12th International Conference on Electrical Engineering, Computing Science and Automatic Control*, pp. 1-6, Oct. 2015.

[5] S. Li and Z. Liu, "Adaptive speed control for permanent-magnet synchronous motor system with variations of load inertia," *IEEE Transactions on Industrial Electronics*, vol. 56, no. 8, pp. 3050-3059, Aug. 2009.

[6] B. Du, S. Wu, S. Han, and S. Cui, "Application of linear active disturbance rejection controller for sensorless control of internal permanent-magnet synchronous motor," *IEEE Transactions on Industrial Electronics*, vol. 63, no. 5, pp. 3019-3027, May 2016.

[7] J. Yao, Z. Jiao, and D. Ma, "Adaptive robust control of DC motors with extended state observer," *IEEE Transactions on Industrial Electronics*, vol. 61, no. 7, pp. 3630-3637, Jul. 2014.

[8] J. Liu, Y. Yin, W. Luo, S. Vazquez, L. G. Franquelo, and L. Wu, "Sliding mode control of a three-phase AC/DC voltage source converter under unknown load conditions: industry applications," *IEEE Transactions on Systems, Man, and Cybernetics: Systems*, vol. 48, no. 10, pp. 1771-1780, Oct. 2018.

[9] H. Liu and S. Li, "Speed control for PMSM servo system using predictive functional control and extended state observer," *IEEE Transactions on Industrial Electronics*, vol. 59, no. 2, pp. 1171-1183, Feb. 2012.

[10] M. Yang, X. Liang, J. Long, and D. Xu, "Flux immunity robust predictive current control with incremental model and extended state observer for PMSM drive," *IEEE Transactions on Power Electronics*, vol. 32, no. 12, pp. 9267-9279, Dec. 2017.

[11] F. Alonge, M. Cirrincione, F. D'Ippoloti, M. Pucci, and A. Sferlazza, "Robust active disturbance rejection control of induction motor systems based on additional sliding-mode component," *IEEE Transactions on Industrial Electronics*, vol. 64, no. 7, pp. 5608-5621, Jul. 2017.

[12] F. Alonge, M. Cirrincione, F. D'Ippoloti, M. Pucci, and A. Sferlazza, "Active disturbance rejection control of linear induction motor," *IEEE Transactions on Industry Applications*, vol. 53, no. 5, pp. 4460-4471, Sep./Oct. 2017.

[13] X. Shao, N. Liu, J. Liu, and H. Wang, "Model-assisted extended state observer and dynamic surface control-based trajectory tracking for quadrotors via output-feedback mechanism," *International Journal of Robust Nonlinear Control*, vol. 28, no. 6, pp. 2404-2423, Apr. 2018.

[14] X. Shao, J. Liu, H. Gao, C. Shen, and H. Wang, "Robust dynamic surface trajectory tracking control for a quadrotor UAV via extended state observer," *International Journal of Robust Nonlinear Control*, vol. 28, no. 7, pp. 2700-2719, May 2018.

[15] J. Yao, Z. Jiao, and D. Ma, "Extended-state-observer-based output feedback nonlinear robust control of hydraulic systems with backstepping," *IEEE Transactions on Industrial Electronics*, vol. 61, no. 11, pp. 6285-6293, Nov. 2014.

[16] C. Luo, J. Yao, and J. Gu, "Extended-state-observer-based output feedback adaptive control of hydraulic system with continuous friction compensation," *Journal of the Franklin Institute*, vol. 356, no. 15, pp. 8414-8437, Oct. 2019.

[17] L. Zhou, L. Cheng, J. She, and Z. Zhang, "Generalized extended state observer-based repetitive control for systems with mismatched disturbances," *International Journal of Robust Nonlinear Control*, vol. 29, no. 11, pp. 3777-3792, Jul. 2019.

[18] L. Zhou, F. Jiang, J. She, and Z. Zhang, "Generalized-extended-state-observer-based repetitive control for DC motor servo system with mismatched disturbances," *International Journal of Control, Automation, and Systems*, vol. 18, no. 9, pp. 1936-1945, Sep. 2020.

[19] S. Li, K. Zong, and H. Liu, "A composite speed controller based on a second-order model of permanent synchronous motor system," *Transactions of the Institute of Measurement and Control*, vol. 33, no. 5, pp. 522-541, Jul. 2011.

[20] J. Wang, S. Li, J. Yang, B. Wu, and Q. Li, "Extended state observer-based sliding mode control for PWM-based DC–DC buck power converter systems with mismatched disturbances," *IET Control Theory and Applications*, vol. 9, no. 4, pp. 579-586, Feb. 2015.

[21] J. Liu, S. Vazquez, L. Wu, A. Marquez, H. Gao, and L. G. Franquelo, "Extended state observer-based sliding-mode control for three-phase power converters," *IEEE Transactions on Industrial Electronics*, vol. 64, no. 1, pp. 22-31, Jan. 2017.

[22] C. Ren, X. Li, X. Yang, and S. Ma, “Extended state observer-based sliding mode control of an omnidirectional mobile robot with friction compensation,” *IEEE Transactions on Industrial Electronics*, vol. 66, no. 12, pp. 9480-9489, Dec. 2019.

[23] E.F. Beckenbach and R. Bellman, *Inequalities*. Berlin, Germany: Springer-Verlag, 1961.

[24] H. K. Khalil, *Nonlinear Systems*, 3rd ed. Englewood Cliffs, NJ, USA: Prentice-Hall, 2001.

6

TYPE-3 COMPOSITE CONTROLLER: DESIGN AND APPLICATION

6.1 Introduction

Apart from the SOSM algorithm, the quasi-sliding-mode algorithm is another popular modified sliding-mode algorithm to alleviate the chattering [1]. In such an algorithm, the discontinuous sign function used in the FOSM algorithm is replaced by a continuous function, including the saturation function, the sigmoid function and the hyperbolic tangent function. Therefore, the quasi-sliding-mode algorithm is a continuous sliding-mode algorithm. Theoretically, however, the quasi-sliding-mode controller, which is based on the quasi-sliding-mode algorithm, can only let the sliding variable reach a small vicinity of the origin, namely the boundary layer, in a finite time, resulting in the degradation of the tracking control performance [1].

To improve the tracking control performance, the complementary sliding-mode (CSM) algorithm has been proposed [2]. In this sliding-mode algorithm, the saturation function is adopted and two different sliding variables, i.e., the generalized sliding variable and the complementary sliding variable, both of which are based on the control objective, are designed. In theory, the tracking error of the classic CSM controller, which is based on the CSM algorithm, can be reduced by half compared with that of the quasi-sliding-mode controller [2]. Nevertheless, like standard and modified STSM controllers, the selection of the gains of the classic CSM controller has to face a trade-off problem between the tracking performance and the disturbance attenuation since the CSM algorithm is dependent on the feedback regulation mechanism. As has been stated in Section 1.2, the development of a composite controller, which is based on the CSM algorithm and the DO, is an

effective method to deal with such an issue.

ANN-DOs are the most popular DOs to construct composite controllers for the classic CSM controller [3]-[9]. Up to now, the composite controller combining the CSM algorithm with an ANN-DO, or as often called the ICSM controller, has found some applications [3]-[9]. In [3] and [4], the ICSM controller using the Takagi-Sugeno-Kang-type fuzzy neural network has been proposed for the speed control of the post-fault six-phase PMSM drive system and the synchronous control of the dual linear motor servo system, respectively. In [5], a recurrent HNN-based ICSM position controller has been proposed for the thrust active magnetic bearing system. In [6], regarding the linear ultrasonic motor system, an ICSM position controller using the recurrent wavelet neural network has been proposed. In [7], an ICSM controller using the recurrent neural fuzzy inference network has been applied to the position control of the one-link robotic manipulator and the DC motor drive system. Regarding the three-phase PMSM drive system, a RBFNN-based ICSM (RBFNN-ICSM) controller and an ENN-ICSM controller have been proposed for the position control in [8] and [9], respectively. Moreover, it has been experimentally demonstrated that the tracking performance of the latter is better than that of the former [9].

In all above-mentioned ICSM controllers, the saturation function used in the classic CSM controller is replaced by various types of ANN-DOs such that the asymptotic stabilization of the tracking error dynamics can be achieved [3]-[9]. Since the ANN is able to approximate any function of interest to any degree of accuracy as long as enough hidden neurons are used [10], each ANN-DO used in an ICSM controller is usually equipped with quite a few hidden neurons and each of them uses a complex activation function. In order to connect neurons in different layers effectively, many connective weights, each of which is updated online by a unique learning law, exist in each adopted ANN-DO. Moreover, since there exists a minimum approximation error in an ANN-DO in theory, an error compensator has to be integrated into the ICSM controller. These significantly increase the computational burden of a hardware controller to implement any one of ICSM controllers.

As mentioned in Section 3.1, besides the model-free DO, the extended DO, which is a type of model-based DO, is another popular choice to construct the composite controller. With respect to the three-phase PMSM drive system, since the classic position, speed or current dynamics of the PMSM is available and not complex, the extended DOs based on these dynamics have simpler structure than the ANN-DOs used in the composite position, speed or current controllers for the PMSM drive system. However, to the best of the author's knowledge, no published scientific literature investigates the composite controller combining the CSM algorithm with an extended DO;

let alone the application of this controller to the PMSM-VSD system.

In this chapter, the type-3 composite controller, which is composed of a sign function-based CSM controller and a STSMO, is proposed for a single-input uncertain nonlinear system with relative degree one. In this composite controller, the sign function-based CSM controller is used to stabilize the output tracking error dynamics asymptotically and the lumped disturbance in the tracking error dynamics is compensated by the STSMO. The rigorous stability analysis of the output tracking error dynamics with the type-3 composite controller is presented.

After the rigorous theoretical analysis of the proposed type-3 composite controller, such a controller applies to the construction of a novel robust FOC strategy for the 2L-VSI-fed SPMSM-VSD system. In this FOC strategy, the proposed type-3 composite controller is used as the rotor speed controller in the speed control loop and two linear PI controllers serve as two stator current controllers in the current control loop. To validate the effectiveness and the superiority of the type-3 composite speed controller, based on the experimental test bench described in Section 2.5, comparative experimental tests among the classic CSM speed controller, three selected ENN-ICSM speed controllers and the type-3 composite speed controller in the frame of the FOC strategy are performed. Finally, the experimental results are presented and analyzed.

6.2 Type-3 Composite Controller Design

6.2.1 Problem Statement

Considering the single-input uncertain nonlinear system with relative degree one presented in (3.1), the output tracking error e_y is defined as

$$e_y = y_r - y \tag{6.1}$$

Based on (3.1), (3.2) and (6.1), the e_x-dynamics can be derived as

$$\begin{aligned} \dot{e}_y &= \dot{y}_r - \dot{x} = \dot{y}_r - \left(a_n + \Delta a\left(x,t\right)\right) - \left(b_n + \Delta b\left(x,t\right)\right)\mu \\ &= -b_n\mu + \underbrace{\dot{y}_r - a_n - \Delta a\left(x,t\right) - \Delta b\left(x,t\right)\mu}_{\rho_e(x,t)} \\ &= -b_n\mu + \rho_e\left(x,t\right) \end{aligned} \tag{6.2}$$

where $\rho_e(x,t)$ denotes the lumped disturbance in the e_x-dynamics.

From (4.3) and (6.2), it can be seen that ρ_e is equal to ρ_s.

Assumption 6.1. ρ_e and its time derivative $\dot{\rho}_e$ are bounded as $|\rho_e| \leq L_1^e$ and $|\dot{\rho}_e| \leq L_2^e$, respectively, for positive constants L_1^e and L_2^e.

The control objective is to let e_x converge to the origin asymptotically.

6.2.2 STSMO Design

As an extended DO, the STSMO design is dependent on the extended dynamics where the lumped disturbance is selected as an augmented state variable to be estimated. As mentioned in Section 5.2.1, the estimation of ρ_s is equivalent to the estimation of ρ_x. Considering (5.1) and the equivalence of ρ_e and ρ_s, the following expression holds

$$\rho_e = \dot{y}_r - \rho_x \tag{6.3}$$

Based on the above expression and Assumption 4.1, it can be said that the estimation of ρ_e is equivalent to the estimation of ρ_x. Therefore, the STSMO designed as (3.11) can be directly used in the type-3 composite controller.

6.2.3 Controller Design

According to [2], for the relative degree one system, the generalized sliding variable s_g and the complementary sliding variable s_c are designed as (6.4) and (6.5), respectively.

$$s_g = e_y + \lambda_y \int_0^t e_y d\tau \tag{6.4}$$

$$s_c = e_y - \lambda_y \int_0^t e_y d\tau \tag{6.5}$$

where λ_y is a positive constant gain.

The time derivatives of s_g and s_c along the trajectory of the e_y-dynamics can be calculated as (6.6) and (6.7), respectively.

$$\dot{s}_g = \dot{e}_y + \lambda_y e_y = -b_n \mu + \rho_e + \lambda_y e_y \tag{6.6}$$

$$\dot{s}_c = \dot{e}_y - \lambda_y e_y = -b_n \mu + \rho_e - \lambda_y e_y \tag{6.7}$$

According to (6.6) and (6.7), the following expression can be derived.

$$\dot{s}_c = \dot{s}_g - \lambda_y \left(s_g + s_c \right) \tag{6.8}$$

To achieve the control objective, the type-3 composite control law μ_{c3} is designed as

$$\mu_{c3} = \frac{1}{b_n}\left(\mu_{CSM} + \dot{y}_r - \hat{\rho}_{ST}\right) \tag{6.9}$$

where μ_{CSM} is the sign function-based CSM algorithm for the asymptotic convergence of e_y to the origin, which is expressed as (6.10), and $\hat{\rho}_{ST}$ is the estimated lumped disturbance from the adopted STSMO for the compensation of ρ_x.

$$\mu_{CSM} = \lambda_y e_y + \lambda_y s_g + k_y \mathrm{sgn}\left(s_g + s_c\right) \tag{6.10}$$

where k_y is a positive constant gain.

Substituting (6.9) into (6.2), the closed-loop e_y-dynamics with the type-3 composite control law is expressed as

$$\begin{aligned} \dot{e}_y &= -\lambda_y e_y - \lambda_y s_g - k_y \mathrm{sgn}\left(s_g + s_c\right) - \underbrace{\left(\rho_x - \hat{\rho}_{ST}\right)}_{e_{ST}} \\ &= -\lambda_y e_y - \lambda_y s_g - k_y \mathrm{sgn}\left(s_g + s_c\right) - e_{ST} \end{aligned} \tag{6.11}$$

where e_{ST} is the lumped disturbance estimation error of the STSMO.

Considering Assumption 3.3, e_{ST} is bounded as $|e_{ST}| \leq L_6^x$ for a positive constant L_6^x. The following Theorem can be used to select k_y for accomplishing the control objective.

Theorem 6.1. Considering the system (6.11) and $|e_{ST}| \leq L_6^x$, for the positive constant λ_y, if k_y is selected as (6.12), e_y will converge to the origin asymptotically.

$$k_y \geq L_6^x \tag{6.12}$$

Proof. The Lyapunov candidate function V_{c3} is selected as

$$V_{c3} = \frac{1}{2}\left(s_g^2 + s_c^2\right) \tag{6.13}$$

Based on (6.8), (6.9), (6.11), (6.13), $\dot{V}_{c3}$ can be calculated as

$$\begin{aligned} \dot{V}_{c3} &= s_g \dot{s}_g + s_c\left[\dot{s}_g - \lambda_y\left(s_g + s_c\right)\right] = \left(s_g + s_c\right)\left(\dot{s}_g - \lambda_y s_c\right) \\ &= \left(s_g + s_c\right)\left(\dot{e}_y + \lambda_y e_y - \lambda_y s_c\right) \\ &= \left(s_g + s_c\right)\left(-\lambda_y e_y - \lambda_y s_g - k_y \mathrm{sgn}\left(s_g + s_c\right) - e_{ST} + \lambda_y e_y - \lambda_y s_c\right) \\ &= -\lambda_y\left(s_g + s_c\right)^2 - \left[k_y \mathrm{sgn}\left(s_g + s_c\right) + e_{ST}\right]\left(s_g + s_c\right) \\ &= -\lambda_y\left(s_g + s_c\right)^2 - k_y\left|s_g + s_c\right| - e_{ST}\left(s_g + s_c\right) \end{aligned} \tag{6.14}$$

Combining (6.14) and (6.12), the following inequality can be obtained.

$$\begin{aligned}\dot{V}_{c3} &\le -\lambda_y\left(s_g+s_c\right)^2 - k_y\left|s_g+s_c\right| + \left|e_{ST}\right|\left|s_g+s_c\right| \\ &\le -\lambda_y\left(s_g+s_c\right)^2 - \left(k_y - L_6^x\right)\left|s_g+s_c\right| \\ &\le -\lambda_y\left(s_g+s_c\right)^2 \le 0\end{aligned} \tag{6.15}$$

From (6.15), it can be concluded that $\dot{V}_{c3}$ is negative semidefinite. Therefore, the following inequality holds.

$$V_{c3}\left(s_g(t), s_c(t)\right) \le V_{c3}\left(s_g(0), s_c(0)\right) \tag{6.16}$$

According to (6.16), $s_g(t)$ and $s_c(t)$ are bounded. Based on (6.15) and (6.16), the following function is defined.

$$\Omega_{CSM}(t) = -\lambda_y\left(s_g(t)+s_c(t)\right)^2 \le -\dot{V}_{c3}\left(s_g(t), s_c(t)\right) \tag{6.17}$$

Since $V_{c3}(s_g(0), s_c(0))$ is bounded and $V_{c3}(s_g(t), s_c(t))$ is a non-increasing bounded function, the following inequality can be derived.

$$\lim_{t\to\infty}\int_0^t \Omega_{CSM}(\tau)\,d\tau < \infty \tag{6.18}$$

Since $\lim_{t\to\infty}\int_0^t \Omega_{CSM}(\tau)d\tau$ exists and $\Omega_{CSM}(t)$ is a uniformly continuous function, according to Barbălat's Lemma [11], $\lim_{t\to\infty}\Omega_{CSM}(t) = 0$ holds. It means that $\lim_{t\to\infty}(s_g(t)+s_c(t)) = 0$ holds. Thus, e_y will converge to the origin asymptotically. The proof is completed. ■

Remark 6.1: In the type-3 composite control law, the use of the sign function is to guarantee the asymptotic convergence of e_y to the origin in theory. In order to avoid severe chattering in practice, the value selected for k_y should be small.

6.3 Application

In this section, the type-3 composite speed controller, which is designed using the practical speed dynamics of the SPMSM presented in (2.54), is applied to the construction of a novel robust FOC strategy for the 2L-VSI-fed SPMSM-VSD system. In such a FOC strategy, two linear PI current controllers are used as stator current controllers. Moreover, i_{dsr} is set to 0 and i_{qsr} is generated by the type-3 composite speed controller. Besides the type-3 composite speed controller, the designs and analyses of the classic CSM speed controller and the ENN-ICSM speed controller using the ENN-DO proposed in [9] are also presented. Results of the comparative experimental tests among the classic CSM speed controller, three selected ENN-ICSM speed controllers and the type-3 composite speed controller in the frame of the FOC strategy for the 2L-VSI-fed SPMSM-VSD

system are presented to demonstrate the superiority of the type-3 composite speed controller.

6.3.1 Classic CSM Speed Controller Design

Considering the speed tracking error $e_{\omega 2}$ expressed as (5.28), the generalized sliding variable $s_{\omega g}$ and the complementary sliding variable $s_{\omega c}$ for the classic CSM speed controller are designed as (6.19) and (6.20), respectively.

$$s_{\omega g} = e_{\omega 2} + \lambda_{\omega}^{c3} \int_0^t e_{\omega 2} d\tau \tag{6.19}$$

$$s_{\omega c} = e_{\omega 2} - \lambda_{\omega}^{c3} \int_0^t e_{\omega 2} d\tau \tag{6.20}$$

where λ_{ω}^{c3} is a positive constant gain.

Based on the $e_{\omega 2}$-dynamics expressed as (5.29), the classic CSM speed control law i_{qsrc}^{c3} is designed as

$$i_{qsrc}^{c3} = \frac{1}{b_{\omega n2}} \left(\mu_{eq} + \mu_{sat} \right) \tag{6.21}$$

where μ_{eq} is the equivalent control term expressed as (6.22), and μ_{sat} is the disturbance attenuation term expressed as (6.23).

$$\mu_{eq} = \dot{\omega}_{mr} + a_{\omega n2} \omega_m + \lambda_{\omega}^{c3} e_{\omega 2} + \lambda_{\omega}^{c3} s_{\omega g} \tag{6.22}$$

$$\mu_{sat} = k_{\omega 1}^{c3} \mathrm{sat} \left(s_{\omega g} + s_{\omega c} \right) \tag{6.23}$$

where $k_{\omega 1}^{c3}$ is the positive constant gain.

Substituting (6.21) into (5.29), the closed-loop $e_{\omega 2}$-dynamics with the classic CSM speed control law is expressed as

$$\dot{e}_{\omega 2} = -\lambda_{\omega}^{c3} e_{\omega 2} - \lambda_{\omega}^{c3} s_{\omega g} - k_{\omega 1}^{c3} \mathrm{sat} \left(s_{\omega g} + s_{\omega c} \right) - \rho_{\omega 2} \tag{6.24}$$

The following Theorem can be used to select $k_{\omega 1}^{c3}$.

Theorem 6.2 [3]. Considering the system (6.24) and Assumption 5.1, for the positive constant λ_{ω}^{c3}, if $k_{\omega 1}^{c3}$ is selected as (6.25), $(s_{\omega g} + s_{\omega c})$ will converge to the boundary layer $\left| s_{\omega g} + s_{\omega c} \right| \leq \Pi$ in a finite time.

$$k_{\omega 1}^{c3} \geq L_{\omega 1}^{c2} \tag{6.25}$$

Remark 6.2. Since $s_{\omega g} + s_{\omega c} = 2e_{\omega 2}$, $e_{\omega 2}$ will be bounded as $|e_{\omega 2}| \leq \Pi/2$ in a finite time with

the classic CSM speed control law. However, the classic CSM speed controller cannot guarantee the convergence of $e_{\omega 2}$ to the origin in theory [3].

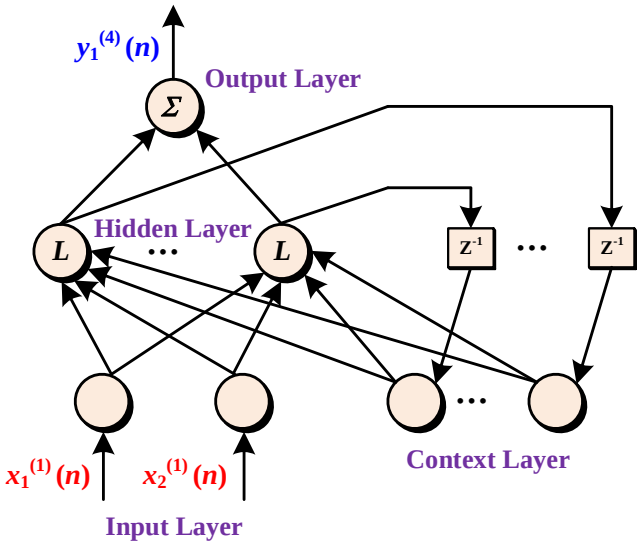

Figure 6.1 Block diagram of the ENN-DO used in the ENN-ICSM speed controller.

6.3.2 ENN-ICSM Speed Controller Design

In [9], based on the three-phase linear PMSM servo system, it has been experimentally demonstrated that the tracking performance of the ENN-ICSM controller is better than that of the RBFNN-ICSM controller. Therefore, the ENN-ICSM speed controller is selected as a representative of the ICSM speed controller to be compared in this chapter. Since the ENN-ICSM controller proposed in [9] is used as the position controller rather the speed controller, the design of the ENN-ICSM speed controller using the ENN-DO proposed in [9] is presented in this subsection.

The ENN-DO proposed in [9] is illustrated in Figure 6.1. There are two input neurons, nine hidden neurons, nine context neurons and one output neuron in such an ANN-DO. The signal propagation and the activation function of each layer are described as follows.

Input Layer: In this layer, two input signals are the normalized speed tracking error and its time derivative. Thus, the output signals of two input neurons can be expressed as

$$y_1^{(1)}(n) = x_1^{(1)}(n) = \frac{e_{\omega 2}(n)}{\omega_{rate}} \quad y_2^{(1)}(n) = x_2^{(1)}(n) = \frac{\dot{e}_{\omega 2}(n)}{\omega_{rate}} \tag{6.26}$$

where $e_{\omega 2}(n)$ is the speed tracking error at the nth instant and ω_{rate} is the rated rotor mechanical speed of the adopted SPMSM.

Hidden Layer: In this layer, regarding the *i*th hidden neuron ($i = 1, 2,\ldots, 9$), the signal propagation can be described as

$$x_i^{(2)}(n) = \Phi_{ei1}^{(1)}(n) y_1^{(1)}(n) + \Phi_{ei2}^{(1)}(n) y_2^{(1)}(n) + \sum_{i=1}^{9} y_i^{(3)}(n), \quad i = 1,2,...,9 \tag{6.27}$$

$$y_i^{(2)}(n) = L(x_i^{(2)}(n)) \tag{6.28}$$

where $\Phi_{ei1}^{(1)}(n)$ and $\Phi_{ei2}^{(1)}(n)$ denote two connective weights between the *i*th hidden neuron and two input neurons at the *n*th instant.

Context Layer: In this layer, regarding the *i*th context neuron ($i = 1, 2,\ldots, 9$), the signal propagation can be described as

$$y_i^{(3)}(n) = x_i^{(3)}(n) = y_i^{(2)}(n-1), \quad i = 1,2,...,9 \tag{6.29}$$

Output Layer: In this layer, the output signal is the estimated lumped disturbance in the ω_m-dynamics, which can be calculated as

$$\hat{\rho}_{ENN} = y_1^{(4)}(n) = \sum_{i=1}^{9} \Phi_{ei}^{(2)}(n) y_i^{(2)}(n) \tag{6.30}$$

where $\hat{\rho}_{ENN}$ is the estimated lumped disturbance from the ENN-DO, $\Phi_{ei}^{(2)}(n)$ denotes the connective weight between the output neuron and the *i*th hidden neuron at the *n*th instant.

Based on the universal approximation property of the ANN, like the HNN-DO presented in Section 4.2.2, there is an optimal estimated lumped disturbance $\hat{\rho}_{ENN}^{*}$ for the ENN-DO such that

$$\rho_{\omega 2} = \hat{\rho}_{ENN}^{*} + \varepsilon_{ENN} = \boldsymbol{\Phi}_e^{(2)*T}(n) \boldsymbol{y}^{(2)}(n) + \varepsilon_{ENN} \tag{6.31}$$

where $\boldsymbol{\Phi}_e^{(2)*}(n) = [\Phi_{e1}^{(2)*}(n), \Phi_{e2}^{(2)*}(n),\ldots, \Phi_{e9}^{(2)*}(n)]^T$ and $\boldsymbol{y}^{(2)}(n) = [y_1^{(2)}(n), y_2^{(2)}(n),\ldots, y_9^{(2)}(n)]^T$ are the optimal output weight vector and the output signal vector of the hidden layer of the ENN-DO, respectively, ε_{ENN} is the minimum approximation error of the ENN-DO.

Owing to the existence of ε_{ENN}, the error compensator has to be integrated into the ENN-ICSM speed controller. Like the error compensator used in the type-1 composite speed controller, the error compensator used in the ENN-ICSM speed controller is updated online and the relevant learning law is derived by the Lyapunov synthesis approach.

Assumption 6.2. $\Phi_{ei}^{(2)*}(n)$ and ε_{HNN} are constant in each sampling period.

Remark 6.3. In the ENN-DO, there are three weight vectors, i.e., two input weight vectors $\boldsymbol{\Phi}_{e1}^{(1)}(n) = [\Phi_{e11}^{(1)}(n), \Phi_{e21}^{(1)}(n),\ldots, \Phi_{e91}^{(1)}(n)]^T$ and $\boldsymbol{\Phi}_{e2}^{(1)}(n) = [\Phi_{e12}^{(1)}(n), \Phi_{e22}^{(1)}(n),\ldots, \Phi_{e92}^{(1)}(n)]^T$, and the output weight vector $\boldsymbol{\Phi}_e^{(2)}(n) = [\Phi_{e1}^{(2)}(n), \Phi_{e2}^{(2)}(n),\ldots, \Phi_{e9}^{(2)}(n)]^T$ need to be updated online. To maintain the stability of the tracking control system, the learning law for $\Phi_{ei}^{(2)}(n)$ is derived by the

Lyapunov synthesis approach, while the learning laws for $\Phi_{ei1}^{(1)}(n)$ and $\Phi_{ei2}^{(1)}(n)$ are derived by the BP algorithm.

Based on the $e_{\omega 2}$-dynamics expressed as (5.29), selecting $s_{\omega g}$ and $s_{\omega c}$ as the generalized and complementary sliding variables, respectively, the ENN-ICSM speed control law i_{qsre}^{c3} can be designed as

$$i_{qsre}^{c3} = \frac{1}{b_{\omega n2}}\left(\mu_{eq} - y_{e\omega} - y_{c\omega 2}\right) \tag{6.32}$$

where $y_{e\omega}$ and $y_{c\omega 2}$ are the output signal of the adopted ENN-DO for the compensation of $\rho_{\omega 2}$ and the output signal of the error compensator for the compensation of the approximation error of the adopted ENN-DO, respectively, which are expressed as

$$y_{e\omega} = \boldsymbol{\Phi}_e^{(2)T}\boldsymbol{y}^{(2)}(n) \tag{6.33}$$

$$y_{c\omega 2} = \varepsilon_{c\omega 2} \tag{6.34}$$

where $\varepsilon_{c\omega 2}$ is the estimated approximation error of the adopted ENN-DO.

Substituting (6.32) into (5.29), the closed-loop $e_{\omega 2}$-dynamics with the ENN-ICSM speed control law is expressed as

$$\dot{e}_{\omega 2} = -\lambda_{\omega}^{c3}e_{\omega 2} - \lambda_{\omega}^{c3}s_{\omega g} + \boldsymbol{\Phi}_e^{(2)T}\boldsymbol{y}^{(2)}(n) + \varepsilon_{c\omega 2} - \rho_{\omega 2} \tag{6.35}$$

The following Theorem can be used to derive the learning laws for $\varepsilon_{c\omega 2}$ and $\boldsymbol{\Phi}_e^{(2)}$.

Theorem 6.3. Considering the system (6.35), for the positive constant λ_{ω}^{c3}, if the learning laws for $\varepsilon_{c\omega 1}$ and $\Phi_{ei}^{(2)}$ are designed as (6.36) and (6.37), respectively, $(s_{\omega g} + s_{\omega c})$ will converge to the origin asymptotically.

$$\dot{\varepsilon}_{c\omega 2} = -\eta_{c\omega\varepsilon}^{c3}\left(s_{\omega g} + s_{\omega c}\right) \tag{6.36}$$

$$\dot{\Phi}_{ei}^{(2)} = -\eta_{c\omega 1}^{c3}\left(s_{\omega g} + s_{\omega c}\right)y_i^{(2)} \tag{6.37}$$

where $\eta_{c\omega\varepsilon}^{c3}$ and $\eta_{c\omega 1}^{c3}$ are positive learning rates.

Proof. The Lyapunov candidate function V_{ENN} is selected as

$$V_{ENN} = \frac{1}{2}\left(s_{\omega g}^2 + s_{\omega c}^2\right) + \frac{1}{2\eta_{c\omega\varepsilon}^{c3}}\tilde{\varepsilon}_{ENN}^2 + \frac{1}{2\eta_{c\omega 1}^{c3}}\tilde{\boldsymbol{\Phi}}_e^{(2)T}\tilde{\boldsymbol{\Phi}}_e^{(2)} \tag{6.38}$$

where $\tilde{\boldsymbol{\Phi}}_e^{(2)} = \boldsymbol{\Phi}_e^{(2)*} - \boldsymbol{\Phi}_e^{(2)} = [\tilde{\Phi}_{e1}^{(2)}, \tilde{\Phi}_{e2}^{(2)}, \ldots, \tilde{\Phi}_{e9}^{(2)}]^T$ and $\tilde{\varepsilon}_{ENN} = \varepsilon_{ENN} - \varepsilon_{c\omega 2}$.

Based on (6.19), (6.20), (6.38), $\dot{V}_{ENN}$ can be calculated as

$$\begin{aligned}\dot{V}_{ENN} &= s_{\omega g}\dot{s}_{\omega g} + s_{\omega c}\left[\dot{s}_{\omega g} - \lambda_{\omega}^{c3}\left(s_{\omega g} + s_{\omega c}\right)\right] \\ &= \left(s_{\omega g} + s_{\omega c}\right)\left(\dot{s}_{\omega g} - \lambda_{\omega}^{c3} s_{\omega c}\right) \\ &= \left(s_{\omega g} + s_{\omega c}\right)\left(\dot{e}_{\omega 2} + \lambda_{\omega}^{c3} e_{\omega 2} - \lambda_{\omega}^{c3} s_{\omega c}\right)\end{aligned} \tag{6.39}$$

Based on (6.31), (6.35), (6.36) and (6.37), $\dot{V}_{ENN}$ can be rewritten as

$$\begin{aligned}\dot{V}_{ENN} &= \left(s_{\omega g} + s_{\omega c}\right)\left(-\lambda_{\omega}^{c3} e_{\omega 2} - \lambda_{\omega}^{c3} s_{\omega g} + \boldsymbol{\Phi}_e^{(2)T}\boldsymbol{y}^{(2)}(n) + \varepsilon_{c\omega 2} - \rho_{\omega 2} + \lambda_{\omega}^{c3} e_{\omega 2} - \lambda_{\omega}^{c3} s_{\omega c}\right) \\ &\quad - \frac{1}{\eta_{c\omega\varepsilon}^{c3}}\tilde{\varepsilon}_{ENN}\dot{\varepsilon}_{c\omega 2} - \frac{1}{\eta_{c\omega 1}^{c3}}\tilde{\boldsymbol{\Phi}}_e^{(2)T}\dot{\boldsymbol{\Phi}}_e^{(2)} \\ &= \left(s_{\omega g} + s_{\omega c}\right)\left(\boldsymbol{\Phi}_e^{(2)T}\boldsymbol{y}^{(2)}(n) + \varepsilon_{c\omega 2} - \boldsymbol{\Phi}_e^{(2)*T}(n)\boldsymbol{y}^{(2)}(n) - \varepsilon_{ENN} - \lambda_{\omega}^{c3} s_{\omega g} - \lambda_{\omega}^{c3} s_{\omega c}\right) \\ &\quad - \frac{1}{\eta_{c\omega\varepsilon}^{c3}}\tilde{\varepsilon}_{ENN}\dot{\varepsilon}_{c\omega 2} - \frac{1}{\eta_{c\omega 1}^{c3}}\tilde{\boldsymbol{\Phi}}_e^{(2)T}\dot{\boldsymbol{\Phi}}_e^{(2)} \\ &= -\lambda_{\omega}^{c3}\left(s_{\omega g} + s_{\omega c}\right)^2 - \left(s_{\omega g} + s_{\omega c}\right)\left(\tilde{\boldsymbol{\Phi}}_e^{(2)T}\boldsymbol{y}^{(2)}(n) - \tilde{\varepsilon}_{ENN}\right) - \frac{1}{\eta_{c\omega\varepsilon}^{c3}}\tilde{\varepsilon}_{ENN}\dot{\varepsilon}_{c\omega 2} - \frac{1}{\eta_{c\omega 1}^{c3}}\tilde{\boldsymbol{\Phi}}_e^{(2)T}\dot{\boldsymbol{\Phi}}_e^{(2)} \\ &= -\lambda_{\omega}^{c3}\left(s_{\omega g} + s_{\omega c}\right)^2 - \tilde{\boldsymbol{\Phi}}_e^{(2)T}\left[\left(s_{\omega g} + s_{\omega c}\right)\boldsymbol{y}^{(2)}(n) + \frac{1}{\eta_{c\omega 1}^{c3}}\dot{\boldsymbol{\Phi}}_e^{(2)}\right] - \tilde{\varepsilon}_{ENN}\left[\left(s_{\omega g} + s_{\omega c}\right) + \frac{1}{\eta_{c\omega\varepsilon}^{c3}}\dot{\varepsilon}_{c\omega 2}\right] \\ &= -\lambda_{\omega}^{c3}\left(s_{\omega g} + s_{\omega c}\right)^2 \le 0\end{aligned} \tag{6.40}$$

It can be observed that (6.40) is equivalent to (6.15). Thus, following the same procedures presented in the proof of Theorem 6.1, it can be demonstrated that $(s_{\omega g} + s_{\omega c})$ will converge to the origin asymptotically. The proof is completed. ■

Remark 6.4. Since $s_{\omega g} + s_{\omega c} = 2e_{\omega 2}$, $e_{\omega 2}$ will converge to the origin asymptotically with the ENN-ICSM speed control law and the learning laws (6.36) and (6.37).

Since the learning laws for $\varepsilon_{c\omega 2}$ and $\boldsymbol{\Phi}_e^{(2)}$ expressed as (6.36) and (6.37) can guarantee the asymptotic convergence of $e_{\omega 2}$ to the origin, based on the BP algorithm, the learning laws for $\boldsymbol{\Phi}_{e1}^{(1)}(n)$ and $\boldsymbol{\Phi}_{e2}^{(1)}(n)$ are derived from the learning laws for $\varepsilon_{c\omega 2}$ and $\boldsymbol{\Phi}_e^{(2)}$.

At first, the $e_{\omega 2}$-based cost function E_{ω} is defined as

$$E_{\omega} = \frac{1}{2}e_{\omega 2}^2 \tag{6.41}$$

Output Layer: The local gradient σ_{ω} is defined as the following expression [10].

$$\sigma_{\omega}(n) = -\frac{\partial E_{\omega}(n)}{\partial y_1^{(4)}(n)} \tag{6.42}$$

With respect to $\Phi_{ei}^{(2)}$, the corresponding correction term $\Delta\Phi_{ei}^{(2)}$ is defined by the so-called delta

rule [10], i.e.,

$$\Delta\Phi_{ei}^{(2)}(n)=-\gamma_{\omega 1}\frac{\partial E_{\omega}(n)}{\partial\Phi_{ei}^{(2)}(n)}=-\gamma_{\omega 1}\frac{\partial E_{\omega}(n)}{\partial y_1^{(4)}(n)}\frac{\partial y_1^{(4)}(n)}{\partial\Phi_{ei}^{(2)}(n)}=\gamma_{\omega 1}\sigma_{\omega}(n)y_i^{(2)}(n) \tag{6.43}$$

where $\gamma_{\omega 1}$ is the positive learning rate for $\Phi_{ei}^{(2)}$.

$\Phi_{ei}^{(2)}$ is updated online by

$$\Phi_{ei}^{(2)}(n+1)=\Phi_{ei}^{(2)}(n)+\Delta\Phi_{ei}^{(2)}(n) \tag{6.44}$$

It can be seen that the learning law for $\Phi_{ei}^{(2)}$ derived from the BP algorithm is dependent on σ_{ω}. Based on the Euler method, the learning law for $\Phi_{ei}^{(2)}$ derived from the Lyapunov synthesis approach presented in (6.37) can be discretized as

$$\Phi_{ei}^{(2)}(n+1)=\Phi_{ei}^{(2)}(n)-\eta_{c\omega 1}^{c3}T_s\left(s_{\omega g}+s_{\omega c}\right)y_i^{(2)}(n) \tag{6.45}$$

In order to guarantee the stability of the rotor speed control system in theory, the learning law for $\Phi_{ei}^{(2)}$ presented in (6.44) should be equivalent to that presented in (6.45). Thus, based on the equivalence of (6.44) and (6.45), $\gamma_{\omega 1}$ and σ_{ω} can be expressed as (6.46) and (6.47), respectively.

$$\gamma_{\omega 1}=\eta_{c\omega 1}^{c3}T_s \tag{6.46}$$

$$\sigma_{\omega}=-\left(s_{\omega g}+s_{\omega c}\right) \tag{6.47}$$

Hidden Layer: With respect to $\Phi_{ei1}^{(1)}$ and $\Phi_{ei2}^{(1)}$, based on the delta rule, the corresponding correction terms $\Delta\Phi_{ei1}^{(1)}$ and $\Delta\Phi_{ei2}^{(1)}$ are derived as

$$\begin{aligned}\Delta\Phi_{ei1}^{(1)}(n)&=-\gamma_{\omega 2}\frac{\partial E_{\omega}(n)}{\partial\Phi_{ei1}^{(1)}(n)}=-\gamma_{\omega 2}\frac{\partial E_{\omega}(n)}{\partial y_1^{(4)}(n)}\frac{\partial y_1^{(4)}(n)}{\partial y_i^{(2)}(n)}\frac{\partial y_i^{(2)}(n)}{\partial x_i^{(2)}(n)}\frac{\partial x_i^{(2)}(n)}{\partial\Phi_{ei1}^{(1)}(n)}\\&=-\gamma_{\omega 2}\left(s_{\omega g}+s_{\omega c}\right)\Phi_{ei}^{(2)}(n)y_i^{(2)}(n)\left[1-y_i^{(2)}(n)\right]x_1^{(1)}(n)\end{aligned} \tag{6.48}$$

$$\begin{aligned}\Delta\Phi_{ei2}^{(1)}(n)&=-\gamma_{\omega 3}\frac{\partial E_{\omega}(n)}{\partial\Phi_{ei2}^{(1)}(n)}=-\gamma_{\omega 3}\frac{\partial E_{\omega}(n)}{\partial y_1^{(4)}(n)}\frac{\partial y_1^{(4)}(n)}{\partial y_i^{(2)}(n)}\frac{\partial y_i^{(2)}(n)}{\partial x_i^{(2)}(n)}\frac{\partial x_i^{(2)}(n)}{\partial\Phi_{ei2}^{(1)}(n)}\\&=-\gamma_{\omega 3}\left(s_{\omega g}+s_{\omega c}\right)\Phi_{ei}^{(2)}(n)y_i^{(2)}(n)\left[1-y_i^{(2)}(n)\right]x_2^{(1)}(n)\end{aligned} \tag{6.49}$$

where $\gamma_{\omega 2}$ and $\gamma_{\omega 3}$ are the positive learning rates for $\Phi_{ei1}^{(1)}$ and $\Phi_{ei2}^{(1)}$, respectively.

Based on (6.48) and (6.49), $\Phi_{ei1}^{(1)}$ and $\Phi_{ei2}^{(1)}$ are updated online by (6.50) and (6.51), respectively.

$$\Phi_{ei1}^{(1)}(n+1)=\Phi_{ei1}^{(1)}(n)+\Delta\Phi_{ei1}^{(1)}(n) \tag{6.50}$$

$$\Phi_{ei2}^{(1)}(n+1)=\Phi_{ei2}^{(1)}(n)+\Delta\Phi_{ei2}^{(1)}(n) \tag{6.51}$$

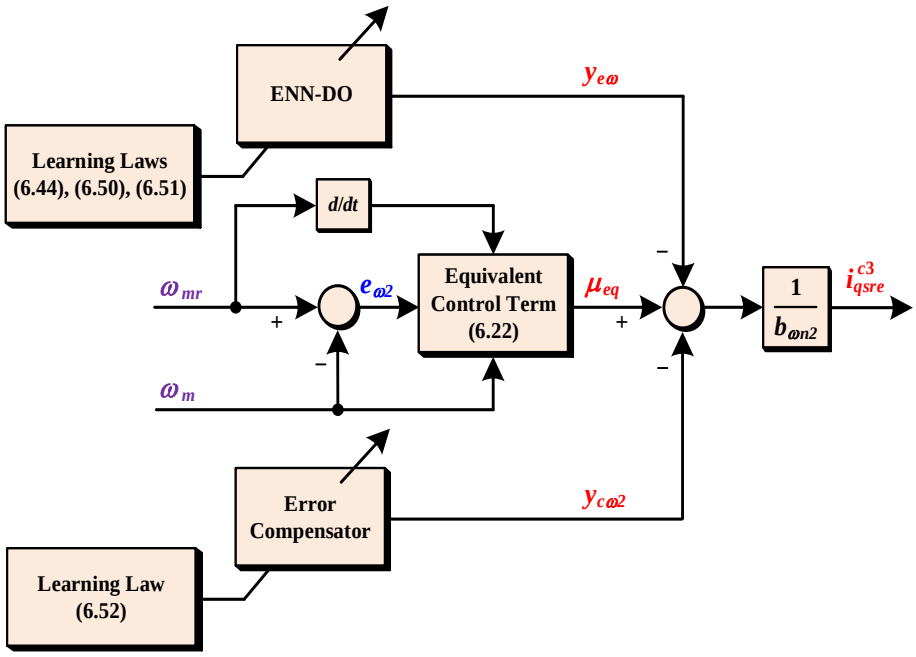

Figure 6.2 Block diagram of the ENN-ICSM speed controller.

Similarly, with respect to the learning law for $\varepsilon_{c\omega 2}$, its discrete form can be expressed as

$$\varepsilon_{c\omega 2}(n+1) = \varepsilon_{c\omega 2}(n) - \gamma_{\varepsilon}\left(s_{\omega g} + s_{\omega c}\right) \tag{6.52}$$

where $\gamma_{\varepsilon} = T_S \eta_{c\omega\varepsilon}^{c3}$ is the positive learning rate for $\varepsilon_{c\omega 2}$.

Remark 6.5. Since there are two input neurons and nine hidden neurons in the adopted ENN-DO, nine logistic functions are used in the hidden layer and twenty-eight learning laws need to be implemented in each sampling period of the hardware controller. Therefore, the implementation of the adopted ENN-DO significantly increases the computational burden of the hardware controller.

The block diagram of the ENN-ICSM speed controller is shown in Figure 6.2.

6.3.3 Type-3 Composite Speed Controller Design

According to the STSMO design presented in Section 3.3.2, the STSMO for the estimation of $\rho_{\omega 2}$ can be designed as (6.53). Considering Theorem 3.1 and Assumption 5.1, two positive constant gains k_{s1}^{c3} and k_{s2}^{c3} of the STSMO are selected as (6.54) such that the finite-time stability of the state estimation error system is guaranteed and the lumped disturbance estimation error $e_{S\omega}$ is bounded as $|e_{S\omega}| \leq L_{\omega 1}^{c3}$ for a positive constant $L_{\omega 1}^{c3}$.

$$\begin{cases} \dot{\hat{z}}_{s\omega 1} = -a_{\omega n2}\omega_m + b_{\omega n2} i_{qsr}^{c3} + \hat{z}_{s\omega 2} + k_{s1}^{c3}\sqrt{|\omega_m - \hat{z}_{s\omega 1}|}\,\mathrm{sgn}(\omega_m - \hat{z}_{s\omega 1}) \\ \dot{\hat{z}}_{s\omega 2} = k_{s2}^{c3}\,\mathrm{sgn}(\omega_m - \hat{z}_{s\omega 1}) \end{cases} \tag{6.53}$$

$$k_{s1}^{c3} > 2, \quad k_{s2}^{c3} > \frac{(k_{s1}^{c3})^2 + 4(L_{\omega 2}^{c2})^2}{4\left(k_{s1}^{c3} - 2\right)} \tag{6.54}$$

where $\hat{z}_{s\omega 1} = \hat{\omega}_m$ and $\hat{z}_{s\omega 2} = \hat{\rho}_{\omega 2}$ denote the estimated rotor mechanical speed and lumped disturbance, respectively, i_{qsre}^{c3} represents the type-3 composite speed control law.

Based on the $e_{\omega 2}$-dynamics expressed as (5.29), selecting $s_{\omega g}$ and $s_{\omega c}$ as the generalized and complementary sliding mode variables, respectively, the type-3 composite speed control law i_{qsre}^{c3} can be designed as

$$i_{qsr}^{c3} = \frac{1}{b_{\omega n2}}\left(\mu_{c\omega} - \hat{\rho}_{s\omega}\right) \tag{6.55}$$

where $\mu_{c\omega}$ denotes the sign function-based CSM control term expressed as (6.56), and $\hat{\rho}_{s\omega}$ is the estimated lumped disturbance from the adopted STSMO for the compensation of $\rho_{\omega 2}$.

$$\mu_{c\omega} = \dot{\omega}_{mr} + a_{\omega n2}\omega_m + \lambda_{\omega}^{c3} e_{\omega 2} + \lambda_{\omega}^{c3} s_{\omega g} + k_{\omega 2}^{c3}\mathrm{sgn}\left(s_{\omega g} + s_{\omega c}\right) \tag{6.56}$$

where $k_{\omega 2}^{c3}$ is the positive constant gain.

Substituting (6.55) into (5.29), the closed-loop $e_{\omega 2}$-dynamics with the type-3 composite speed control law is expressed as

$$\begin{aligned} \dot{e}_{\omega 2} &= -\lambda_{\omega}^{c3} e_{\omega 2} - \lambda_{\omega}^{c3} s_{\omega g} - k_{\omega 2}^{c3}\mathrm{sgn}\left(s_{\omega g} + s_{\omega c}\right) - \underbrace{\left(\rho_{\omega 2} - \hat{\rho}_{s\omega}\right)}_{e_{S\omega}} \\ &= -\lambda_{\omega}^{c3} e_{\omega 2} - \lambda_{\omega}^{c3} s_{\omega g} - k_{\omega 2}^{c3}\mathrm{sgn}\left(s_{\omega g} + s_{\omega c}\right) - e_{S\omega} \end{aligned} \tag{6.57}$$

Based on Theorem 6.1, it can be concluded that, for the positive constant λ_{ω}^{c3}, with the type-3 composite speed control law (6.55), $e_{\omega 2}$ will converge to the origin asymptotically if $k_{\omega 2}^{c3}$ is selected as

$$k_{\omega 2}^{c3} > L_{\omega 1}^{c3} \tag{6.58}$$

In the type-3 composite speed controller, $\rho_{\omega 2}$ is compensated by the STSMO, and the role of the sign function is to guarantee the asymptotic stability of the $e_{\omega 2}$-dynamics in theory, as discussed in Remark 6.1. Therefore, the value selected for $k_{\omega 2}^{c3}$ should be small such that the implementation of the type-3 composite speed controller in the DSP does not yield severe chattering phenomena in practice.

The block diagram of the type-3 composite speed controller is shown in Figure 6.3.

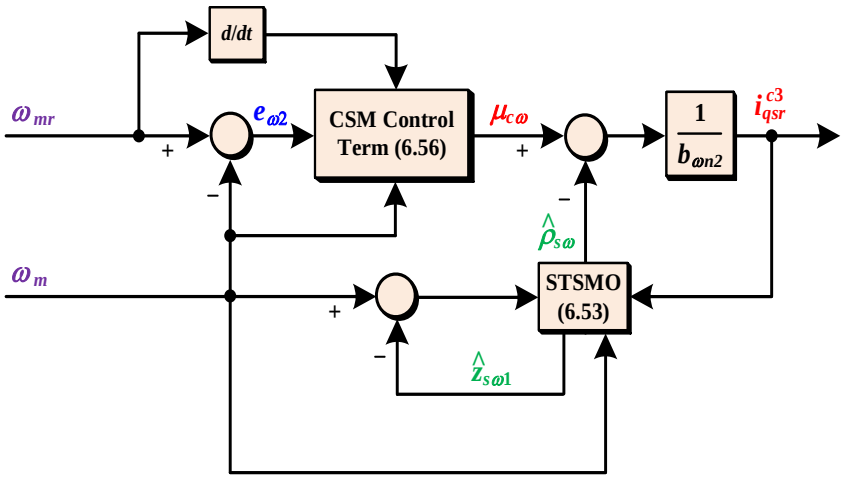

Figure 6.3 Block diagram of the type-3 composite speed controller.

Table 6.1 Parameters of tested rotor speed controllers

Rotor speed controller	Controller parameters	Observer parameters	Compensator parameter
Classic CSM speed controller	$\lambda_{\omega}^{c3} = 220$, $k_{\omega 1}^{c3} = 300, \Pi = 3$	—	—
ENN-ICSM speed controller 1	$\lambda_{\omega}^{c3} = 220$	$\gamma_{\omega 1} = 0.1$, $\gamma_{\omega 2} = 0.1$, $\gamma_{\omega 3} = 0.1$	$\gamma_{\varepsilon} = 0.3$
ENN-ICSM speed controller 2	$\lambda_{\omega}^{c3} = 220$	$\gamma_{\omega 1} = 0.2$, $\gamma_{\omega 2} = 0.1$, $\gamma_{\omega 3} = 0.1$	$\gamma_{\varepsilon} = 0.3$
ENN-ICSM speed controller 3	$\lambda_{\omega}^{c3} = 220$	$\gamma_{\omega 1} = 0.4$, $\gamma_{\omega 2} = 0.1$, $\gamma_{\omega 3} = 0.1$	$\gamma_{\varepsilon} = 0.3$
Type-3 composite speed controller	$\lambda_{\omega}^{c3} = 220$, $k_{\omega 2}^{c3} = 10$	$k_{s1}^{c3} = 7000$, $k_{s2}^{c3} = 1200000$	—

6.3.4 Experimental Results

The experimental test bench described in Section 2.5 is used to perform comparative experimental tests among the classic CSM speed controller, three selected ENN-ICSM speed controllers with different values of $\gamma_{\omega 1}$ and the type-3 composite speed controller in the frame of the FOC strategy whose block diagram is illustrated in Figure 5.2. With respect to the construction of these tested speed controllers, 75%, 125% and 75% of rated values of J, B_m and λ_m, respectively, are used.

The parameters of these speed controllers are listed in Table 6.1. Furthermore, in all tested FOC strategies, the proportional and integral gains of each PI stator current controller are set to 20.42 and 7379, respectively.

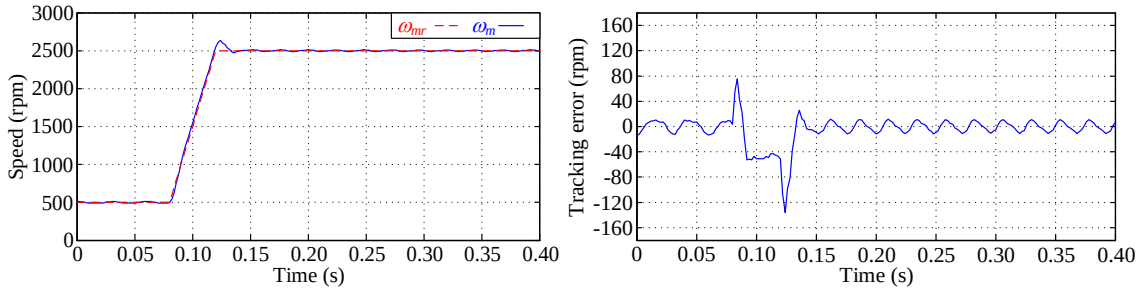

(a)

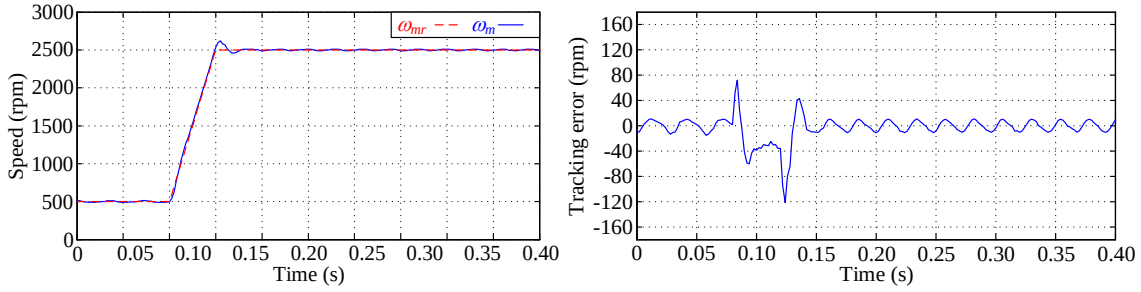

(b)

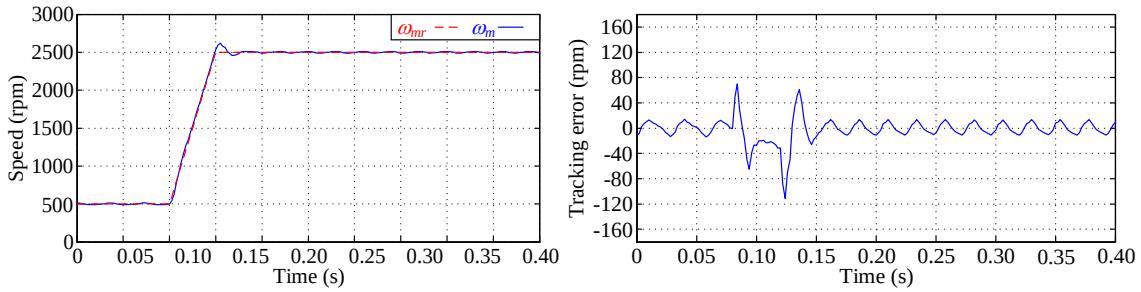

(c)

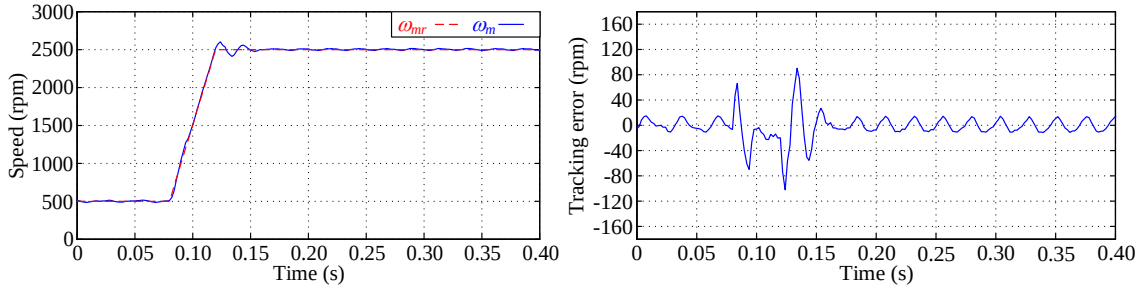

(d)

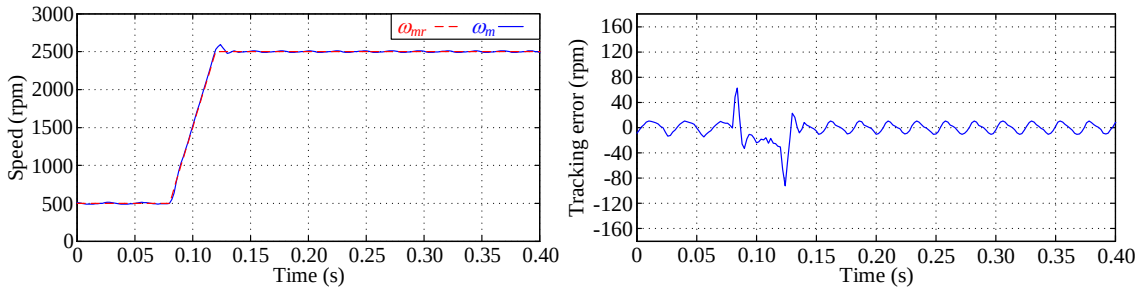

(e)

Figure 6.4 Rotor mechanical speed responses and corresponding tracking errors for the first test. (a) Classic CSM speed controller. (b) ENN-ICSM speed controller 1. (c) ENN-ICSM speed controller 2. (d) ENN-ICSM speed controller 3. (e) Type-3 composite speed controller.

Table 6.2 Dynamic performance of tested rotor speed controllers in the first test

Rotor speed controller	Overshoot (%)	Settling time (ms)
Classic CSM speed controller	5.440	58
ENN-ICSM speed controller 1	4.859	60
ENN-ICSM speed controller 2	4.448	68
ENN-ICSM speed controller 3	4.082	76
Type-3 composite speed controller	3.696	48

In the first test, the value of the load torque is set to 0 N·m, while the value of the reference rotor mechanical speed is increased from 500 rpm to 2500 rpm with the acceleration of 50 rpm/ms. The rotor mechanical speed responses and corresponding tracking errors for five tested rotor speed controllers are shown in Figure 6.4. The dynamic performance of five tested rotor speed controllers are summarized in Table 6.2. Note that the tolerance band is chosen as $\pm$ 25 rpm, namely $\pm$ 1 % of 2500 rpm, for the settling time calculation. It can be seen that, among all tested rotor speed controllers, the use of the classic CSM speed controller results in the largest overshoot, i.e., 5.440 % (136.01 rpm). Using the ENN-ICSM speed controller to replace the classic CSM speed controller can reduce the value of the overshoot. Moreover, with the increase of the value of $\gamma_{\omega 1}$, the value of the overshoot is further reduced. However, it results in the growth of the settling time and the appearance of undesired oscillations in the transient period, as shown in Figure 6.4(b)-(d). According to Figure 6.4(e), among all test rotor speed controllers, the use of type-3 composite speed controller generates the smallest overshoot, i.e., 3.696 % (92.41 rpm), which is only 67.94 % of the overshoot resulted from the use of the classic CSM speed controller, respectively. Furthermore, compared with

three selected ENN-ICSM speed controllers, the use of the type-3 composite speed controller does not lead to the growth of the settling time and the appearance of the oscillation phenomenon.

Table 6.3 Dynamic performance of tested rotor speed controllers in the second test

Rotor speed controller	Maximum tracking error (rpm)	Settling time (ms)
Classic CSM speed controller	315.30	34
ENN-ICSM speed controller 1	292.12	26
ENN-ICSM speed controller 2	274.05	32
ENN-ICSM speed controller 3	255.31	48
Type-3 composite speed controller	232.18	12

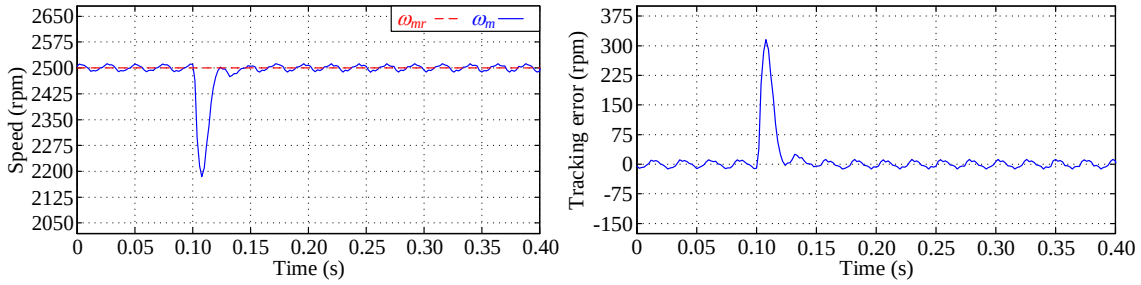

(a)

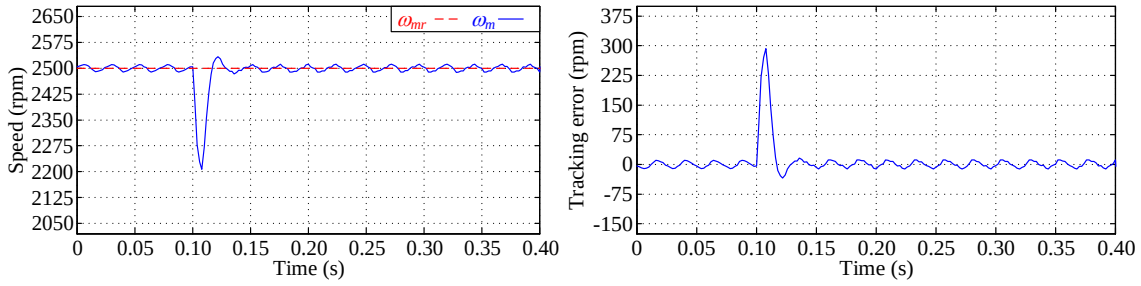

(b)

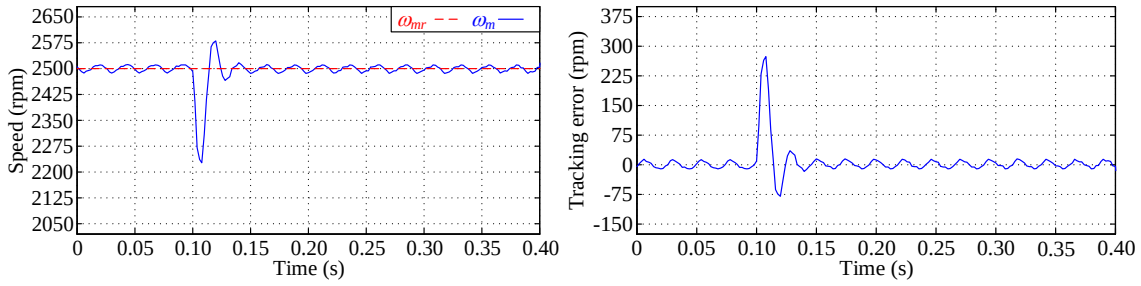

(c)

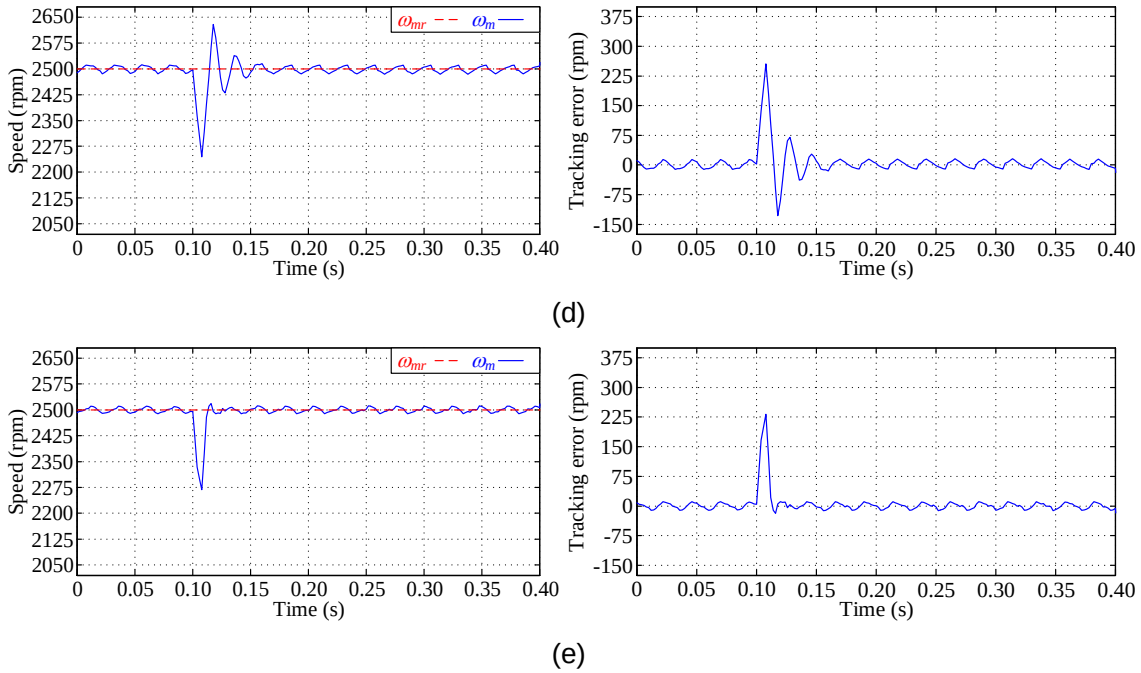

Figure 6.5 Rotor mechanical speed responses and corresponding tracking errors for the second test. (a) Classic CSM speed controller. (b) ENN-ICSM speed controller 1. (c) ENN-ICSM speed controller 2. (d) ENN-ICSM speed controller 3. (e) Type-3 composite speed controller.

In the second test, the value of the reference rotor mechanical speed is kept at 2500 rpm, whereas the value of the load torque is stepped from 0 N·m to 1.0 N·m at 0.1 s. Figure 6.5 presents the rotor mechanical speed responses and corresponding tracking errors for five tested rotor speed controllers. Table 6.3 summaries the dynamic performance of five tested rotor speed controllers, where the criterion for the settling time calculation is the same as the first test. It can be observed that the maximum tracking error for the use of the classic CSM speed controller is 315.30 rpm, which is the highest value in this test. Compared with such a rotor speed controller, the use of the selected ENN-ICSM speed controller can reduce the maximum tracking error when the value of the load torque steps. As illustrated in Figure 6.5(b)-(d), the maximum tracking errors for the three selected ENN-ICSM speed controllers are 292.12 rpm, 274.05 rpm and 255.31 rpm, respectively, when the value of the load torque is stepped from 0 N·m to 1.0 N·m. Nevertheless, similar to the first test, the growth of the value of $\gamma_{\omega 1}$ results in the increase of the settling time and the appearance of the undesired oscillations in the transient period. Regarding the type-3 composite speed controller, the corresponding maximum tracking error is 232.18 rpm, which is the lowest value in this test. Moreover, in comparison with three selected ENN-ICSM speed controllers, the type-3 composite speed controller reduces the settling time and avoids the undesired oscillations in the transient period.

Table 6.4 Calculation time in each sampling period

Classic CSM speed controller-based FOC strategy	Selected ENN-ICSM speed controller-based FOC strategy	Type-3 composite speed controller-based FOC strategy
10.84 μs	29.72 μs	12.44 μs

In order to evaluate the implementation complexities of the classic CSM speed controller, the selected ENN-ICSM speed controller and the type-3 composite speed controller, the calculation time of the FOC strategy in each sampling period is chosen as the index. Table 6.4 shows such indexes for FOC strategies using the classic CSM speed controller, the selected ENN-ICSM speed controller and the type-3 composite speed controller. It can be seen that the use of the selected ENN-ICSM speed controller or the type-3 composite speed controller to replace the classic CSM speed controller in the FOC strategy inevitably increases the calculation time of the FOC strategy in each sampling period. More specifically, compared with the FOC strategy using the classic CSM speed controller, the calculation times of the FOC strategies using the selected ENN-ICSM speed controller and the type-3 composite speed controller in each sampling period increases by 174.17 % and 14.76%, respectively. Based on above analyses, it can be concluded that the type-3 composite speed controller is more computationally efficient than the ENN-ICSM speed controller that uses the ENN-based DO proposed in [9].

6.4 Summary

In this chapter, a novel composite controller named as the type-3 composite controller is proposed for a single-input uncertain nonlinear system with relative degree one. The proposed composite controller is composed of the sign function-based CSM algorithm and a STSMO. The asymptotic convergence of the output tracking error is accomplished by the sign function-based CSM controller and the STSMO is adopted to compensate the lumped disturbance in the output tracking error dynamics for the disturbance attenuation ability improvement. The rigorous stability analysis of output tracking error dynamics with the type-3 composite controller is presented.

With respect to the 2L-VSI-fed SPMSM-VSD system, a novel robust FOC strategy is proposed. In this FOC strategy, a type-3 composite speed controller and two linear PI current controllers are adopted. Comparative experimental tests among the classic CSM speed controller, three selected ENN-ICSM speed controllers and the type-3 composite speed controller in the frame of the FOC

strategy are performed on the experimental test bench described in Section 2.5. Corresponding experimental results demonstrate that the type-3 composite speed controller can achieve the minimum rotor speed transient variation and the fastest dynamic response. Moreover, compared with the selected ENN-ICSM speed controller, the computational burden of the DSP to implement the type-3 composite speed controller is lower.

References

[1] Y. Shtessel, C. Edwards, L. Fridman, and A. Levant, *Sliding Mode Control and Observation*. Basel, Switzerland: Birkhäuser, 2014.

[2] J. P. Su and C. -C. Wang, "Complementary sliding control of non-linear systems," *International Journal of Control*, vol. 75, no. 5, pp. 360-368, Jun. 2002.

[3] F. -J. Lin, Y. -C. Hung, and M. -T. Tsai, "Fault-tolerant control for six-phase PMSM drive system via intelligent complementary sliding-mode control using TSKFNN-AMF," *IEEE Transactions on Industrial Electronics*, vol. 60, no. 12, pp. 5747-5762, Dec. 2013.

[4] F. -J. Lin, P. -H. Chou, C. -S. Chen, and Y. -S. Lin, "DSP-based cross-coupled synchronous control for dual linear motors via intelligent complementary sliding mode control," *IEEE Transactions on Industrial Electronics*, vol. 59, no. 2, pp. 1061-1073, Feb. 2012.

[5] F. -J. Lin, S. -Y. Chen, and M. -S. Huang, "Adaptive complementary sliding-mode control for thrust active magnetic bearing system," *Control Engineering Practice*, vol. 19, no. 7, pp. 711-722, Jul. 2011.

[6] F. -J. Lin, S. -Y. Chen, K. -K. Shyu, and Y. -H. Liu, "Intelligent complementary sliding-mode control for LUSMs-based X-Y-θ motion control stage," *IEEE Transactions on Ultrasonics, Ferroelectrics, and Frequency Control*, vol. 57, no. 7, pp. 1626-1640, Jul. 2010.

[7] C. -F. Hsu and T. -C. Kuo, "Intelligent complementary sliding-mode with dead-zone parameter modification," *Applied Soft Computing*, vol. 23, pp. 355-365, Oct. 2014.

[8] F. -J. Lin, J. -C. Hwang, P. -H. Chou, and Y. -C. Hung, "FPGA-based intelligent-complementary sliding-mode control for PMLSM servo-drive system," *IEEE Transactions on Power Electronics*, vol. 25, no. 10, pp. 2573-2587, Oct. 2010.

[9] H. Jin and X. Zhao, "Complementary sliding-mode control via Elman neural network for permanent magnet linear servo system," *IEEE Access*, vol. 7, pp. 82183-82193, Jun. 2019.

[10] S. Haykin, *Neural Networks: A Comprehensive Foundation*, 2nd ed. Upper Saddle River, USA: Prentice Hall, 1998.

[11] P. A. Ioannou and J. Sun, *Robust Adaptive Control*. Moneola, USA: Dover Publications, 2012.

7

TYPE-4 COMPOSITE CONTROLLER: DESIGN AND APPLICATION

7.1 Introduction

The adaptive control is a widely used nonlinear control technique for the single-input uncertain nonlinear system with relative degree one. It can be regarded as a combination of a control law with one or more online parameter estimators, commonly known as adaptive laws, which accomplish online estimation of unknown parts in the control law [1], [2]. The types and combinations of control laws and adaptive laws lead to a wide class of adaptive controllers. The MRA controller is one of the most popular adaptive controllers. In general, the first step of designing the MRA controller is to select a reference model to specify the desired output trajectory for the system. Afterward, to make the actual output of the system follow such a trajectory, a control law is designed, where one or more compensation terms updated online by the adaptive laws are used to deal with the unknown parts of the system. Until now, MRA controllers have found wide applications [3]-[13]. However, the classic MRA controller is based on the feedback regulation mechanism, which may not be able to react fast enough for strong disturbances [14]. To overcome this limitation, the composite controller combining the classic MRA controller with a DO can be developed.

For AC motor-based VSD systems, the ANN-DO is a popular choice to construct the MRA-based composite speed controller [15]-[17]. However, as has been stated in Section 6.1, the implementation of the ANN-DO significantly increases the computational burden of the hardware controller, and the model-based extended DO is a better choice in terms of simplicity. As mentioned in Section 3.1, the STSMO is one of the most popular nonlinear extended DO for the DOC of AC

motor drive systems. However, to the best of the author's knowledge, no published literature investigates the composite controller combining a classic MRA controller with a STSMO; let alone the application of this controller to the PMSM-VSD system.

In this chapter, the type-4 composite controller, which is composed of a classic MRA controller and a STSMO, is proposed for a single-input uncertain nonlinear system with relative degree one. A stable first-order linear model is selected as the reference model to describe the desired output trajectory for the system. The proposed composite controller consists of three terms. The first term is the stabilization term dependent on known parts of the system and the selected reference model. The second term is the disturbance compensation term based on the STSMO. The third term is the error compensation term updated online by an adaptive law, which is derived by the Lyapunov synthesis approach. The rigorous stability analysis of the dynamics of the output tracking error between the desired and actual outputs of the system with the type-4 composite controller is presented.

After the rigorous theoretical analysis of the proposed type-4 composite controller, this controller is applied to the construction of a novel robust FOC strategy for the 2L-VSI-fed SPMSM-VSD system. In this FOC strategy, the proposed type-4 composite controller is used as the rotor speed controller in the speed control loop and two linear PI controllers serve as two stator current controllers in the current control loop. To validate the effectiveness and the superiority of the type-4 composite speed controller, based on the experimental test bench described in Section 2.5, comparative experimental tests among three selected classic MRA speed controllers, three selected RBFNN-MRA speed controllers and the type-4 composite speed controller in the frame of the FOC strategy are carried out. Finally, the experimental results are presented and analyzed.

7.2 Type-4 Composite Controller Design

7.2.1 Problem Statement

Considering the single-input uncertain nonlinear system with relative degree one presented in (3.1), based on (3.3), the y-dynamics can be written as

$$\dot{y} = b_n \mu + \rho_x(x,t) \tag{7.1}$$

A stable first-order reference model for the system is selected as

$$\dot{y}_r^* = -\alpha_r y_r^* + \beta_r y_r \tag{7.2}$$

where y_r^* is the desired output of the system generated by the reference model, α_r and β_r are two positive constants determining the dynamic performance of the reference model.

The output tracking error between the desired and actual outputs of the system is defined as

$$e_r = y_r^* - y \tag{7.3}$$

According to (7.1)-(7.3), the e_r-dynamics is expressed as

$$\dot{e}_r = \dot{y}_r^* - \dot{y} = -\alpha_r y_r^* + \beta_r y_r - b_n \mu - \rho_x \tag{7.4}$$

The control objective is to let e_r converge to the origin asymptotically.

7.2.2 STSMO Design

From (7.4), it can be seen that the only unknown part in the e_r-dynamics is ρ_x. Therefore, the STSMO designed as (3.11) for the estimation of ρ_x can be directly used in the type-4 composite controller.

7.2.3 Controller Design

To achieve the control objective, the type-4 composite control law μ_{c4} is designed as

$$\mu_{c4} = \frac{1}{b_n}\left(\mu_s - \hat{\rho}_{ST} - \varepsilon_{c3}\right) \tag{7.5}$$

where μ_s is the stabilization term for the asymptotic convergence of e_y to the origin, which is expressed as (7.6), $\hat{\rho}_{ST}$ is the estimated lumped disturbance from the adopted STSMO for the compensation of ρ_x, and ε_{c3} is the error compensation term for confronting of the estimation error of the adopted STSMO.

$$\mu_s = -\alpha_r y + \beta_r y_r \tag{7.6}$$

Substituting (7.5) into (7.4), the closed-loop e_r-dynamics with the type-4 composite control law is expressed as

$$\begin{aligned} \dot{e}_r &= -\alpha_r e_r + \hat{\rho}_{ST} + \varepsilon_{c3} - \rho_x = -\alpha_r e_r + \varepsilon_{c3} - e_{ST} \\ &= -\alpha_r e_r - \tilde{\varepsilon}_{c3} \end{aligned} \tag{7.7}$$

where $\tilde{\varepsilon}_{c3} = e_{ST} - \varepsilon_{c3}$.

Assumption 7.1. e_{ST} is constant in each sampling period.

The following Theorem can be used to derive the adaptive law for ε_{c3} to accomplish the control

objective.

Theorem 7.1. Considering the system (7.7), for the positive constant α_r, if the adaptive law for ε_{c3} is designed as (7.8), e_r will converge to the origin asymptotically.

$$\dot{\varepsilon}_{c3} = -\eta_s e_r \tag{7.8}$$

where η_s is the positive constant gain.

Proof. The Lyapunov candidate function V_{c4} is selected as

$$V_{c4} = \frac{1}{2}e_r^2 + \frac{1}{2\eta_s}\tilde{\varepsilon}_{c3}^2 \tag{7.9}$$

Based on (7.7) and (7.10), $\dot{V}_{c3}$ can be calculated as

$$\begin{aligned} \dot{V}_{c4} &= e_r\dot{e}_r - \frac{1}{\eta_s}\dot{\varepsilon}_{c3}\tilde{\varepsilon}_{c3} = -e_r\left(\alpha_r e_r + \tilde{\varepsilon}_{c3}\right) - \frac{1}{\eta_s}\dot{\varepsilon}_{c3}\tilde{\varepsilon}_{c3} \\ &= -\alpha_r e_r^2 - \tilde{\varepsilon}_{c3}\left(e_r + \frac{1}{\eta_s}\dot{\varepsilon}_{c3}\right) \end{aligned} \tag{7.10}$$

Combining (7.10) with (7.8), $\dot{V}_{c4}$ can be expressed as

$$\dot{V}_{c4} = -\alpha_r e_r^2 \le 0 \tag{7.11}$$

From (7.11), it can be concluded that $\dot{V}_{c4}$ is negative semidefinite. Therefore, the following inequality holds.

$$V_{c4}\left(e_r(t)\right) \le V_{c4}\left(e_r(0)\right) \tag{7.12}$$

According to (7.12), $e_r(t)$ is bounded. Based on (7.11) and (7.12), the following function is defined.

$$\Omega_{MRA}(t) = -\alpha_r e_r^2(t) \le -\dot{V}_{c4}\left(e_r(t)\right) \tag{7.13}$$

Since $V_{c4}(e_r(0))$ is bounded and $V_{c4}(e_r(t))$ is a non-increasing bounded function, the following inequality can be derived.

$$\lim_{t\to\infty}\int_0^t \Omega_{MRA}(\tau)\,d\tau < \infty \tag{7.14}$$

Since $\lim_{t\to\infty}\int_0^t \Omega_{MRA}(\tau)d\tau$ exists and $\Omega_{MRA}(t)$ is a uniformly continuous function, according to Barbălat's Lemma [2], $\lim_{t\to\infty}\Omega_{MRA}(t) = 0$ holds. It means that $\lim_{t\to\infty} e_r(t) = 0$ holds. Thus, e_r will converge to the origin asymptotically. The proof is completed. ■

Remark 7.1. Different from the classic MRA controller, the type-4 composite controller uses the adaptive law to update the compensation term for the estimation error of the STSMO rather than the lumped disturbance in the output tracking error dynamics.

7.3 Application

In this section, the type-4 composite speed controller, which is designed using the practical speed dynamics of the SPMSM presented in (2.54), is applied to the construction of a novel robust FOC strategy for the 2L-VSI-fed SPMSM-VSD system. In such a FOC strategy, two linear PI current controllers are used as stator current controllers. Moreover, i_{dsr} is set to 0 and i_{qsr} is generated by the type-4 composite speed controller. Besides the type-4 composite speed controller, the designs and analyses of the classic MRA speed controller and the RBFNN-MRA speed controller proposed in [16] are also presented. Results of the comparative experimental tests among three selected classic MRA speed controllers, three selected RBFNN-MRA speed controllers and the type-4 composite speed controller in the frame of the FOC strategy for the 2L-VSI-fed SPMSM-VSD system are presented to demonstrate the superiority of the type-4 composite speed controller.

7.3.1 Problem Statement

According to (5.25), the ω_m-dynamics of the SPMSM can be rewritten as

$$\dot{\omega}_m = b_{\omega n2} i_{qsr} - \underbrace{\left(a_{\omega n2}\omega_m - \rho_{\omega 2}\right)}_{\rho_{\omega r}} = b_{\omega n2} i_{qsr} - \rho_{\omega r} \tag{7.15}$$

where $\rho_{\omega r}$ denotes the lumped disturbance in the derived ω_m-dynamics.

Assumption 7.2. $\rho_{\omega r}$ and its time derivative $\dot{\rho}_{\omega r}$ are constant in each sampling period and bounded as $|\rho_{\omega r}| \leq L_{\omega 1}^{c4}$ and $|\dot{\rho}_{\omega r}| \leq L_{\omega 2}^{c4}$, respectively, for positive constants $L_{\omega 1}^{c4}$ and $L_{\omega 2}^{c4}$.

A stable first-order reference model for all rotor speed controllers presented in this section is selected as

$$\dot{\omega}_{mr}^{*} = -\alpha_{\omega r}^{c4}\omega_{mr}^{*} + \beta_{\omega r}^{c4}\omega_{mr} \tag{7.16}$$

where ω_{mr}^{*} is the desired rotor mechanical speed generated by the reference model, $\alpha_{\omega r}^{c4}$ and $\beta_{\omega r}^{c4}$ are two positive constants determining the dynamic performance of the reference model.

The speed tracking error between the desired and actual rotor mechanical speeds is defined as

$$e_{\omega r} = \omega_{mr}^{*} - \omega_m \tag{7.17}$$

According to (7.15)-(7.17), the $e_{\omega r}$-dynamics is expressed as

$$\begin{aligned} \dot{e}_{\omega r} &= \dot{\omega}_{mr}^{*} - \dot{\omega}_{m} \\ &= -\alpha_{\omega r}^{c4}\omega_{mr}^{*} + \beta_{\omega r}^{c4}\omega_{mr} - b_{\omega n2}i_{qsr} + \rho_{\omega r} \end{aligned} \tag{7.18}$$

The control objective is to let $e_{\omega r}$ converge to the origin asymptotically.

7.3.2 Classic MRA Speed Controller Design

On the basis of the $e_{\omega r}$-dynamics expressed as (7.18) and the reference model expressed as (7.16), the classic MRA speed control law i_{qsrc}^{c4} is designed as

$$i_{qsrc}^{c4} = \frac{1}{b_{\omega n2}}\left(\mu_{\omega s} + \hat{\rho}_{A}\right) \tag{7.19}$$

where $\mu_{\omega s}$ is the stabilization term for the asymptotic convergence of $e_{\omega r}$ to the origin, which is expressed as (7.20), $\hat{\rho}_{A}$ is the estimated lumped disturbance from the adaptive law for the compensation of $\rho_{\omega r}$,

$$\mu_{\omega s} = -\alpha_{\omega r}^{c4}\omega_{m} + \beta_{\omega r}^{c4}\omega_{mr} \tag{7.20}$$

Substituting (7.19) into (7.18), the closed-loop $e_{\omega r}$-dynamics with the classic MRA speed control law is expressed as

$$\dot{e}_{\omega r} = -\alpha_{\omega r}^{c4}e_{\omega r} - \hat{\rho}_{A} + \rho_{\omega r} = -\alpha_{\omega r}^{c4}e_{\omega r} + e_{A} \tag{7.21}$$

where $e_{A} = \rho_{\omega r} - \hat{\rho}_{A}$.

The following Theorem can be used to derive the adaptive law for $\hat{\rho}_{A}$ to achieve the control objective.

Theorem 7.2. Considering the system (7.21), for the positive constant $\alpha_{\omega r}^{c4}$, if the adaptive law for $\hat{\rho}_{A}$ is designed as (7.22), $e_{\omega r}$ will converge to the origin asymptotically.

$$\dot{\hat{\rho}}_{A} = \eta_{\omega A}e_{\omega r} \tag{7.22}$$

where $\eta_{\omega A}$ is the positive constant gain.

Proof. The Lyapunov candidate function V_{A} is selected as

$$V_{A} = \frac{1}{2}e_{\omega r}^{2} + \frac{1}{2\eta_{\omega A}}e_{A}^{2} \tag{7.23}$$

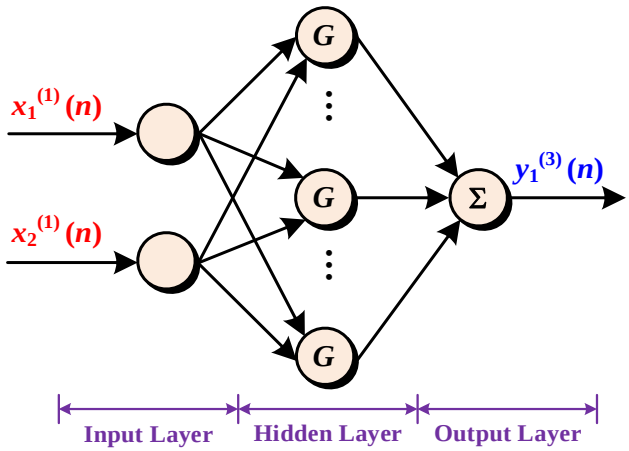

Figure 7.1 Block diagram of the RBFNN-DO used in the RBFNN-MRA speed controller.

Based on (7.21) and (7.23), $\dot{V}_A$ can be calculated as

$$\begin{aligned}\dot{V}_A &= e_{\omega r}\dot{e}_{\omega r} - \frac{1}{\eta_{\omega A}} e_A \dot{\hat{\rho}}_A = e_{\omega r}\left(-\alpha_{\omega r}^{c4} e_{\omega r} + e_A\right) - \frac{1}{\eta_{\omega A}} e_A \dot{\hat{\rho}}_A \\ &= -\alpha_{\omega r}^{c4} e_{\omega r}^2 + e_A\left(e_{\omega r} - \frac{1}{\eta_{\omega A}}\dot{\hat{\rho}}_A\right)\end{aligned} \tag{7.24}$$

Combining (7.24) with (7.22), $\dot{V}_A$ can be expressed as

$$\dot{V}_A = -\alpha_{\omega r}^{c4} e_{\omega r}^2 \le 0 \tag{7.25}$$

It can be observed that (7.25) is equivalent to (7.11). Thus, following the same procedures presented in the proof of Theorem 7.1, it can be demonstrated that $e_{\omega r}$ will converge to the origin asymptotically. The proof is completed. ■

7.3.3 RBFNN-MRA Speed Controller Design

In [16], a RBFNN-MRA speed controller has been proposed for the five-phase PMSM-VSD system, and it has been experimentally demonstrated that the tracking performance of such a speed controller is better than that of the linear PI speed controller. Therefore, the RBFNN-MRA speed controller proposed in [16] is selected as a representative of the composite speed controller combining a classic MRA speed controller with an ANN-DO to be compared in this chapter.

The adopted RBFNN-DO is illustrated in Figure 7.1. There are two input neurons, fifty-one hidden neurons and one output neuron in such an ANN-DO. The signal propagation and the activation function of each layer are described as follows.

Input Layer: In this layer, two input signals are the normalized rotor mechanical speed and the normalized RBFNN-MRA speed control law [16]. Thus, the output signals of two input neurons can be expressed as

$$y_1^{(1)}(n) = x_1^{(1)}(n) = \frac{\omega_m(n)}{\omega_{rate}} \quad y_2^{(1)}(n) = x_2^{(1)}(n) = \frac{i_{qsrb}^{c4}(n)}{10} \tag{7.26}$$

where $\omega_m(n)$ and $i_{qsrb}^{c4}(n)$ are the rotor mechanical speed and the RBFNN-MRA speed control law at the *n*th instant, respectively.

Hidden Layer: In this layer, regarding the *i*th hidden neuron ($i = 1, 2,\ldots, 51$), the signal propagation can be described as

$$x_i^{(2)}(n) = \frac{\left[y_1^{(1)}(n) - c_{r1i}\right]^2}{2\delta_{r1i}^2} + \frac{\left[y_2^{(1)}(n) - c_{r2i}\right]^2}{2\delta_{r2i}^2}, \quad i = 1,2,...,51 \tag{7.27}$$

$$y_i^{(2)}(n) = e^{-x_i^{(2)}(n)} \tag{7.28}$$

where c_{r1i} and c_{r2i} denote the centers for two Gaussian functions in the *i*th hidden neuron at the *n*th instant, δ_{r1i} and δ_{r2i} represent the widths for two Gaussian functions in the *i*th hidden neuron at the *n*th instant.

Output Layer: In this layer, the output signal is the estimated lumped disturbance in the ω_m-dynamics, which can be calculated as

$$\hat{\rho}_{RBF} = y_1^{(3)}(n) = \sum_{i=1}^{51} W_{ri}^{(2)}(n) y_i^{(2)}(n) \tag{7.29}$$

where $\hat{\rho}_{RBF}$ is the estimated lumped disturbance from the RBFNN-DO, $W_{ri}^{(2)}(n)$ denotes the connective weight between the output neuron and the *i*th hidden neuron at the *n*th instant.

Remark 7.2. In the RBFNN-DO adopted by the RBFNN-MRA speed controller proposed in [16], the values of c_{r1i}, c_{r2i}, δ_{r1i} and δ_{r2i} are set in advance, and $W_{ri}^{(2)}(n)$ is updated online by the adaptive law.

On the basis of the $e_{\omega r}$-dynamics expressed as (7.18) and the reference model expressed as (7.17), the RBFNN-MRA speed control law i_{qsrb}^{c4} is designed as follow [16]:

$$i_{qsrb}^{c4} = \frac{1}{b_{\omega n2}}\left(\mu_{\omega s} + y_{r\omega}\right) \tag{7.30}$$

where $y_{r\omega}$ is the output signal of the adopted RBFNN-DO for the compensation of $\rho_{\omega r}$, which is expressed as

$$y_{r\omega} = \boldsymbol{W}_r^{(2)T} \boldsymbol{y}^{(2)}(n) \tag{7.31}$$

where $\boldsymbol{W}_r^{(2)}(n) = [W_{r1}^{(2)}(n),\ W_{r2}^{(2)}(n),\ldots,\ W_{r51}^{(2)}(n)]^T$ and $\boldsymbol{y}^{(2)}(n) = [y_1^{(2)}(n),\ y_2^{(2)}(n),\ldots,\ y_{51}^{(2)}(n)]^T$ are the output weight vector and the output signal vector of the hidden layer of the RBFNN-DO, respectively.

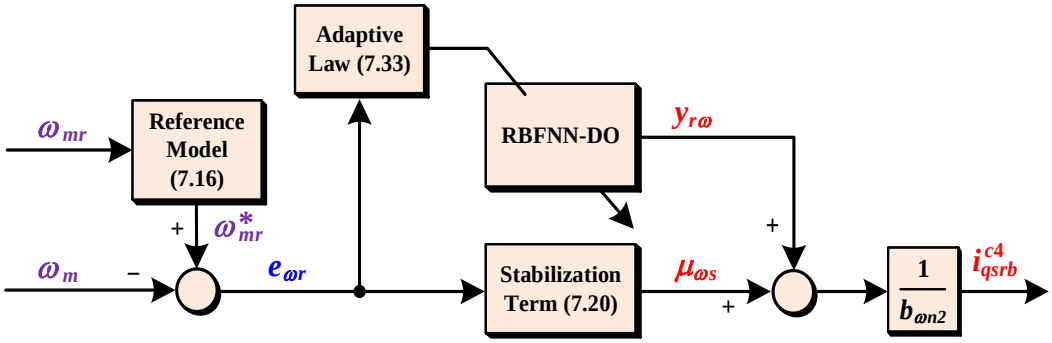

Figure 7.2 Block diagram of the RBFNN-MRA speed controller.

Substituting (7.30) into (7.18), the closed-loop $e_{\omega r}$-dynamics with the RBFNN-MRA speed control law is expressed as

$$\dot{e}_{\omega r} = -\alpha_{\omega r}^{c4} e_{\omega r} - \boldsymbol{W}_r^{(2)T} \boldsymbol{y}^{(2)}(n) + \rho_{\omega r} \tag{7.32}$$

The following Theorem can be used to derive the adaptive laws for $\boldsymbol{W}_r^{(2)}(n)$ for accomplishing the control objective.

Theorem 7.3 [16], [18]. Considering the system (7.21), for the positive constant $\alpha_{\omega r}^{c4}$, if the adaptive law for $W_{ri}^{(2)}$ is designed as (7.33), $e_{\omega r}$ will converge to the origin asymptotically.

$$\dot{W}_{ri}^{(2)} = \eta_{\omega R1} e_{\omega r} y_i^{(2)} - \eta_{\omega R2} W_{ri}^{(2)} \tag{7.33}$$

where $\eta_{\omega R1}$ and $\eta_{\omega R2}$ are two positive constant gains.

Remark 7.3. In the RBFNN-MRA speed controller, the construction of the disturbance compensation term is achieved by the RBFNN-DO. The adaptive laws are employed for the online update of the connective weights of the RBFNN-DO, rather than the estimation of $\rho_{\omega r}$.

Remark 7.4. From a practical point of view, the existence of the second term in the right side of (7.33) leads to the fact that the low-pass filter rather than the pure integrator is adopted by each adaptive law of the RBFNN-DO presented in [16].

The block diagram of the RBFNN-MRA speed controller is illustrated in Figure 7.2.

7.3.4 Type-4 Composite Speed Controller Design

The design of the STSMO for the estimation of $\rho_{\omega r}$ is dependent on the extended ω_m-dynamics. Based on (7.15), selecting $-\rho_{\omega r}$ as an augmented state variable, the extended ω_m-dynamics can be derived as

$$\begin{cases} \dot{z}_{r\omega 1} = b_{\omega n2} i_{qsr}^{c4} + z_{r\omega 2} \\ \dot{z}_{r\omega 2} = -\dot{\rho}_{\omega r} \end{cases} \tag{7.34}$$

where $z_{r\omega 1} = \omega_m$ and $z_{r\omega 2} = -\rho_{\omega r}$ denote two state variables of the extended ω_m-dynamics.

On the basis of the STSMO design presented in Section 3.3.2, the STSMO can be designed as (7.35) for the estimation of $\rho_{\omega r}$.

$$\begin{cases} \dot{\hat{z}}_{r\omega 1} = b_{\omega n2} i_{qsr}^{c4} + \hat{z}_{r\omega 2} + k_{s1}^{c4} \sqrt{|\omega_m - \hat{z}_{r\omega 1}|}\, \mathrm{sgn}(\omega_m - \hat{z}_{r\omega 1}) \\ \dot{\hat{z}}_{r\omega 2} = k_{s2}^{c4}\, \mathrm{sgn}(\omega_m - \hat{z}_{r\omega 1}) \end{cases} \tag{7.35}$$

where $\hat{z}_{r\omega 1} = \hat{\omega}_m$ and $\hat{z}_{r\omega 2} = -\hat{\rho}_{rST}$ represent the estimated two state variables of the extended ω_m-dynamics.

Based on (7.34) and (7.35), the state estimation error system for the adopted STSMO can be described as

$$\begin{cases} \dot{e}_{r\omega 1} = -k_{s1}^{c4} \sqrt{|e_{r\omega 1}|}\, \mathrm{sgn}(e_{r\omega 1}) + e_{r\omega 2} \\ \dot{e}_{r\omega 2} = -k_{s2}^{c4}\, \mathrm{sgn}(e_{r\omega 1}) + \dot{z}_{r\omega 2} \end{cases} \tag{7.36}$$

where $e_{r\omega 1} = \omega_m - \hat{\omega}_m$ and $e_{r\omega 2} = -\rho_{\omega r} + \hat{\rho}_{rST}$ represent two state estimation errors.

Considering Theorem 3.1 and Assumption 7.2, two positive constant gains k_{s1}^{c4} and k_{s2}^{c4} for the STSMO are selected as (7.37) such that the finite-time stability of the state estimation error system is guaranteed.

$$k_{s1}^{c4} > 2, \quad k_{s2}^{c4} > \frac{(k_{s1}^{c4})^2 + 4(L_{\omega 2}^{c4})^2}{4\left(k_{s1}^{c4} - 2\right)} \tag{7.37}$$

On the basis of the $e_{\omega r}$-dynamics expressed as (7.18) and the reference model expressed as (7.16), the type-4 composite speed control law i_{qsr}^{c4} is designed as

$$i_{qsr}^{c4} = \frac{1}{b_{\omega n2}} \left(\mu_{\omega s} + \hat{\rho}_{rST} - \varepsilon_{c\omega 3} \right) \tag{7.38}$$

where $\varepsilon_{c\omega 3}$ is the error compensation term for the estimation error of the adopted STSMO in practice.

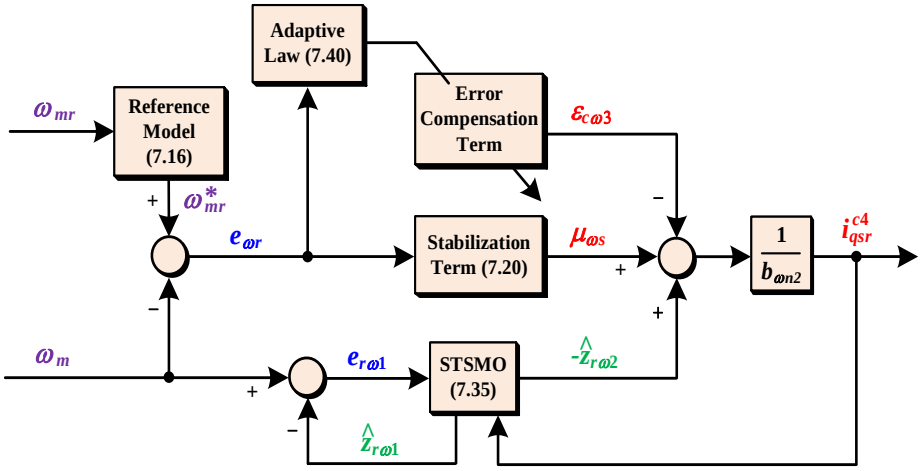

Figure 7.3 Block diagram of the type-4 composite speed controller.

Substituting (7.38) into (7.18), the closed-loop $e_{\omega r}$-dynamics with the type-4 composite speed control law is expressed as

$$\begin{aligned}\dot{e}_{\omega r} &= -\alpha_{\omega r}^{c4} e_{\omega r} - \hat{\rho}_{rST} + \varepsilon_{c\omega 3} + \rho_{\omega r} = -\alpha_{\omega r}^{c4} e_{\omega r} + \varepsilon_{c\omega 3} - e_{r\omega 2} \\ &= -\alpha_{\omega r}^{c4} e_{\omega r} - \tilde{\varepsilon}_{c\omega 3}\end{aligned} \tag{7.39}$$

where $\tilde{\varepsilon}_{c\omega 3} = e_{r\omega 2} - \varepsilon_{c\omega 3}$.

Based on Theorem 7.1, it can be concluded that, for the positive constant $\alpha_{\omega r}^{c4}$, with the type-4 composite speed control law (7.38), $e_{\omega r}$ will converge to the origin asymptotically if the adaptive law for $\varepsilon_{c\omega 3}$ is designed as

$$\dot{\varepsilon}_{c\omega 3} = -\eta_{\omega s} e_{\omega r} \tag{7.40}$$

where $\eta_{\omega s}$ is the positive constant gain.

The block diagram of the type-4 composite speed controller is shown in Figure 7.3.

7.3.5 Experimental Results

The experimental test bench described in Section 2.5 is used to perform comparative experimental tests among three selected classic MRA speed controllers with different values of $\eta_{\omega A}$, three selected ENN-ICSM speed controllers with different values of $\eta_{\omega R1}$ and the type-4 composite speed controller in the frame of the FOC strategy whose block diagram is illustrated in Figure 5.2. The parameters of these rotor speed controllers are listed in Table 7.1. Note that, in accordance with [16], both δ_{r1i} and δ_{r2i} are equal to 0.5, and the values of c_{r1i} and c_{r2i} are evenly distributed between -2 and 2. Furthermore, in all tested FOC strategies, the proportional and integral gains of each PI

stator current controller are set to 20.42 and 7379, respectively.

Table 7.1 Parameters of tested rotor speed controllers

Rotor speed controller	Parameters
Classic MRA speed controller 1	$\alpha_{\omega r}^{c4} = 400,\ \beta_{\omega r}^{c4} = 400,\ \eta_{\omega A} = 40000$
Classic MRA speed controller 2	$\alpha_{\omega r}^{c4} = 400,\ \beta_{\omega r}^{c4} = 400,\ \eta_{\omega A} = 80000$
Classic MRA speed controller 3	$\alpha_{\omega r}^{c4} = 400,\ \beta_{\omega r}^{c4} = 400,\ \eta_{\omega A} = 120000$
RBFNN-MRA speed controller 1	$\alpha_{\omega r}^{c4} = 400,\ \beta_{\omega r}^{c4} = 400,$ $\eta_{\omega R1} = 9000,\ \eta_{\omega R1} = 2,\ \delta_{r1i} = \delta_{r2i} = 0.5,$ $c_{r1i} = c_{r2i} = -2 + 0.08(i - 1)$
RBFNN-MRA speed controller 2	$\alpha_{\omega r}^{c4} = 400,\ \beta_{\omega r}^{c4} = 400,$ $\eta_{\omega R1} = 13000,\ \eta_{\omega R1} = 2,\ \delta_{r1i} = \delta_{r2i} = 0.5,$ $c_{r1i} = c_{r2i} = -2 + 0.08(i - 1)$
RBFNN-MRA speed controller 3	$\alpha_{\omega r}^{c4} = 400,\ \beta_{\omega r}^{c4} = 400,$ $\eta_{\omega R1} = 17000,\ \eta_{\omega R1} = 2,\ \delta_{r1i} = \delta_{r2i} = 0.5,$ $c_{r1i} = c_{r2i} = -2 + 0.08(i - 1)$
Type-4 composite speed controller	$\alpha_{\omega r}^{c4} = 400,\ \beta_{\omega r}^{c4} = 400,$ $k_{s1}^{c4} = 6000,\ k_{s2}^{c4} = 1000000,\ \eta_{\omega s} = 3000$

Table 7.2 Dynamic performance of tested rotor speed controllers in the first test

Rotor speed controller	Overshoot (%)	Settling time (ms)
Classic MRA speed controller 1	3.933	44
Classic MRA speed controller 2	2.990	60
Classic MRA speed controller 3	2.696	66
RBFNN-MRA speed controller 1	2.515	40
RBFNN-MRA speed controller 2	2.166	50
RBFNN-MRA speed controller 3	1.839	58
Type-4 composite speed controller	1.462	36

In the first test, the value of the load torque is set to 0 N·m, while the value of the reference rotor mechanical speed is increased from 500 rpm to 2500 rpm with the acceleration of 100 rpm/ms. The rotor mechanical speed responses and corresponding tracking errors for seven tested rotor speed

controllers are shown in Figure 7.4. The dynamic performance of seven tested rotor speed controllers are summarized in Table 7.2. Note that the tolerance band is chosen as $\pm$ 25 rpm, namely $\pm$ 1 % of 2500 rpm, for the settling time calculation. It can be seen that the increase of the values of $\eta_{\omega A}$ and $\eta_{\omega R1}$ can reduce the overshoot for the rotor mechanical speed responses of the classic MRA speed controller and the RBFNN-MRA speed controller, respectively. However, the price we pay for the reduction of the overshoot is the growth of the settling time and the appearance of undesired oscillations in the transient period. Compared with these two rotor speed controllers, the proposed type-4 composite speed controller achieves the smallest overshoot and the shortest settling time for the rotor mechanical speed response.

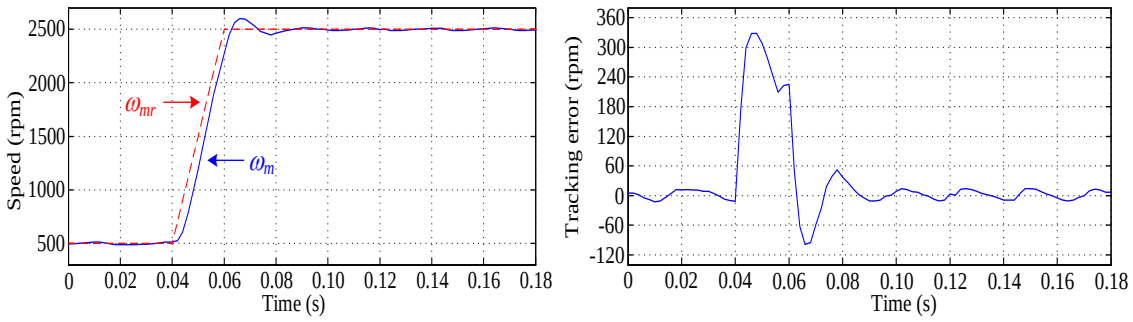

(a)

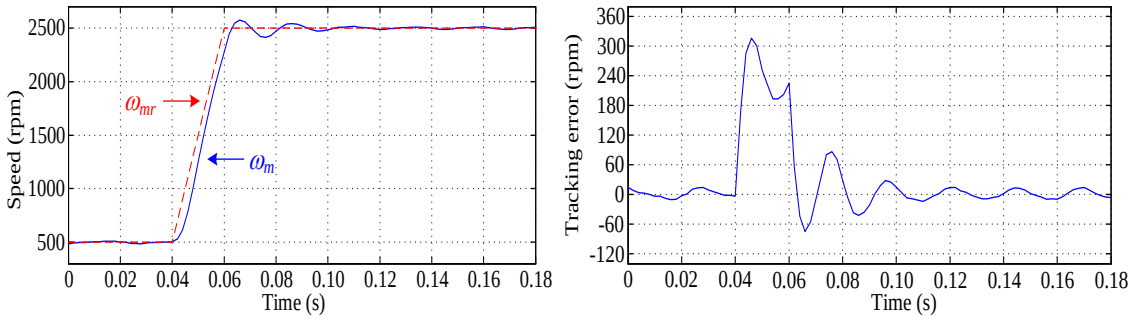

(b)

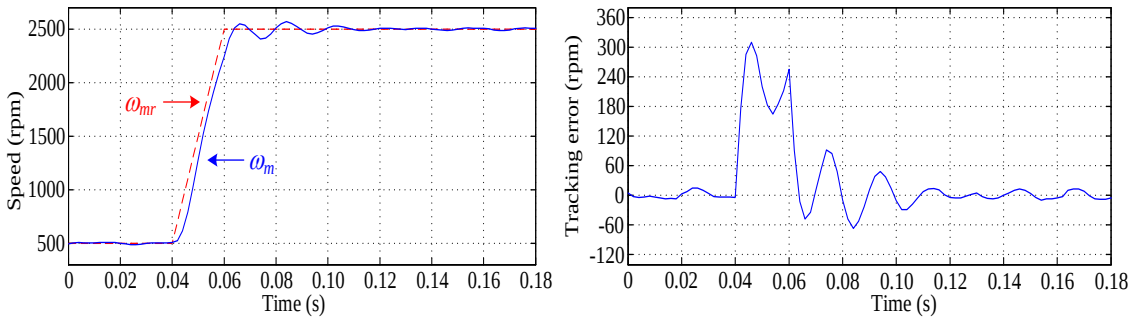

(c)

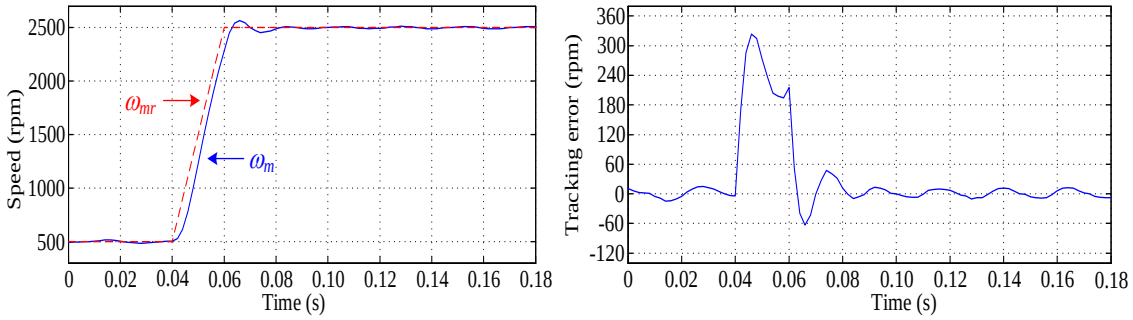

(d)

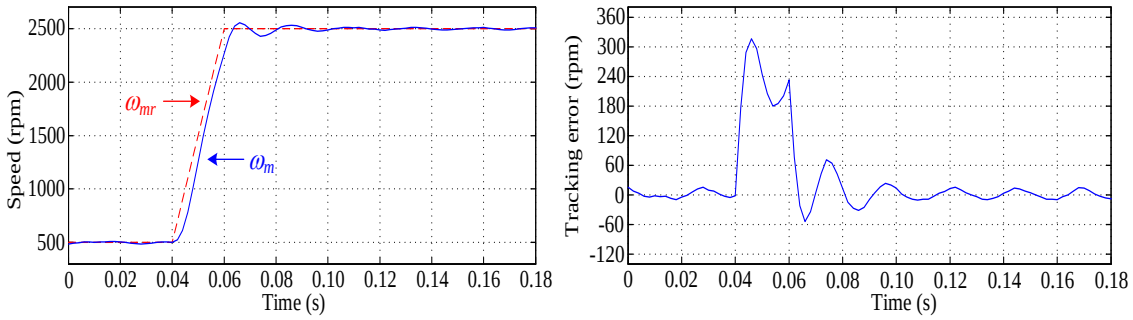

(e)

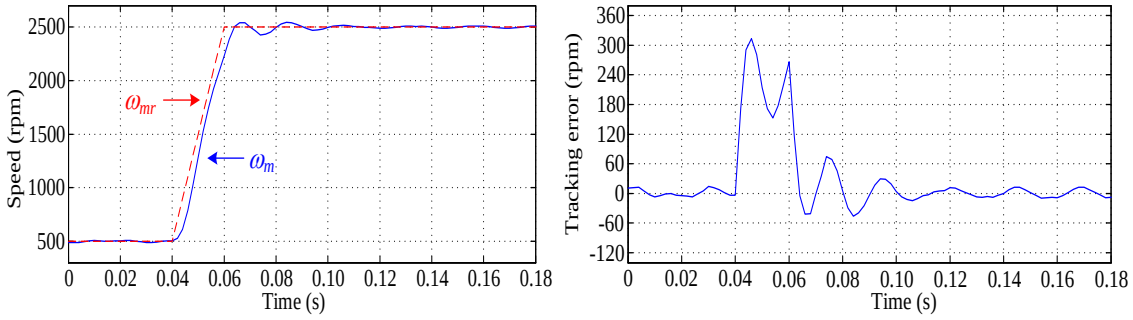

(f)

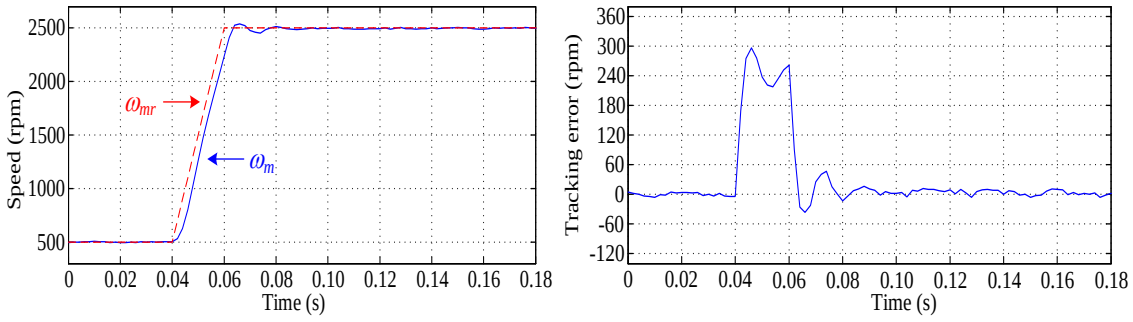

(g)

Figure 7.4 Rotor mechanical speed responses and corresponding tracking errors for the first test. (a) Classic MRA speed controller 1. (b) Classic MRA speed controller 2. (c) Classic MRA speed controller 3. (d) RBFNN-MRA speed controller 1. (e) RBFNN-MRA speed controller 2. (f) RBFNN-MRA speed controller 3. (g) Type-4 composite speed controller.

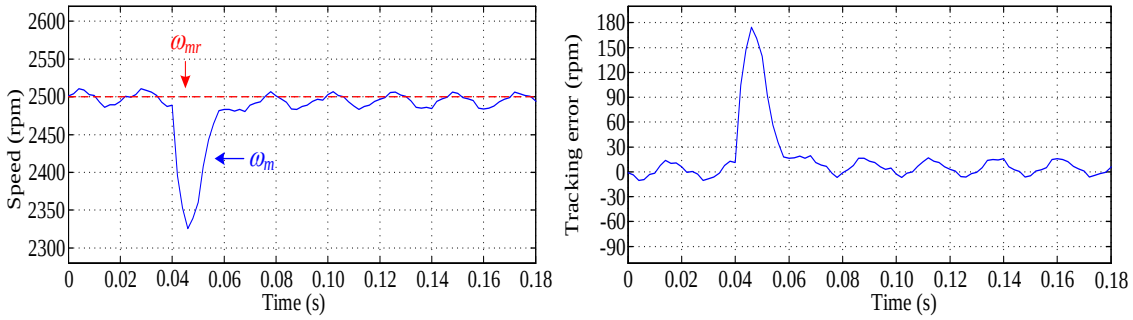
Speed (rpm)
Time (s)
ω_{mr}
ω_m
Tracking error (rpm)
Time (s)

(a)

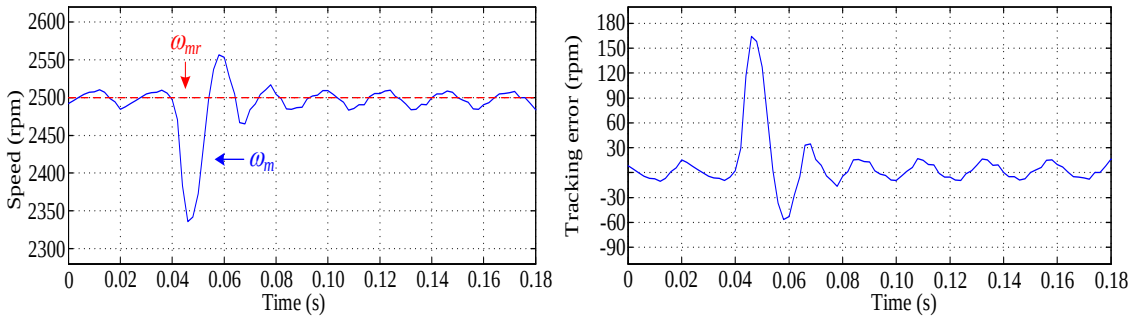
Speed (rpm)
Time (s)
ω_{mr}
ω_m
Tracking error (rpm)
Time (s)

(b)

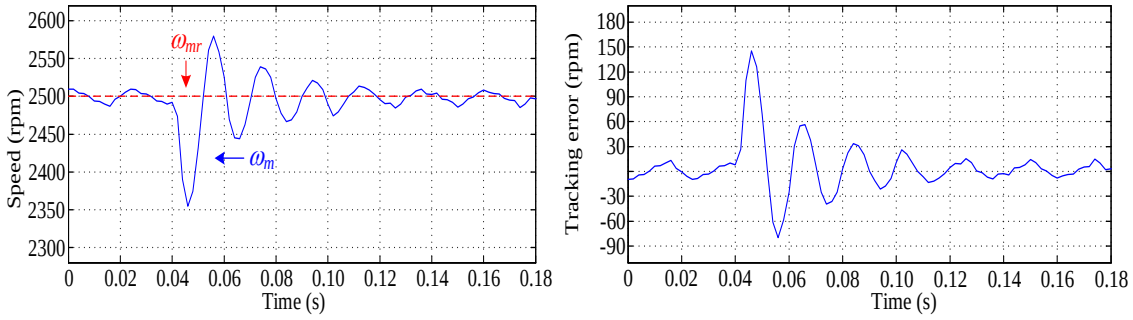
Speed (rpm)
Time (s)
ω_{mr}
ω_m
Tracking error (rpm)
Time (s)

(c)

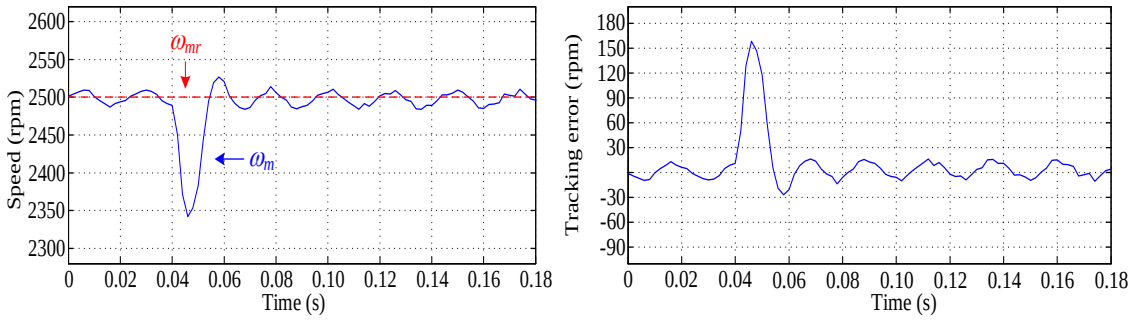
Speed (rpm)
Time (s)
ω_{mr}
ω_m
Tracking error (rpm)
Time (s)

(d)

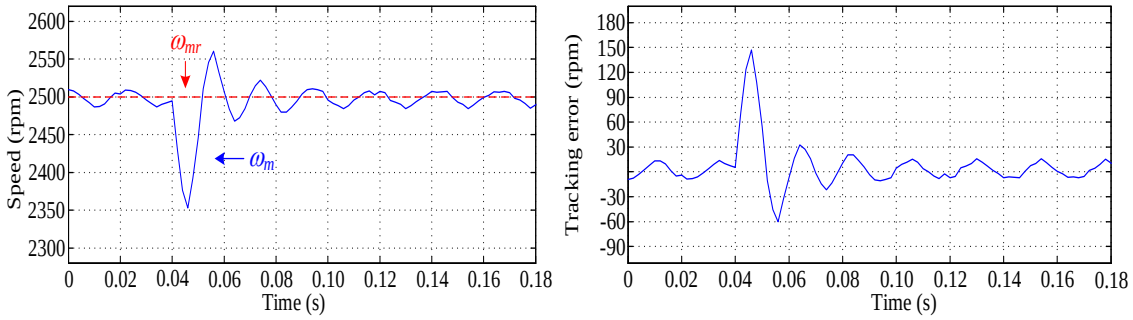

(e)

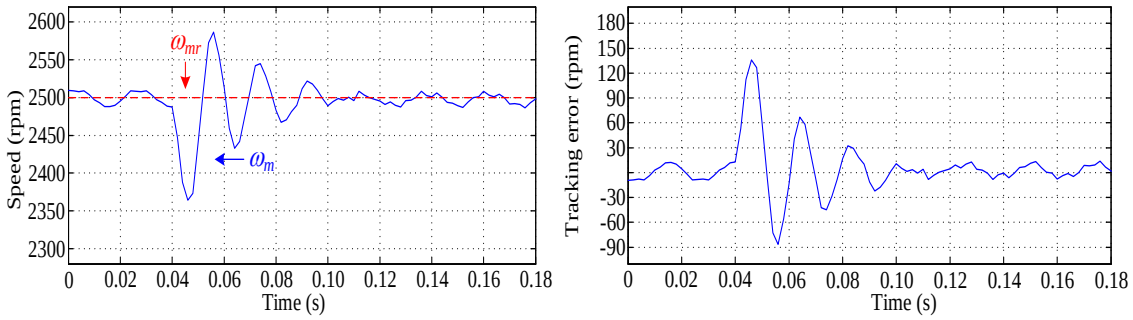

(f)

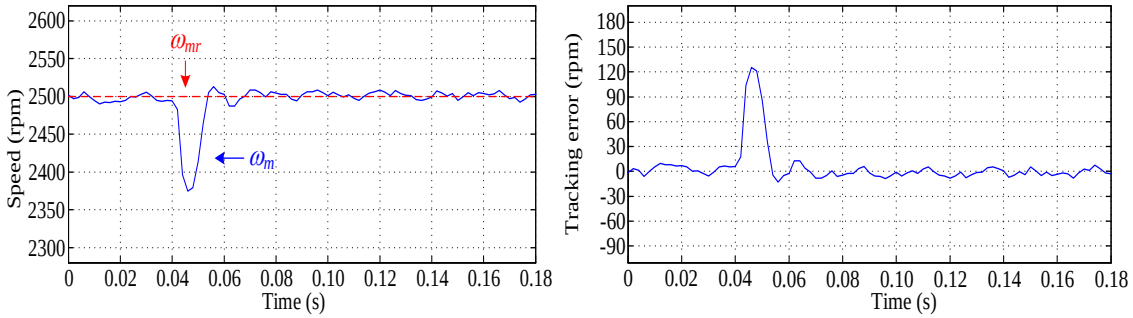

(g)

Figure 7.5 Rotor mechanical speed responses and corresponding tracking errors for the second test. (a) Classic MRA speed controller 1. (b) Classic MRA speed controller 2. (c) Classic MRA speed controller 3. (d) RBFNN-MRA speed controller 1. (e) RBFNN-MRA speed controller 2. (f) RBFNN-MRA speed controller 3. (g) Type-4 composite speed controller.

In the second test, the value of the applied reference rotor mechanical speed is kept at 2500 rpm, and the value of the load torque steps from 0 N·m to 0.6 N·m at 0.04 s. The rotor mechanical speed responses and corresponding tracking errors for seven tested rotor speed controllers are shown in Figure 7.5. The dynamic performance of seven tested rotor speed controllers are summarized in Table 7.3 in which the criterion for the settling time calculation is the same as the first test. It can be observed that, with the increase of the value of $\eta_{\omega A}$ and $\eta_{\omega R1}$, the maximum tracking error for the

classic MRA speed controller and the RBFNN-MRA speed controller decrease, respectively. Nevertheless, similar to the first test, the price we pay for the reductions of the maximum tracking error is the growth of the settling time and the appearance of undesired oscillations in the transient period. Among all tested rotor speed controllers, the proposed type-4 composite speed controller achieves the shortest settling time and the smallest maximum tracking error.

Table 7.3 Dynamic performance of tested rotor speed controllers in the second test

Rotor speed controller	Maximum tracking error (rpm)	Settling time (ms)
Classic MRA speed controller 1	174.63	18
Classic MRA speed controller 2	164.07	30
Classic MRA speed controller 3	145.59	64
RBFNN-MRA speed controller 1	158.02	20
RBFNN-MRA speed controller 2	147.09	28
RBFNN-MRA speed controller 3	135.65	46
Type-4 composite speed controller	125.26	14

Table 7.4 Calculation time in each sampling period

Classic MRA speed controller-based FOC strategy	Selected RBFNN-MRA speed controller-based FOC strategy	Type-4 composite speed controller-based FOC strategy
10.81 μs	93.59 μs	12.18 μs

In order to evaluate the implementation complexities of the classic MRA speed controller, the selected RBFNN-MRA speed controller and the type-4 composite speed controller, the calculation time of the FOC strategy in each sampling period is chosen as the index. Table 7.4 shows such indexes for FOC strategies using the classic MRA speed controller, the selected RBFNN-MRA speed controller and the type-4 composite speed controller. It can be seen that, compared with the classic MRA speed controller-based FOC strategy, the calculation times of the FOC strategies using the selected RBFNN-MRA speed controller and the type-4 composite speed controller in each sampling period rise by 765.77 % and 12.67 %, respectively. Therefore, the implementation of the RBFNN-DO presented in [16] significantly increases the computational burden of the DSP, such that it may be difficult for the corresponding RBFNN-MRA speed controller-based FOC strategy to incorporate the schemes for other purposes, such as the rotor position observation and the inverter

nonlinearity effect compensation. Moreover, the type-4 composite speed controller is more computationally efficient than the selected RBFNN-MRA speed controller.

7.4 Summary

In this chapter, a novel composite controller named as the type-4 composite controller is proposed for a single-input uncertain nonlinear system with relative degree one. The proposed composite controller is composed of a classic MRA controller and a STSMO. A stable first-order linear model is selected as the reference model to describe the desired output trajectory for the system. There are three terms in the proposed composite controllers. The first term is the stabilization term dependent on known parts of the system and the selected reference model for stabilizing the dynamics of the output tracking error between the desired and actual outputs of the system asymptotically. The second term is the disturbance compensation term based on the STSMO for compensating the lumped disturbance in the dynamics of the output tracking error between the desired and actual outputs of the system. The third term is the error compensation term updated online by an adaptive law, which is derived from the Lyapunov synthesis approach, for confronting the estimation error of the STSMO in practice. The rigorous stability analysis of the dynamics of the output tracking error between the desired and actual outputs of the system with the type-4 composite controller is presented.

With respect to the 2L-VSI-fed SPMSM-VSD system, a novel robust FOC strategy is proposed. In this FOC strategy, a type-4 composite speed controller and two linear PI current controllers are adopted. Comparative experimental tests among three selected classic MRA speed controllers, three selected RBFNN-MRA speed controllers and the type-4 composite speed controller in the frame of the FOC strategy are performed on the experimental test bench described in Section 2.5. Corresponding experimental results demonstrate that the type-4 composite speed controller can achieve the minimum rotor speed transient variation and the fastest dynamic response. Moreover, compared with the selected RNFNN-MRA speed controller, the computational burden of the DSP to implement the type-4 composite speed controller is lower.

References

[1] J. J. E. Slotine and W. Li, *Applied Nonlinear Control*. Englewood Cliffs, NJ, USA: Prentice-Hall, 1991.

[2] P. A. Ioannou and J. Sun, *Robust Adaptive Control*. Moneola, USA: Dover Publications, 2012.

[3] S. Nicosia and P. Tomei, "Model reference adaptive control algorithms for industrial robots," *Automatica*, vol. 20, no. 5, pp. 635-644, Jan. 1984.

[4] P. K. Sinha and A. N. Pechev, "Model reference adaptive control of a maglev system with stable maximum descent criterion," *Automatica*, vol. 35, no. 8, pp. 1457-1465, Aug. 1999.

[5] T. -H. Liu and H. -H. Hsu, "Adaptive controller design for a synchronous reluctance motor drive system with direct torque control," *IET Electric Power Applications*, vol. 1, no. 5, pp. 815-824, Sep. 2007.

[6] K. -K. Shyu, M. -J. Yang, Y. -M. Chen, and Y. -F. Lin, "Model reference adaptive control design for a shunt active-power-filter system," *IEEE Transactions on Industrial Electronics*, vol. 55, no. 1, pp. 97-106, Jan. 2008.

[7] M. Tárník and J. Murgaš, "Model reference adaptive control of permanent magnet synchronous motor," *Journal of Electrical Engineering*, vol. 62, no. 3, pp. 117-125, May 2011.

[8] J. Yao and C. Wang, "Model reference adaptive control for a hydraulic underwater manipulator," *Journal of Vibration and Control*, vol. 18, no. 6, pp. 893-902, May 2012.

[9] Z. T. Dydek, A. M. Annaswamy, and E. Lavretsky, "Adaptive control of quadrotor UAVs: a design trade study with flight evaluations," *IEEE Transactions on Control Systems Technology*, vol. 21, no. 4, pp. 1400-1406, Jul. 2013.

[10] Y. Zhou and Z. Zhang, "High-speed train control based on multiple-model adaptive control with second-level adaptation," *Vehicle System Dynamics*, vol. 52, no. 5, pp. 637-652, Feb. 2014.

[11] R. Khanna, Q. Zhang, W. E. Stanchina, G. F. Reed, and Z. -H. Mao, "Maximum power point tracking using model reference adaptive control," *IEEE Transactions on Power Electronics*, vol. 29, no. 3, pp. 1490-1499, Mar. 2014.

[12] A. T. Nguyen, M. S. Rafaq, H. H. Choi, and J. W. Jung, "A model reference adaptive control based speed controller for a surface-mounted permanent magnet synchronous motor drive," *IEEE Transactions on Industrial Electronics*, vol. 65, no. 12, pp. 9399-9409, Dec. 2018.

[13] J. Han, S. Yu, and S. Yi, "Oxygen excess ratio control for proton exchange membrane fuel cell using model reference adaptive control," *International Journal of Hydrogen Energy*, vol. 44, no. 33, pp. 18425-18437, Dec. 2018.

[14] S. Li, J. Yang, W. -H. Chen, and X. Chen, *Disturbance Observer-Based Control Methods and Applications*. Boca Raton, USA: CRC Press, 2017.

[15] K. -K. Shyu, H. -J. Shieh, and S. -S. Fu, "Model reference adaptive speed control for induction motor drive using neural network," *IEEE Transactions on Industrial Electronics*, vol. 45, no. 1, pp. 180-182, Feb. 1998.

[16] L. Guo and L. Persa, "Model reference adaptive control of five-phase IPM motors based on neural network," *IEEE Transactions on Industrial Electronics*, vol. 59, no. 3, pp. 1500-1508, Mar. 2012.

[17] H. -K. Chiang and C.-T. Chu, "Reference model with an adaptive Hermite fuzzy neural network controller for tracking a synchronous reluctance motor," *Electric Power Components and Systems*, vol. 43, no. 7, pp. 770-780, Apr. 2015.

[18] H. D. Patiño and D. Liu, "Neural network-based model reference adaptive control system," *IEEE Transactions on Systems, Man, and Cybernetics, Part B (Cybernetics)*, vol. 30, no. 1, pp. 1500-1508, Feb. 2000.

8

CONCLUSIONS AND PERSPECTIVES

Conclusions

Combining a feedback controller with a well-designed DO is an effective way to improve the robustness of such a controller-based closed-loop tracking control system against the unmodeled dynamics, parametric uncertainties and external disturbances. In this thesis, four novel composite controllers, each of which combines a nonlinear feedback controller with a DO, are proposed for a single-input uncertain nonlinear system with relative degree one for the disturbance attenuation ability improvement and applied to the construction of novel robust FOC strategies for 2L-VSI-fed SynRM-VSD and 2L-VSI-fed SPMSM-VSD systems.

The first proposed composite controller is named as the type-1 composite controller. Such a composite controller consists of a standard STSM controller, a HNN-DO and an error compensator. The standard STSM controller is used to achieve the finite-time convergence of the sliding variable to the origin. The HNN-DO is used to compensate the lumped disturbance in the sliding variable dynamics. The error compensator is used to compensate the approximation error of the adopted HNN-DO. The rigorous stability analysis of the sliding variable dynamics with the type-1 composite controller is presented. On the basis of that, the learning laws for the connective weights between the output neuron and the hidden neurons in the HNN-DO and the error compensator are rigorously derived. Besides the HNN-DO and its corresponding error compensator, these learning laws are suitable for any other type of ANN-DO and its corresponding error compensator used in a standard STSM controller-based composite controller. After the rigorous theoretical analysis, the type-1 composite controller is applied to the construction of a novel robust FOC strategy for the 2L-VSI-fed SynRM-VSD system. In this FOC strategy, the type-1 composite controller is used as a rotor

speed controller for achieving the robust rotor speed tracking control. The type-1 composite speed controller is design using the practical speed dynamics of the SynRM considering unmodeled dynamics, parametric uncertainties and external disturbances. Since the magnetic saturation effect makes each practical current dynamics of the SynRM become a nonlinear system in terms of two stator current components in the rotor reference frame, two composite current controllers, each of which is composed of two standard STSM controllers, are proposed to achieve the robust stator current tracking control. Each composite current controller is designed using the corresponding practical current dynamics of the SynRM considering unmodeled dynamics, parametric uncertainties and external disturbances. Rigorous stability analysis for each current tracking error dynamics using the corresponding composite current controller is also presented. Comparative HIL tests between the proposed FOC strategy and the classic STA-based FOC strategy for the 2L-VSI-fed SynRM-VSD system, which is based on a standard STSM speed controller and two linear PI current controllers, are performed. The results of HIL tests demonstrate that the proposed FOC strategy can accomplish better tracking performance and higher robustness against disturbances/ uncertainties.

The second proposed composite controller is named as the type-2 composite controller. Such a composite controller consists of a modified STSM controller and a second-order ESO. The modified STSM controller is used to stabilize the sliding variable dynamics in a finite time. The second-order ESO is used to compensate the lumped disturbance in the sliding variable dynamics. The rigorous stability analysis of the sliding variable dynamics with the type-2 composite controller is presented. After the rigorous theoretical analysis, the type-2 composite controller is applied to the construction of a novel robust FOC strategy for the 2L-VSI-fed SPMSM-VSD system. In this FOC strategy, the type-2 composite controller is used as a rotor speed controller for achieving the robust rotor speed tracking control. The type-2 composite speed controller is designed using the practical speed dynamics of the SPMSM considering unmodeled dynamics, parametric uncertainties and external disturbances. As for the current control loop of this FOC strategy, two linear PI controllers are adopted. Comparative experimental tests among the FOC strategy using the standard STSM speed controller, the FOC strategy using the ESO-based standard STSM speed controller, the FOC strategy using the modified STSM speed controller and the proposed FOC strategy using the type-2 composite speed controller are performed. Experimental results demonstrate that, among four tested FOC strategies, the proposed FOC strategy using the type-2 composite speed controller can achieve the minimum rotor speed transient variation and the fastest dynamic response.

The third proposed composite controller is named as the type-3 composite controller. Such a composite controller consists of a sign function-based CSM controller and a STSMO. The sign

function-based CSM controller is used to stabilize the output tracking error dynamics asymptotically. The STSMO is used to compensate the lumped disturbance in the output tracking error dynamics. The rigorous stability analysis of the output tracking error dynamics with the type-3 composite controller is presented. After rigorous theoretical analysis, the type-3 composite controller is applied to the construction of a novel robust FOC strategy for the 2L-VSI-fed SPMSM-VSD system. In this FOC strategy, the type-3 composite controller, which is designed using the practical speed dynamics of the SPMSM considering unmodeled dynamics, parametric uncertainties and external disturbances, is used as a rotor speed controller for achieving the robust rotor speed tracking control, and two linear PI controllers are adopted as two stator current controllers. Comparative experimental tests among the FOC strategy using classic CSM speed controller, three FOC strategies, which use three selected ENN-ICSM speed controllers, respectively, and the proposed FOC strategy using the type-3 composite speed controller are performed. Experimental results demonstrate that: 1) among five tested FOC strategies, the proposed FOC strategy using the type-3 composite speed controller can achieve the minimum rotor speed transient variation and the fastest dynamic response; and 2) the type-3 composite speed controller is more computationally efficient than the selected ENN-ICSM speed controllers.

The fourth proposed composite controller is named as the type-4 composite controller. Such a composite controller consists of a classic MRA controller and a STSMO. A stable first-order linear model is selected as the reference model to generate the desired output trajectory for the system. The type-4 composite controller comprises three terms. The first term is the stabilization term, which is based on the known parts of the system and the selected reference model, for the asymptotic convergence of the output tracking error between the desired and actual outputs of the system to the origin. The second term is the disturbance compensation term, which is dependent on the STSMO, for compensating the lumped disturbance in the dynamics of the above-mentioned tracking error. The third term is the error compensation term, which is updated by an adaptive law online, for confronting the estimation error of the STSMO in practice. The rigorous stability analysis of the dynamics of the above-mentioned tracking error with the type-4 composite controller is presented. Based on that, the adaptive law for the error compensation term is derived. After rigorous theoretical analysis, the type-4 composite controller is applied to the construction of a novel robust FOC strategy for the 2L-VSI-fed SPMSM-VSD system. In this FOC strategy, the type-4 composite controller, which is designed using the practical speed dynamics of the SPMSM considering unmodeled dynamics, parametric uncertainties and external disturbances, is used as a rotor speed controller for achieving the robust rotor speed tracking control, and two linear PI controllers are adopted as two stator current controllers. Comparative experimental tests among three FOC

strategies, which use three selected classic MRA speed controllers, respectively, three FOC strategies, which adopt three selected RBFNN-MRA speed controllers, respectively, and the proposed FOC strategy using the type-4 composite speed controller are performed. Experimental results demonstrate that: 1) among seven tested FOC strategies, the proposed FOC strategy using the type-4 composite speed controller can achieve the minimum rotor speed transient variation and the fastest dynamic response; and 2) the type-4 composite speed controller is more computationally efficient than the selected RBFNN-MRA speed controllers.

Future Work

For future work, the following research topics will be taken into account:

1) A comparative study between the composite controller combining a standard STSM controller with an ANN-DO and the composite controller combining a standard STSM controller with a model-based extended DO.

2) Applying four proposed composite controllers to the current control loop of the FOC strategy for the 2L-VSI-fed SPMSM-VSD system to further improve the robustness of the FOC strategy against the unmodeled dynamics, parametric uncertainties and external disturbances in the stator current dynamics

3) Developing a novel magnetic model for the SynRM.